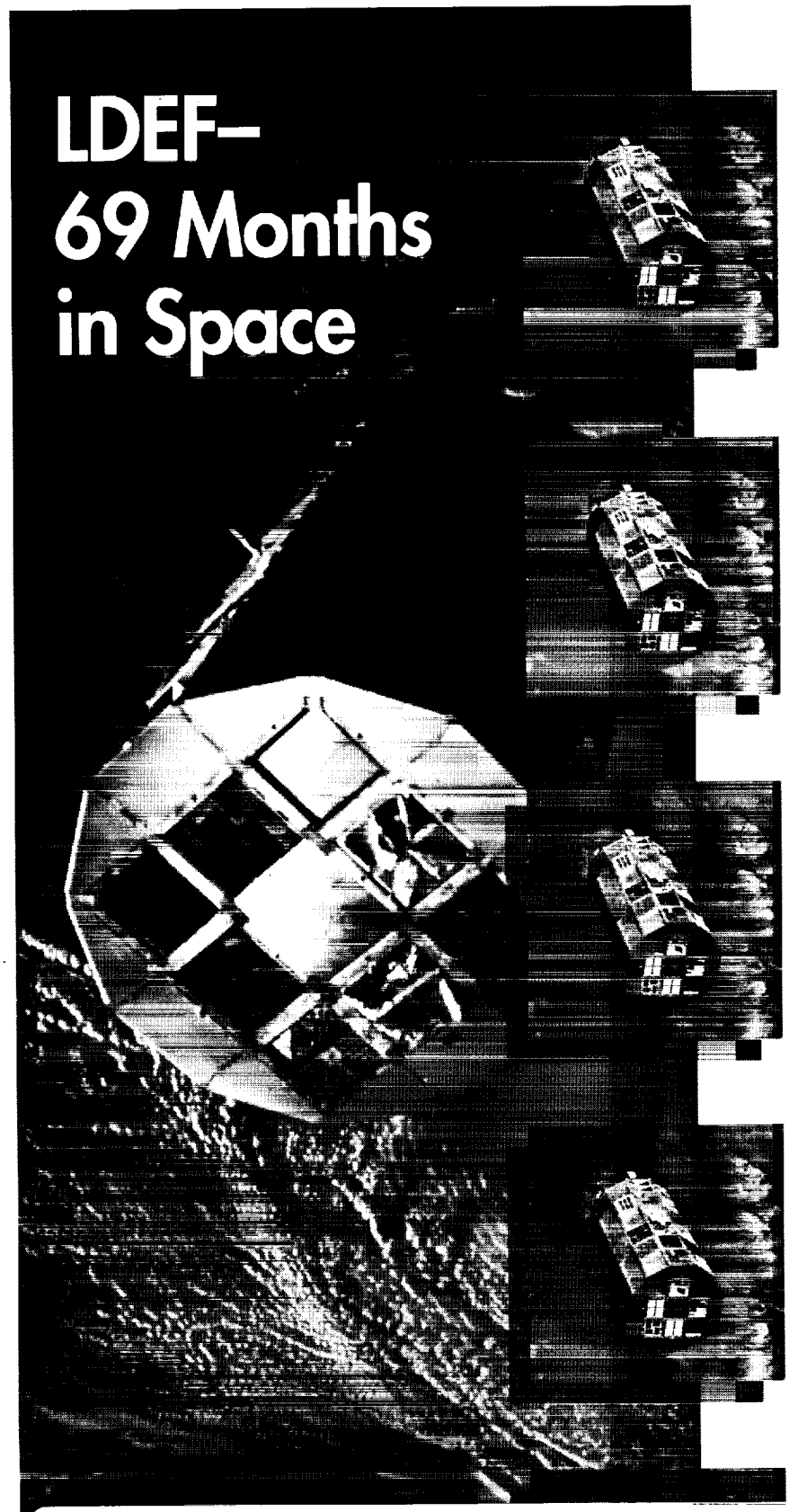

LDEF–69 Months in Space

Second Post - Retrieval Symposium

June 1-5, 1992
San Diego, California

Sponsors:

LDEF Science Office
NASA Langley Research Center

American Institute of
Aeronautics and Astronautics

NASA Conference Publication 3194
Part 1

National Aeronautics and
Space Administration

n Institute of
tics and Astronautics

NASA Conference Publication 3194
Part 1

LDEF–
69 Months
in Space

Second
Post - Retrieval
Symposium

Edited by
Arlene S. Levine
NASA Langley Research Center
Hampton, Virginia

Proceedings of a symposium sponsored by the National Aeronautics and Space Administration, Washington, D.C., and the American Institute of Aeronautics and Astronautics, Washington, D.C., and held in San Diego, California
June 1-5, 1992

National Aeronautics and
Space Administration

Office of Management

Scientific and Technical
Information Program

1993

FOREWORD

Nineteen hundred ninety-two, designated The International Space Year (ISY), coincided with the 35th anniversary of the International Geophysical Year (IGY). The International Space Year honored space exploration and the planet Earth and also marked the 500th Anniversary of Christopher Columbus's discovery of the New World. Langley Research Center, the home of the Long Duration Exposure Facility (LDEF), celebrated its 75th anniversary. In addition, 1992 marked the second anniversary of the LDEF retrieval. Since publication of the First LDEF Post-Retrieval Symposium Conference Publication in January 1992, the LDEF principal investigators, co-investigators, and collaborating investigators have had an additional 12 months to analyze and interpret the data from LDEF's 57 onboard experiments and to reach a better understanding of the space environment (ionizing radiation, meteoroids, space debris, and atomic oxygen in the upper atmosphere) and the effects that prolonged exposure in this environment will have on future spacecraft such as large low-Earth orbit (LEO) platforms, Earth-orbiting spacecraft, and on future manned and unmanned spacecraft to the Moon and to other planets.

Results of the second year LDEF studies were presented at the Second LDEF Post-Retrieval Symposium, held at the Town and Country Hotel, San Diego, California, June 1 to 5, 1992. This symposium was co-sponsored by NASA Langley Research Center and the American Institute of Aeronautics and Astronautics. This document contains the full-length papers presented at the second symposium. The collection includes invited review papers on ionizing radiation, meteoroids and debris, environmental effects on materials, environmental effects on systems, and archiving of the LDEF data. Contributed papers on ionizing radiation, meteoroids and debris, space effects on materials and systems, the LDEF mission and induced environments, microgravity, and life science are also included. The document organization is very similar to that of the symposium.

LDEF Mission and Induced Environments
Space Environments - Ionizing Radiation
Space Environments - Meteoroid and Debris
Space Environments - Microgravity
Space Environmental Effects - Materials
Space Environmental Effects - Systems
Space Environmental Effects - Biology
The Future

During the symposium William H. Kinard chaired the first half of the general session containing the invited review papers, and Bland A. Stein chaired the second half of the general session containing the invited review papers, plus the Mission and Induced Environments papers, and a Microgravity paper. Thomas Parnell chaired the Ionizing Radiation sessions; J.A.M. McDonnell, Jean-Claude Mandeville, Dale R. Atkinson, Michael Zolensky, and Donald Humes chaired Meteoroid and Debris sessions; Joan Funk and John Davis chaired the Data basing session; Ann Whitaker and Bruce Banks chaired the Coating session; Philip Young chaired the Polymer session, and R.C. Tennyson chaired the Polymer Matrix Composites session. Roger Linton chaired the Metals and Metal Matrix Composites session. Gale Harvey and Bland Stein chaired the Contamination session. James Mason, Joel Edelman, and Harry Dursch chaired the Systems sessions. William H. Kinard chaired the closing general session containing papers on biology and future activities.

I wish to thank the contributing authors whose research greatly enhanced the knowledge of space environments and their effects on materials, systems, and biology. The papers contained in this volume underwent a technical review by peer reviewers and an editorial review. I also wish to thank the technical reviewers for their time and effort in making this collection as current and accurate as it is. I would like to thank Maureen Sgambelluri, who assisted with the symposium logistics, and who cheerfully reformatted some of the papers contained in this publication. I would like to gratefully acknowledge Susan Hurd, Mary Edwards, Lisa Levine, Alisa Hollins, and Jeanne Gordon, for their support in editing this document.

This conference publication is the second in a series of three LDEF Post-Retrieval documents. In June 1991, over 400 LDEF investigators and data users convened in Kissimmee, Florida for the First LDEF Post-Retrieval Symposium. The results of the symposium (130 papers) are printed in a three-part NASA Conference Publication, ***LDEF-69 Months in Space: First LDEF Post-Retrieval Symposium,*** January 1992, (NASA CP-3134.) The LDEF Science Office plans to hold a third symposium in November 1993, in Williamsburg, Virginia. Published abstracts for the third symposium will be available at the meeting. Additional information on these symposia may be obtained by contacting:

Arlene S. Levine
LDEF Science Office M/S 404
NASA Langley Research Center
Hampton, Virginia 23681-0001
Telephone: 804 864-3318
Fax: 804 864-8094

CONTENTS

Part 2*

Space Environments - Meteoroid and Debris

---

* Part 2 is presented under separate cover.

Space Environments - Microgravity

Part 3*

Space Environmental Effects - Materials

---

* Part 3 is presented under separate cover.

Part 4*

Space Environmental Effects - Systems

* Part 4 is presented under separate cover.

Space Environmental Effects - Biology

The Future

*Poster Presentation
† Oral and Poster Presentation

PART 1

LDEF MISSION AND INDUCED ENVIRONMENTS

Long Duration Exposure Facility (LDEF)

Mission Overview

Facts:

- 1st spacecraft developed to fully utilize Shuttle
- 57 Experiments:
  - Technology
  - Science
  - Applications
- Involvement:
  - Private Companies
  - 21 Universities
  - 7 NASA Centers
  - 9 DoD Laboratories
  - 8 Foreign Countries
  - 300+ Investigators
  - 3.5 Million Students

Post retrieval operations have proven LDEF to be a "Treasure Trove" of science and technology data.

Launched
April, 1984
STS-41C Mission

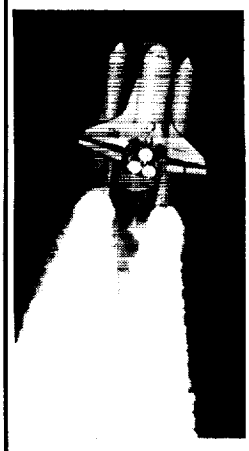

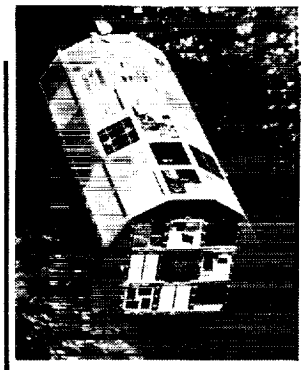

69 Months in Space
32,422 Orbits
741,928,837 Miles

Retrieved
January, 1990
STS-32 Mission (Night Landing)

L-93-1653

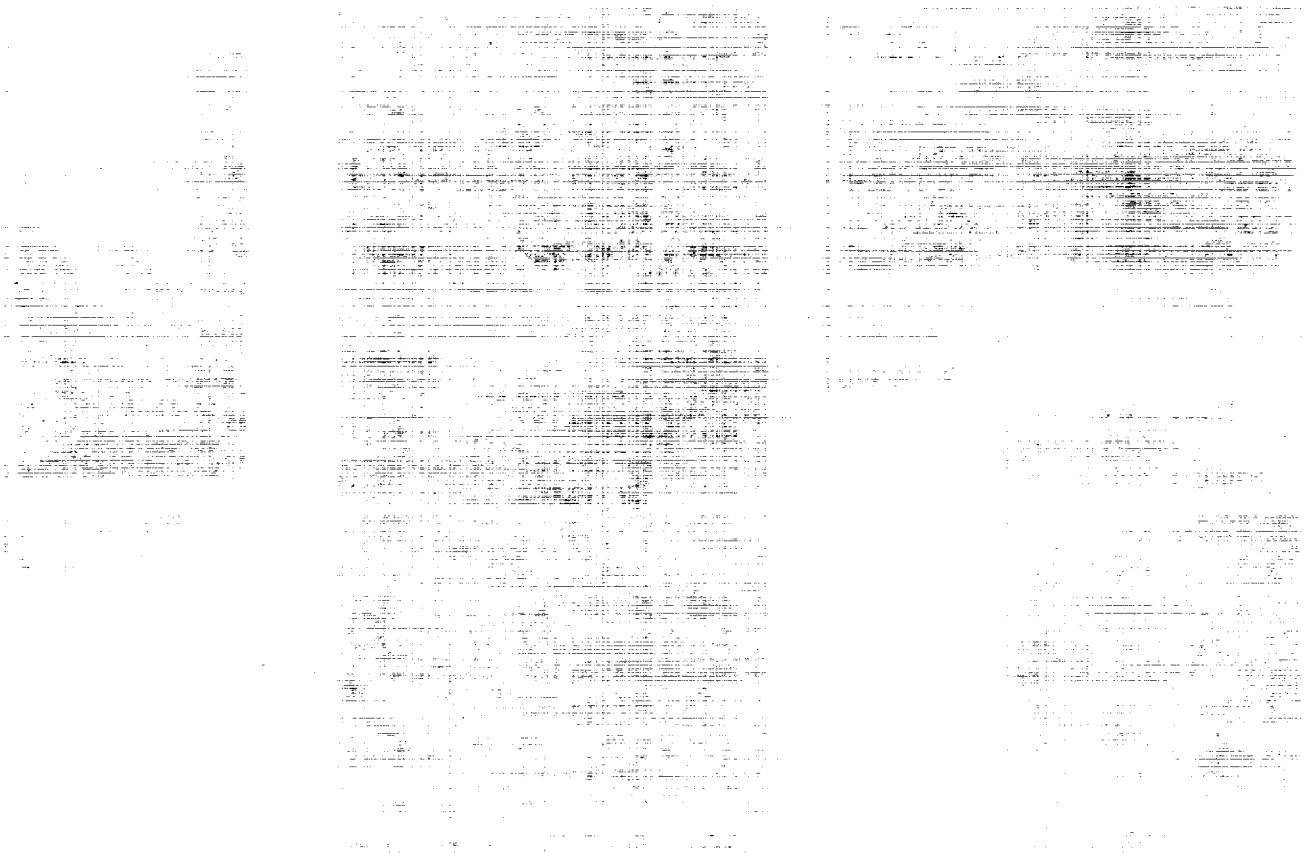

REFINEMENTS ON THE PINHOLE CAMERA MEASUREMENTS OF THE LDEF ATTITUDE

Palmer N. Peters, and Paul L. Whitehouse
Space Science Laboratory, NASA/MSFC
Huntsville, Alabama 35812
Phone: 205/544-7728, Fax: 205/544-7754

John C. Gregory
The University of Alabama in Huntsville
Huntsville, Alabama 35899
Phone: 205/895-6028, Fax: 205/895-6349

ABSTRACT

The results from the UAH pinhole camera have been reanalyzed to include the effects of corotation of the atmosphere with the Earth as well as satellite oscillation. Previous results[1] from the instrument showed that the satellite had stable attitude offsets in yaw of 8.0° and 1.0° in pitch; these offsets are unchanged by the present analysis. The primary impact zone of oxygen, i.e. the directly exposed spot on a silver detector, had a ratio of major to minor axes equal to 1.05, which was interpreted as being caused by a small oscillation of ±0.35° (with precision ±0.15°). The present analysis shows that the observed effect can largely be accounted for by atmospheric corotation, but that an additional oscillation in yaw of the order of a degree cannot be excluded. The sensitivity of the pinhole camera to satellite oscillations is shown to decrease nonlinearly with decreasing magnitude of the oscillation and to vary inversely with the gas temperature.

INTRODUCTION

As a satellite in low-Earth orbit moves through the atmosphere, the velocity distributions of gas molecules striking its surfaces may be calculated if the satellite velocity, air bulk velocity and gas temperature are known. The predominant species in the atmosphere at altitudes of principal interest (200-500 km) is the ground-state oxygen atom. The velocity distributions of these atoms relative to orbiting surfaces need to be known for detailed calculation of satellite lift and drag, erosion of carbonaceous materials, satellite glow, etc.. We have used the method of Nocilla[2] to combine the orbital velocity with the Maxwell-Boltzmann distribution of molecular speeds to reproduce certain erosion morphologies observed on polymer surfaces exposed to atomic oxygen on Shuttle flight STS-8.[3] Details of the method given in reference 3 are not reproduced here. Our prior analyses, as have most, did not account for effects due to a corotation of the atmosphere with the Earth. The rotational speed of a point on the Earth's surface at the equator is 492 m s^{-1}. Ignoring weather perturbations, the bulk of the air moves in the same direction at the same angular velocity as the surface of the Earth beneath it. This bulk motion is maintained into the upper atmosphere, but the actual velocity may not be known within 10%. In our analysis we have assumed the same angular velocity about the Earth's axis for all regions. The pinhole camera of the LDEF Experiment A0114 imaged the drifting Maxwellian velocity distribution as a spot on a silvered hemisphere, and because of overexposure also appears to have a very large background from multiply scattered atoms, as previously described.[4] The refinements that we now introduce are: (1) inclusion of a corotating atmosphere, and (2) simulation of the exposed spot in the pinhole camera by integrating atom intensities over an orbit while oscillations occur. The physical yaw oscillation of the LDEF had a longer period than the corotation period of 91.836 minutes and, when combined with the corotation effect, resulted in a wave-

function that was the sum of the two. Lacking greater details, and since the experimental results do not permit separation of such effects, the total oscillation was approximated by a simple cosine function with same phase but larger amplitude than the corotation effect alone.

PROCEDURE

Several assumptions were made as approximations: the pinhole was treated as a source of atoms with intensity given by a Nocilla-type distribution[2] for a given speed ratio; a constant speed ratio was assumed for one orbit and the intensities were determined for a number of locations in that orbit and averaged, while assuming a sinusoidal oscillation with a period the same as the orbital period; the exposed spot in the pinhole camera was assumed to be an image of this "resultant intensity" and several physical features of the spot were associated with contours of the same flux level. Such contours would be circles centered on the point of maximum flux for a constant ram direction. These contours would become elongated along any axis associated with an oscillation. Since gravity-gradient restoring torques for the LDEF have been reported as being 2 orders of magnitude higher than restoring torques for a yaw displacement, we have assumed pitch oscillation to be negligible compared to yaw oscillation.

Intensities were averaged for various numbers of orbital positions, up to 365 per orbit. Contours associated with such intensities with no oscillatory effects were compared to contours of intensities resulting when various peak-to-peak oscillations were assumed in the yaw of the LDEF. Any resultant asymmetries in the contours were expressed as the ratio of the major to minor axes; these ratios were compared to each other and to that measured for the "outer contour" of the spot in the pinhole camera. The intensities were plotted in three dimensions and as 2-dimensional cross sections in the yaw and pitch planes and in various spherical and rectangular representations to better visualize the results.

RESULTS

Using averaged orbital parameters for December 6, 1989, we obtained a peak-to-peak oscillation in the incident atom directions due to a corotating atmosphere equal to $\pm 1.853°$, in agreement with Bourassa, et al..[5] These parameters are summarized in Fig.1. Average atom intensities were obtained for a number of hypothetical cases of the LDEF orbiting with its leading surface C-9 having different fixed yaws relative to the ram direction, different peak-to-peak oscillations in the yaw, different numbers of intensities used in the average (number of equally spaced locations in one orbit), and other parameters. The intensity was determined in 3-dimensions and plotted in spherical coordinates, as shown in Fig. 2. This figure shows the example of a beam entering through a pinhole with a fixed 8° yaw. The beam's intensity is also shown in Fig. 2 on a hemisphere, simulating the exposure of the silver in the pinhole camera to oxygen. The intensity plot is also shown in two views in Fig. 3; Figure 3(b) most accurately represents the photographed hardware 3(c) from which spot measurements were made. This photograph, and its enlargement 3(d), show that at some lower level of atom intensity, the spot contours are obscured by background from multiply scattered atoms. Intensities in Figs. 2 and 3 were computed for a speed ratio of 7.139, which corresponds to a temperature of 1000 K and includes corotation of the Earth's atmosphere. Other results for the higher temperature limit and different assumed oscillation amplitudes are shown in Table I. The simulation of a large angle oscillation of $\pm 10°$ produced an average intensity with large elongation in the yaw direction of about $\pm 6°$ compared to the pitch direction, as shown in Fig. 4. In contrast, for smaller oscillations such as the $\pm 1.85°$ associated with a corotating atmosphere, the elongation is much smaller, about $\pm 0.2°$. Actual values are temperature dependent, as can be seen in the table. The effect of higher temperature is to spread the intensity distribution and lower its maximum and to reduce the influence of oscillation on elongating the major axis of the spot compared to the minor axis (decreases sensitivity of the pinhole camera to satellite oscillation). This smaller effect is shown in Fig. 5 as yaw and pitch profiles and in Fig. 6 as contours having slightly elongated yaw dimensions.

These computed results are compared in Table I to the experimental data. The measured spot had angular dimensions of 14.8° and 14.1°, or expressed differently, the major axis was ±0.35° wider than the minor. Using the worst case temperature (1600 K) it can be seen that a total oscillation of ±3° provided a good fit. On the other hand, the oscillation of ±1.853° associated with the corotation almost satisfies the measured value within stated errors. A total oscillation of ±4° is clearly inconsistent with the measurements.

CONCLUSIONS

The measured values of spot ellipticity of the AO114 silver pinhole camera are, within errors, consistent with the ±1.853° oscillation caused by atmospheric corotation and a 28.5° inclination orbit. A better fit is given by a total oscillation of ±3° including the ±1.853° corotation contribution; while ±4° gives too large an effect. While we have not attempted to account properly for the differences in period and phase for the two components, our best estimate of the yaw oscillation of the LDEF satellite about its stable 8° offset is ±1°(±1°).

The analysis has shown that the pinhole camera becomes more sensitive to angular motion at larger angular amplitudes and lower gas temperatures.

REFERENCES

1. Gregory, J. C.; and Peters, P. N.: Measurement of the Passive Attitude Control Performance of a Recovered Spacecraft, *J. of Guidance, Control, and Dynamics*, vol. 15, no. 1, Jan. - Feb. 1992, pp. 282-284.

2. Nocilla, S.: The Surface Re-Emission Law in Free Molecule Flow, *Rarefied Gas Dynamics*, ed. by J. A. Laurmann, Academic Press, New York, 1963, pp. 327-346.

3. Peters, P. N.; Sisk, R. C.; and Gregory, J. C.: Velocity Distributions of Oxygen Atoms Incident on Spacecraft Surfaces, *J. of Spacecraft and Rockets*, vol. 25, no. 1, Jan. - Feb. 1988, pp. 53-58.

4. Peters, P. N.; and Gregory, J. C.: Pinhole Cameras as Sensors for Atomic Oxygen in Orbit; Application to Attitude Determination of the LDEF, *Proc. of LDEF First Post-Retrieval Symposium*, ed. by A. S. Levine, NASA CP-3134, Part 1, June 1991, pp. 61-67.

5. Bourassa, R. J.; Gillis, J. R.; and Rousslang, K. W.: Atomic Oxygen and Ultraviolet Radiation Mission Total Exposures For LDEF Experiments, *Proc. of LDEF First Post-Retrieval Symposium*, ed. by A. S. Levine, NASA CP-3134, Part 2, June 1991, pp. 643-661.

6. Bourassa, R. J.; and Gillis, J. R.: *Atomic Oxygen Flux and Fluence Calculation for Long Duration Exposure Facility (LDEF)*, NAS1-18224, Task 12, Boeing Defense and Space Group, Seattle, WA, 1990.

Table I. Calculated and Measured Atom "Average" Intensity (Spot) Parameters

	Assumed Temperature (K)	Speed Ratio[a]	Assumed[b] Yaw Oscillation (Degrees)	Contour Width Yaw[c] (Degrees)	Ratio Major to Minor (Yaw:Pitch) Axes	Elongation (Yaw-Pitch) (Degrees)
SIMULATIONS						
Corotation Effect of ±1.853°	1000	7.139	±1.853	14.46	1.026	±0.18
	1600	5.645	±1.853	14.36	1.018	±0.13
Large Oscillation of ±10°	1000	7.139	±10	27.0	1.92	±6.5
	1600	5.645	±10	23.4	1.59	±4.7
3° Oscillation (Nearly Equal to Measured Effect)	1000	7.139	±3	15.2	1.08	±0.55
	1600	5.645	±3	14.7	1.04	±0.32
4° Oscillation (Excessive)	1600	5.645	±4	15.3	1.09	±0.60
EXPERIMENT DATA						
From Pinhole Camera Spot Contour Having 14.1° Pitch Width	----	----	----	14.8	1.05	±0.35 ±0.15

[a] Ratio of orbital speed, relative to a corotating atmosphere, to the most probable thermal speed of the impinging atoms

[b] Simple sinusoidal oscillation about zero yaw is assumed with the peak-to-peak amplitudes shown.

[c] Yaw widths were determined on contours having pitch widths of 14.1° to match the contour measured for the spot in the pinhole camera.

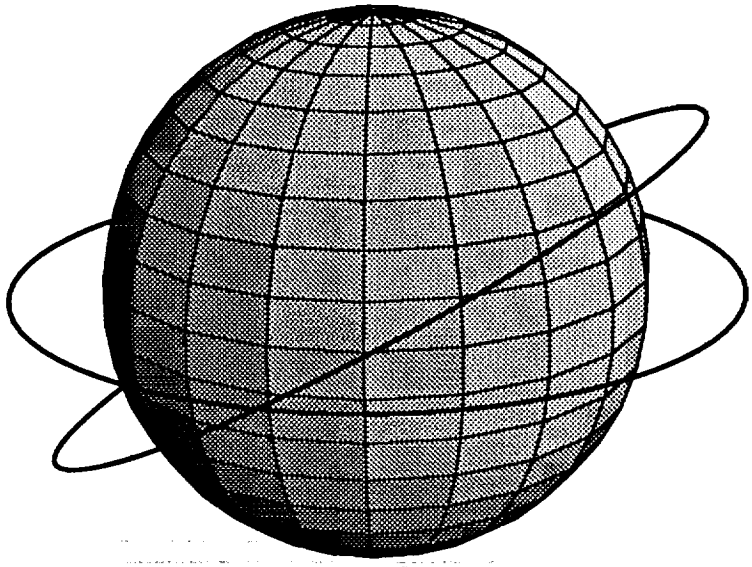

AVERAGE LDEF ORBITAL PARAMETERS FOR DECEMBER 6,1989*

INCLINATION: 28.52°

ORBITAL SPEED: 7.690 km s^{-1}

TEMPERATURE: 1008 K to 1587 K

ALTITUDE: 364 km

COROTATING ATMOSPHERE'S SPEED:
0.4918 km s^{-1} @ equator @ altitude & 0.4321 km s^{-1}
for component parallel to orbit

PEAK-TO-PEAK OSCILLATION DUE TO COROTATION:
+ 1.853° with the maximum negative
at the ascending node and the maximum
positive at the descending node

Figure 1. Average orbital parameters used in the calculations.

* From Bourassa and Gillis[6]

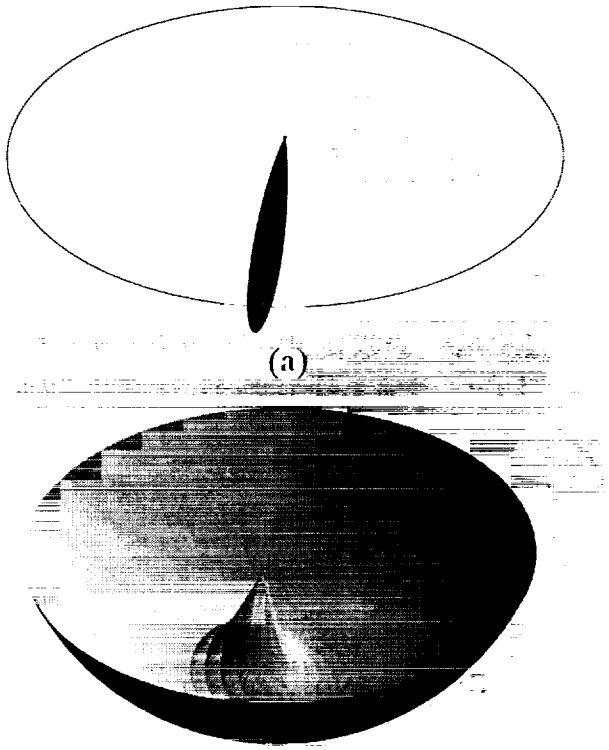

Figure 2. (a) Beam of oxygen atoms passing through a pinhole as computed for 8° yaw; (b) same intensity beam imaged on hemisphere to simulate exposure of silver.

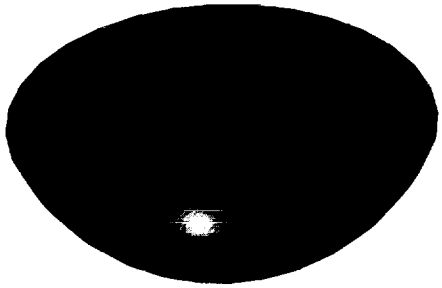

(a)

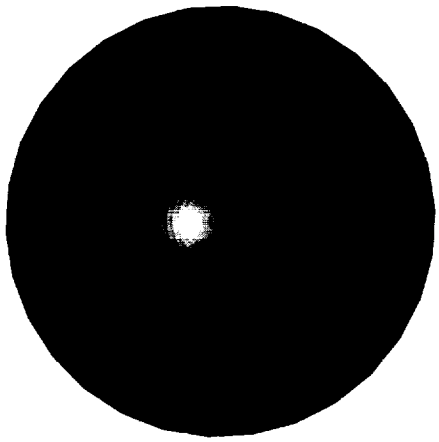

(b)

Figure 5. (a) A different representation of the intensity imaged on the hemisphere by the same intensity viewed as the pinhole camera photograph.

(c)

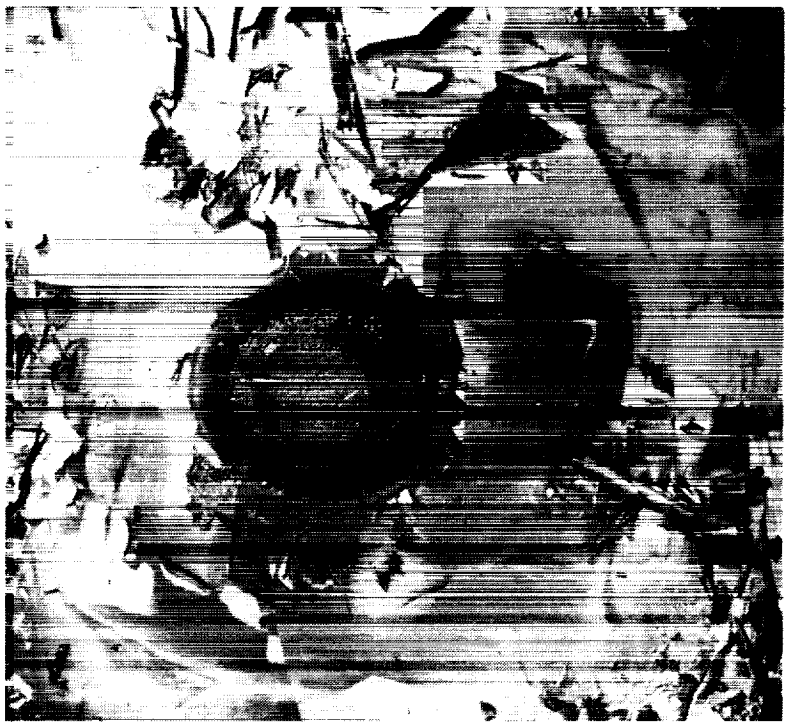

(d)

(c) photograph of the exposed pinhole camera, showing spot and background;
(d) enlarged region of photograph near the exposed spot.

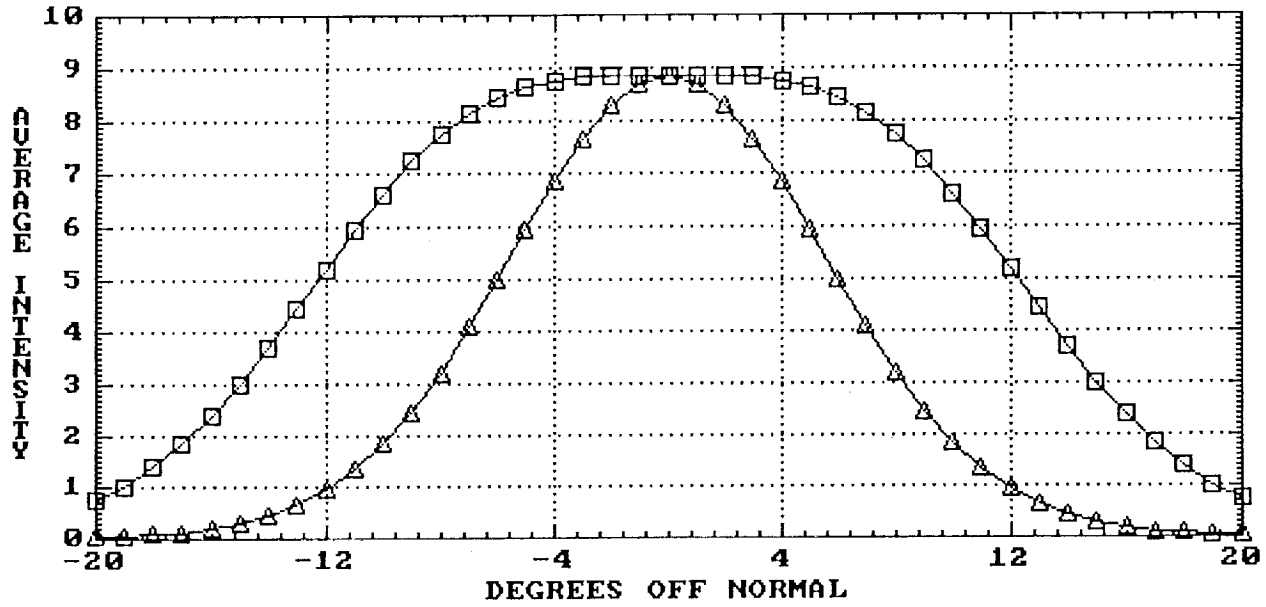

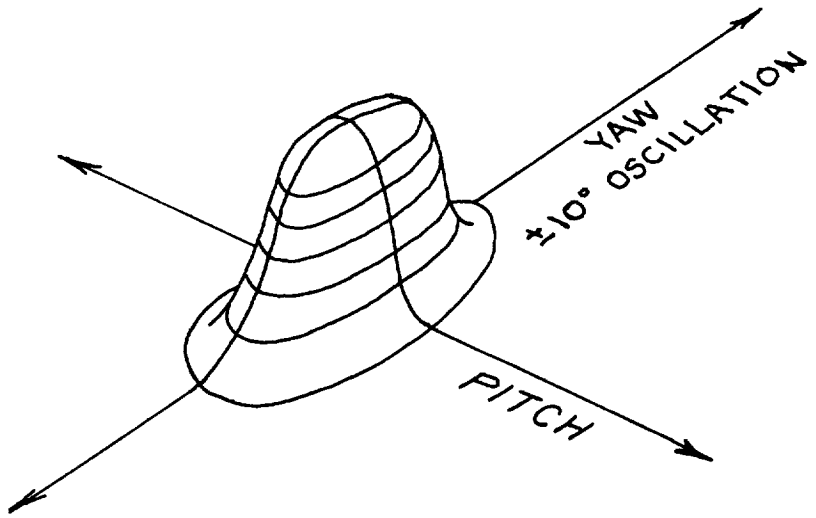

Figure 4. (a) Yaw (□) and pitch (△) profiles of average oxygen atom intensities in terms of degrees off normal of a surface that oscillated ±10°while pointing in the orbital direction;

(b) 3-d representation of profiles in (a), illustrating the elongation in yaw.

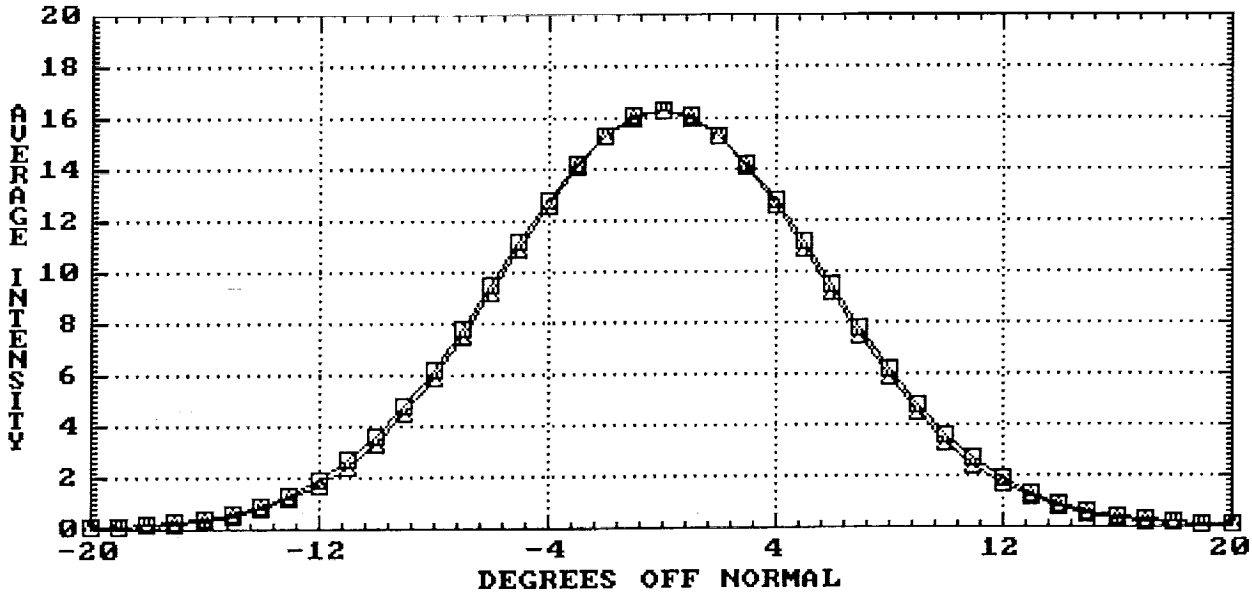

Figure 5. Yaw and pitch profiles, as in Fig. 4(a), but for ±1.853° oscillation in yaw.

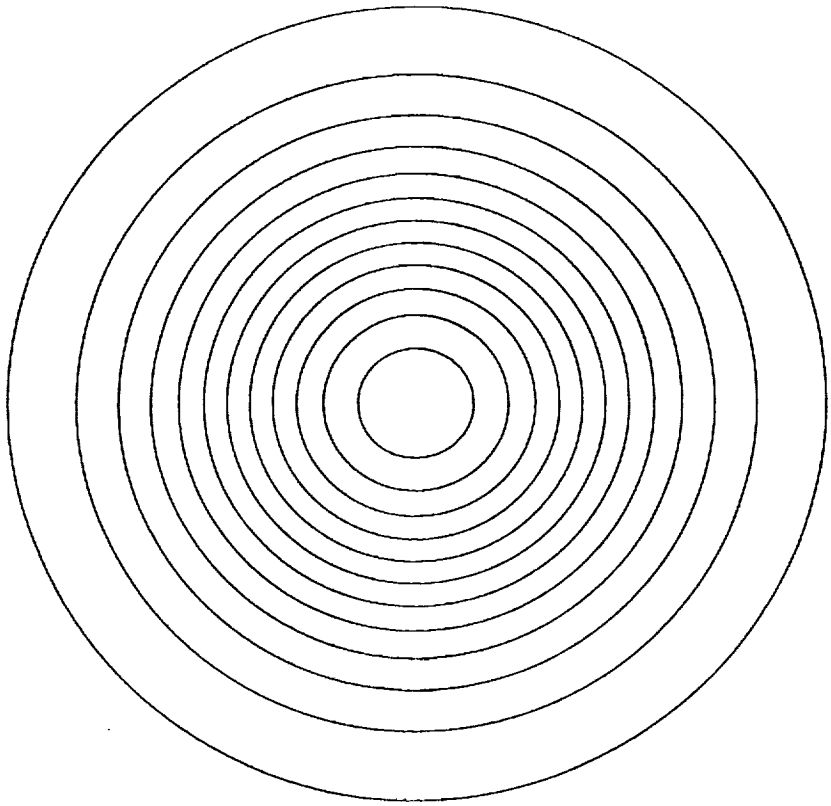

Figure 6. Contours taken from an atom intensity representing ±1.853° oscillation in yaw; the major axes in yaw direction are slightly larger than minor for all contours.

LDEF MICROENVIRONMENTS, OBSERVED AND PREDICTED*

R. J. Bourassa, H. G. Pippin and J. R. Gillis
Boeing Defense and Space Group
P. O. Box 3999, M/S 82-32
Seattle, WA 98124
Phone: 206/773-8437; Fax: 206/773-4946

SUMMARY

A computer model for prediction of atomic oxygen exposure of spacecraft in low earth orbit, referred to herein as the primary atomic oxygen model, was originally described at the First LDEF Post-Retrieval Symposium (ref 1). The primary atomic oxygen model accounts for variations in orbit parameters, the condition of the atmosphere, and for the orientation of exposed surfaces relative to the direction of spacecraft motion. The use of the primary atomic oxygen model to define average atomic oxygen exposure conditions for a spacecraft is discussed herein and a second mircoenvironments computer model is described that accounts for shadowing and scattering of atomic oxygen by complex surface protrusions and indentations. Comparisons of observed and predicted erosion of FEP thermal control blankets using the models are presented. Experimental and theoretical results are in excellent agreement. Work is in progress to expand the modeling capability to include ultraviolet radiation exposure and to obtain more detailed information on reflecting and scattering characteristics of material surfaces.

INTRODUCTION

Atomic oxygen erosion of materials varies with exposure conditions and differences in the geometry of exposed surfaces. Modeling of atomic oxygen exposure is needed to derive material performance parameters from orbital test data. Modeling is also important in design of hardware to be used under conditions differing from those of test. Two computer models have been developed to define atomic oxygen exposure for a spacecraft in low earth orbit. The first of these is a primary atomic oxygen model that accounts for orbit altitude, atmospheric conditions, mission duration, surface orientation and other factors that define the macroenvironment. The primary atomic oxygen model was discussed at the First LDEF Post-Retrieval Symposium (ref 1) and is described in further detail in NASA Contractor Report 189627 (ref 2). The second model, presented herein, accounts for the effects of complex surface protrusions and indentations of spacecraft equipment on atomic oxygen exposure. These variations in geometry alter the atomic oxygen exposure environment by casting shadows, producing reflections and scattering incident atomic oxygen flux. The microenvironments model accounts for any arbitrary size, shape, orientation, or curvature of exposed surfaces and for interferences between nearby surfaces. The task of modeling atomic oxygen exposure is simplified by using the two models together. The first model is used to reduce orbital and atmospheric variables to mission average conditions. The second model is used to account for variations in detailed design of exposed hardware.

The LDEF experiment offers an ideal opportunity to compare model predictions with observations. Data are presented herein showing comparisons of predicted erosion with experimental results for FEP thermal control film at three locations on LDEF. Experimental and

* Work done under Contract NAS1-19247

theoretical erosion of surfaces shows similar trends. The magnitudes of observed and predicted erosion of FEP blankets are in agreement even for surfaces of very complex shape.

OBJECTIVE

To show how the primary atomic oxygen model may be used to define average conditions of exposure for a spacecraft over extended periods of time, to describe the microenvironments model for atomic oxygen exposure, and to verify the accuracy of both models by comparing observed and predicted atomic oxygen effects on FEP thin film materials flown on LDEF.

PRIMARY ATOMIC OXYGEN MODEL AND AVERAGE EXPOSURE CONDITIONS

The details of the primary atomic oxygen model are presented in Reference (2). A summary of the factors affecting atomic oxygen exposure handled by the model are shown in Figure 1. All of the factors shown in Figure 1 significantly affect exposure. Orbit altitude and atmospheric conditions are especially important. At an altitude of 400 km, a 25 km decrease in altitude causes atomic oxygen density to increase by 50 percent. At this same altitude, atomic oxygen densities may differ by a factor of 20 between maximum and minimum conditions of solar activity.

These wide swings in the severity of the exposure environment make it necessary to integrate atomic oxygen rates with time to determine precise exposures. It was not considered practical to add further to the complications of the calculation by linking microenvironment variables directly to the integration. The solution to this complex problem is to divide it into parts that can be handled in succession. Fluences to plane surfaces of a spacecraft can be calculated efficiently with the primary model while treating the variables shown in Figure 1. The results of the primary exposure calculation are then used to define average exposure conditions for a mission or pertinent portions of a mission. These constant average conditions for the macroenvironment become inputs for the microenvironments model.

The calculation of average conditions from fluences to plane surfaces on a vehicle is very straight forward. The required formulas are readily derived from Equation (8) presented in Reference (2). Resulting equations for the average conditions are as follows:

$$F_0 = (\text{Fluence in ram direction})/(\text{Time for event or mission}) \quad (1)$$

$$F_{90} = (\text{Fluence } 90^\circ \text{ to ram direction})/(\text{Time for event or mission}) \quad (2)$$

$$N_{Average} = F_0/(\text{Average orbital speed}) \quad (3)$$

$$\langle c \rangle = 4F_{90}/N_{Average} \quad (4)$$

$$T_{Average} = (\pi M/8R)\langle c \rangle^2 \quad (5)$$

Where:

<c>	Average molecular speed, cm/sec
F	Atomic oxygen flux, atoms/cm^2-sec
M	Molecular weight, 16.00 g/g-mole
N	Number density, molecules/cm^3
R	Universal gas constant, 8.314 x 10^7 ergs/g-mole-K°
T	Absolute temperature, K°
π	Value of pi, 3.14 . . .

Averages for atomic oxygen number density, atmospheric temperature, and orbital speed together with parameters describing the geometry and surface properties of the vehicle hardware become the inputs for the atomic oxygen microenvironments model.

MICROENVIRONMENTS MODEL

The relationships between the primary atomic oxygen model and the microenvironments model are shown in the Figure 2. The purpose of the microenvironments model is to account for local geometry variations and surface conditions affecting atomic oxygen exposure. The microenvironments model uses the average conditions derived from outputs for plane noninterfering surfaces calculated using the primary model. The new variables introduced by way of the microenvironments model are those that cause shadowing and scattering of incident atomic oxygen flux.

Examples of shadowing and scattering are shown in Figure 3. Shadowing and scattering represent interactions between exposed surfaces that affect molecular flux. Shadowing is caused by irregularities on an exposed surface or its surroundings that block out a portion of the sky as seen from specific locations on the surface. Scattering is caused by either specular or diffuse reflection of incident atomic oxygen such that reflected oxygen molecules intercept another exposed surface. These effects depend on protrusions, indentations and curvature of exposed surfaces or on interference between surfaces. Neither shadowing nor scattering can affect the flux on a surface unless other nearby surfaces can be seen from points on the given surface or unless the given surface can see itself. Thus, plane surfaces facing away from each other are not affected by shadowing or scattering. The same is true of surfaces with convex curvature. Shadowing reduces molecular flux. Scattering by either specular or diffuse reflection increases molecular flux to the receiving surface.

Figure 4 shows how the microenvironments model handles shadowing and direct exposure. Direct exposure is molecular flux that reaches a surface without first being reflected by another surface. Scattered flux is determined by a Monte Carlo technique. The microenvironments program has four major elements: (1) a geometric routine; (2) a ray tracing routine; (3) a source function; and, (4) a Monte Carlo integration routine.

The geometric routine defines the shape of exposed surfaces and their spatial relationships. The defined surfaces may be faced in any direction. Exposed areas of entirely arbitrary shape may

be simulated. Areas of complex shape are represented by assembling simple unit surfaces and shapes. Up to 100 planes, cylinders and other shapes may be handled by the geometric routine at one time.

The ray tracing routine is very similar to other routines developed for such applications as calculating view factors for radiant heat transfer, fugitive light intensities in dark rooms, and for computation of perspective views from orthographic architectural drawings. Nodes are established for the ray tracing calculation, each representing a finite area of exposed surface. Directions are assigned to a specified number of a primary rays originating from each node. Direction is defined by two angles relative to the local surface normal and the bow of the vehicle. The ray tracing routine determines if a primary ray originating from a node on a surface can see the sky. For each unblocked direction, the projected surface area represented by the node is multiplied by the source function to determine direct flux.

The source function specifies the flux per unit solid angle that originates from a given direction in the sky. The function depends on three environmental parameters: number density, atmospheric temperature and orbital speed, all three treated as constant average values. The source function has only one independent variable, angle from the ram direction. Tabular files of this function in terms of its independent variable need be calculated only once for each use of the microenvironments program. This simplification, made possible by the primary atomic oxygen program, speeds the computations.

Reflected molecular flux is handled by a Monte Carlo technique. Each time a direction from a node is identified that is unblocked by other surfaces, primary flux is calculated for that direction and the incident flux is considered to be represented by a specified number of secondary rays for the Monte Carlo computation. A weighted random choice for disposition of the flux represented by each secondary ray is assigned as follows: reaction of atomic oxygen with the surface material; recombination of monatomic oxygen to form diatomic oxygen; specular reflection; and diffuse reflection.

If the atomic oxygen represented by a secondary ray is specularly or diffusely reflected, then the ray is followed to a new impact point and the process is repeated. The directions of rays experiencing diffuse reflection are weighted according to Lambert's cosine law. If a reflected ray does not strike the vehicle, the flux represented by the ray is considered lost to space.

If surface reaction or recombination is the random disposition selected, then the selection is noted and no further consideration is given to the atomic oxygen represented by that secondary ray. Atomic oxygen undergoing reactions at this place in the computation are cataloged only to arrive at a correct answer for reflected flux reaching surrounding areas of the exposed surface. Surface erosion is calculated later based on the total atomic oxygen flux determined for each node and a reaction coefficient for the surface material.

The integration routine tabulates two items: (1) the total direct flux reaching the finite area assigned to a node from all directions that are unblocked, and (2) the total of all reflected flux striking the assigned area. The work of this routine amounts to arithmetic and bookkeeping. Once all directions from a node have been examined, the entire summation process is repeated for the next node.

The microenvironments calculation requires properties for reflectance and reactivity of exposed surface materials. The values of reflectance used in this study, shown on Table 1, are not based on actual test data. They are only estimates made to support this initial assessment of the models. Also, it should be noted that the reaction rate coefficient was considered constant, independent of incidence angle and impact velocity. If reaction rate coefficient is later shown to be

a function of other variables, then the model can be refined to account for this dependence. The value of the reaction coefficient used is based on the average of values reported by various LDEF experimenters.

Table 1. PROPERTIES OF EXPOSED MATERIALS

PROPERTY	FEP BLANKET	ALUMINUM
Specular Reflectance	49%	50%
Diffuse Reflectance	49%	46%
Recombination and Reaction	2%	4%
Reaction Coefficient	0.34E-24 cm^3/atm	Zero

OBSERVED AND PREDICTED ATOMIC OXYGEN EFFECTS

Angle Bracket, Experiment Tray F9

Figure 5 shows the locations of the three FEP film materials that were selected for comparison of observed and predicted erosion. The first of these locations was on Experiment Tray F9. This tray carried an angle bracket that was covered on both sides with an adhesively bonded FEP film. A section of the angle bracket was made available to Boeing by McDonnell Douglas for this study.

Figure 6 shows a cross-section of the angle bracket. The bracket has three flat portions, as follows: one extending outside the envelope of the experiment tray, facing the ram vector; a second in a horizontal position nearly parallel with the ram vector; and a third recessed inside the tray envelope and facing the ram vector. Normals to the first and third portions of the bracket make an angle of 8.1 degrees with the ram vector. A normal from the second surface makes an angle of 89.2 degrees with the ram vector. The shape of the bracket defines the shape of the FEP film surface. The film covered bracket was potted in plastic and polished to display the thickness of the coating. Photomicrographs of the coating were taken along the edge of the bracket at 100 magnification. A mosaic, about 17 feet in length, was prepared from the photomicrographs. Thickness of the coating and distance from the outside edge of the bracket were scaled from the mosaic.

A comparison of observed and predicted post flight thicknesses for the angle bracket FEP covering is shown in Figure 7. The cover thickness is a minimum on the recessed portion of the bracket. This is because the recessed area was subject to exposure from both primary and reflected atomic oxygen. The calculation shows that had it not been for reflected flux, the final thickness of the cover would have been the same on both areas of the bracket facing the ram vector. Minimum erosion occurred on the portion of the bracket that was nearly parallel to the ram vector (horizontal area). Note that even this area received some reflected flux. Reflected flux reaching the horizontal portion of the bracket would have originated from the recessed area.

Observed and predicted thickness are in good agreement. Some allowance must be made for accuracy in measurements of both thickness and distance along the bracket. Also, the reflected molecular flux, both specular and diffuse are based on estimated reflectances. Trends shown by observed and predicted thickness are in good agreement. The model appears to be very accurate after allowances for accuracy of physical measurements.

Figure 8 shows three calculations of total flux for the angle bracket made with widely differing molecular reflectances. The allowance for surface recombination and reaction was held constant at 2% for these calculations. The calculation shows that if all molecular reflections were specular, then the area of the angle bracket parallel to the ram vector would not have received scattered atomic oxygen. Under this condition, the recessed area of the bracket would have received maximum scattering. Had the situation been reversed, had all scattering been caused by diffuse reflectance, then the recessed area would have received a minimum of scattered atomic oxygen and the scattered flux reaching the area parallel to the ram vector would have been maximized.

Blanket Edge Attachments, Experiment Trays B7 and D11

The leading edges of the thermal control blankets on Experiment Trays B7 and D11 face the ram vector at angles such that rolled edge portion of the blanket experiences a large variation in exposure over a short distance. Also, the experiment frame shielded the blanket between the roll and blanket edge. The geometry of the blanket edge attachment is shown in Figure 9. The only difference between the locations shown for Experiment Trays B7 and D11 is the angle the trays make with the ram vector. Comparisons of observed and predicted post flight thicknesses at these points offer an excellent opportunity for verification of the atomic oxygen exposure models.

The shape of the FEP foil at the edge attachment was estimated as closely as possible by Francois Levadou of ESTEC/ESA for this study. Measurements were taken on the experiment frame and combined with Levadou's measurements to yield the geometry shown in Figure 9. Thickness of blanket film materials were made on samples supplied to Boeing by NASA. The samples were first potted and polished, then thicknesses and edge distances were obtained from photomicrographs. Prediction of post flight thicknesses for these specimens was made using the microenvironments model.

Observed and predicted results are shown in Figures 10 and 11 for the specimens exposed on Experiment Trays B7 and D11, respectively. Good agreement between experimental observations and model predictions is displayed at both locations. Observed and predicted trends in erosion with distance measured from the blanket edge are in agreement . Measured and predicted thicknesses are within the limits of experimental accuracy.

The minimum thicknesses predicted for two exposure conditions, primary flux only and primary flux plus reflected flux, are shown in Figure 10 for the Tray B7 specimen. The two curves illustrate a noteworthy point. The minimum thicknesses predicted for primary flux only and for primary flux plus reflected flux occur at different distances from the edge of the blanket. Maximum exposure does not necessarily correspond to a zero incidence angle (between the surface normal and the ram vector) when reflected flux is considered. The difference is even more evident in the data shown in Figure 11 for the Tray D11 specimen.

CONCLUSIONS

Two computer models have been developed to predict atomic oxygen exposure of spacecraft materials. These models work together. The first model functions to calculate atomic oxygen exposure to simple noninterfering surfaces of a vehicle and to reduce orbital and atmospheric variables to mission average conditions. The second model is used to account for detailed hardware design features that may cause shadowing and scattering of atomic oxygen flux. Observed erosion of FEP samples flown on LDEF and predictions made with the models are in agreement even for specimens of complex shape.

REFERENCES

1. Bourassa, R. J., Gillis, J. R., and Rousslang, K. W.: Atomic Oxygen and Ultraviolet Radiation Mission Total Exposures for LDEF Experiments. *LDEF 69 Months in Space, First Post-Retrieval Symposium,* NASA Conference Publication 3134, 1991.

2. Bourassa, R. J. and Gillis, J. R., *Atomic Oxygen Exposure of LDEF Experiment Trays*, May 1992, NASA Contractor Report 189627.

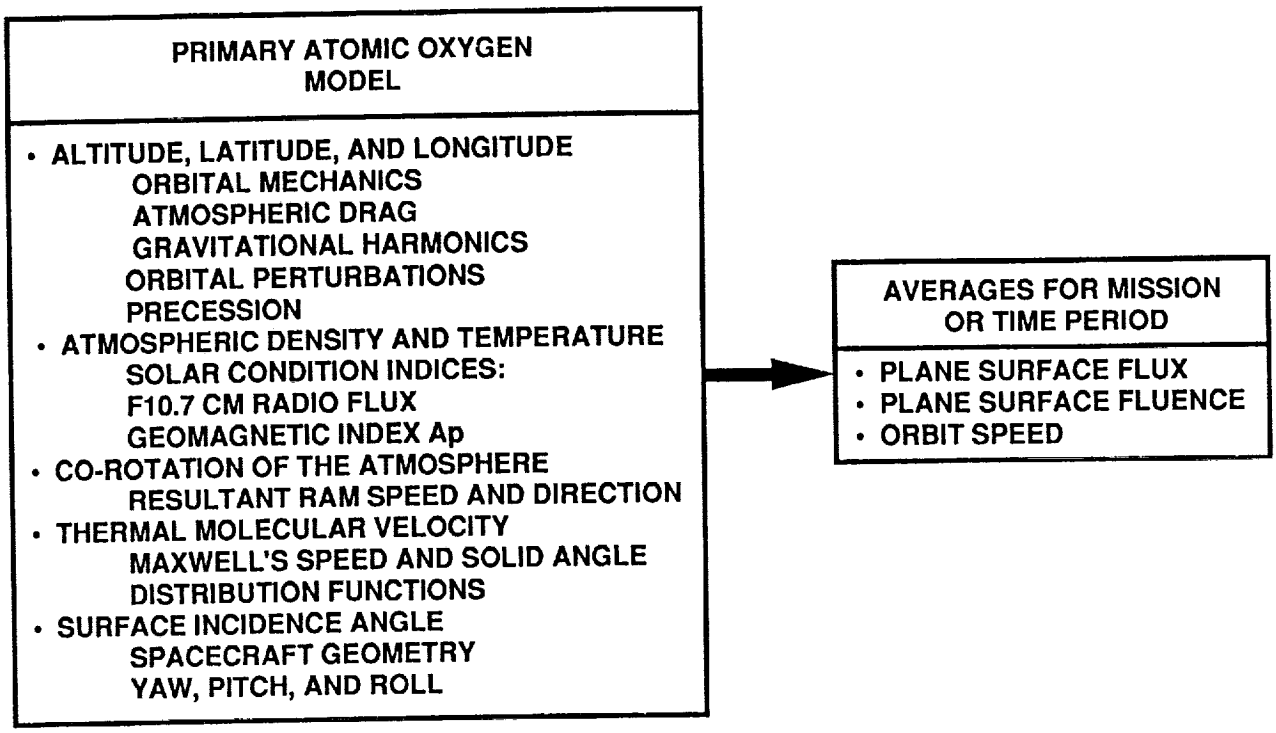

Figure 1. Attributes of the primary atomic oxygen model.

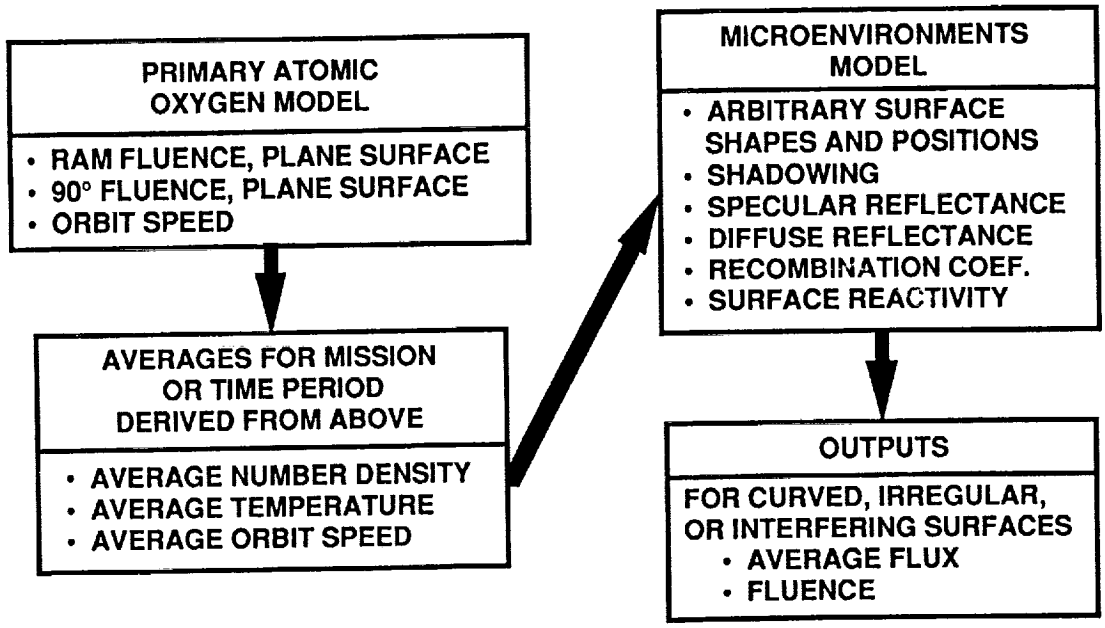

Figure 2. Attributes of the microenvironments model.

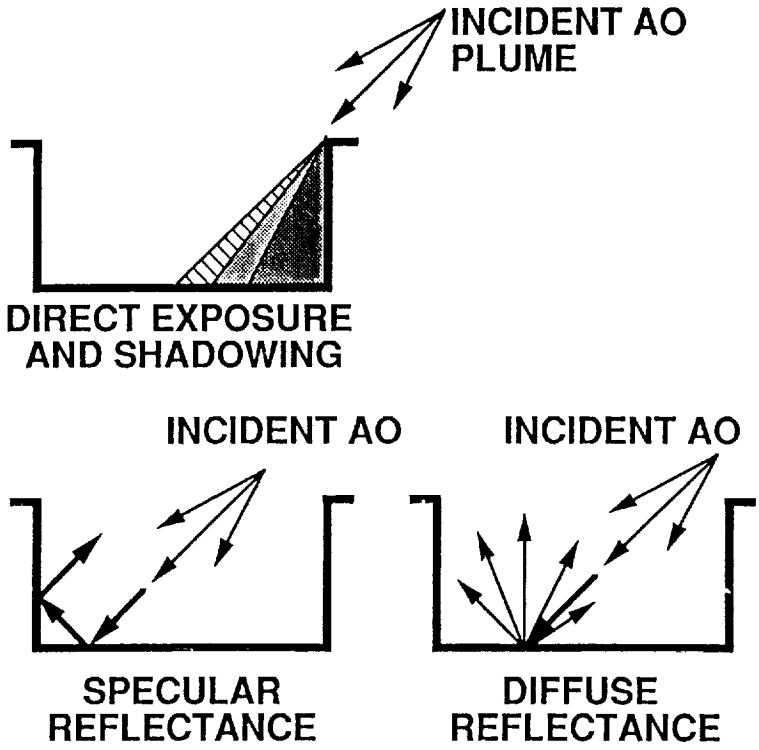

Figure 3. Shadowing, specular reflection and diffuse reflection of atomic oxygen on a spacecraft surface of complex shape.

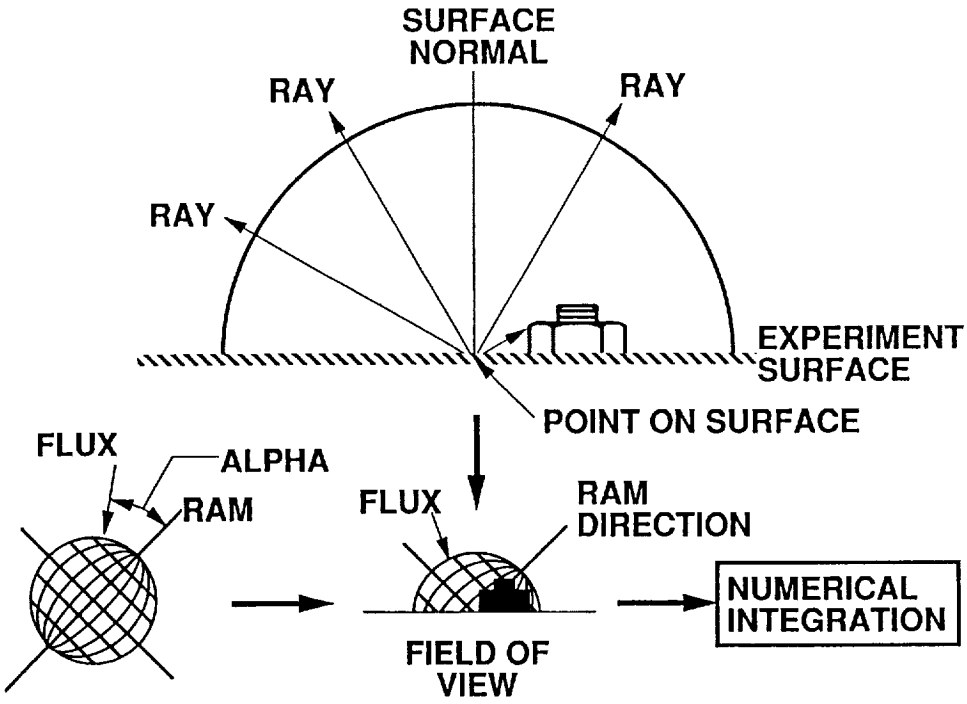

Figure 4. Four major elements of the microenvironments model; geometric routine, ray tracing routine, source function, and numerical integration routine.

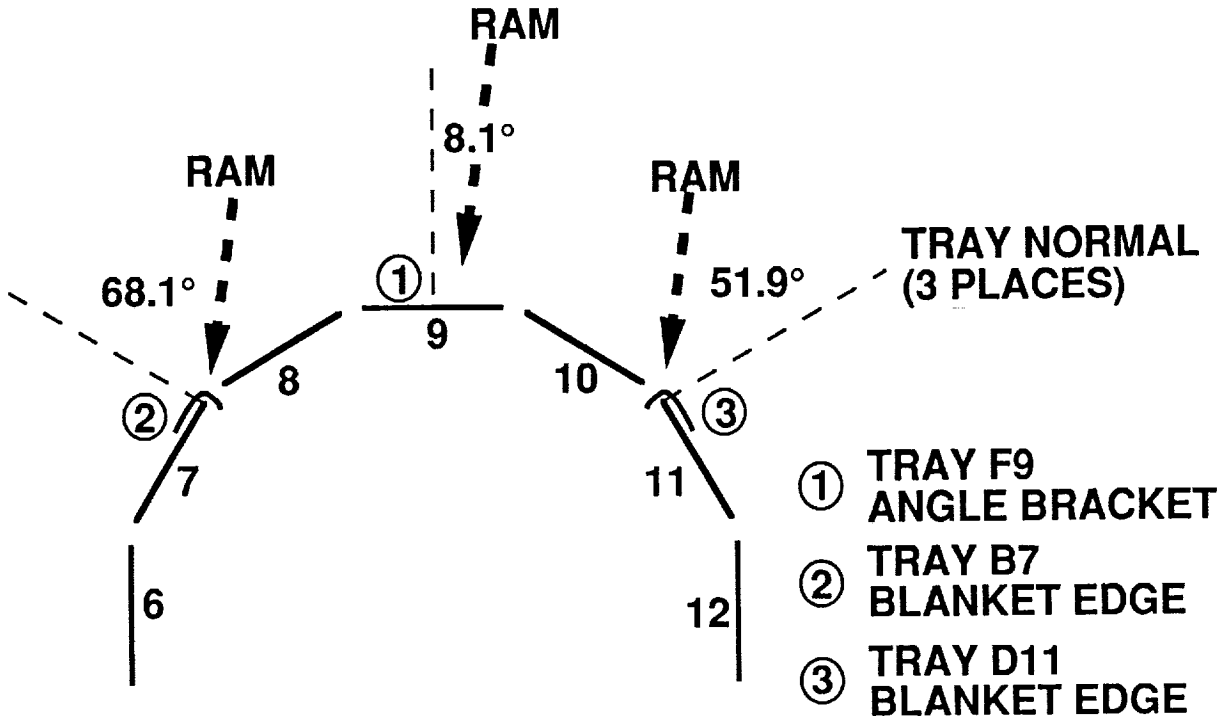

Figure 5. Location of FEP specimens used for experimental verification of the microenvironments model.

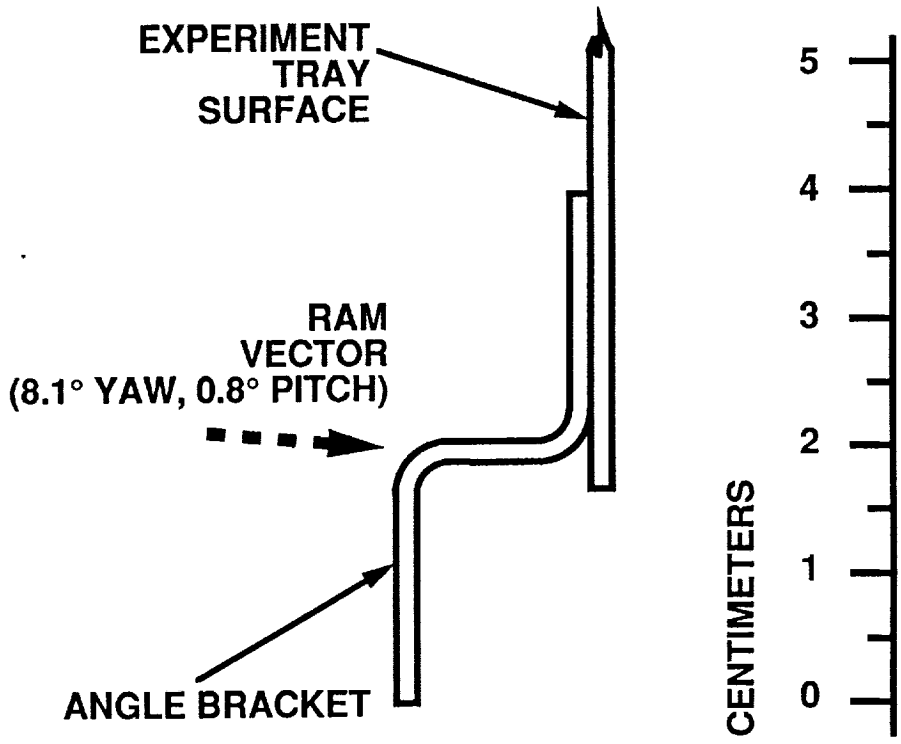

Figure 6. Shape of the angle bracket on Experiment Tray F9.

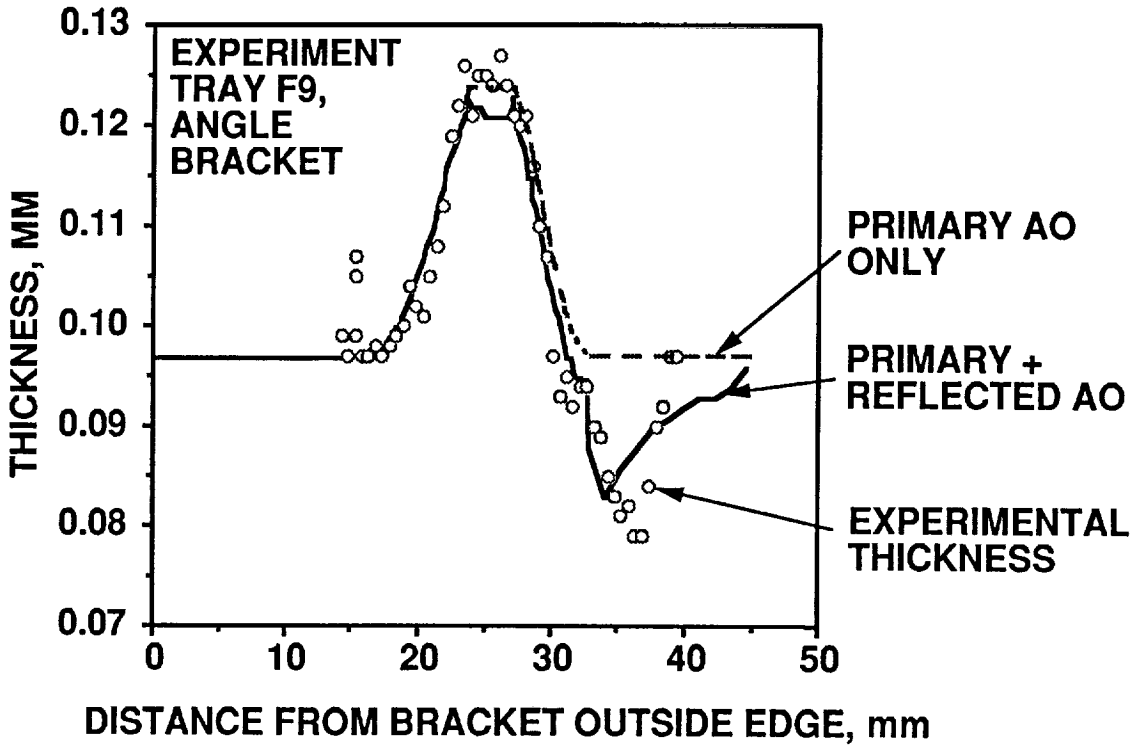

Figure 7. Comparison of observed and predicted erosion of the FEP film covering on the angle bracket.

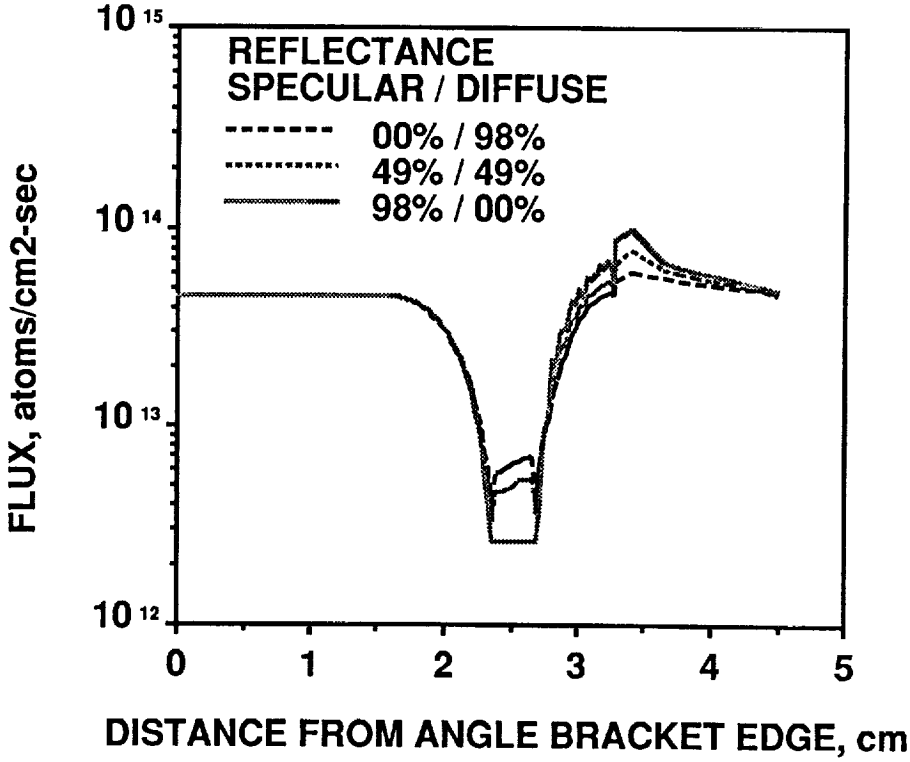

Figure 8. Effect on exposure of the angle bracket FEP film covering caused by varying molecular reflectance.

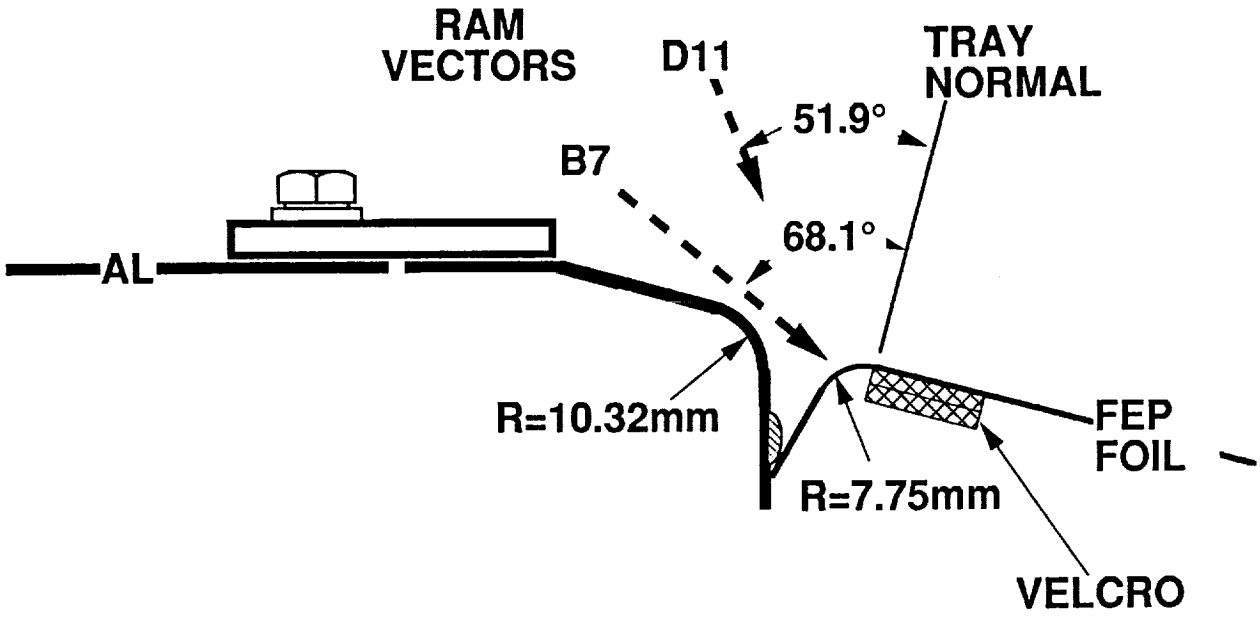

Figure 9. Shape of the edge attachment holding the thermal control blanket, Experiment Trays B7 and D11.

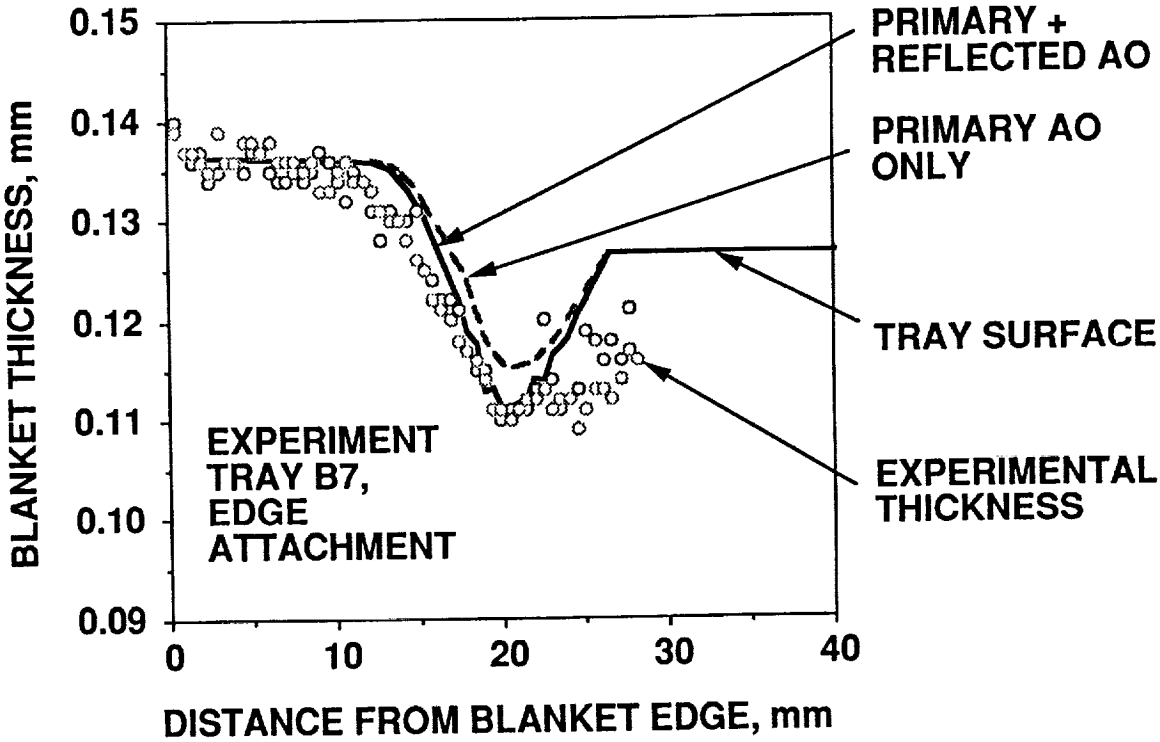

Figure 10. Comparison of observed and predicted erosion of the thermal control blanket at its edge attachment, Experiment Tray B7.

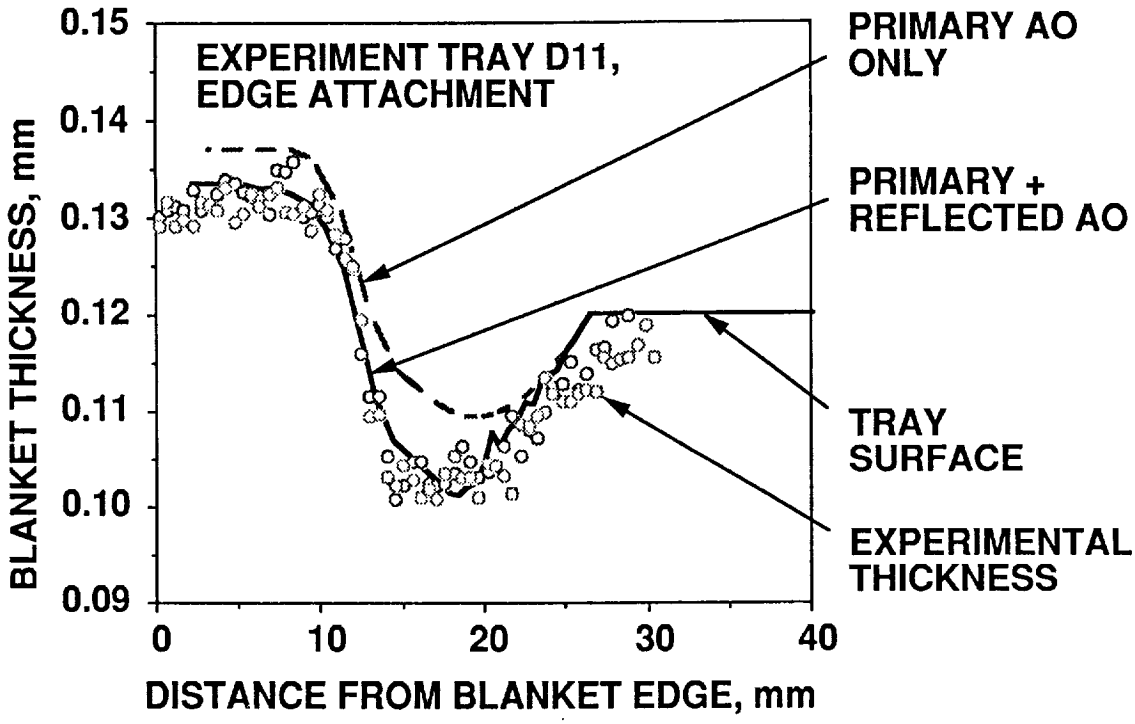

Figure 11. Comparison of observed and predicted erosion of the thermal control blanket at its edge attachment, Experiment Tray D11.

A GENERALIZED APPROACH TO THE THERMAL ANALYSIS OF THE LONG DURATION EXPOSURE FACILITY'S FLIGHT EXPERIMENTS

Thomas R. Sampair
Lockheed Engineering & Sciences Co.
144 Research Dr.
Hampton, Va. 23666

SUMMARY

The generalized method employed in the thermal analysis of a Long Duration Exposure Facility (LDEF) flight experiment is presented (ref 1). The method consists of thermal math model development, defining the orbital heating rates, and applying the appropriate temperature boundary conditions. This approach has proven to be an accurate method for predicting experiment component temperatures for the worst case orbital environments and calculating daily average component temperatures for any part or all time portions of the 5.8 year mission. The application of this method to the thermal analysis of the Ultra-Heavy Cosmic-Ray Nuclei experiment (UHCRE) is presented as an example of this approach.

INTRODUCTION

The generalized method used in the thermal analysis of LDEF's flight experiments is presented in Figure 1. The approach consists of developing a mathematical lumped parameter node representation of the experiment; calculating the albedo, infrared, and solar orbital heating fluxes; defining the source and sink temperature boundary conditions; and solving with a finite difference technique. Minimum and maximum temperature cycling due to the LDEF rotating around the Earth (Day/Night cycling) can be calculated for the worst case heat flux and structure temperature boundary conditions. Daily average component temperatures can also be calculated for any length of mission time using daily average heat flux data derived from time averaging the orbital heat flux over one complete orbit and superimposing this flux on the mission beta angle (β). Temperatures calculated by this method are the experiment's orbital average thermal equilibrium temperature for any given day over the mission lifetime. The thermal analysis of the UHCRE (A0178-C6) located on row six at bay C is presented as an example of this approach.

The High-Resolution Study of Ultra-Heavy Cosmic-Ray Nuclei Experiment was flown aboard the LDEF with the objective of studying the charge spectra of ultra-heavy cosmic-ray nuclei from Zinc to Uranium using solid-state track detectors. The experiment tray consisted of three pressurized aluminum cylinders containing four detector stack modules per cylinder. Each detector stack module was typically made up

of 60 layers of 250 μm lexan, 6 layers of 0.5 mm lead sheets, and 4 layers of 750 μm CR-39 enclosed in molded polyurethane foam resin. The formation and stability of the etchable latent nuclei tracks in these solid state detectors are highly dependent upon the temperature of the detector modules during registration and the thermal history of these modules after nuclei registration. Therefore it is extremely important to have an accurate post-flight thermal analysis of each tray location in order for the experiment data reduction effort to be successful. This experiment occupied 16 peripheral tray locations (fig. 2) providing the principal investigators with a total of 192 nuclei track detector modules for collecting heavy nuclei. The experiment tray located on row six at holding bay C is used as an example.

LDEF THERMAL CONTROL AND TRAY THERMAL DESIGN

The thermal control of the LDEF was totally passive by design, thus relying on internal radiation heat transfer, heat conduction paths, and the external surface coatings (α/ε) for facility temperature control (fig. 3). Over 90% of the interior structure and tray surfaces were coated with Chemglaze Z306 high emissivity black paint ($\varepsilon = 0.90$) to minimize any circumferential thermal gradients and to maximize the radiation heat transfer across the facility. To minimize conduction heat transfer from the structure, the experiment trays were attached to the LDEF structure by eight 2" × 5" aluminum clamps along the tray perimeter. The tray mounting scheme minimizes the contact conduction area through which heat can be transferred between the facility and the experiment trays. The passive thermal control of the LDEF results in a wide variation in the experiment's structure boundary temperature due to the orbiting nature of the spacecraft. In the case of the UHCRE-C6 experiment, the average structural boundary temperature ranged from 5°C to 48°C (41°F to 119°F) over the mission lifetime.

The objectives of the UHCRE thermal design were to minimize the temperature fluctuations experienced by the detector modules, to minimize any thermal gradients through the module stacks, and to maintain the temperature of the modules at or below 30°C (86°F) over the mission lifetime. This was accomplished by :

- Using 5 mil silver teflon for the thermal cover, featuring a low solar heat absorptance ($\alpha = 0.080$) and high heat dissipation to space ($\varepsilon = 0.80$).
- Establishing a large radiation couple from the detector case to the thermal cover.
- Establishing a small radiation couple from the detector cases to the surrounding experiment tray.
- Minimizing the heat conduction from the mounting tray to the detector cylinders by employing 5 mm delrin acetal resin insulation washers.
- Enclosing the detector modules in molded polyurethane foam resin (Eccofoam FPH) which provided mechanical stability and excellent thermal isolation from the cylindrical aluminum case.

The materials and optical properties used in the construction of the UHCRE are presented in Figure 4.

NODAL MODEL DEVELOPMENT

The objective of developing a thermal mathematical model is to accurately calculate the component temperatures of the experiment for any orbital condition. A finite difference thermal mathematical code was used to determine the temperature response of the experiment components at specific points called nodes. Temperatures are computed by performing an energy balance on each node in the model at the specified time points in the orbit or mission. The assumptions made in this analysis are that heat transfer due to convection can be neglected, each node is homogenous and isothermal, all node surfaces reflect energy diffusely, and finally there is no internal heat generation to consider for this experiment. The experiment is divided at the appropriate hardware boundaries or at desired locations into lumped-capacitance nodes which are connected to each other by the conduction and radiation conductor network. In developing a thermal math model the three essential components needed for temperature calculations are the node's thermal mass or capacitance, the conduction heat transfer paths, and the radiation interchange factors between each node. The thermal capacitance of a node is defined as its thermal energy storage capacity and is calculated by multiplying the node mass by the material's specific heat (C_p). The thermal capacitance governs the rate at which thermal energy is stored or released from the node during transient temperature calculations. Nodes which have a finite thermal mass or capacitance are known as diffusion nodes and nodes which have an infinite capacitance are considered temperature boundary nodes.

The UHCRE tray was divided into 20 diffusion nodes and three boundary temperature nodes. Each detector cylinder was divided into six nodes as shown in Figure 5. Because the detector cylinders were painted black on the top half and left bare on the bottom half for thermal control, the cylinders were split into two nodes along this line. The four modules in each cylinder were modeled as two nodes, a top layer and a bottom layer, which have the same mass and dimensions as the four separate modules. The remaining two nodes represent the top and bottom supporting eccofoam layers which were molded as two separate pieces. The experiment tray was lumped into one node and the thermal cover is represented as one node. The experiment has three temperature boundary conditions which consist of the average of the two supporting longerons and section of the center ring structure, the average LDEF interior, and the space sink temperature (0°K).

Heat conduction paths (conductance) between nodes are known as conductors and are shown schematically as electrical resistors in Figure 6. Linear conductors represent heat transfer by conduction and are calculated by taking the product of the node material's thermal conductivity (κ) and the cross sectional area (A), divided by the effective path length (L) between the two adjacent nodes. Heat conduction paths ($\kappa A/L$) were calculated between the experiment tray and each of the three detector cylinders and between each of the six nodes representing the detector module layers, eccofoam, and aluminum cylinders.

Nonlinear conductors represent heat transfer by radiation and are calculated for the nodal geometry as the product of the Stefan-Boltzmann (σ) constant, the node surface area, the surface emissivity (ε), and the gray body factor from one node surface to another. The gray body factors are a combination of the geometry shape or view factor and the reflected energy coefficients. The reflected energy coefficients account for multiple reflections which occur inside of enclosed spaces as a result of energy being emitted from one surface that strikes another node and is reflected to a third. The geometry shape factor represents the fraction of the radiative energy leaving one node surface that reaches another node surface directly. The internal radiation couplings for this analysis were calculated using the Thermal Radiation Analyzer System (TRASYS, ref. 2) computer code. A TRASYS model of the experiment tray was constructed to match the nodalization chart in Figure 5. The radiation interchange couplings were calculated using a numerical integration technique in TRASYS by calling the appropriate solution subroutines.

LDEF ORBITAL ENVIRONMENT

There are four heat sources (fig. 7) to consider when performing a thermal analysis on any LDEF experiment and they are the solar irradiation, Earth reflected solar irradiation (albedo), Earth emitted energy (planetary infrared), and any internally generated heat resulting from electronics or heaters. Since this experiment lacks any internally generated heat sources only the solar induced heat sources will be considered. The angle β is defined as the angle between the spacecraft's orbit plane and the Sun's illumination rays and its minimum and maximum amplitudes are calculated by adding the declination of the Earth's equator ($\pm 23.5°$) with the inclination of the spacecraft's orbit plane ($\pm 28.5°$). The β angle history for the LDEF mission is presented in Figure 8. The TRASYS computer program was employed to calculate the albedo, solar, and planetary incident heat fluxes. A TRASYS model of the LDEF spacecraft was constructed which represented a 12 sided polygon closed on both ends. Program inputs consisted of the LDEF spacecraft orientation (fig. 9), orbit β angle, and altitude (255 NM). Transient orbital heat fluxes were calculated for 10° beta angle increments within the range from -52° to + 52° for the row six location (figs. 10 & 11). This was done to develop a matrix of points which characterizes the orbital heat flux versus orbit β angle. The mission incident surface fluxes were calculated by time averaging the orbital heat flux over one complete orbit and plotting the average flux versus orbit β angle (fig. 12). Figure 12 shows that for the row six location, the peak heat flux occurs at a β angle of -52° and the minimum heat flux is at a β of +52°. The β angle history was used as the independent variable to interpolate between the orbit averaged flux to generate a daily average mission flux history (fig. 13) for experiments on row six.

Surface incident orbital heat fluxes in 10° increments within the β angle range and the mission daily average flux for the first 390 days of the LDEF mission have already been calculated for each row and both ends of the LDEF spacecraft. Heat flux and structure temperature boundary condition data are documented in Reference 3 for the LDEF to provide a set of thermal boundary conditions which are common to all LDEF experiments.

The thermal incident fluxes (q) in the above referenced document were evaluated with both the absorptance (α) and emissivity (ε) set to unity. These fluxes were then converted into absorbed surface heat flux(Q) by multiplying the albedo and solar component by the exposed surface node area (A) and α; this heat flux was then added to the planetary infrared heat flux ($q_{IR}A\varepsilon$) according to the following equation for each exposed experiment surface:

$$Q_{absorbed} = q_{Solar}A\alpha + q_{Albedo}A\alpha + q_{IR}A\varepsilon \qquad (1)$$

TEMPERATURE BOUNDARY CONDITIONS

Structure temperature boundary conditions have been calculated for each of the 86 LDEF tray locations. A thermal math model of the LDEF facility was constructed and the calculated temperatures were matched to flight data recorded by the Thermal Measurements System (THERM - P0003) for the first 390 days of the mission (ref 4). One of the objectives of the THERM experiment was to provide the principal investigators with a consistent set of data-matched thermal boundary conditions to be used in the math modeling of their experiments. Each LDEF tray was typically surrounded by two longeron nodes with the exception of experiments located on the ends of the facility and at the center ring. All experiments used the LDEF average interior temperature as one of their boundary temperatures. The structural boundary temperatures for the UHCRE-C6 location consisted of two longerons and a center ring. Since the experiment tray was lumped into one node the three structural temperatures were averaged into one boundary temperature for this analyses. Three sets of temperature boundary conditions were needed to predict the mission thermal history and the worst case orbital conditions for this UHCRE tray location, which were the minimum temperature boundary case of 0° β, the maximum temperature boundary case of -52° β (figs 14 & 15), and the daily average boundary temperature for the entire LDEF mission (figs 16 & 17).

METHOD OF SOLUTION

The Systems Improved Numerical differencing Analyzer (SINDA, ref. 5) finite differencing computer code is used for the problem solution. SINDA is a general thermal analyzer which utilizes resistor - capacitor (R-C) network representation of lumped parameter thermal systems for solving physical problems governed by diffusion-type equations. Analyzer inputs needed for problem solution include thermal node capacitance, conduction and radiation conductor networks, exposed surface absorbed heating fluxes, and temperature boundary conditions. Tray transient thermal analyses for both the worst case orbital and the full length mission were performed using SINDA's implicit forward-backward differencing solution subroutine. The assembled thermal model was used to calculate the extreme temperatures encountered by the experiment during the LDEF mission. Three cases were analyzed, the minimum and maximum thermal boundary orbital environments and the daily average for the 5.8 year mission history. The worst case orbital environment thermal conditions for any LDEF

experiment can be determined by inspecting both the structural temperature boundaries and the orbital heat fluxes for the combinations which yield both the minimum and maximum heat flux and temperature boundary conditions. For the UHCRE experiment located at C6, the maximum combined thermal boundary conditions occur when β equals -52° and the minimum is at a β of 0°. The two orbit conditions were investigated to determine the maximum thermal gradient between the top and bottom nodes of the detector modules and to calculate the magnitude of the temperature variations caused by the orbiting day-to-night flux cycling. Mission component temperature histories are computed by substituting the mission thermal flux and structure temperature boundary conditions in place of the orbital boundary conditions. The mission minimum and maximum experiment component temperatures were determined using this method. The analysis method was then repeated for the remaining 15 UHCRE trays.

If flight temperature data were available for this LDEF experiment (no flight data available for this experiment), the thermal model calculations would be compared to the flight data so that any necessary model adjustments could be made, such as model geometry changes, conduction contact resistance, or radiation network assumptions, before proceeding with the final analysis. Figure 1 shows this step in the procedure.

RESULTS and CONCLUSIONS

The minimum and maximum temperatures for the experiment tray, thermal cover, and both detector node layers are presented in Figures 18 and 19 for the worst case orbit environments of 0° and -52° beta angles. The largest calculated thermal gradient between the detector top and bottom node layers was found to be no more than 0.20°C for any of the 16 UHRCE locations. Orbital detector module temperature variations were found to be small with an average temperature for both layers of -2.2± 0.02°C at β equals -52° and -31.0 ±0.003°C for the cold case of 0° β. The C6 component mission thermal history shown in figure 20 represents the thermal equilibrium temperatures reached for any given day during the 69 months spent in space. The mode temperature for each detector module (Table 1) is defined as the most days spent at a given temperature in the range experienced by the nuclei track detectors. The mode temperature is calculated from the full length mission analysis by counting the number of days spent at each temperature in the range. Since the charge resolution of the etchable nuclei tracks is highly dependent upon the temperature of the detector stacks during and after nuclei registration, the mode temperature gives the principal investigator important information which is needed to control the stack etching process used to develop the nuclei tracks. Tables 2 and 3 summarize the minimum and maximum daily mission temperatures reached by the experiment components for all 16 UHCRE tray locations. All detector modules were below the target maximum of 30.0°C by a comfortable margin with the warmest detector temperature of -2.2°C occurring at the C6 location.

It was concluded that the UHCRE experiment successfully met its thermal design objectives which were to maintain the detector modules at or below 30°C over the mission lifetime and to thermally isolate the detector stacks from the orbital day and night temperature fluctuations as well as minimizing any detector stack thermal gradients.

The generalized method presented in this paper is intended to provide a sense of direction for performing thermal analyses to obtain accurate temperature calculations of LDEF experiments. Since the heat flux and temperature boundary conditions have already been calculated, the analysis needs only to build a nodal math model of the experiment and assemble the given information from the reference into the desired thermal analyzer format for problem solution.

REFERENCES

1. Long Duration Exposure Facility (LDEF) Mission 1 Experiments, NASA SP-473, 1984.

2. Thermal Radiation Analysis System (TRASYS), User's Manual, NAS9-15832, June 1983.

3. Berrios,W. M.; Sampair, T.R.: Long Duration Exposure Facility Post-Flight Thermal Analysis, NASA TM-104208 Part 1 and 2, January 1992.

4. Berrios, W. M.: Use of the Long Duration Exposure Facility's Thermal Measurement System for the Verification of Thermal Models, First LDEF Post-Retrieval Symposium June 2-8 1991, NASA CP- 3134.

5. Systems Improved Numerical Differencing Analyzer (SINDA), User's Manual, NASA 9-15800, March 1983,

Table 1. UHCRE Mode Temperatures for Each Tray Location (69 Month Mission).

	LOCATION															
Tray Temp -°C	A2 Days	A4 Days	A10 Days	B5 Days	B7 Days	C5 Days	C6 Days	C8 Days	C11 Days	D1 Days	D5 Days	D7 Days	D11 Days	E2 Days	E10 Days	F4 Days
-1	0	0	0	0	0	0	0	0	0	0	0	0	0	0	0	0
-2	0	0	0	0	0	0	5	0	0	0	0	0	0	0	0	0
-3	0	0	0	0	12	0	29	0	0	0	0	0	0	0	0	0
-4	0	0	0	0	35	0	35	0	0	0	0	0	0	0	0	0
-5	3	0	0	0	29	0	18	0	18	0	0	25	0	0	0	0
-6	29	0	0	0	25	0	22	0	14	18	0	40	0	0	0	0
-7	27	0	0	20	17	0	21	0	21	14	0	26	0	0	0	0
-8	55	0	0	45	24	11	20	20	34	24	5	21	24	0	0	0
-9	47	2	44	26	35	36	36	50	38	41	21	25	11	0	0	0
-10	46	75	81	23	33	38	36	29	34	41	47	28	33	0	0	0
-11	59	68	68	29	44	28	34	37	37	29	28	38	44	0	0	0
-12	84	115	101	43	39	34	36	57	33	27	31	34	42	28	0	6
-13	93	111	134	51	27	38	29	72	57	21	31	43	38	34	0	87
-14	77	129	101	60	35	53	32	56	58	29	53	36	33	60	21	128
-15	77	185	199	43	31	65	25	53	76	47	65	28	53	64	83	171
-16	128	411	322	47	38	43	35	73	58	49	53	33	75	57	86	156
-17	158	821	868	67	45	64	30	100	58	56	61	39	80	98	133	209
-18	218	30	76	76	51	66	51	106	65	44	56	33	64	110	131	344
-19	290	43	37	91	63	86	37	119	104	46	71	56	62	90	147	428
-20	475	70	38	84	62	93	56	204	118	44	93	53	81	120	308	274
-21	185	42	25	158	117	130	45	361	167	42	82	61	135	195	696	205
-22	41	5	13	234	167	235	91	598	211	58	121	63	143	282	400	37
-23	13	0	0	398	215	379	121	21	364	97	207	77	199	355	37	39
-24	2	0	0	460	316	562	165	61	461	130	264	156	366	564	36	23
-25	0	0	0	56	408	52	237	52	29	208	514	223	520	35	22	0
-26	0	0	0	42	152	45	286	34	33	275	209	283	60	13	7	0
-27	0	0	0	45	38	43	383	4	17	353	42	435	32	2	0	0
-28	0	0	0	9	33	6	134	0	2	366	41	180	10	0	0	0
-29	0	0	0	0	14	0	29	0	0	22	12	39	2	0	0	0
-30	0	0	0	0	2	0	26	0	0	19	0	27	0	0	0	0
-31	0	0	0	0	0	0	3	0	0	7	0	5	0	0	0	0
-32	0	0	0	0	0	0	0	0	0	0	0	0	0	0	0	0
-33	0	0	0	0	0	0	0	0	0	0	0	0	0	0	0	0
-34	0	0	0	0	0	0	0	0	0	0	0	0	0	0	0	0
-35	0	0	0	0	0	0	0	0	0	0	0	0	0	0	0	0

Table 2. Detector Module Mission Temperature Summary 4/7/84 to 1/12/90.

Tray Location	Detector Node	Min-°C	Max-°C	Mission Average-°C	Standard Devation-°C	Mission Median-°C
A2	Top Layer	-23.8	-5.4	-16.9	4.0	-18.2
	Bottom Layer	-23.7	-5.3	-16.8	4.0	-18.2
A4	Top Layer	-21.7	-9.4	-15.7	2.3	-16.4
	Bottom Layer	-21.6	-9.3	-15.7	2.3	-16.4
A10	Top Layer	-22.2	-8.5	-15.6	2.5	-16.5
	Bottom Layer	-22.1	-8.4	-15.5	2.5	-16.4
B5	Top Layer	-28.1	-6.5	-20.5	4.6	-22.3
	Bottom Layer	-28.1	-6.6	-20.5	4.5	-22.3
B7	Top Layer	-29.6	-3.0	-20.7	6.0	-23.0
	Bottom Layer	-29.5	-2.9	-20.8	5.9	-23.0
C5	Top Layer	-27.9	-7.5	-20.9	4.2	-22.6
	Bottom Layer	-27.9	-7.6	-20.9	4.3	-22.6
C6	Top Layer	-31.1	-2.2	-21.9	6.8	-24.7
	Bottom Layer	-31.1	-2.3	-22.0	6.6	-24.7
C8	Top Layer	-26.7	-7.7	-19.2	4.0	-20.7
	Bottom Layer	-26.6	-7.9	-19.2	3.9	-20.7
C11	Top Layer	-27.8	-4.9	-19.8	4.9	-21.8
	Bottom Layer	-27.6	-4.8	-19.8	4.9	-21.7
D1	Top Layer	-31.2	-5.9	-23.0	5.8	-25.4
	Bottom Layer	-31.0	-5.9	-23.0	5.8	-25.4
D5	Top Layer	-29.0	-7.8	-21.8	4.6	-23.6
	Bottom Layer	-28.9	-7.8	-21.8	4.5	-23.6
D7	Top Layer	-31.1	-4.6	-22.5	6.3	-25.2
	Bottom Layer	-31.1	-4.4	-22.6	6.1	-25.1
D11	Top Layer	-28.7	-7.6	-21.3	4.5	-23.2
	Bottom Layer	-28.4	-7.6	-21.3	4.5	-23.1
E2	Top Layer	-26.8	-11.9	-21.1	3.2	-22.2
	Bottom Layer	-26.6	-11.9	-21.1	3.2	-22.2
E10	Top Layer	-26.1	-14.2	-20.1	2.2	-20.8
	Bottom Layer	-25.9	-14.1	-20.0	2.2	-20.8
F4	Top Layer	-24.2	-12.1	-18.0	2.4	-18.3
	Bottom Layer	-24.1	-12.0	-18.0	2.4	-18.3

Table 3. UHCRE Tray Component Minimum and Maximum Mission Temperatures.

A0178 Location	Silver Teflon Cover Blanket		Top Detector Case		Top Eccofoam Layer		Bottom Eccofoam Layer		Bottom Detector Case		Tray	
	Min-°C	Max-°C	Min-°C	Max-°C	Min-°C	Max-°C	Min-°C	Max-°C	Min-°C	Max-°C	Min-°C	Max-°C
A2	-42.2	-23.8	-26.1	-8.5	-25.3	-7.4	-21.7	-3.2	-20.6	-2.1	5.3	28.8
A4	-40.7	-28.8	-24.4	-12.6	-23.5	-11.5	-19.8	-7.2	-18.9	-6.1	7.4	24.9
A10	-39.7	-26.7	-24.7	-11.6	-23.8	-10.5	-20.2	-6.4	-19.2	-5.3	6.4	24.4
B5	-47.1	-22.4	-30.9	-9.4	-29.9	-8.5	-26.2	-4.7	-25.3	-3.6	0.1	25.2
B7	-49.1	-18.1	-32.4	-5.6	-31.4	-4.7	-27.7	-1.1	-26.8	0.0	-0.8	27.8
C5	-47.2	-24.5	-30.7	-10.4	-29.7	-9.5	-26.1	-5.6	-25.2	-4.4	0.1	23.7
C6	-50.4	-17.2	-33.9	-4.9	-32.9	-4.1	-29.3	-0.5	-28.4	0.6	-2.6	28.4
C8	-45.9	-24.3	-29.4	-10.7	-28.4	-9.8	-24.8	-6.0	-23.9	-5.0	1.1	23.3
C11	-45.7	-20.6	-30.0	-7.6	-29.2	-6.7	-25.8	-3.0	-24.8	-1.9	-0.2	25.1
D1	-49.7	-21.6	-33.4	-8.6	-32.6	-7.8	-29.1	-4.1	-28.1	-3.1	-3.5	23.7
D5	-48.4	-24.7	-29.0	-7.8	-28.9	-7.8	-30.7	-9.8	-28.9	-7.8	-1.1	23.3
D7	-50.3	-19.2	-33.8	-7.1	-32.9	-6.2	-29.3	-2.6	-28.4	-1.5	-2.9	26.2
D11	-46.3	-22.6	-30.8	-10.2	-30.1	-9.3	-26.7	-5.8	-25.7	-4.8	-1.5	20.7
E2	-44.3	-28.6	-28.9	-14.6	-28.2	-13.7	-24.8	-10.0	-23.9	-9.0	-0.2	18.8
E10	-42.8	-31.2	-28.3	-17.0	-27.6	-16.0	-24.2	-12.3	-23.2	-11.3	1.0	16.9
F4	-43.6	-30.8	-27.0	-15.1	-26.0	-14.1	-22.3	-10.0	-21.3	-8.9	5.1	20.6

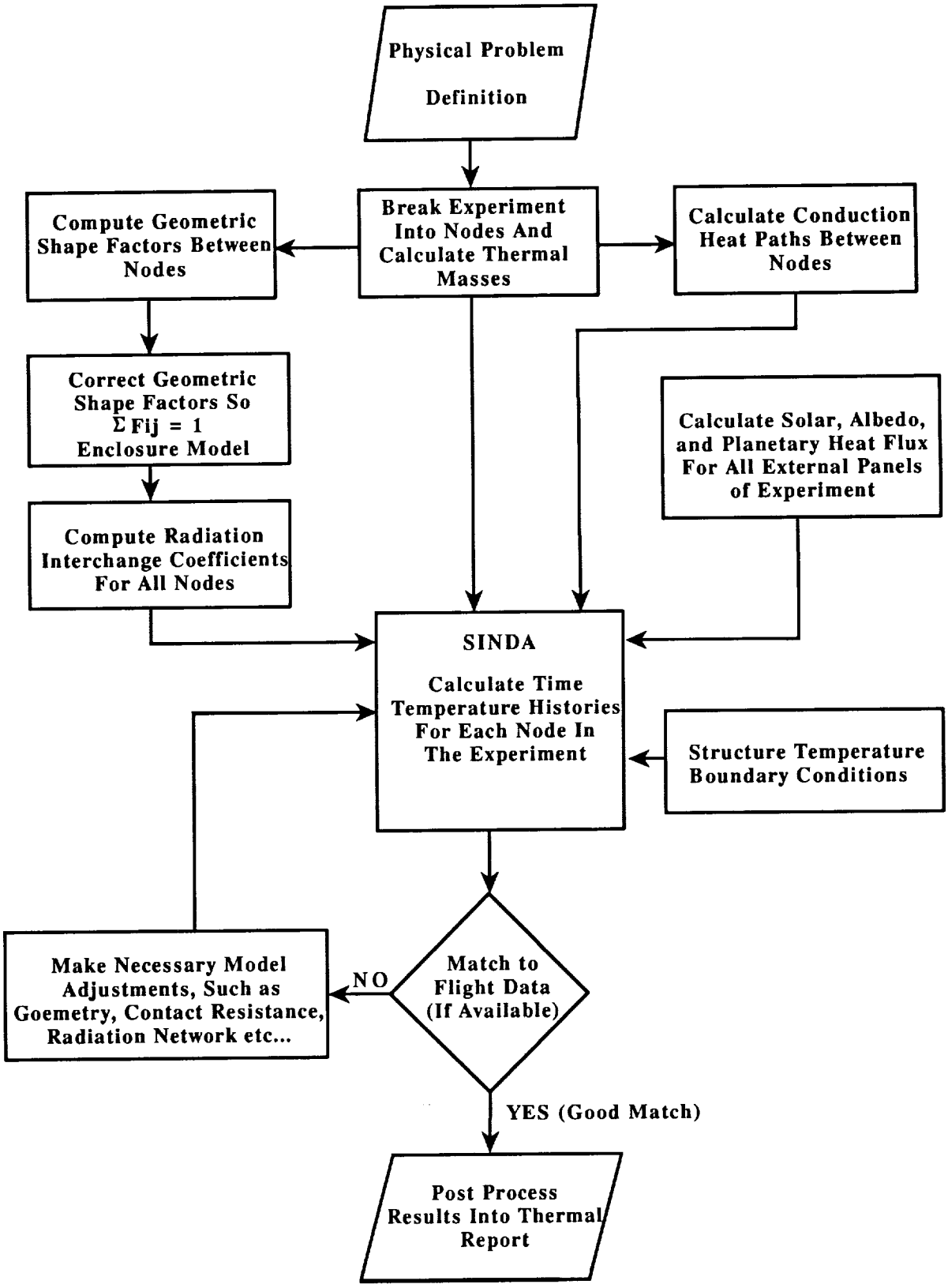

Figure 1. Experiment thermal analysis summary.

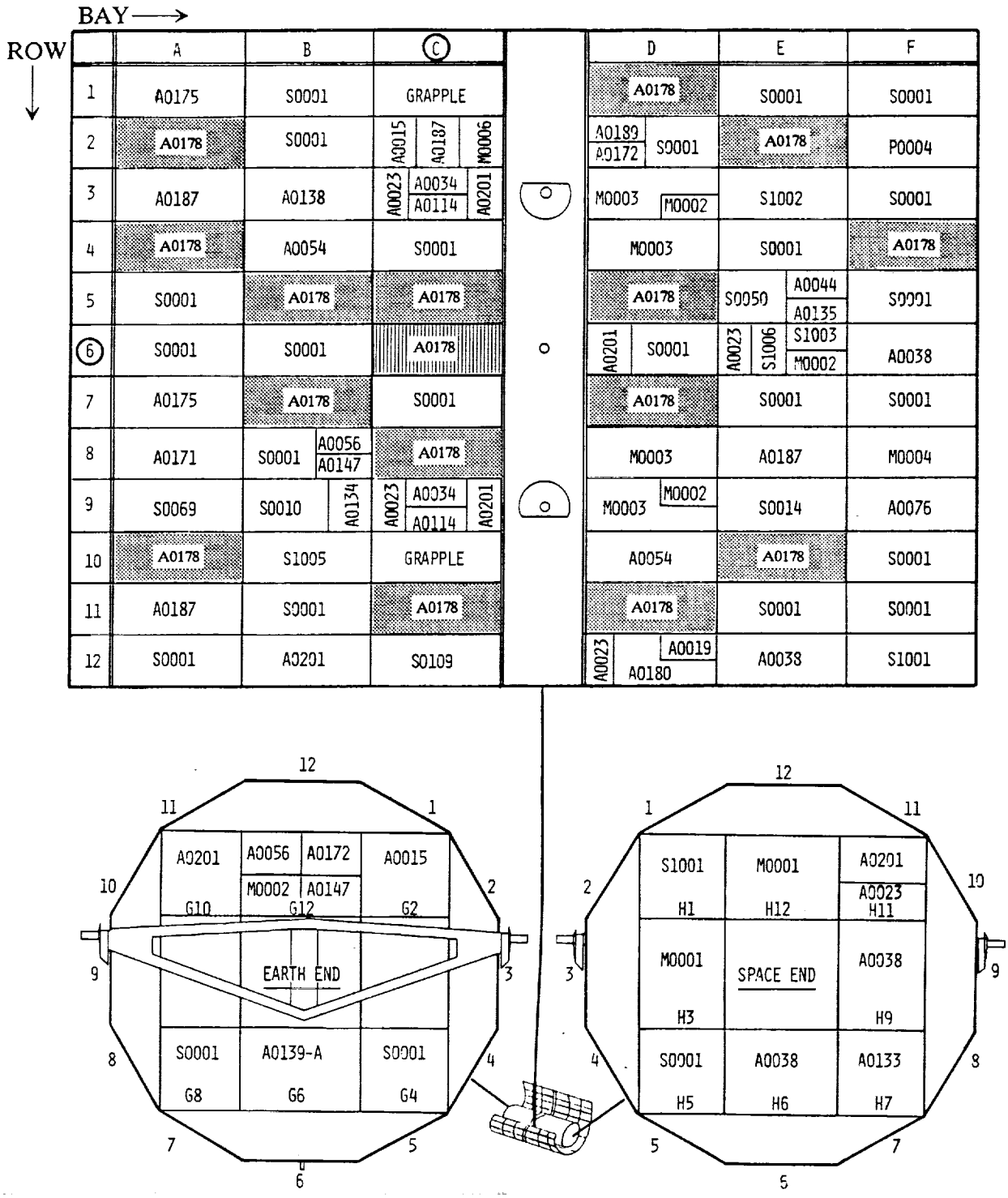

Figure 2. Experiment intergration chart showing the locations of the 16 Ultra-Heavy Cosmic-Ray trays.

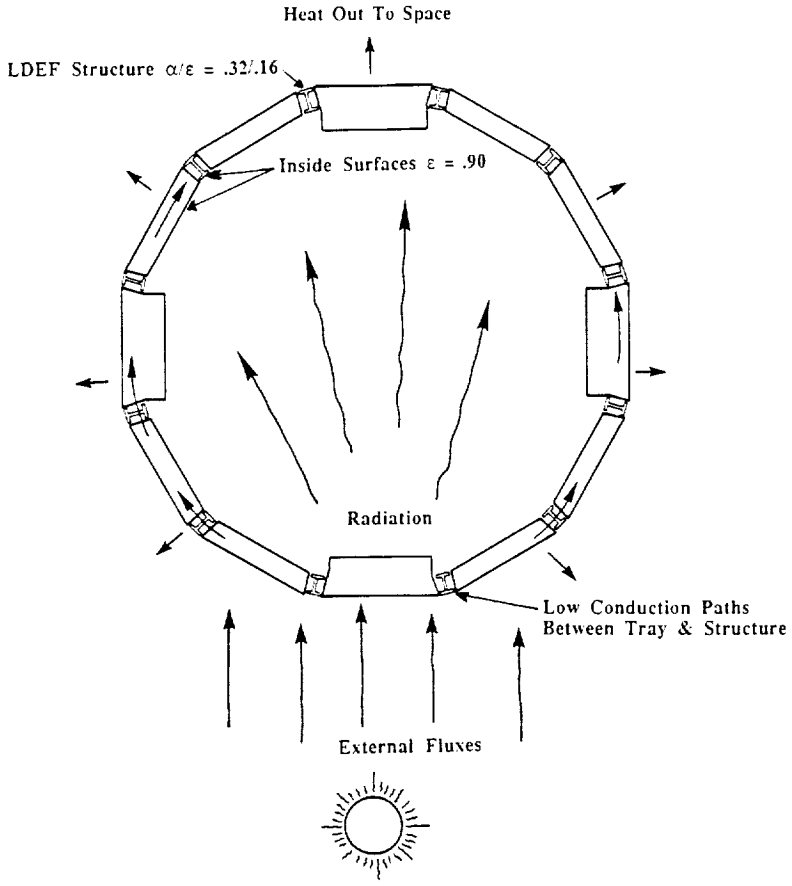

Figure 3. LDEF temperature control is passive by design.

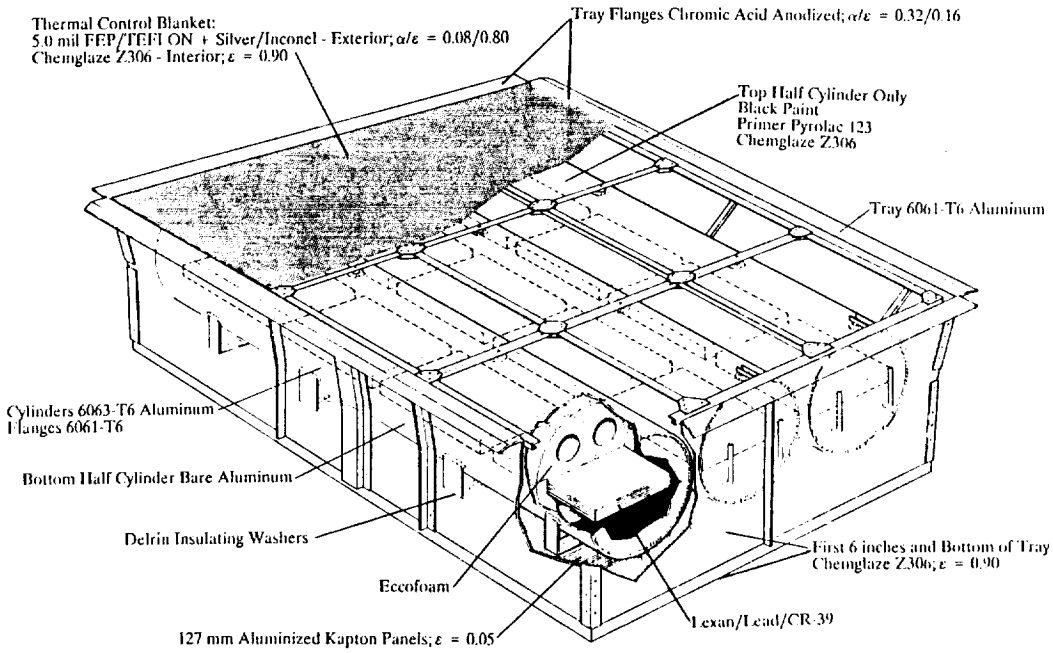

Figure 4. Construction and materials of the UHCRE tray.

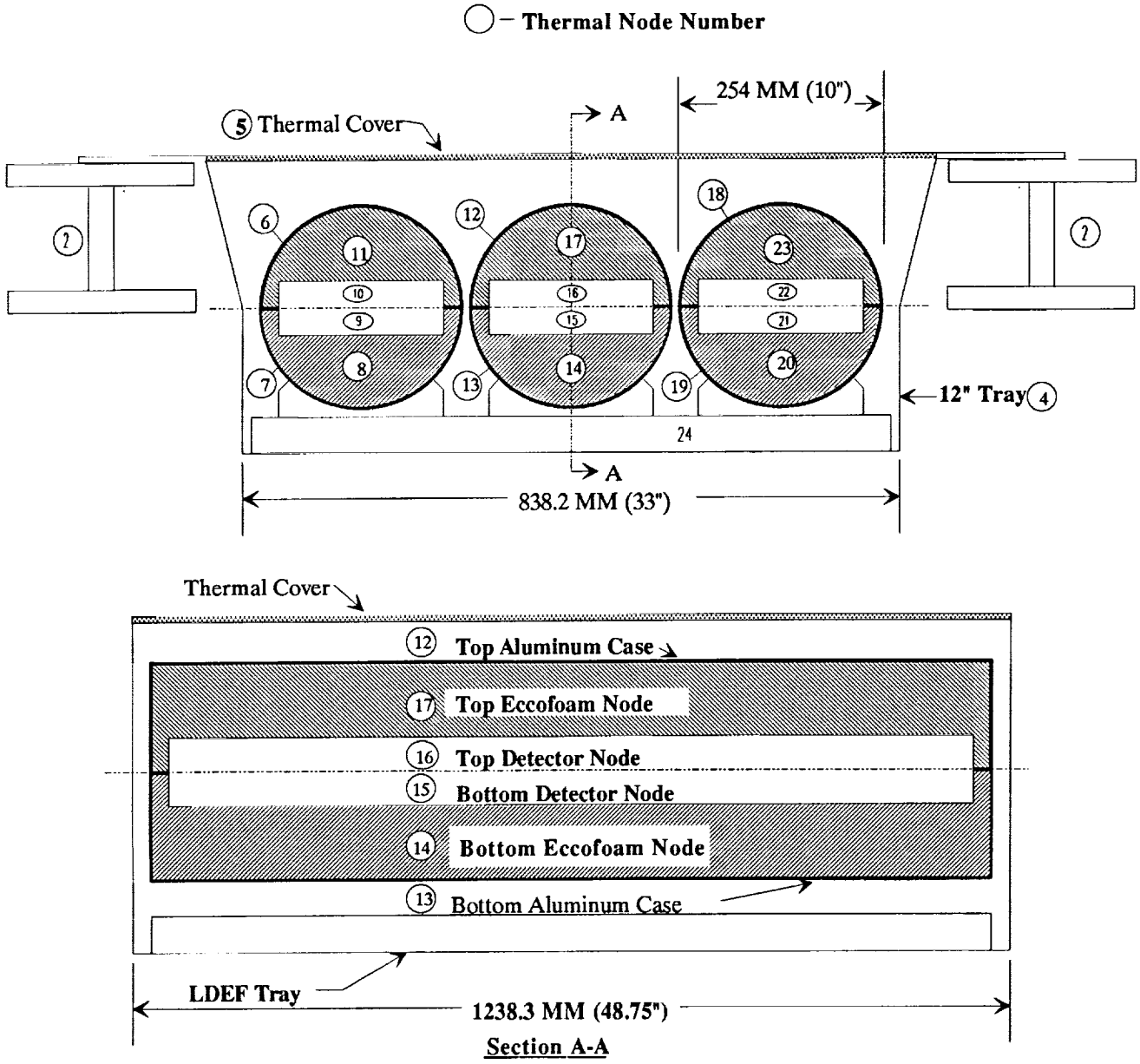

Figure 5. Thermal nodalization of the UHCRE experiment.

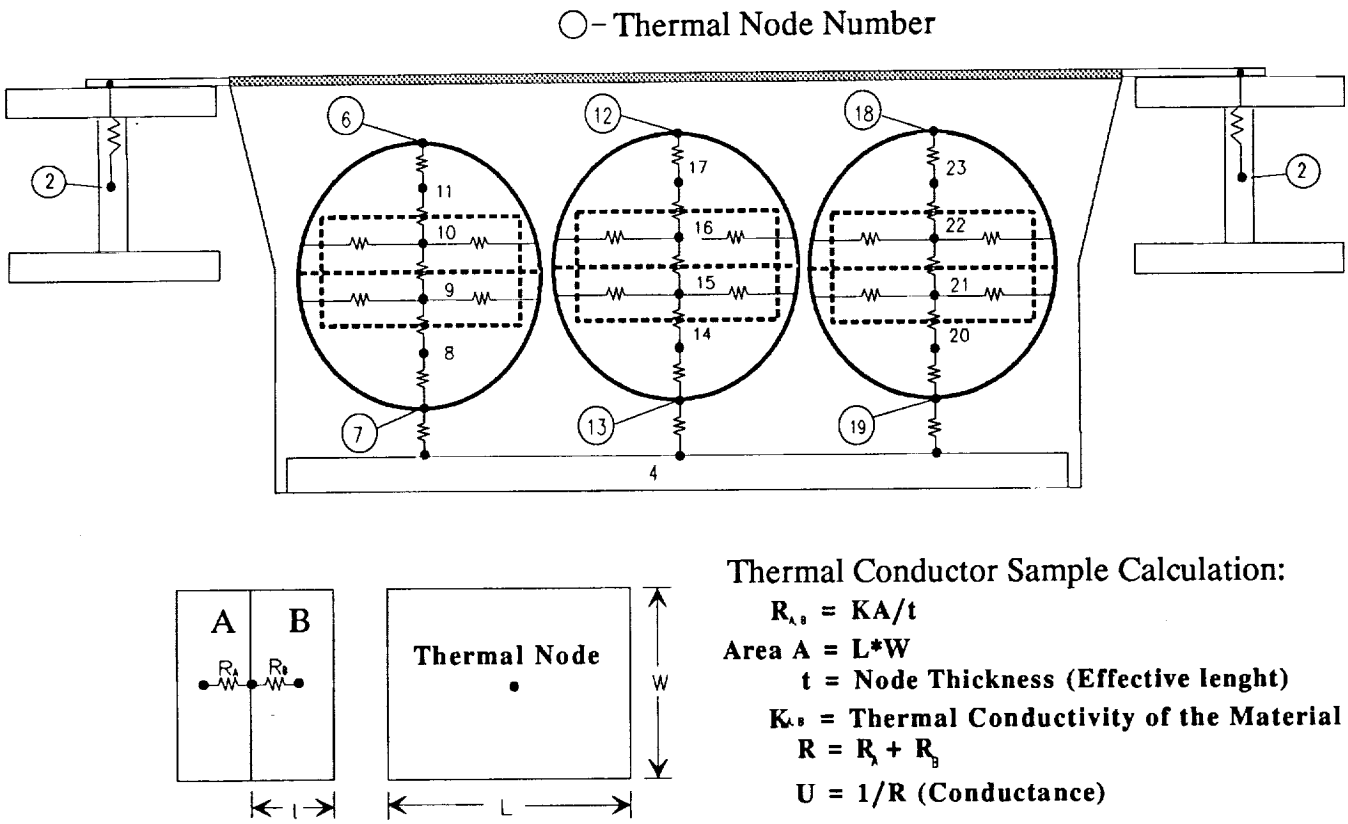

Figure 6. Thermal conduction network for the UHCRE experiment.

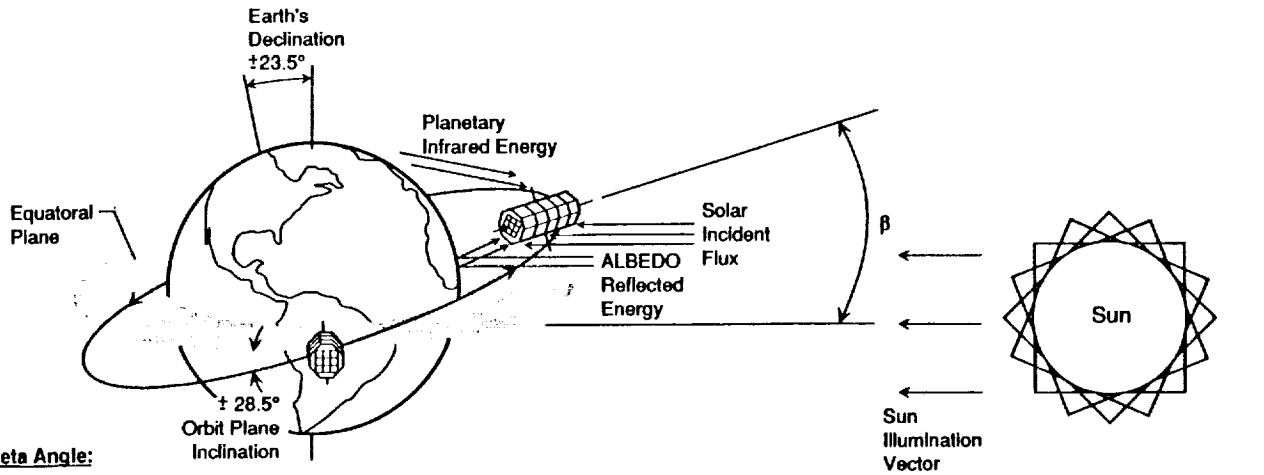

Beta Angle:

β = Angle between the plane of the orbit and the sun illumination vector.
Range = $-52° < \beta > +52°$, Calculated by adding the declination of the Earth ($\pm 23.5°$) to the inclination of the orbit plane ($\pm 28.5°$).

Principal Heating sources in Space:

Solar Incident Flux = Heat due to the direct illumination from the sun (Watts/M²).
Albedo = Heat due to the portion of the solar incident energy reflected from the planet on to the LDEF (23% - 32% for this type of orbit, Watts/M²).
Planetary = Heat emitted from the planet (Watts/M²).

Altitude:

Apogee = Point in the elliptical orbit which is the farthest from the Earth.
Perigee = Point in the elliptical orbit which is the closest to the Earth.
Semi-Major Axis = The distance between the center of the ellipse and the apogee or the perigee.
Line of Apsides = The major axis (2a) of the ellipse which passes through both the apogee and the perigee.

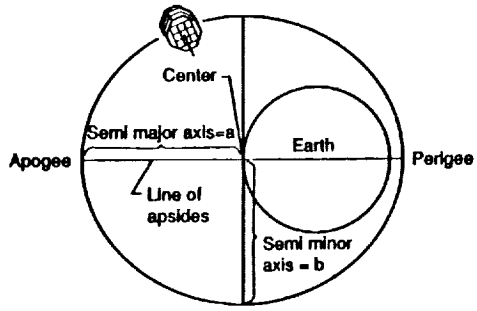

Figure 7. LDEF orbital environment definition.

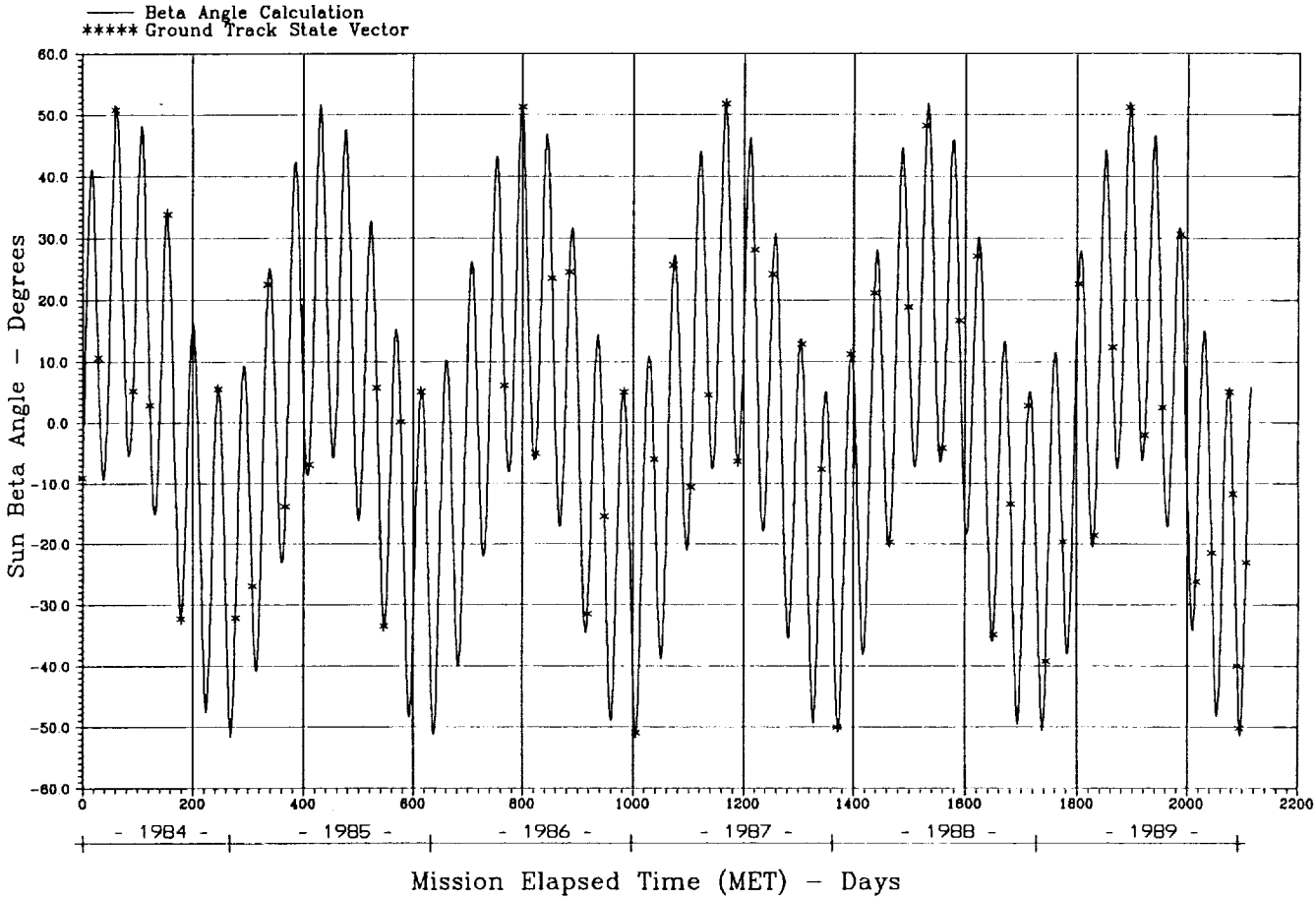

Figure 8. LDEF Beta angle history: April 7, 1984 – January 12, 1990.

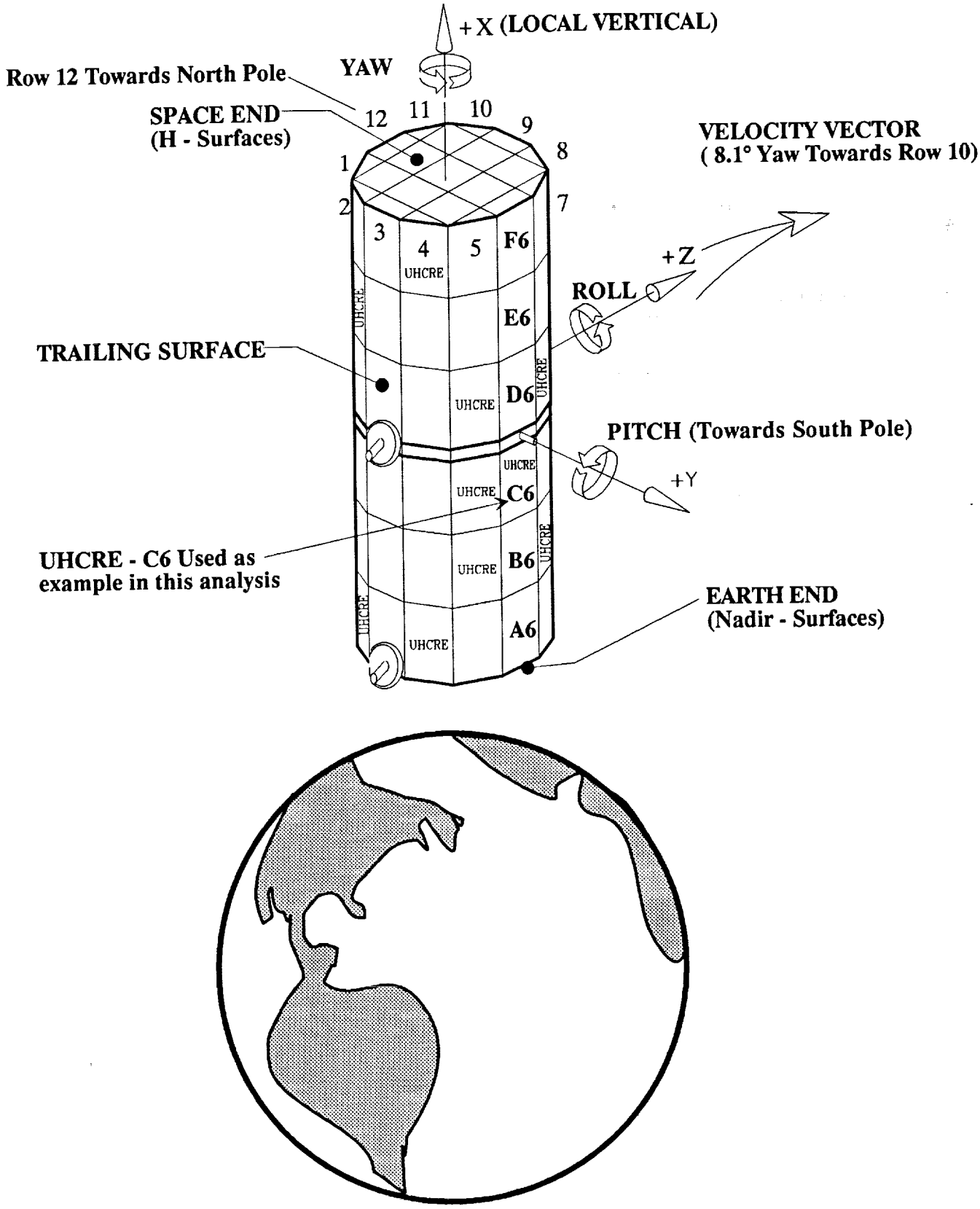

Figure 9. LDEF's orientation in free flight.

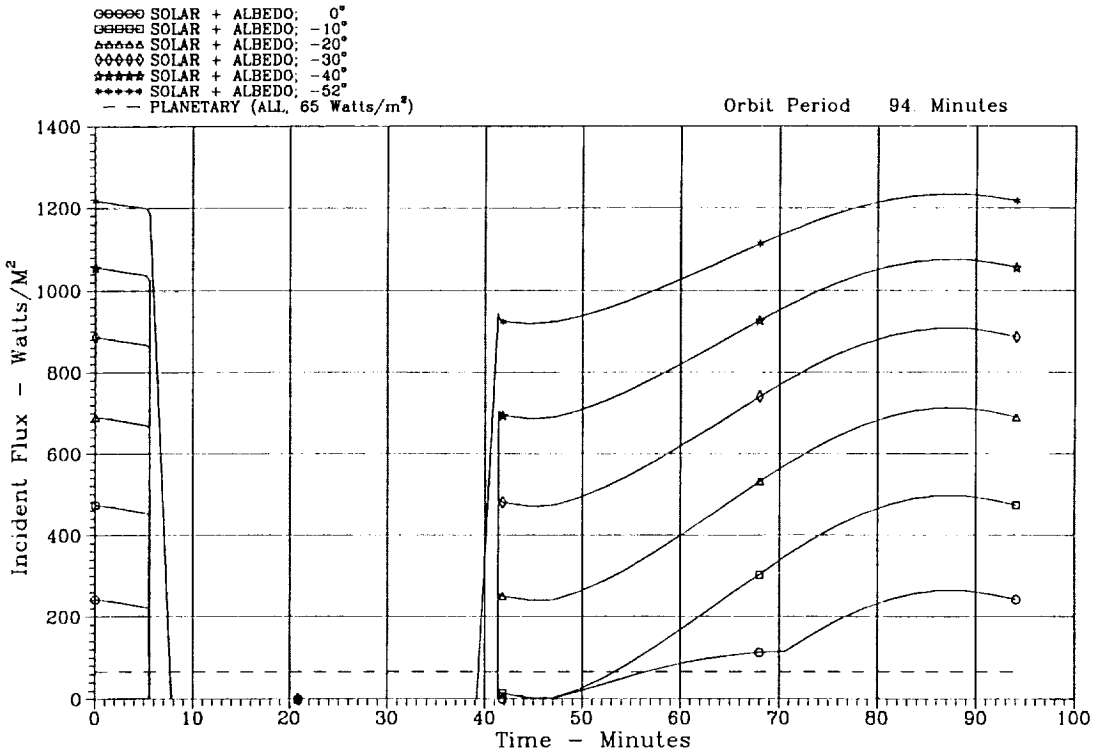

Figure 10. Row 6 orbital heat flux for negative beta angles.

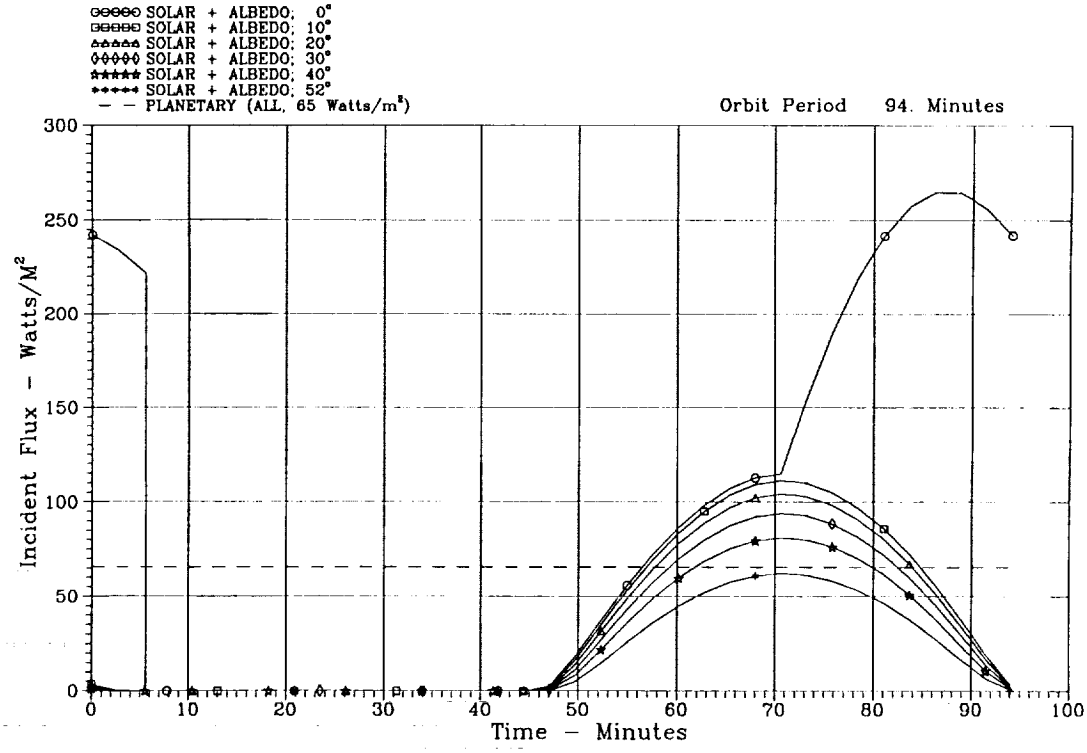

Figure 11. Row 6 orbital heat flux for postive beta angles.

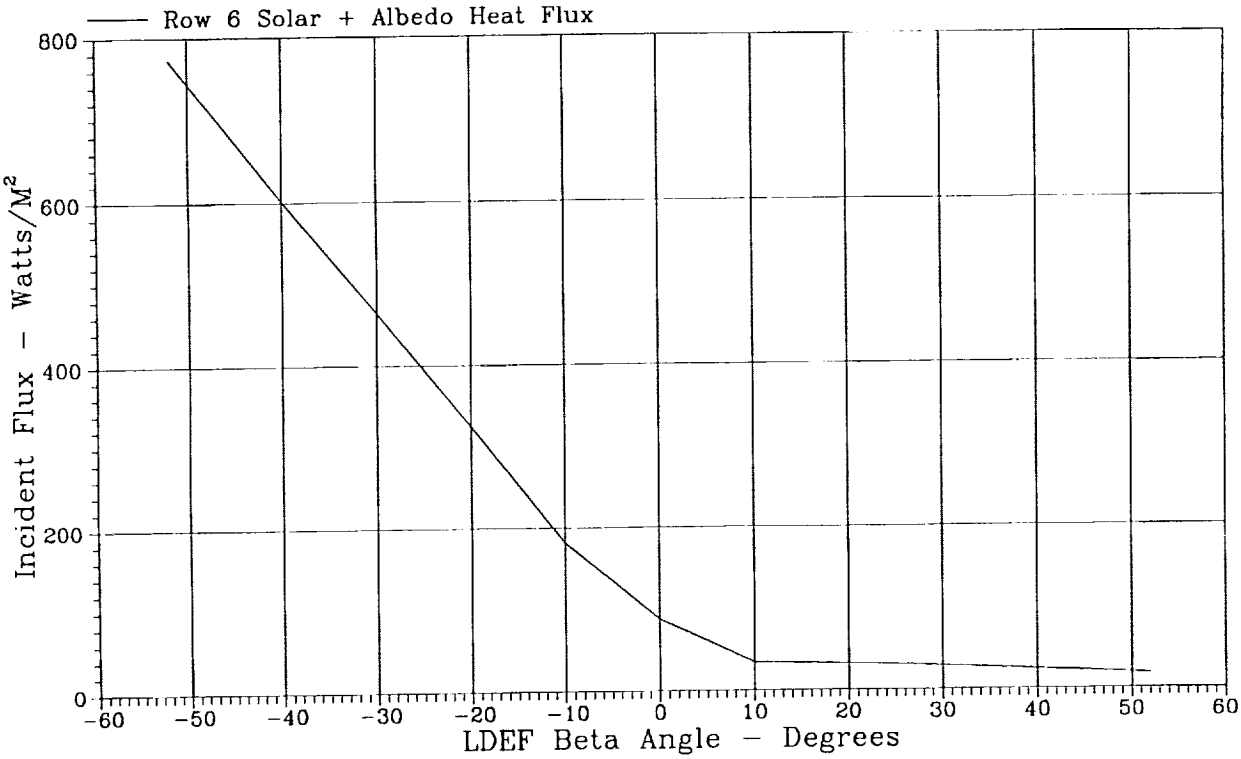

Figure 12. Row 6 orbital average heat flux vs LDEF beta angle.

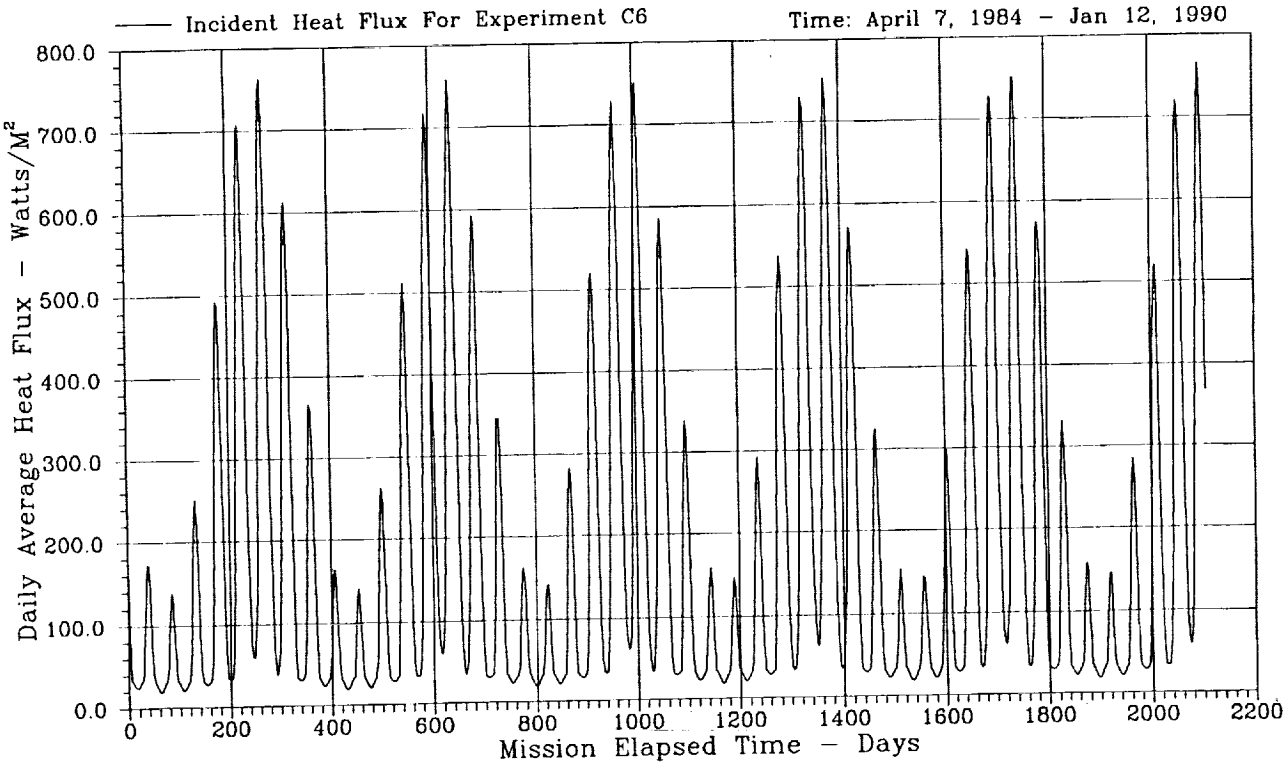

Figure 13. Solar plus albedo mission incident heat flux for the UHCRE located on row 6.

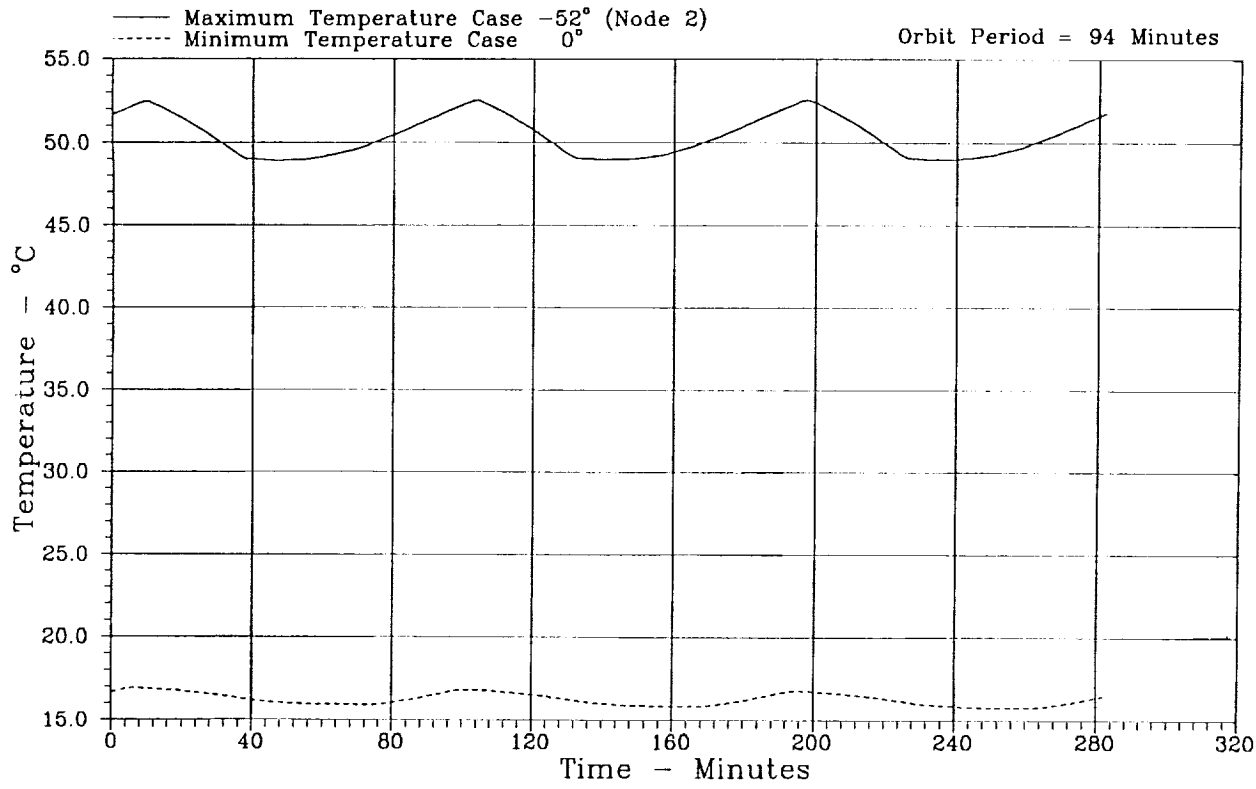

Figure 14. Average structure orbital boundary temperature.

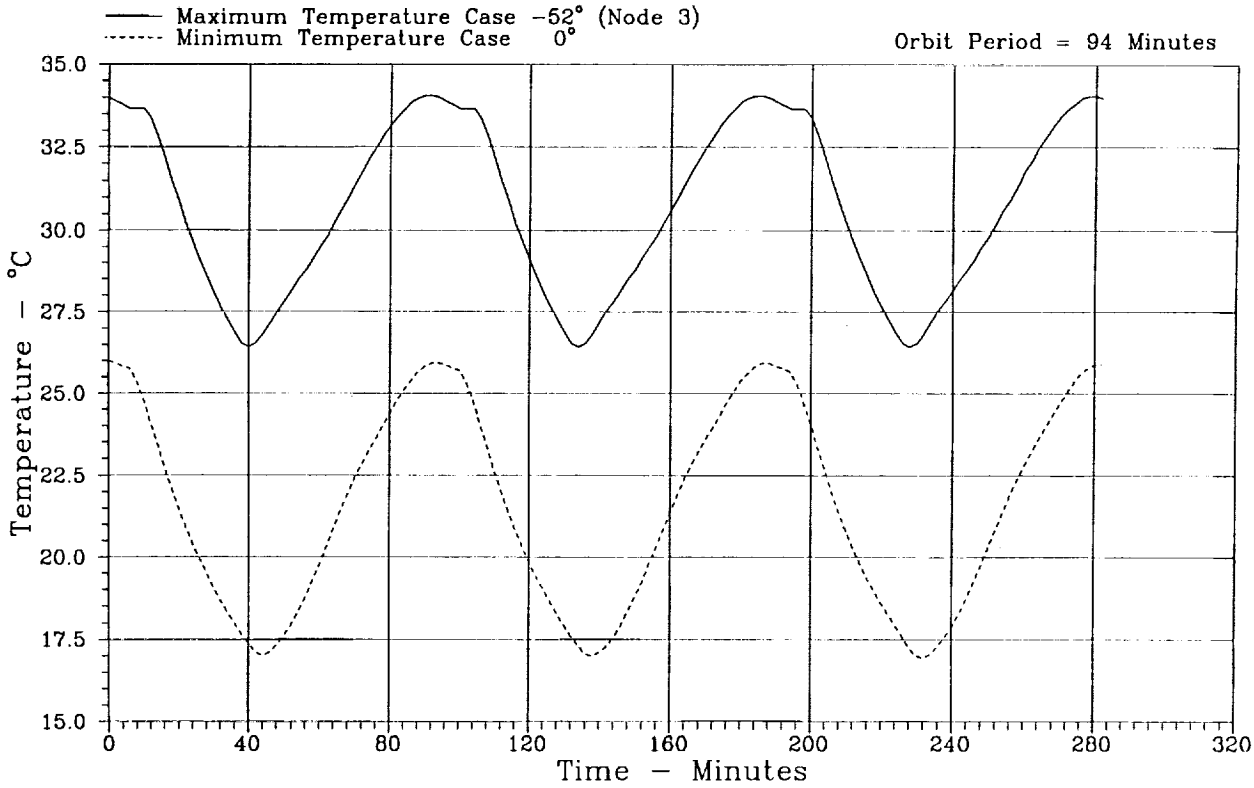

Figure 15. LDEF interior average orbital boundary temperature.

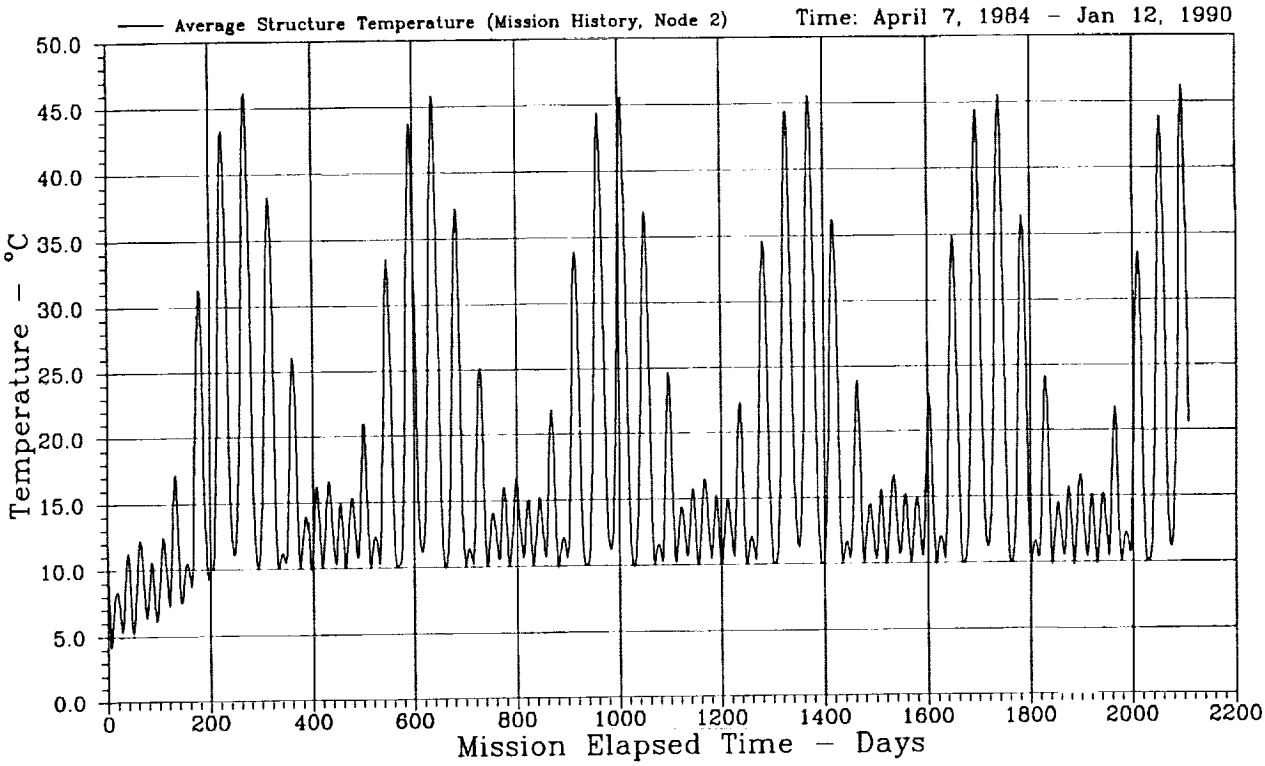

Figure 16. Mission average structure boundary temperature.

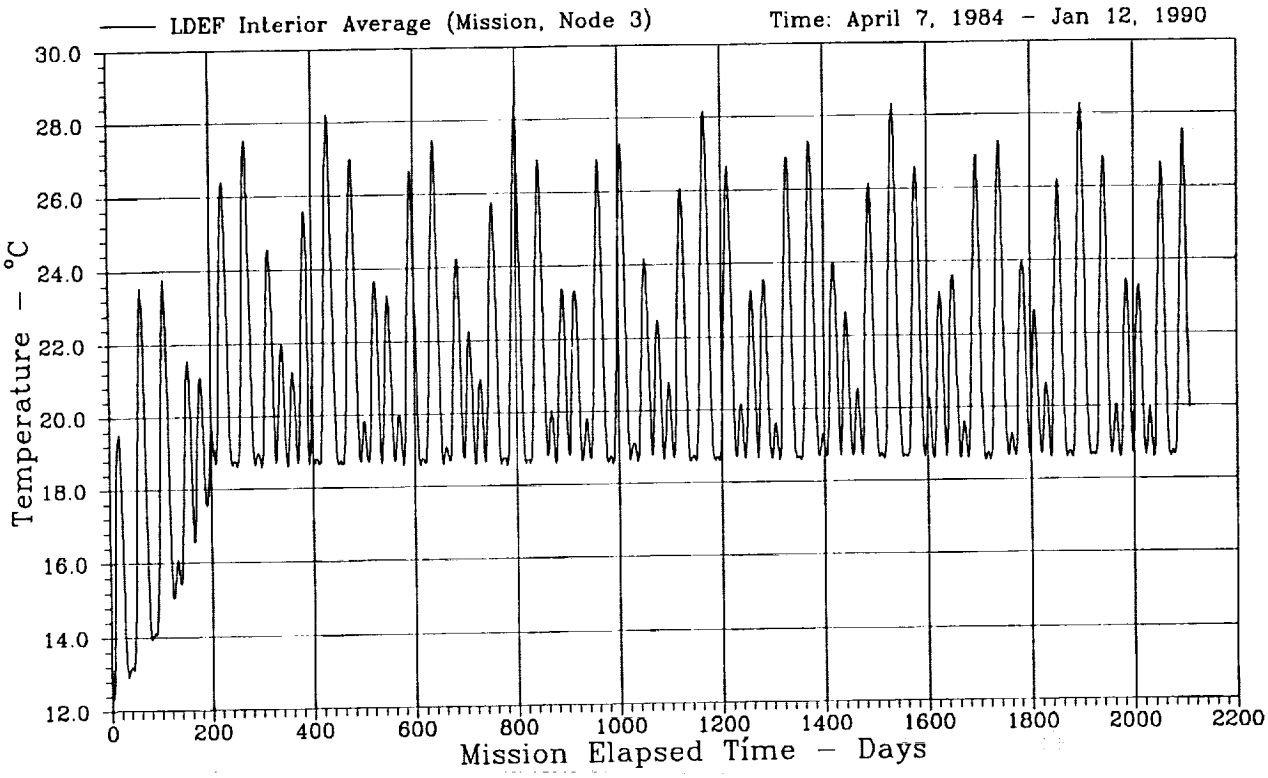

Figure 17. LDEF interior average mission boundary temperature.

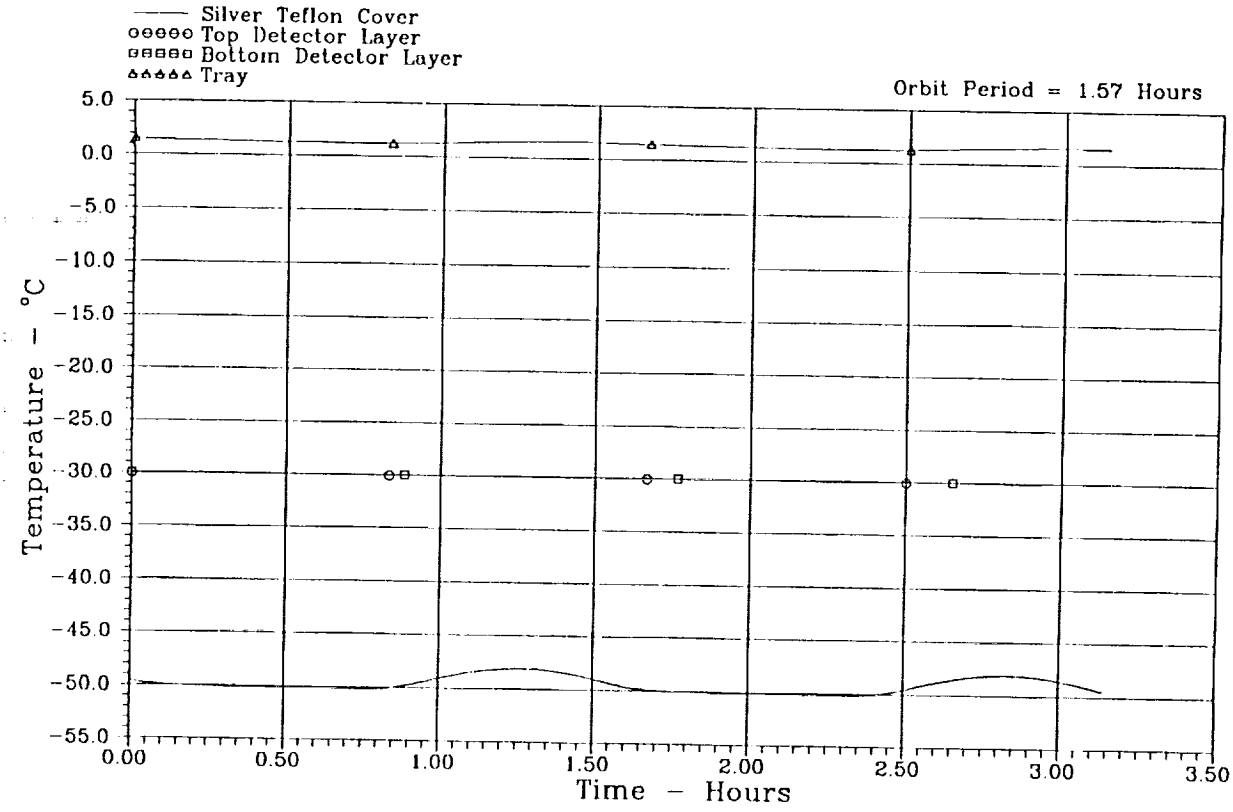

Figure 18. UHCRE-C6 Minimum orbtial temperature at 0°.

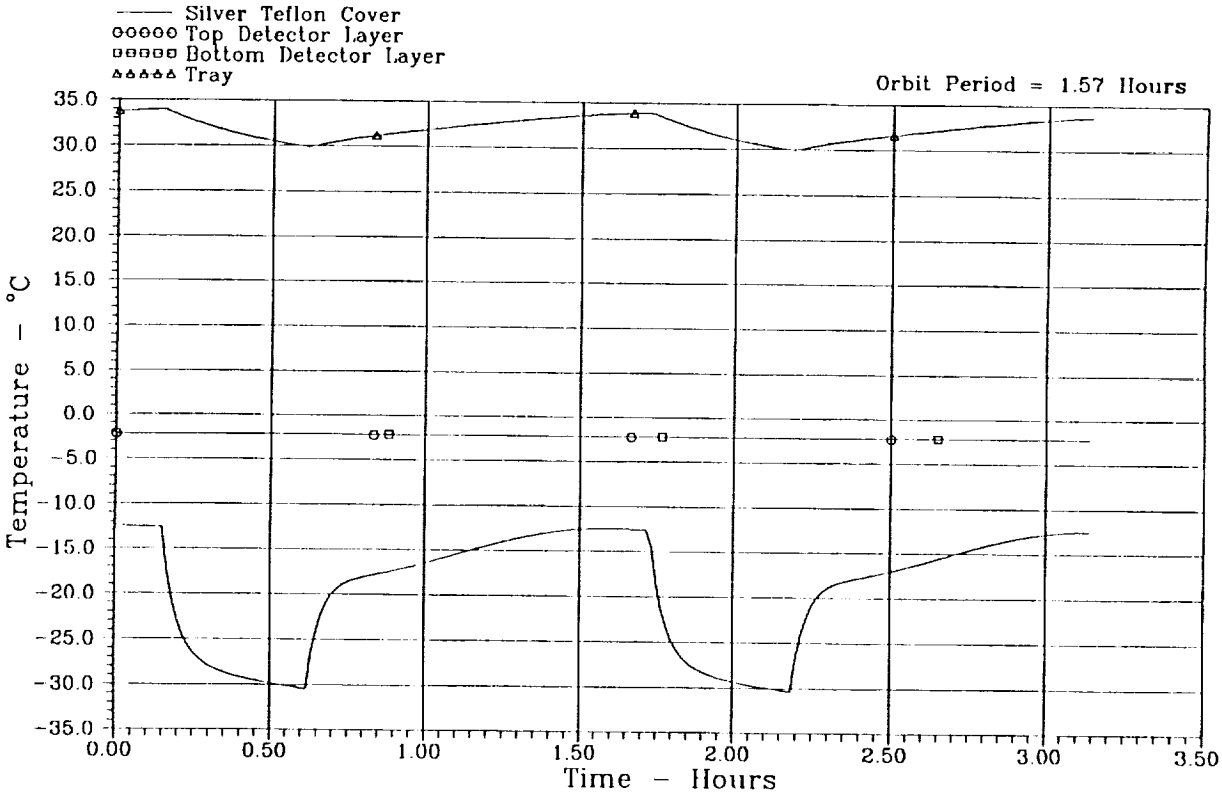

Figure 19. UHCRE-C6 Maximum orbital temperature at -52°.

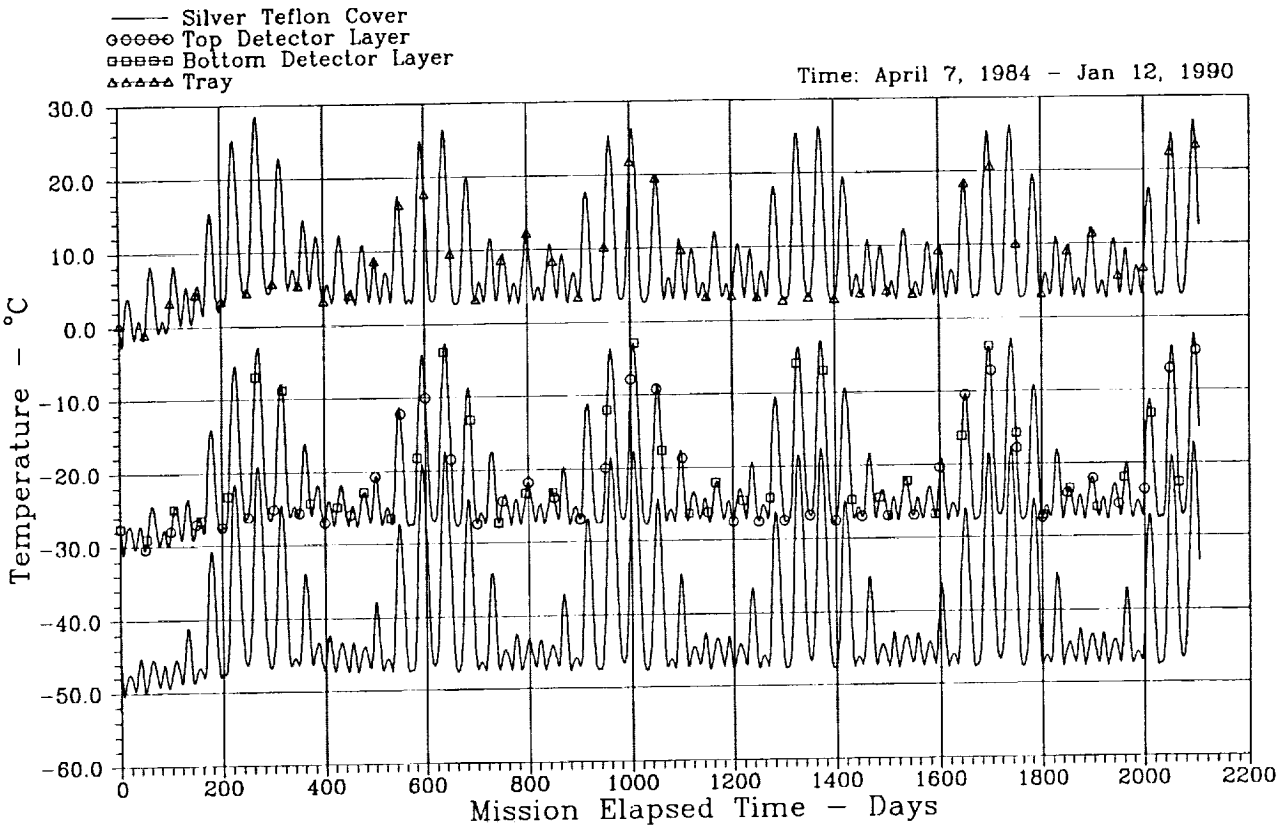

Figure 20. A0178-C6 Mission temperature history.

N93-29625

ENVIRONET: ON-LINE INFORMATION FOR LDEF

Michael Lauriente
NASA Goddard Space Flight Center
Code 420
Greenbelt, MD 20771-0001
Phone: 301/286-5690, Fax: 301/286-5198

ABSTRACT

EnviroNET is an on-line, free-form database intended to provide a centralized repository for a wide range of technical information on environmentally induced interactions of use to Space Shuttle customers and spacecraft designers. It provides a user-friendly, menu-driven format on networks that are connected globally and is available twenty-four hours a day — every day. The information, updated regularly, includes expository text, tabular numerical data, charts and graphs, and models. The system pools space data collected over the years by NASA, USAF, other government research facilities, industry, universities, and the European Space Agency. The models accept parameter input from the user, then calculate and display the derived values corresponding to that input. In addition to the archive, interactive graphics programs are also available on space debris, the neutral atmosphere, radiation, magnetic fields, and the ionosphere. A user-friendly, informative interface is standard for all the models and includes a pop-up help window with information on inputs, outputs and caveats. The system will eventually simplify mission analysis with analytical tools and deliver solutions for computationally intense graphical applications to do "What if..." scenarios. A proposed plan for developing a repository of information from the Long Duration Exposure Facility (LDEF) for a user group concludes the presentation.

INTRODUCTION

LDEF is an example of a highly cost effective experiment whose results will provide a major contribution to the design of spacecraft operating in Low Earth Orbits (LEO). Knowledge of the operating environments is important to the prevention of anomalies in the operation of spacecraft. After all the results have been analyzed and verified, EnviroNET would like to be considered as a centralized repository for technical information on environmentally induced interactions likely to be encountered in the LDEF orbit. These results will enhance the value of text that is presently available on other orbits. Features such as a user-friendly, menu-driven format on networks connected globally, available twenty-four hours a day will assist engineers and scientists in the retrieval and acquisition of this valuable information. This data will supplement the data

collected over the years by NASA, USAF, other government research facilities, industry, universities, and the European Space Agency. This information, updated regularly, contains text, tables, and over one hundred high resolution figures and graphs based on empirical data.

The topics, shown in Figure 1, act like files containing information on the space environment. Topic titles evolved from the Space Shuttle's concerns. Information emerging from LDEF should fit neatly into these topics. Text on space debris/meteoroids is considered a natural environment subject, as is text on the ionizing radiation environment. Finding specific information, however, is not solely dependent on knowing under which topic it has been filed. Searches of the entire database are possible using a key word search function.

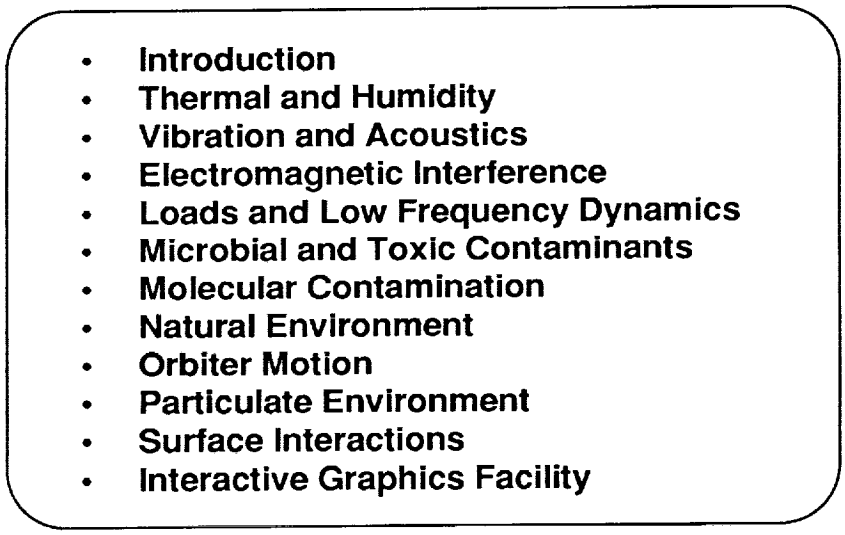

Figure 1. Current Topics.

A Working Group, Figure 2, is proposed to handle the task of developing the results of LDEF suitable for insertion into the EnviroNET library. A good deal of the groundwork has already been done. The User Panel has yet to be organized, but the Information Management Panel is provided by the staff of EnviroNET.

Figure 3 is a chart of the Natural and Induced Environments Panel. The Natural Environment Panel would include space debris/meteoroids and ionizing radiation. For LDEF it may be desirable to make modifications to the types of sub-panels. The purpose of the panel is to make assessments of reliability and traceability of data.

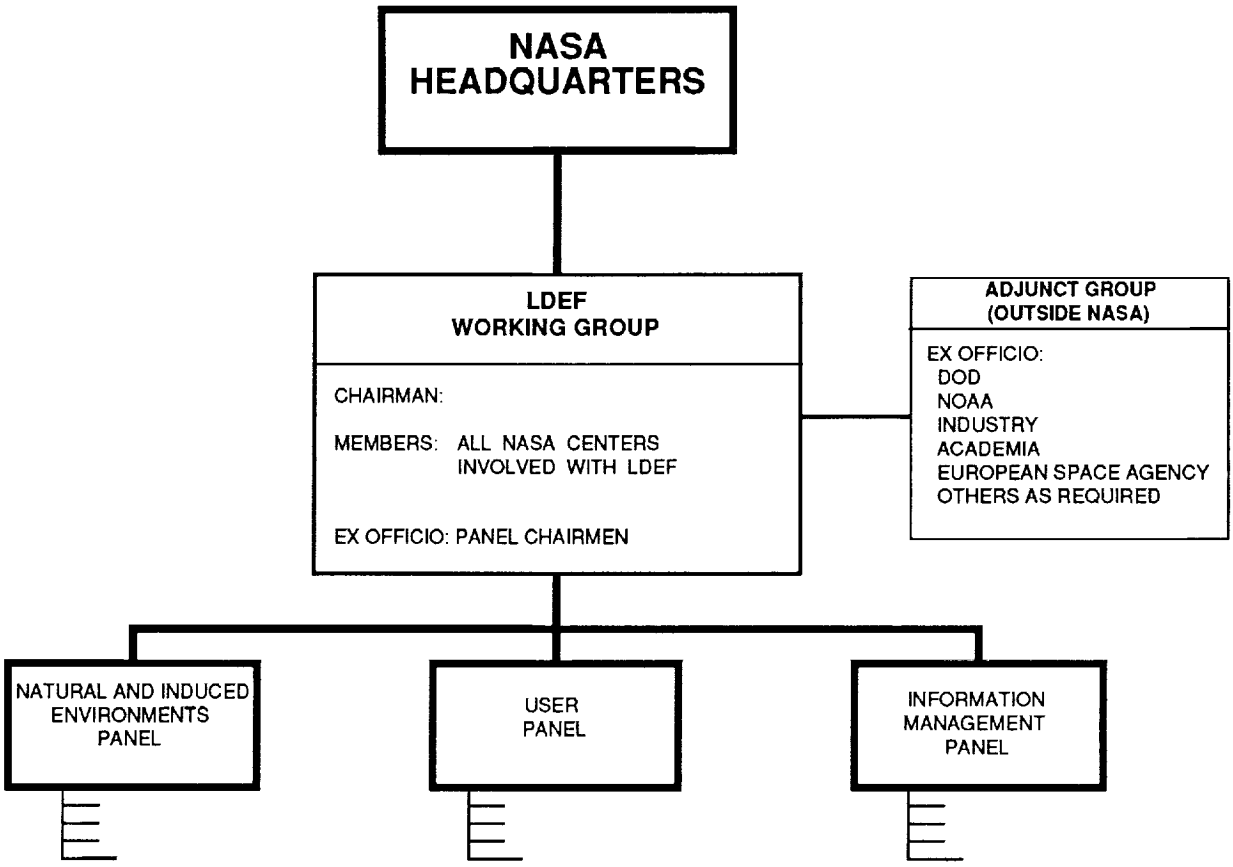

Figure 2. LDEF Working Group.

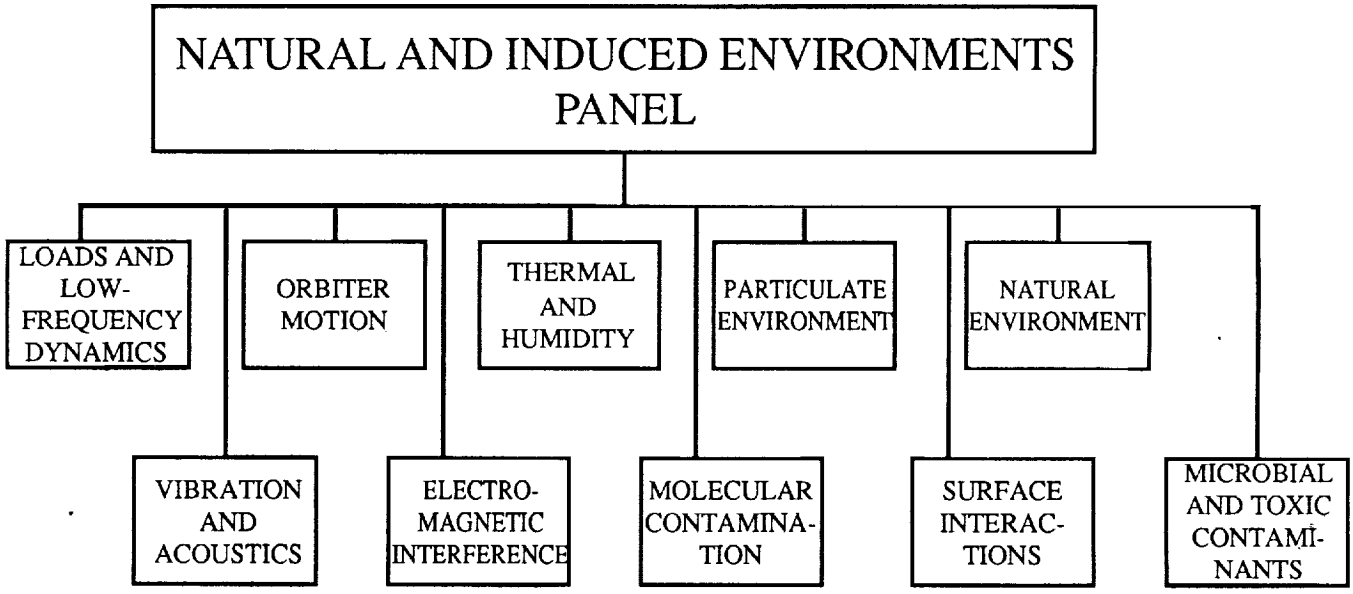

Figure 3. Natural and Induced Environments Panel.

The implementation of on-line, simplified computational models in the EnviroNET database was strongly recommended by many EnviroNET users. A review of published prediction models indicated that selective computational models could be sufficiently simplified to meet the user-friendly requirement of the EnviroNET database. The scope of the interactive models is shown in Figure 4.

EnviroNET models provide a readily accessible method to do quick accurate calculations. These models encompass many important environments for engineers. A user-friendly informative interface is standard and all models have a pop-up help window which gives more information on inputs, outputs and caveats. Figure 5 is an example of a model help window for the International Geomagnetic Reference Field (IGRF) model[1]. These models, based on data from satellites which orbit the earth in the thermospheric and exospheric regions of the atmosphere, will benefit from the LDEF data.

Use of the models has been simplified by providing outputs in a tabular form which can be viewed directly on the user's screen. In addition the data is available in file format for downloading or for plotting using EnviroNET's interactive graphics feature. Orbit dosage programs are designed to allow the user to analyze the radiation dosage for a given orbital configuration or to predict densities and temperatures encountered along a given orbit.

Figure 6 is an example of a user-friendly model for space debris[2]. The Orbital Debris Model provides essential data needed for risk assessment; it is widely used to predict current and future debris environments. A provision to make order-of-magnitude estimates of collision probabilities is being developed. The input parameters are on the left and input ranges on the right. After the computer is asked to run the model, the output appears in a pop-up window.

- **Mass Spectrometer Incoherent Scatter Model (MSIS-86)**
- **MSIS-E (Altitude Extended version of MSIS)**
- **Marshall Engineering Thermosphere Model (MET)**
- **International Reference Ionosphere Model (IRI)**
- **International Geomagnetic Reference Field Model (IGRF)**
- **Radbelt Model**
- **Energetic Particles Model**
- **Cosmic Ray Effects on Microelectronics Model (CREME)**
- **Orbital Debris Model**
- **Meteoroid Model**
- **Orbital Decay Model**
- **Thermal Analysis Tool**
- **F10.7 Solar Flux Model**
- **Mars Neutral Atmosphere Model**

Figure 4. Scope of Interactive Models.

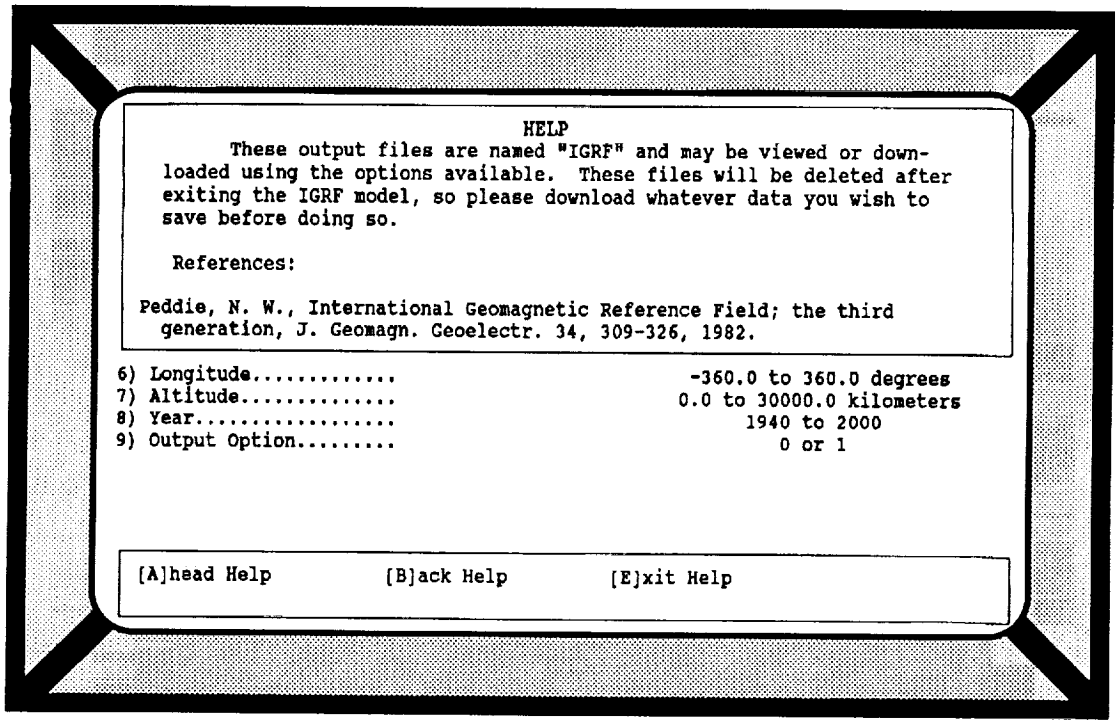

Figure 5. Help Window from the IGRF Model.

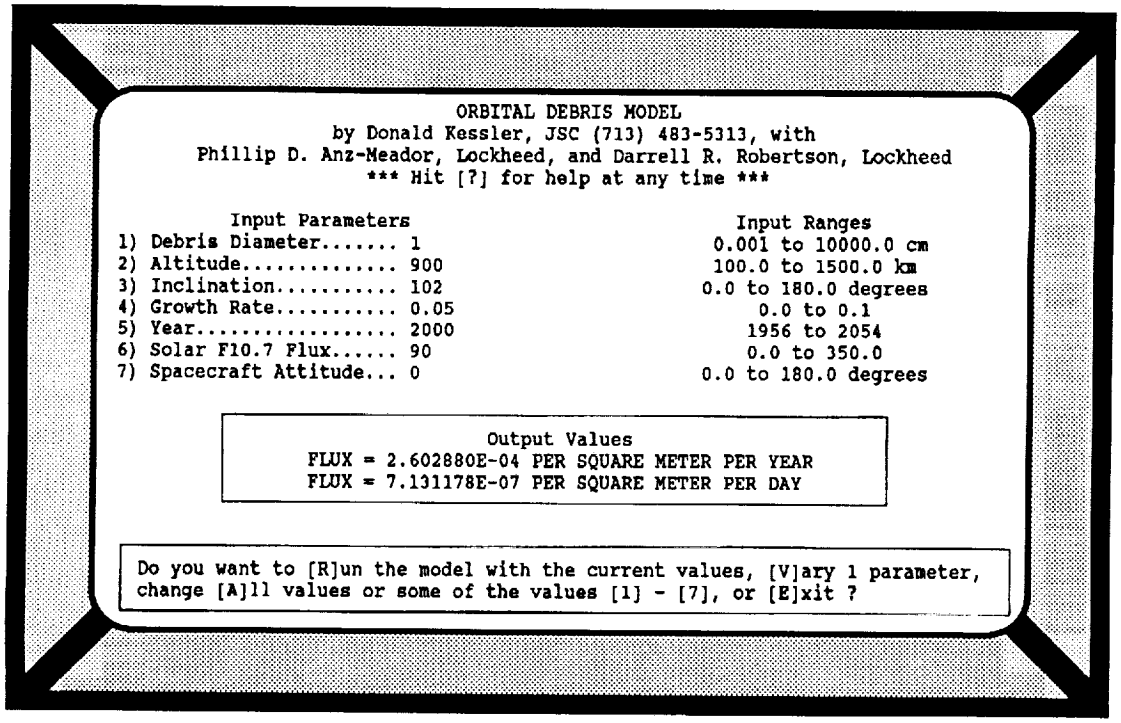

Figure 6. User-friendly Orbital Debris Model.

The system allows plotting of output versus any input parameter. By varying parameters within a model, "What if..." scenarios, as shown in Figure 7, can be graphically depicted on a remote user's computer screen. Graphs are generated using Interactive Data Language (IDL), a commonly used commercial package, which can be viewed on any terminal using Tektronix emulation.

Figure 8 is an example of a user-friendly interface for the Mass Spectrometer Incoherent Scatter (MSIS-86) Model[3]. MSIS is the standard empirical neutral atmosphere model. Output of temperatures and densities of atmospheric constituents, including atomic oxygen, are displayed in a clear, concise format on the screen. As shown below, by integrating over a specified orbit, mission fluences are easily calculated. Such information would be valuable for drag calculations or for calculating erosion due to atomic oxygen.

Environmental scientists can even map the atmosphere in spatial dimensions. Affordable tools now make it feasible to provide graphical representation to the scientific data. C programming is used to deliver computationally intense graphical representations. Figure 9 is an example of a surface plot superimposed over a topographic plot from the output of the MSIS-86 model. Day of the year is along the x-axis, latitude along the y-axis, and density along the z-axis.

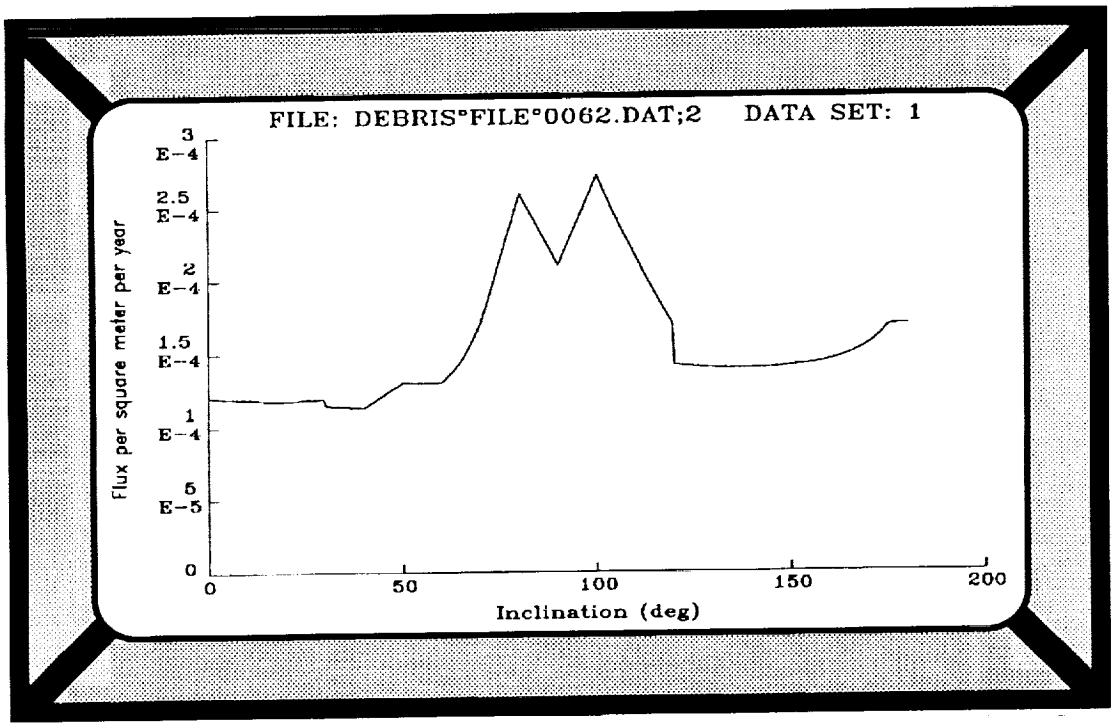

Figure 7. Plot from the Orbital Debris Model.

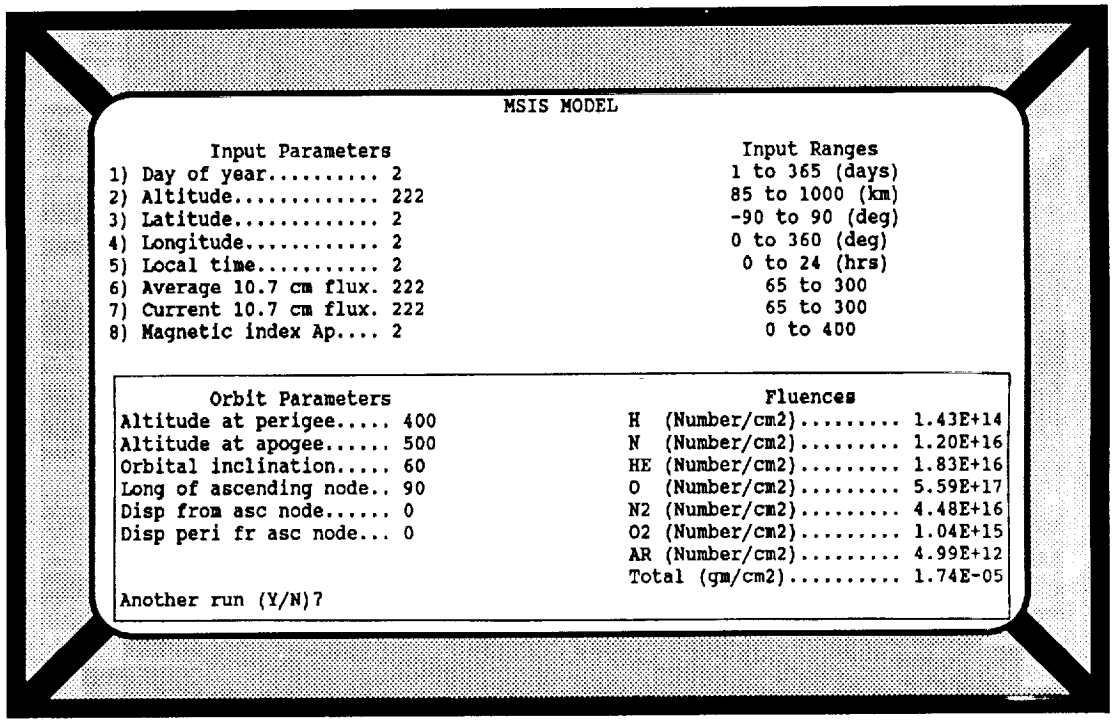

Figure 8. MSIS Model output showing orbital fluence of species.

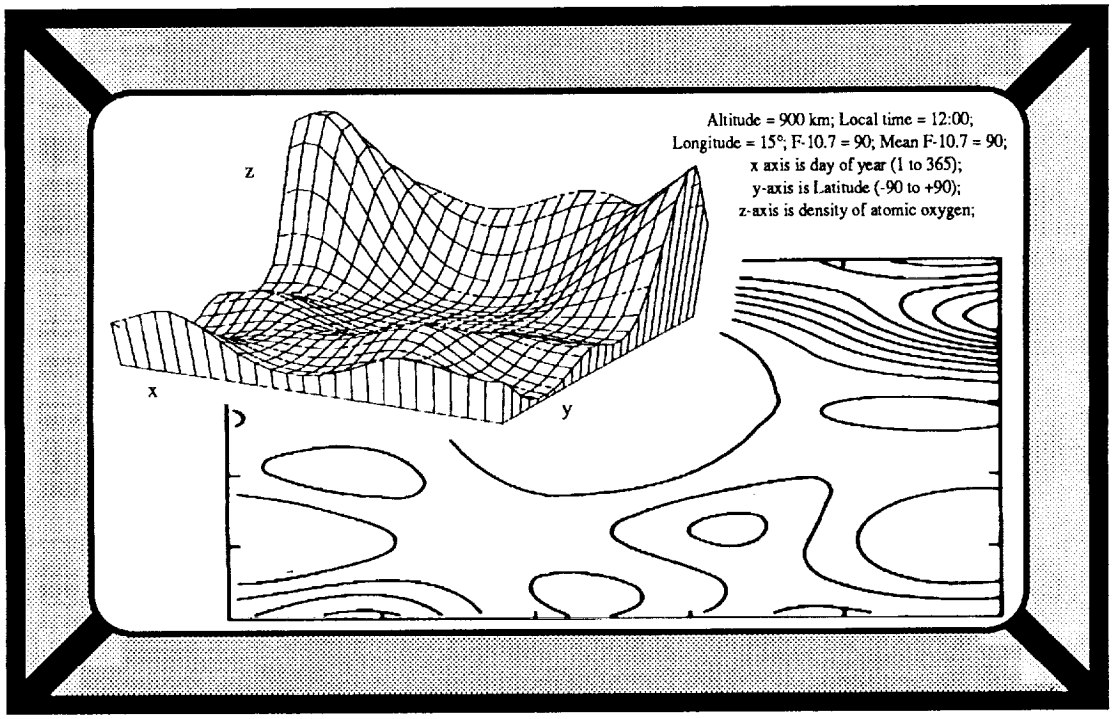

Figure 9. Sample output graphic from MSIS Model.

Figure 10 is an example of the Cosmic Ray Effects on Microelectronics (CREME) model. A prime use of the model is the calculation of the linear energy transfer (LET) spectra for a number of elements and range of densities for any orbit. This information, when used in conjunction with electronic part information, can be used to calculate the single-event upset (SEU) rate of the component. The model includes effects of solar flares, geomagnetic cutoff, and trapped protons.

Figure 11 is a review of EnviroNET's main menu. The aforementioned models fall under the Interactive Modeling Function. The Browse text retrieval system allows the user to literally "browse" through the textual library of EnviroNET. All written information is transportable, including graphics. The mail system, one of EnviroNET's sources of user feedback, has played a major role in improvements that have been implemented. Other features are the modeling function, message service, and bulletin notices. The systems manager, upon request, can establish an exclusive account for LDEF so that its constituents can have their own e-mail service.

Figure 12 shows the text as it is displayed on the screen by the Browse system. The window on the bottom gives the menu for performing actions within Browse such as paging forward and backward, dog-earing pages, searching the text topically by key word, or switching to the table of contents or index. The text often includes references to graphics which are separated into separate files in order to shorten the time required for downloading the text. Figure 13 is a sample screen presentation of the bit map graphics.

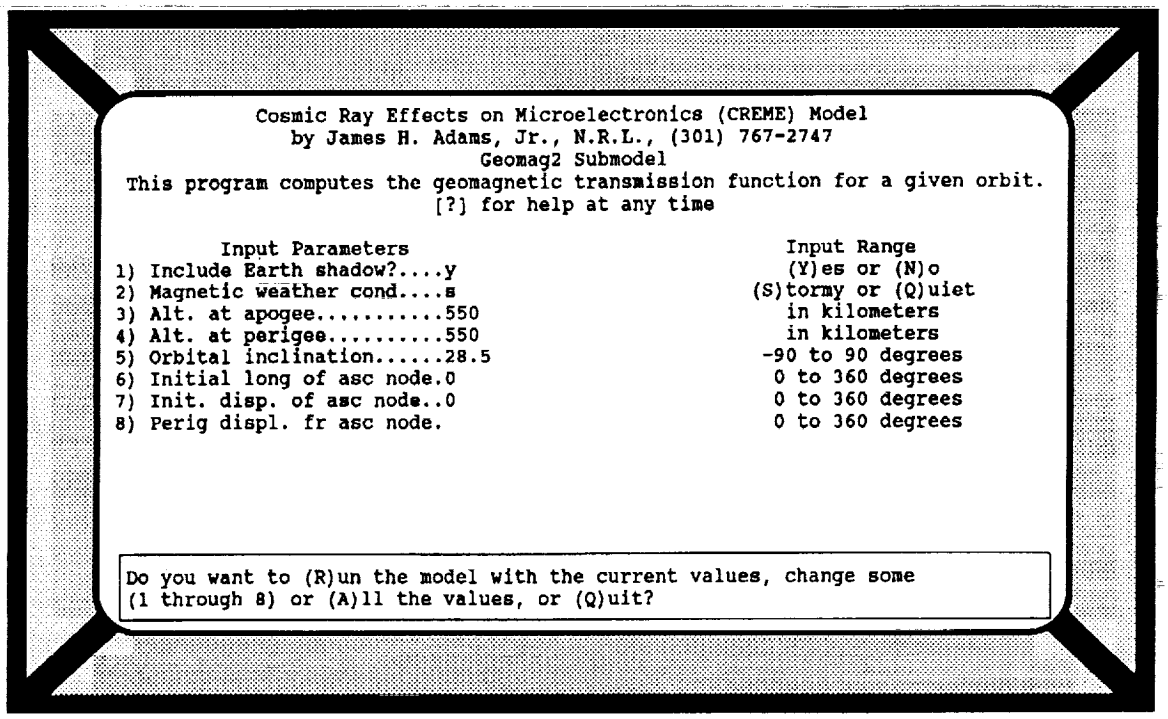

Figure 10. CREME Model.

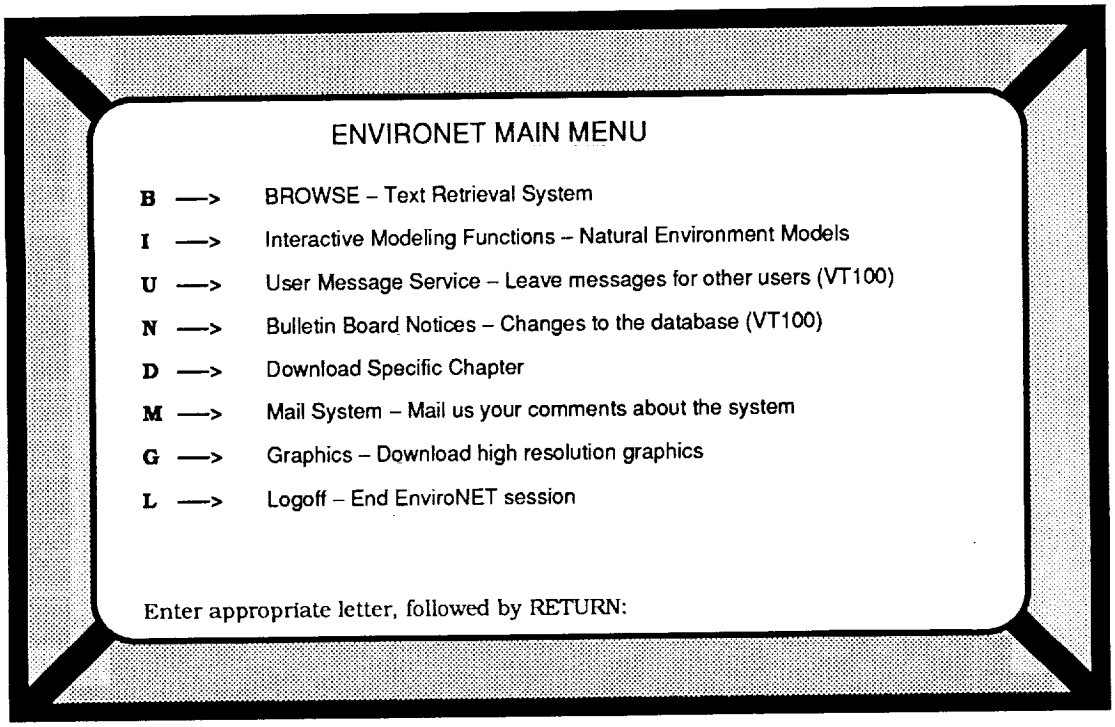

Figure 11. EnviroNET main menu.

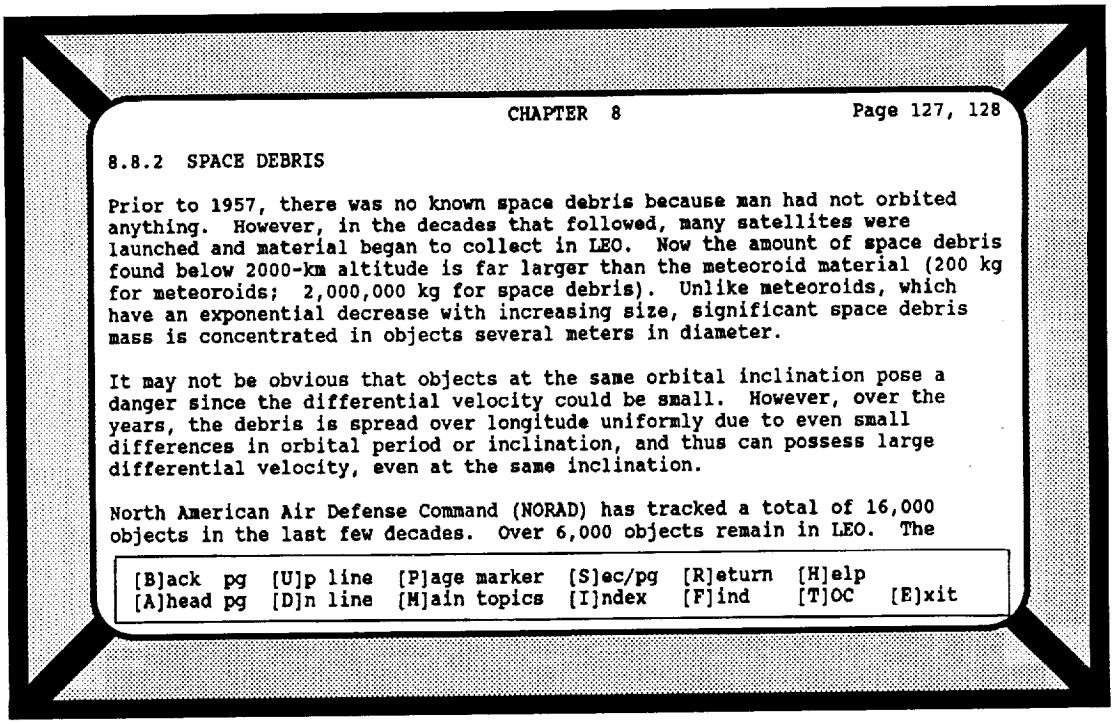

Figure 12. Browse text retrieval sub-system.

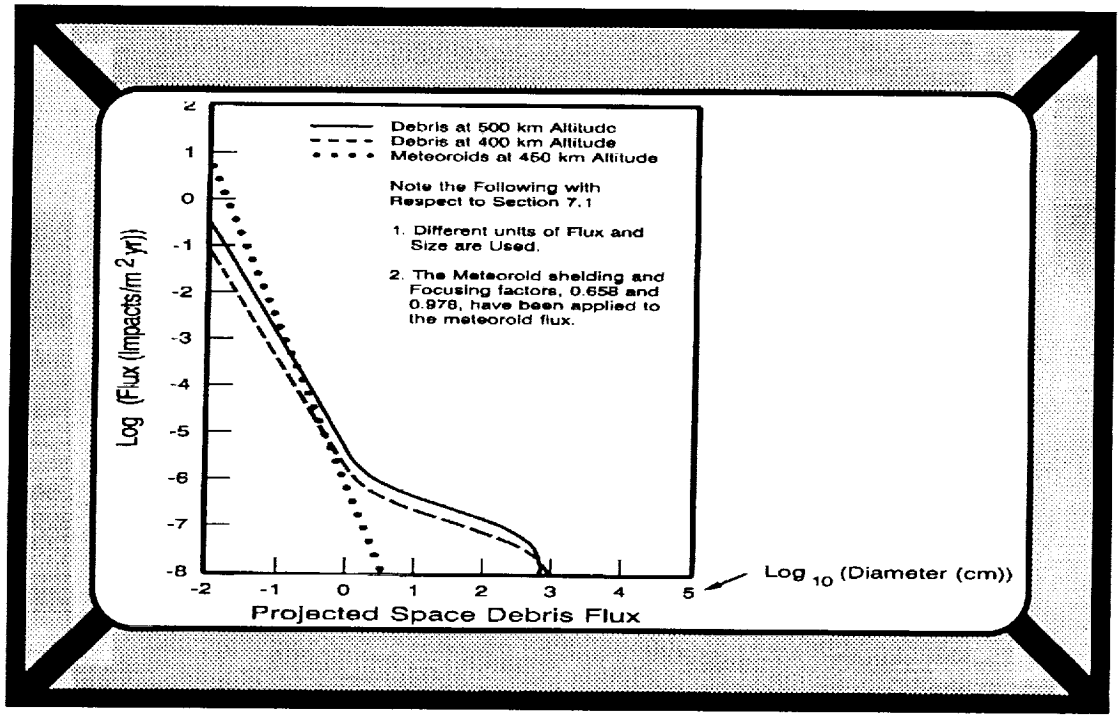

Figure 13. High resolution graphic.

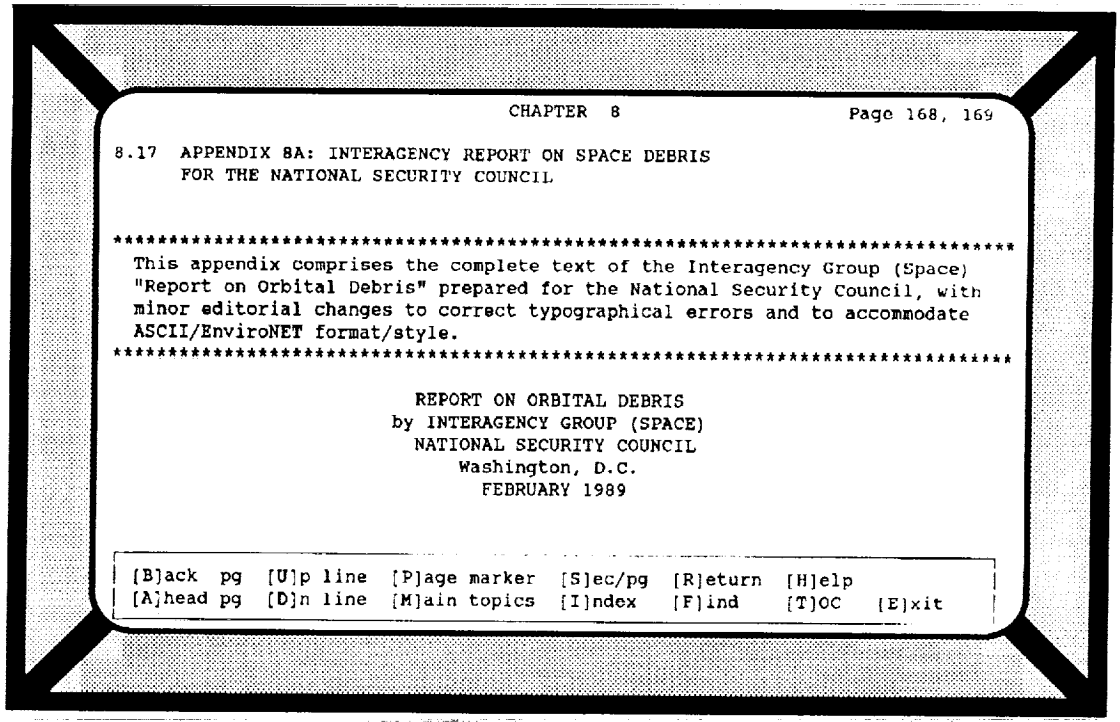

Figure 14. Interagency Report on Orbital Debris.

As a rule, full text of reports is not included in EnviroNET. Exceptions have been made for reports which were considered of strategic importance and not readily available to the community. The Interagency Report on Orbital Debris[4] is one such report. It was added as an appendix to the section covering the natural environment (Figure 14). A copy of the report was forwarded directly to EnviroNET as a text file on floppy disk. This "electronic transfer" of information saved much labor and time by allowing the report to be included with minimal formatting. The other document included in its entirety is the Spacecraft Anomalies Handbook[5].

Figure 15 is a schematic of the suggested data management and flow plan. The concept for a central data network is shown in Figure 16. The various access opportunities are shown at the bottom.

Figure 17 shows the model access and organization that is in use. Environmental models, written in either FORTRAN or C language are transparent to the user. The user works with a friendly input/output screen presentation. Other options available include reviewing data tables and viewing interactive graphics using C and Interactive Data Language (IDL).

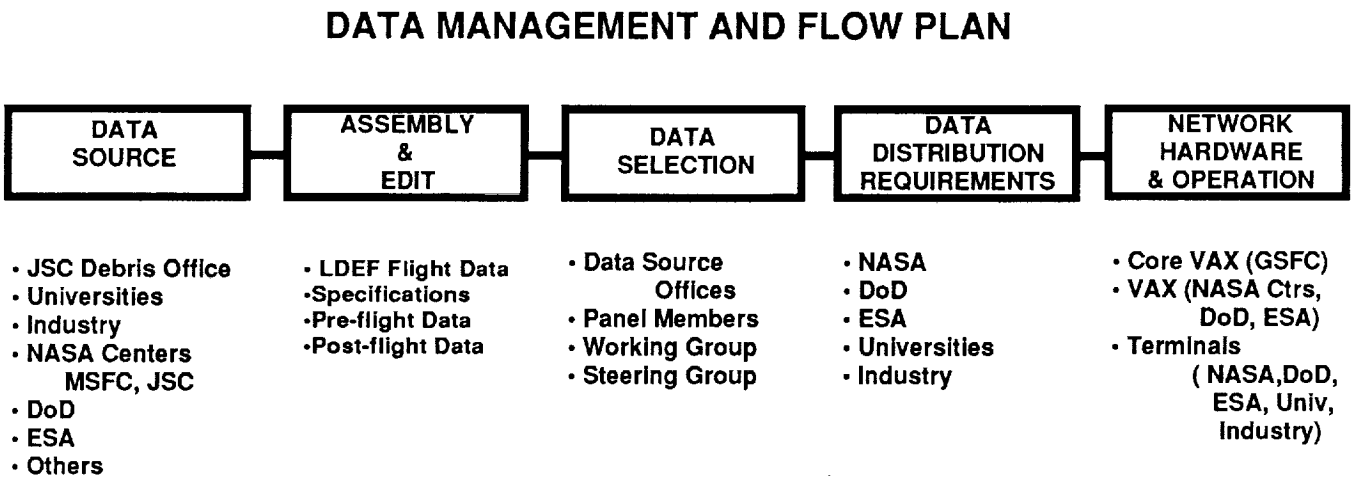

Figure 15. Data management and flow plan.

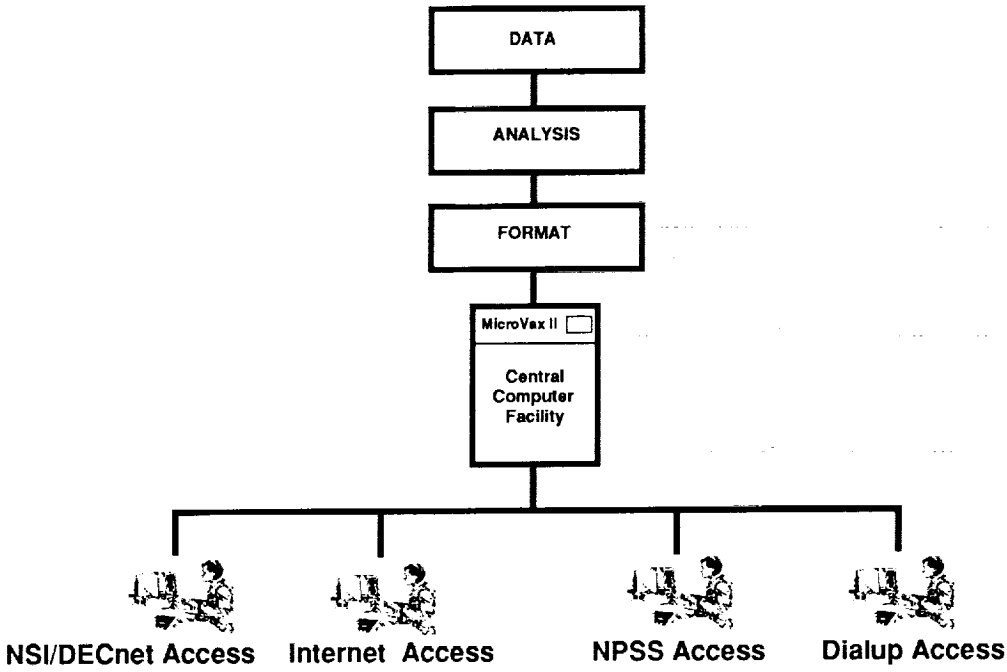

Figure 16. Central data network.

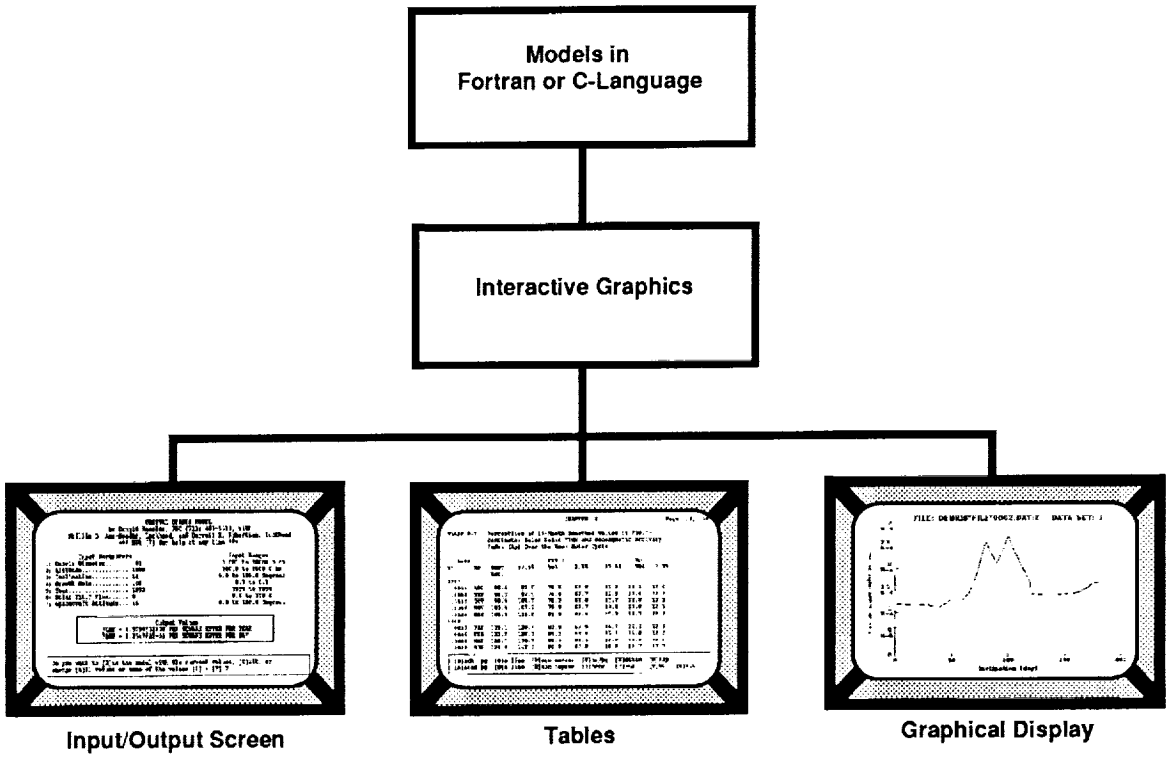

Figure 17. Model access exchange.

SPACECRAFT ANOMALIES EXPERT SYSTEM

Through the years, a host of information related to spacecraft anomalies has been accumulated. This information is principally located in EnviroNET's sections dealing with the natural environment and surface interactions. We are coordinating with all the agencies working in this area to help us develop an on-line facility to diagnose anomalies. In this category, Harry Koons and David Gorney of the Aerospace Corporation, who have been working on an expert system to address anomalies due to surface charging, bulk charging, single event upsets and total radiation dosage, have agreed to share their experience with us. We also have the assistance of NASA which publishes an annual report of anomalies on its own satellites. Lastly, there is NOAA, with its on-line reporting system. Expert systems provide an effective method for saving corporate knowledge, the experiences of researchers and engineers. They also allow computers to sift through large amounts of data and pinpoint significant parts. Figure 18 shows the expert system interface. Heuristics are used for predictions instead of algorithms. Approximate reasoning and inference are used to attack problems not rigidly defined.

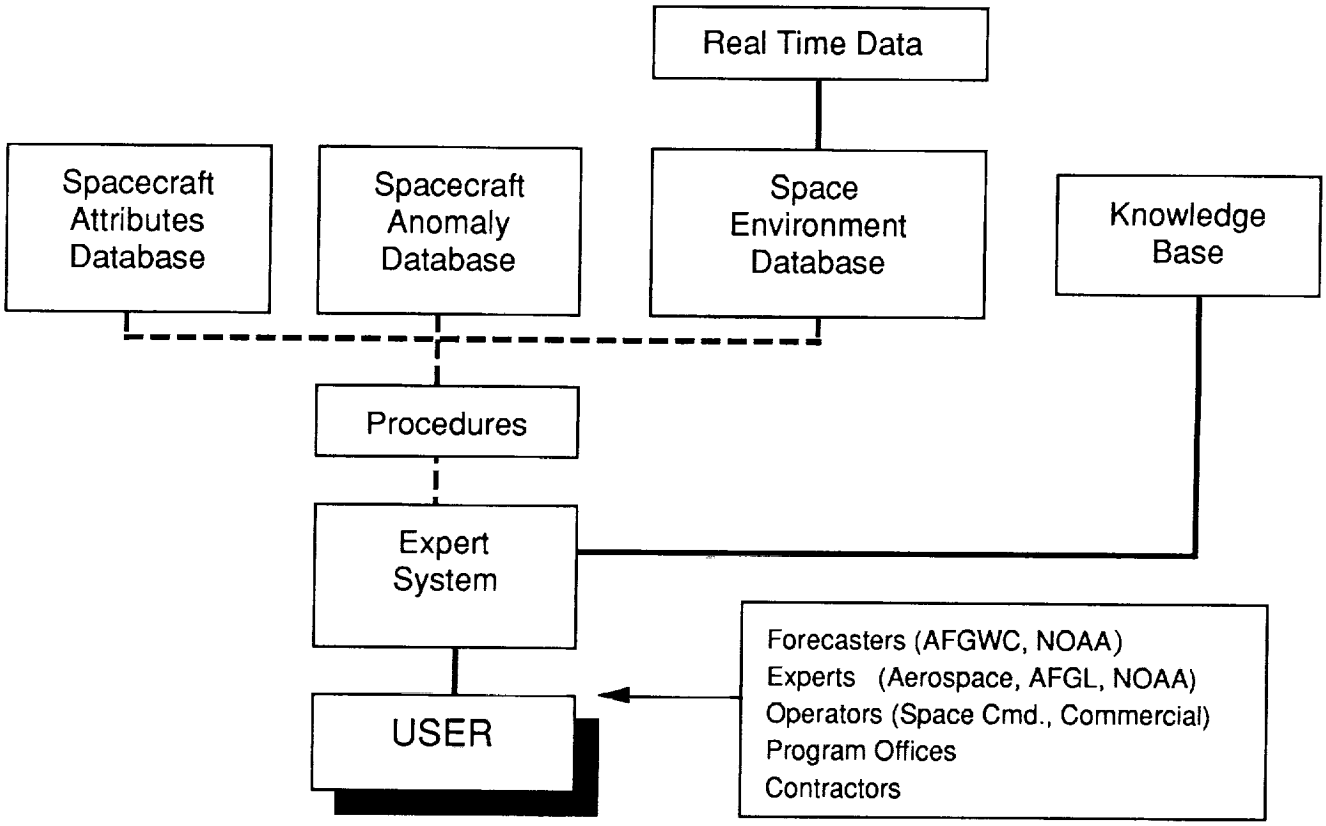

Figure 18. The Expert System Interface.

The Spacecraft Anomalies Expert System is a tool to diagnose causes of environmentally induced anomalies. It is also effective as a learning tool on environments. Modular systems allow easy expansion of satellite, technology, and past environmental conditions databases. The rules and facts generated by LDEF data can easily be formatted into the environment database.

Figure 19 is an adoption of the previous system which could be designed for LDEF. The software for the interface engine is reusable.

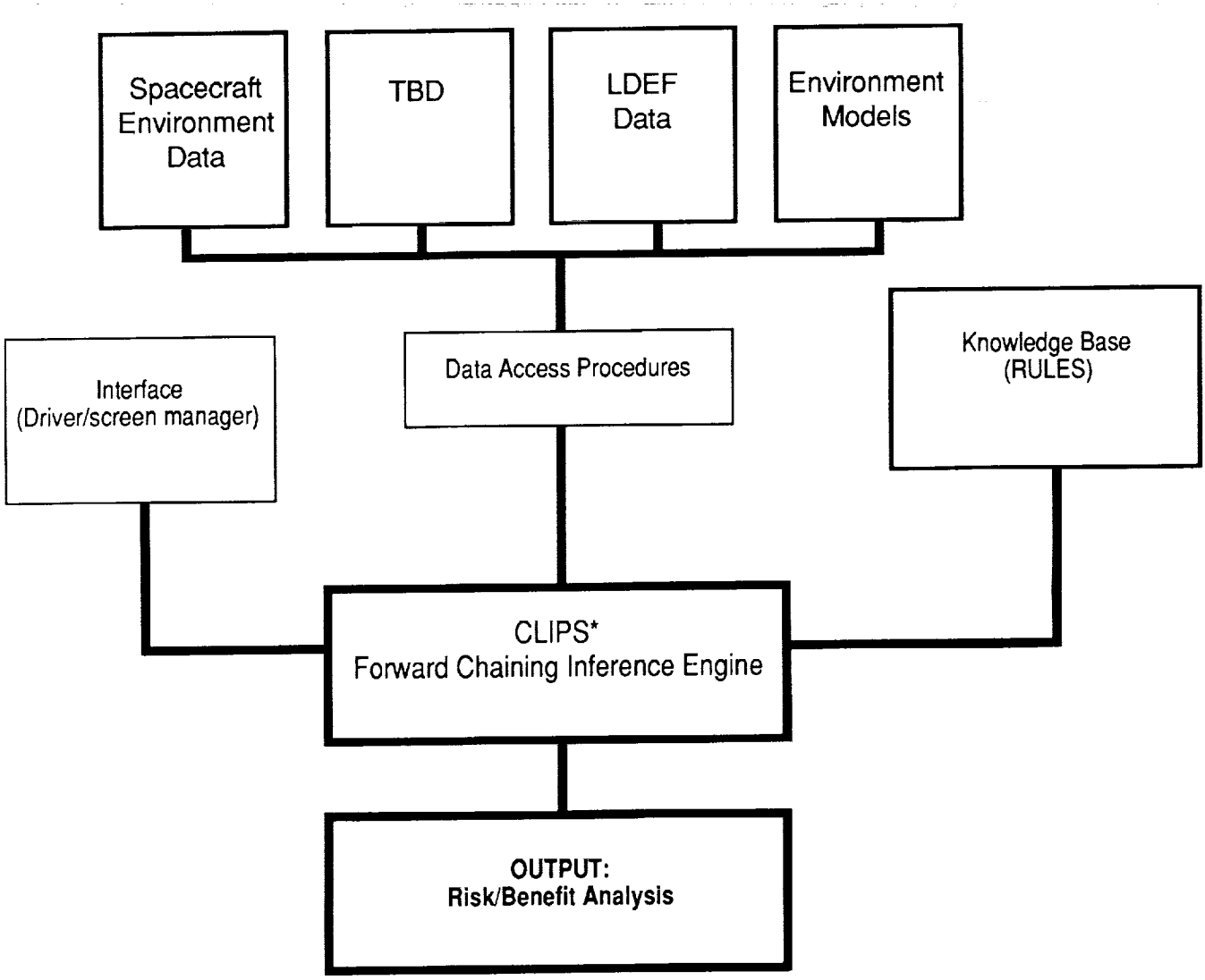

*C-Language Integrated Production System (NASA/JSC)

Figure 19. Proposed Expert System for LDEF.

TELESCIENCE TESTBED

EnviroNET is ideally suited for investigators to cooperate with their colleagues from their "remote" home laboratories and computers by computer networking. This is an expansion of the concept which started with the Atmosphere Explorer and Dynamics Explorer programs where many scientists were connected over dedicated phone lines to a central "remote" computer site containing their data and programs.

EnviroNET has always drawn on the NASA centers, other government laboratories, industry, and universities for help. It welcomes the opportunity to draw on the LDEF community.

CONCLUSION

EnviroNET is an operational system available to the scientists, engineers, satellite operators and users concerned with space environments who have access to a terminal or dial-up port. It is a logical host for LDEF data to be used for extending the life of satellites and providing safety for manned missions.

REFERENCES

1. Peddie, N. W., International Geomagnetic Reference Field; the third generation, *Journal Geomagn. Geoelectr.*, vol. 34, 1982, pp. 309-326.

2. Kessler, D. J., Phillip D. Anz-Meador, and Robert C. Reynolds, Orbital Debris Environment for Spacecraft Designed to Operate in Low Earth Orbit, NASA TM-100471, 1989.

3. Hedin, Alan E., The MSIS-86 Thermospheric Model, *Journal Geophysical Research*, vol. 92, 1987, pp. 4648-4662.

4. Report on Orbital Debris by Interagency Group (SPACE) for National Security Council, Washington, D.C., February, 1989.

5. Robinson, Paul A., Spacecraft Environmental Anomalies Handbook, NTIS, August 1, 1989.

SPACE ENVIRONMENTS

IONIZING RADIATION

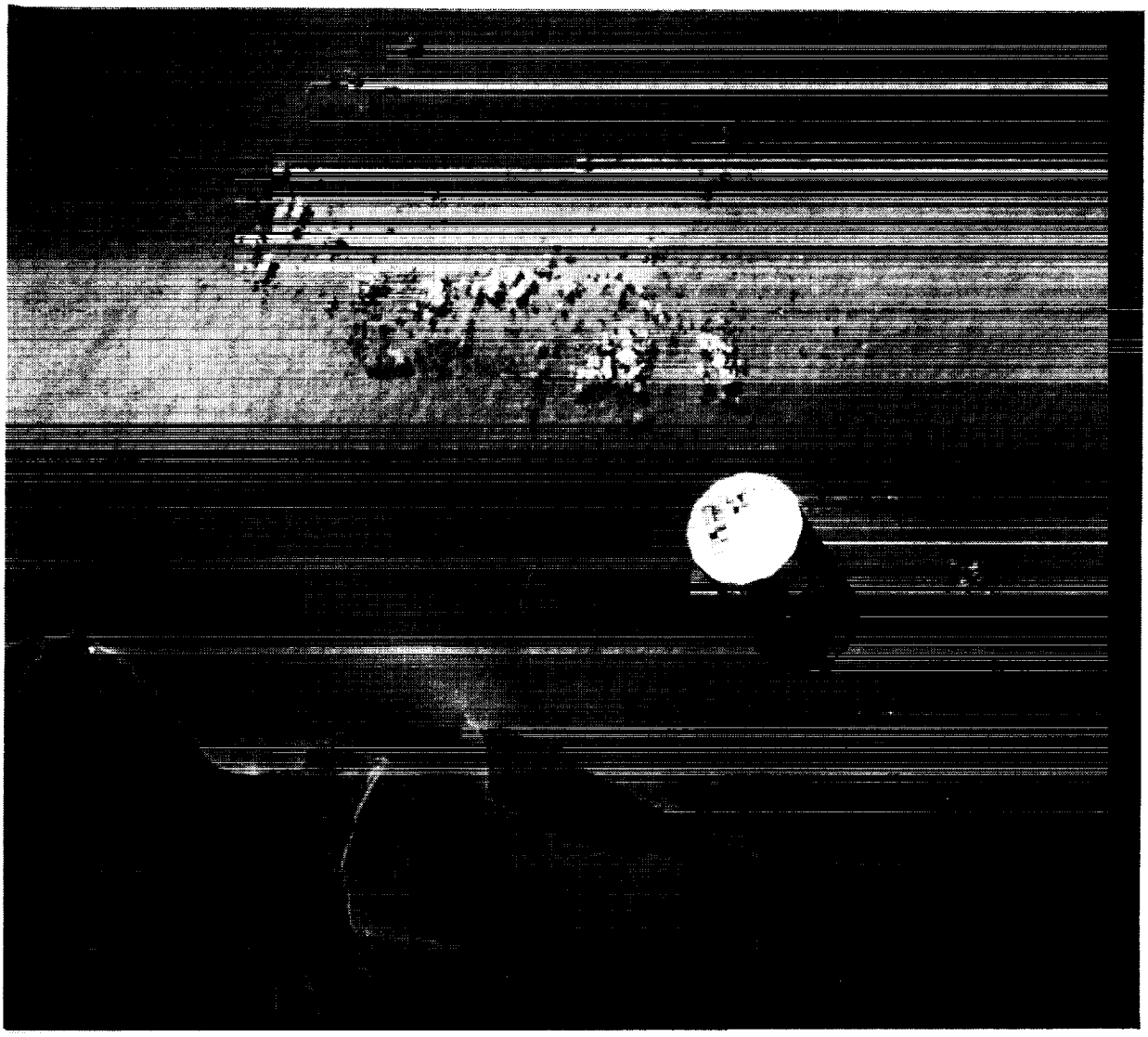

L-84-4313

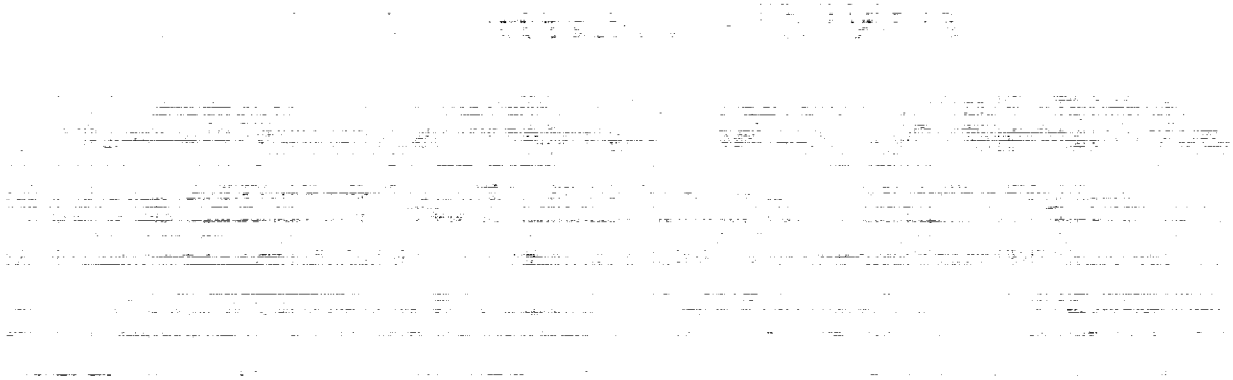

STATUS OF LDEF IONIZING RADIATION MEASUREMENTS AND ANALYSIS

Thomas A. Parnell
NASA Marshall Space Flight Center
Huntsville, AL 35812
Telephone: (205)544-7690, Fax: (205)544-7754

INTRODUCTION

At this symposium significant new data and analyses have been reported in cosmic ray research, radiation dosimetry, induced radioactivity and radiation environment modeling. Measurements of induced radioactivity and absorbed dose are nearly complete, but much analysis and modeling remains. Measurements and analyses of passive nuclear track detectors (PNTD), used to derive the cosmic ray composition and spectra, and linear energy transfer (LET) spectra, are only a few percent complete, but important results have already emerged.

As one might expect at this stage of the research, some of the new information has produced questions rather than answers. Low-energy heavy nuclei detected by two experiments are not compatible with known solar or cosmic components. Various data sets on absorbed dose are not consistent, and a new trapped proton environment model does not match the absorbed dose data. A search for cosmogenic nuclei other than ^{7}Be on LDEF surfaces has produced an unexpected result, and some activation data relating to neutrons is not yet understood. Most of these issues will be resolved by the analysis of further experiment data, calibrations, or the application of the large LDEF data set that offers alternate data or analysis techniques bearing on the same problem.

The scope of the papers at this symposium defy a compact technical summary. In this paper I have attempted to group the new information that I noted under the topics listed below. The papers generally are expository and have excellent illustrations, and I refer to their figures rather than reproduce them here. The general program and objectives of ionizing radiation measurements and analyses on LDEF has been described previously (ref. 1).

A. INDUCED RADIOACTIVITY

The induced radioactivity program for LDEF has a number of objectives. The induced activity when carefully measured, converted to specific activity, and compared to calculations from environment models serves as a "dosimeter" separate from techniques such as thermoluminescence dosimetry (TLD). While each technique has potential sources of systematic errors, they are mostly independent. The study of induced radioactivity in spacecraft materials, and methods to model it, are of strong interest in gamma ray astronomy where the local background is often a limiting factor in detector sensitivity. A few nuclear transmutations occur principally by neutron absorbtion, and these may be used to study the secondary neutron flux in the presence of the large primary proton flux.

Papers were presented at this symposium (ref. 2,3,4,5) which describe the instrumentation used for low background high resolution spectroscopy, the data reduction techniques, and some of the results measured at each facility. References (2) and (6) describe some of the considerations required to correct gamma ray line counting rates to specific activity (picoCuries/kg). Calculations which use the trapped proton and cosmic ray environments to predict results for specific nuclide production, and some results, were described in reference (3). Progress in collecting all activation data and placing it in a corrected data set for an eventual archive is described (ref. 6).

A comprehensive status report on the activation measurements and analyses was reported at this symposium (ref. 7). A summary of the sample materials, current results, and preliminary analyses is included. That paper contains new data from aluminum and steel structural samples, and on neutron activation in the cobalt, indium, and tantalum "intentional samples." Preliminary analysis of the induced activity in LDEF was presented at the First LDEF Symposium (ref. 8). Three dimensional calculations using a detailed LDEF mass model and directional proton models are in progress, but results were not presented at the 2nd Symposium. The induced radioactivity team has obviously made considerable progress as summarized in references (6) and (7), and will produce an archived data set which will be invaluable to space radiation environments research and gamma ray astronomy. The induced activity data, along with the three-dimensional calculations, may be required to help resolve the differences in LDEF absorbed dose data sets (ref. 9,10,11).

B. ABSORBED DOSE MEASUREMENTS

At the First Symposium absorbed dose measurements were presented from experiments M0004, P0004, P0006, and A0015 (ref. 12,13), which gave a tidy picture of the dose from 0.5 to 15 g/cm^2 shielding depth on the west side and from 1.37 to 2.90 g/cm^2 on the east side of LDEF, with a west/east ratio close to pre-recovery dose-shielding-depth profiles (ref. 14). Those early results, although they did not match pre-recovery calculations (ref. 14,15), were consistent with first-order calculations using a new directional proton model folded with a simple plane-slab shielding (ref. 16). The P0004, P0006, M0004, and A0015 data was summarized at this symposium (ref. 11), with additional details for the P0006 results.

New data from two experiments, in several more trays, have been presented at the second symposium. This data extends to shielding depths of 8×10^{-2} g/cm^2 for AO 138-7 (ref. 10) and to thinner shielding ($<10^{-2}$ g/cm^2) for experiment M0003 (ref. 9), where the trapped electrons contribute the majority of the absorbed dose. Some data from these experiments overlap the shielding range of experiments M0004, P0004, P0006, and A0015, where protons dominate the dose.

In the range of shielding thickness dominated by trapped protons and where most data overlap (≥ 0.2 g/cm^2), the absorbed dose picture is no longer so tidy (see Figure 3, ref. 17). The differences between data are greatest at the thinner shielding depths (a factor of 2 -3 at ~1 gm/cm^2). The agreement is much better (~30%) at 5 g/cm^2 (where fewer experiments contribute data). Figure 3, ref. 17, summarizes the available data above 0.2 g/cm^2 and contains data from the west, east, and Earth sides of LDEF. Accounting for different locations and local shielding variations will not reconcile all differences.

At thin shielding depths where the electron dose dominates (less than ~$3x10^{-1}$ g/cm^2), the measurements (refs. 9,10) agree with pre-recovery calculations within a factor of ~2 down to shielding depths ~.01 g/cm^2, where the dose measurement ($2x10^4$ rads) becomes asymptotic for thinner shielding. We note that in pre-recovery estimates (ref. 14) the dose increased to ~$3x10^5$ rads at "zero" effective shielding. Possible detector saturation effects are being investigated (ref. 9).

Effort is underway to resolve the differences between measurements and between modeling predictions and measurements. Further calibrations and studies of detector effects are in progress (ref. 9). In the environmental modeling effort, data on induced radioactivity will be used to derive an independent estimate of the absorbed dose in the 0.2 - 5.0 g/cm^2 shielding range (ref. 18).

C. LET SPECTRA AND HEAVY ION DOSIMETRY

Plastic Nuclear Track Detectors (PNTD's) were used on LDEF to measure both external (charge and energy spectra) and internal (charge and energy spectra of slowed primaries, secondary particles, and the Linear Energy Transfer spectra) radiation environments. Thin sheets of CR39, Lexan, Cellulose nitrate (CN), polycarbonates, mica, and others, are etched after the flight with strong base solutions. The geometry of the resulting microscopic conical pits at the entrance to radiation damage tracks are measured in multiple layers of detector, and further analysis provides the charge, energy, etc. of the charged ionizing particles. The technique is powerful, but time consuming. No more than 10% of the PNTD's on LDEF have been analyzed (including the cosmic ray experiments discussed below). Nevertheless, important new results have been reported at this conference, and these results confirm the significance of LDEF data in the fields of cosmic rays and radiation dosimetry.

With the attitude stability of LDEF, it is possible for the first time to comprehensively study the directional properties of LET spectra in spacecraft. These properties are a consequence of the directionality of the primary radiation and secondary particles produced by them, and the geometry of the shielding around the detection point. Such directional effects in the composite LET spectra from all particles (ref. 19, Figure 3) and in the directional characteristics of short range secondary recoils from trapped protons (ref. 20) were reported at this symposium.

The long exposure of LDEF has permitted a unique study of short range recoil particles. These particles have very high LET values, exceeding that of relativistic iron nuclei. New detector etching and analysis procedures have been developed, which coupled with the high density of the short range (~3 μm to ~20 μm) "recoil" particles in the LDEF exposure, has given a new measure of their LET contribution, which extends above 10^3 keV/μm - H_2O (ref. 19, Figure 4). These data will allow new modeling techniques to be applied that promise a more physically complete and more accurate prediction of LET spectra for future missions (ref. 18). The data already available will permit an assessment of the shortcomings in the present methods of predictions.

Improvement in the accuracy of LET predictions is significant for all future space programs. The decreased device size and increased number of devices per chip in contemporary microcircuits, along with a growing awareness of the SEU problem, have recently motivated design requirements for SEU susceptibility analysis on future spacecraft electronic systems. The

recoil particles dominate the high end of the LET spectra and have a large quality factor (QF), or effectiveness, in producing biological damage. An accurate prediction of the LET spectra is therefore important for assessing crew health risk.

D. ENVIRONMENT MODELING AND THREE-DIMENSIONAL SHIELDING EFFECTS

At the First Post-Retrieval Symposium, preliminary model calculations (ref. 16) of absorbed dose and some activation products were reported. Those calculations used a new trapped proton directional model coupled with a simple planar shield located perpendicular to each proton flux vector. This "3D/1D" calculation assumed a typical LDEF altitude of 450 km. The directional (3D) proton model incorporates the flux and spectra from the omnidirectional AP8 "Vette" models. This preliminary modeling effort produced results for absorbed dose on the east and west sides of LDEF, for Na^{22} in aluminum experiment tray clamps, and for Mn^{54} in samples from the steel trunnions. The model predictions were all within 50% of the measured values.

The next logical steps were to provide a more accurate proton fluence, reflecting in detail the altitude profile of LDEF and the effects of the solar activity during the mission, and to incorporate an accurate three-dimensional mass model of LDEF.

Reference (21) describes the factors that were used to derive a "corrected" proton flux and fluence. These include a continuous correction for solar activity rather than the MAX/MIN step used before, a 10-step altitude and atmospheric scale height profile and a modified magnetic moment. These changes reduced the calculated mission proton fluence by 20% from pre-recovery estimates.

The three-dimensional mass model of the LDEF structure and experiments is described in reference 22. This model includes the LDEF ring and longeron structure and all LDEF experiment trays, with four of the trays which contain dosimeters modeled in detail. The mass model is also being used in the analysis of the cosmic ray experiments.

The full three-dimensional environment modeling has been applied to predict the absorbed dose at measurement locations on LDEF (ref. 17). This produced some surprises! On the west and Earth sides of LDEF at shielding depths between 0.5 - 15 g/cm^2, the model predicts about half the dose measured in three experiments (Figures 4, 5, 7 (ref. 17)). On the east side the model predicts about 80% of the measured dose (Fig. 6, ref. 17). One may conclude from this that the flux in the AP8 proton model, which is the basis for the flux values in the directional proton model, is too low.

The full three-dimensional LDEF model predicts a smaller east/west anisotropy than measured. In the three-dimensional trapped proton model, this is affected by atmospheric scale height, which is a model parameter. In Figures 10 and 11 (ref. 17) the anisotropy is shown to be strongly dependent on the shielding depth and geometry with the larger west side flux influencing the results at east side measurement points.

The 3D model is presently being applied to the induced activity data from aluminum tray clamps around the circumference of LDEF (ref. 18) to provide a test of the model independent of

the absorbed dose data. An examination of the effect of varying parameters that depend on the environment (flux, atmospheric scale height, etc.) is also planned.

Absorbed dose measurements on LDEF at shielding depths of less than 0.2 g/cm^2 (ref. 9, 10) are almost entirely due to trapped electrons. These measurements have been compared with calculations using the AE8 electron environment model and the results are shown in Fig. 12 (ref. 18) and Fig. 2 (ref. 10). The measurements and predictions agree within a factor of 2 between 0.2 g/cm^2 and 0.01 g/cm^2. Measurements at smaller shielding depths were well below predictions, but the differences are likely due to detector saturation effects that are being investigated with calibrations (ref. 9).

The directional properties of the primary particles combined with the attitude stability of LDEF, and its shielding geometry, caused directional effects that were observed in data from passive nuclear track detectors (PNTD). Anisotropy of detected heavy cosmic ray nuclei, protons, and secondary particles in P0006 were reported (ref. 23) and the LET spectra from experiments P0006 and A0015 exhibited directional characteristics (ref. 19, 20). These observed directional characteristics depend strongly on the local shielding, and modeling of them will require the three-dimensional mass model.

E. COSMOGENIC NUCLEI (^{7}Be, ^{10}Be, ETC.)

The radioisotope ^{7}Be was discovered on the leading side (east) of LDEF, but was absent on the trailing side (ref. 24). It was quickly determined that its most likely source was the transmutation of atmospheric oxygen and nitrogen by cosmic ray protons and secondary neutrons. This occurs predominantly in the stratosphere (~25 km altitude) and its production rate is easily calculated and has been well documented by air sample measurements. Its concentration at the LDEF altitude (~350 km), per unit mass of air, must be several orders of magnitude higher than in the stratosphere to explain the amount (~10^6 radioactive nuclei/cm^2) accommodated on the front surface of LDEF.

Since the half life of ^{7}Be is 53 days, no new measurement from LDEF since the first symposium (reference 24) have been possible. However, the LDEF discovery has motivated new studies to understand the atmospheric transport mechanisms (25) and the spacecraft surface accommodation of ^{7}Be and similar metallic ions. Further experiments on the Concorde aircraft (See 1*) the shuttle (See 2*), and on the Russian RESURS-F1 spacecraft (See 3*) are planned.

At this symposium a project to detect other cosmogenic nuclei (^{10}B, ^{14}C, etc.) by the technique of accelerator mass spectrometry (AMS) is described (ref. 26). A measurement of ^{10}Be is of particular interest as a test of the diffusion transport hypothesis. The ratio ^{7}Be/^{10}Be at orbital altitudes should depend only on half-life and isotopic mass, with atmospheric chemical effects being the same for both isotopes. ^{10}Be was found on both leading and trailing edge Al tray clamps by AMS at levels >10^6 atoms cm^{-2}. In a post-conference addendum (ref. 26) the authors report the contamination by ^{10}Be ($t_{1/2}$ ~ Myrs) of a variety of industrial aluminums. It is known that ^{10}Be is detectable in thunderstorm precipitation (See 4*) and that the principal ore of Al, bauxite, is usally found in surface deposits. AMS experiments are continuing to measure ^{10}Be on other LDEF substrates, and to search for other cosmogenic nuclei.

*Private communications: P.R. Truscott [1], J.C. Gregory [2], G.W. Phillips [3], C. Frederick [4]

Additional information on Phillips [3] found on last page, below references.

F. COSMIC RAYS AND OTHER HEAVY IONS

From scanning of etched Lexan detector material, the "Ultra Heavy Cosmic Ray Experiment" (A0178) investigators, have determined that ≥ 2800 ultra-heavy cosmic rays (UHCR) with atomic number $Z > 65$ will eventually be analyzed. This is more than 10 times the UHCR data produced by previous orbiting experiments (Skylab, Ariel 6, and HEAO-3), and should yield ~30 actinides ($Z \geq 90$). Following extensive post-flight calibrations and detector tests to achieve optimum elemental resolution, 65 events have been fully analyzed. Figure 5 in reference (27) displays the analyzed events and shows two actinide nuclei clearly separated from the heaviest stable elements ($Z \leq 83$). This appears to support the excellent charge resolution (± 0.8 e) estimated from detector temperature history, track fading studies, and calibrations. This experiment will significantly advance the knowledge of nucleosynthesis in supernovae (the only site of actinide production), the relative contributions of various nucleosynthetic processes to the cosmic ray flux, and the propagation history of the UHCR in the galaxy.

The "Heavy Ions in Space" Experiment (M0001), although it suffered some loss in CR39 detector sensitivity, shows excellent charge resolution (reference 28). Significant effort has been placed in understanding the detector sensitivity, resolution, and optimum etching conditions of the CR39 detector, which is detailed in reference 28. UHCR events above $Z = 45$ are being measured and about 1100 events will eventually be analyzed (more than twice the previous data available for $45 \leq Z \leq 92$). The complementary data of A0178 and M0001 will place stringent tests on models of cosmic ray nucleosynthesis and propagation in the galaxy.

In the analysis of M0001 data reported at this Symposium the emphasis was on the heavy nuclei with energies below the "geomagnetic cut off" of fully ionized galactic cosmic rays, which have a minimum energy of 800 MeV/nucleon in the LDEF orbit. About 250 events below 800 MeV/n which stopped in the thick detector stack have been analyzed to yield the composition and spectra. An unexpected fluence of "iron group" particles, with manganese ($Z = 25$) the most abundant, over the energy range ~100 to 500 MeV/n were found. As detailed in reference 28, these results are inconsistent with "anomalous cosmic rays" (because of their composition) and solar energetic particles (because of composition and energy). Only a few percent of the available data on these particles has been analyzed, and further work may confirm a new low-energy component of the cosmic ray flux. The present data also indicate that partially ionized iron nuclei from the strong solar flares in 1989 might have reached the LDEF orbit. Analysis at this point also shows that the spectra of argon and neon "anomalous cosmic rays" will be measured up to ~300 MeV, or at least a stringent upper limits on their fluence will be set at that energy.

The "Heavy Ion Measurement" (M0002), and corrollary detectors carried in "Biostack" (A0015) have produced data on low energy (10 - 240 MeV/n) heavy ions ($Z = 6 \rightarrow 26$) (ref. 29). The analysis of these data extends the "new cosmic ray component" measurement (ref. 28, Figure 7), to lower energy and has provided important new information about low energy heavy ions in the trapped radiation belts (Figure 2, ref. 29). The M0002 data contain new information on their composition, and temporal changes in their intensity. Such data are required to understand their injection and loss in the trapped belts.

G. STATUS SUMMARY, AND THE FUTURE

The papers at this symposium show not only the progress in data analysis and the significant results already achieved, but indicate what is yet to be done.

The absorbed dose measurements with thermoluminescent dosimeters (TLD's) have been completed, but some proton acceleration calibrations are in progress to resolve differences with predictions, and to confirm pre-flight calibrations. The final absorbed dose results, calibrations and other ground tests, information concerning detector shielding, and comparisons with model predictions, will be collected for the LDEF archive.

Most of the induced activity measurements have been performed, although a few measurements are continuing on samples with long half-life nuclides. There is a significant effort remaining to resolve small systematic differences between counting laboratories, to reduce all sample data to specific activity, and to convert the data from different laboratories to a standard format for archive. The final archive will contain the standard format data, correction methods, specific activity for samples, shielding information, and relevant comparisons with environment models.

The passive nuclear track detectors (PNTD) used for dosimetry (LET spectra and heavy ion fluences and spectra) and for cosmic ray composition and spectra required considerable test sample processing and analysis, and post-flight calibration. About 10% of the PNTDs have been processed, measured, and analyzed, and the analysis rate is increasing. However, it will be three or more years (depending upon the experiment and specific objective) before all this analysis is completed. Significant dosimetry data with shielding information and environment comparisons will be placed in the LDEF final report. Final results and interpretations for galactic and anomalous cosmic rays, trapped heavy ions, and the possible new component of heavy ions will be published in refereed journals.

In the radiation environment modeling the preliminary analysis of absorbed dose and induced radioactivity have been completed with the approximate "3D/1D" approach. The full three-dimensional approach (which includes the directional trapped proton flux and the full LDEF mass model) has been applied to the absorbed dose data. The model predicts less dose (~50%) and anisotrophy than observed, demonstrating the need for model adjustment. Reference (18) summarizes the LDEF data available now, and in the future, for environment model comparisons. That paper also describes the status and the future program of model comparisons. The first priority is to compare the induced activity data with a full three-dimensional model to determine if the absorbed dose model/data differences are confirmed. Deficiencies in the directional trapped proton model can then be addressed and model parameters (flux, atmospheric scale height, etc.) adjusted accordingly. The next major effort in modeling is to develop techniques to predict the feature in the LET spectra (beyond 10^3 keV/μm) that is due to target recoils and other secondaries. This feature, which is not included in present methods, will be modeled with a combination of the primary particle spectra and secondaries from the High Energy Transport Code. Neutrons are a yet uncertain component to radiation dose in spacecraft, and LDEF has data from fission foil detectors and induced radioactivity to help resolve this question. Modeling calculations are planned to examine in detail the proton vs neutron effects in the fission foil detectors, and to examine specific activation lines that are principally due to neutrons. The

revised and new environment models developed with the LDEF data will be documented and placed in an accessible data base for use in future programs.

The discovery of ^{7}Be on LDEF has motivated a number of efforts to explain its surprisingly large concentration at LDEF altitudes. These include future measurements in the stratosphere on high altitude aircraft, and on several spacecraft. Atmospheric circulation modeling of ^{7}Be transport is also in progress. Accelerator mass spectrometery is being employed on a number of LDEF substrates to detect other cosmogenic species such as ^{10}Be. These efforts will hopefully resolve the LDEF ^{7}Be origin as due to exceptionally efficient vertical transport in the atmosphere, or some other process such as solar flare particle interactions in the atmosphere.

This symposium demonstrated the power of experiments with passive radiation detectors and induced activity measurements, exposed for a long period in space, to make significant advances in radiation dosimetry, environment modeling, and cosmic ray astrophysics. The radiation experiments were not designed as an ensemble, nor was the long exposure anticipated; but every experiment that has been analyzed has made a significant contribution, some with unexpected, and remarkable, results. However, these experiments leave significant measurement to be made. Reference (30) describes a number of "radiation" experiments (but not all) that would be important to perform on a future LDEF spacecraft. They would utilize recently developed detectors of higher resolution and detectors with better sensitivity to further explore the ultra heavy and anomalous cosmic rays. Low power motor-driven arrays of PNTDs would allow time resolution for anomalous cosmic ray studies. Cosmogenic nuclei would be studied with small motor-driven, time-resolved sample plates. Many aspects of dosimetry, such as the "recoil" feature in the LET spectra, and neutrons, need to be further studied with detectors specifically designed for the purpose. Rapid post-flight analysis of activation to measure short lifetime nuclides would be important in several contexts. Such experiments on an LDEF-2 would be as productive, and cost-effective, as those on LDEF-1.

REFERENCES

1. Parnell, T. A.: Summary of Ionizing Radiation Analysis on the Long Duration Exposure Facility. LDEF - 69 Months in Space, NASA CP 3134, pp. 199-212 (1991).

2. Reeves, J. H., R. J. Arthur, and R. L. Brodzinski: Sensitivity of LDEF Foil Analyses Using Ultra-Low Background Germanium vs. Large NaI(TI) Multidimensional Spectrometers. Second LDEF Post-Retrieval Symposium, NASA CP-3194 (1993).

3. Reedy, R. C., C. E. Moss, S. G. Bobias, and J. Masarik: Radioactivities Induced in Some LDEF Samples. Second LDEF Post-Retrieval Symposium, NASA CP-3194 (1993).

4. Smith, A. R., and D. L. Hurley: A Photon Phreak Digs the LDEF Happening, Second LDEF Post-Retrieval Symposium, NASA CP-3194 (1993).

5. Olmez, Ilhan, F. Burns, and P. Sagalyn: Charged Particle Activation Studies on the Surface of LDEF Spacecraft. Second LDEF Post-Retrieval Symposium, NASA CP-3194 (1993).

6. Laird, C. E., B. A. Harmon, G. J. Fishman, and T. A. Parnell: Collection, Analysis, and Archival of LDEF Activation Data, Second LDEF Post-Retrieval Symposium, NASA CP-3194 (1993).

7. Harmon, B. A., G. J. Fishman, T. A. Parnell, and C. E. Laird: Induced Activation Study of LDEF. Second LDEF Post-Retrieval Symposium, NASA CP-3194 (1993).

8. Armstrong, T. W., B. L. Colborn, J. W. Watts: Ionizing Radiation Calculations and Comparisons with LDEF Data. First LDEF Post Retrieval Symposium, LDEF-69 Months in Space, NASA CP 3134, p. 347 (1991).

9. Blake, J. B., and S. S. Imamoto: A Measurement of the Radiation Dose to LDEF by Passive Dosimetry. Second LDEF Post-Retrieval Symposium, NASA CP-3194 (1993).

10. Bourrieau, J.: LDEF Dosimetric Measurement Results (AO 138-7 Experiment). Second LDEF Post-Retrieval Symposium, NASA CP-3194 (1993).

11. Frank, A. L., E. V. Benton, T. W. Armstrong, and B. L. Colborn: Absorbed Dose Measurements and Predictions on LDEF. Second LDEF Post-Retrieval Symposium, NASA CP-3194 (1993).

12. Benton, E. V., A. Frank, E. R. Benton, I. Csige, T. A. Parnell, and J. W. Watts, Jr.: Radiation Exposure of LDEF: Initial Results. LDEF-69 Months in Space, NASA CP 3134, p.a 325 (1991).

13. Reitz, G.: Preliminary Total Dose Measurements on LDEF, LDEF-69 Months in Space. NASA CP 3134, p. 1643 (1991).

14. Benton, E. V., W. Heinrich, T. A. Parnell, T. W. Armstrong, J. H. Derrickson, G. J. Fishman, A. L. Frank, J. W. Watts, Jr., and B. Wiegel: Ionizing Radiation Exposure of LDEF (Pre-Recovery Estimates), Nuclear Tracks and Radiation Measurements, V20:1, 75-100 (1992).

15. Watts, J. W., T. A. Parnell, J. H. Derrickson, T. W. Armstrong, and E. V. Benton: Predictions of LDEF Ionizing Radiation Environment, LDEF-69 Months in Space. NASA CP 3134, p. 213 (1991).

16. Armstrong, T. W., B. L. Colborn: J. W. Watts, Jr., Ionizing Radiation Calculations and Comparison with LDEF Data, LDEF-69 Months in Space. NASA CP 3134, p. 347 (1991).

17. Armstrong, T. W., and B. L. Colborn: Radiation Model Predictions and Validation Using LDEF Satellite Data, Second LDEF Post-Retrieval Symposium. NASA CP-3194 (1993).

18. Armstrong, T. W., and B. L. Colborn: Future Directions for LDEF Ionizing Radiation Modeling and Assessments. Second LDEF Post-Retrieval Symposium, NASA CP-3194 (1993).

19. Benton, E. V., I. Csige, K. Oda, R. P. Henke, A. L. Frank, E. R. Benton, L. A. Frigo, T. A. Parnell, J. W. Watts, Jr., and J. H. Derrickson: LET Spectra Measurements of Charged Particles in P0006 Experiment of LDEF, Second LDEF Post-Retrieval Symposium, NASA CP-3194 (1993).

20. Csige, I., E. V. Benton, S. Soundararajan, and E. R. Benton, Light-Heavy Ion Measurements in CR-39 Located on the Earth Side of LDEF, Second LDEF Post-Retrieval Symposium, NASA CP-3194 (1993).

21. Watts, J. W., T. W. Armstrong, and B. L. Colborn: Revised Predictions of LDEF Exposure to Trapped Protons, Second LDEF Post-Retrieval Symposium, NASA CP-3194 (1993).

22. Colborn, B. L., and T. W. Armstrong: Development and Application of a 3-D Geometry/Mass Model for LDEF Satellite Ionizing Radiation Assessments. Second LDEF Post-Retrieval Symposium, NASA CP-3194 (1993).

23. Csige, I., E. V. Benton, L. Frigo, T. A. Parnell, J. Watts, Jr., T. W. Armstrong, and B. L. Colborn: Three-Dimensional Shielding Effects on Charged Particle Fluences Measured in the P0006 Experiment of LDEF. Second LDEF Post-Retrieval Symposium, NASA CP-3194 (1993).

24. Fishman, G. J., et al., Observation of ^{7}Be on the Surface of LDEF Spacecraft, Nature, V 349, pp. 678-680 (1991).

25. Petty, G. W.: Geophysical Research Letters, 18a, 1687 (1991).

26. Gregory, J. C., A. Albrecht, G. Herzog, J. Klein, and R. Middleton: Cosmogenic Radioisotopes on LDEF Surfaces. Second LDEF Post-Retrieval Symposium, NASA CP-3194 (1993).

27. O'Sullivan, D., J. Bosch, R. Keegan, K.-P. Wenzel, F. Jansen, and C. Domingo: Progress Report on the Ultra Heavy Cosmic Ray Experiment (AO 178). Second LDEF Post-Retrieval Symposium, NASA CP-3194 (1993).

28. Adams, J. H., Jr., L. P. Beahm, P. R. Boberg, and A. J. Tylka: Progress Report on the Heavy Ions in Space (HIIS) Experiment, Second LDEF Post-Retrieval Symposium, NASA CP-3194 (1993).

29. Jonathal, D., R. Beaujean, and W. Enge: Heavy Ion Measurement on LDEF, Second LDEF Post-Retrieval Symposium, NASA CP-3194 (1993).

30. Adams, J., Future Radiation Measurements in Low Earth Orbit. Second LDEF Post-Retrieval Symposium, NASA CP-3194 (1993).

3 * Phillips, G. W., and S. E. King: An experiment "Beryllium Induced Radiation (BINRAD)" is planned in 1993 on the Russian RESURS F1 spacecraft, by a NRL-Moscow State University team (private communications).

SENSITIVITY OF LDEF FOIL ANALYSES USING ULTRA-LOW BACKGROUND GERMANIUM VS. LARGE NaI(Tl) MULTIDIMENSIONAL SPECTROMETERS

James H. Reeves
Richard J. Arthur
Ronald L. Brodzinski
Pacific Northwest Laboratory*
Richland, Washington 99352
Phone: 509/376-2135, Fax: 509/376-2329

ABSTRACT

Cobalt foils and stainless steel samples were analyzed for induced ^{60}Co activity with both an ultra-low background germanium gamma-ray spectrometer and with a large NaI(Tl) multidimensional spectrometer, both of which use electronic anticoincidence shielding to reduce background counts resulting from cosmic rays. Aluminum samples were analyzed for ^{22}Na. The results, in addition to the relative sensitivities and precisions afforded by the two methods, are presented.

INTRODUCTION

High-purity germanium (HPGe) diodes with photopeak efficiencies greater than 100% relative to a standard 3 in. × 3 in. cylindrical NaI(Tl) scintillation crystal are now available. HPGe gamma-ray spectrometers have become the instrument of choice for low-background counting in most laboratories with a gamma-ray counting facility because of their high energy resolution and the large sizes currently available. However, there are instances where large NaI(Tl) detector systems offer better results. The measurement of ^{22}Na in random shaped samples of aluminum of various thickness retrieved from the Long-Duration Exposure Facility (LDEF) is an example. Measurement of ^{60}Co in many stainless steel and cobalt foils can also be made with more precision and accuracy by counting between two large NaI(Tl) detectors operating in coincidence with each other and in anticoincidence with an active veto shield. For radionuclides in which the gamma rays are in coincidence and have at least moderate energies, NaI(Tl) systems are competitive with even the largest and lowest-background germanium detectors in effective resolution, Compton interference, system background, and counting efficiency. In addition, large dual-crystal NaI(Tl) systems vastly reduce geometrical uncertainties when compared to results obtained using single-diode HPGe detectors. Such NaI(Tl) systems have been previously described in the literature (ref. 1).

---

* Operated for the U.S. Department of Energy by Battelle Memorial Institute under contract DE-AC06-76RLO 1830.

MEASUREMENTS: HPGe AND NaI(Tl) SPECTROMETERS

An ultra-low background HPGe gamma-ray spectrometer as illustrated in Figure 1 was used for these measurements (refs. 2-3). The system is located above ground in our laboratory and has the lowest background of any above-ground device known to be operating. The NaI(Tl) detector system, located in the same counting room, is pictured in Figure 2. Comparisons of counting efficiencies and system backgrounds for ^{60}Co are given in Table 1 along with those for a low background germanium system located 50 ft. underground at the Savannah River Laboratory in Aiken, SC, which uses a 90% HPGe crystal (ref. 4). Counting efficiencies and backgrounds use the summation of the peak areas for the 1172.7- and 1332.5-keV gamma rays.

The 31.5% HPGe detector was efficiency calibrated for ^{60}Co with a 5.08-cm square source with thickness of approximately 0.03-mm supplied through Alan Harmon, Marshall Space Flight Center. The thin source was positioned on the detector side of a sample (or sample blank) for one counting interval and positioned on the opposite side for a second counting interval. The efficiency was determined from the average of the two counts. Efficiencies and backgrounds for the 90% HPGe detector were derived from data contained in ref. 4.

The NaI(Tl) spectrometer was efficiency calibrated using 9.53-cm diameter right circular cylinders containing various thicknesses of sea sand and/or copper powder homogeneously mixed with known amounts of NIST-traceable radionuclides. Tests conducted using copper powder vs. sea sand of thicknesses up to 5 g/cm^2 show differences of less than 1%. Gamma-ray attenuation in the sample material is primarily due to Compton interactions which are not dependent on atomic number (Z).

Three cobalt samples and 5 stainless steel samples were analyzed for ^{60}Co with the NaI(Tl) system. All were about 5 cm square but varied in thickness. The three cobalt samples and one of the stainless samples were also analyzed with the HPGe spectrometer. Counting intervals were about one week in all cases. The results are shown in Table 2.

The activities determined for the cobalt samples I-C9 and G12-A-1-F-N with the NaI(Tl) spectrometer are higher than the activities from the HPGe system while the activity determined for sample I-H12 with the NaI(Tl) spectrometer is comparable to the activity determined with the HPGe system. Sample I-H12 consisted of two components about 1.91-cm wide by 5.08-cm long and was analyzed as one sample of dimensions 3.82 cm by 5.08 cm. The placement of activity on the 5-cm-square thin-film standard SC-12-Pt90 may approximate sample I-H12 more closely than samples I-C9 and G12-A-1-F-N. There are no corrections made for sample inhomogeneity or for non-uniform activity within the standard. Additionally, the NaI(Tl) system is known to be less sensitive to location of activity within a sample than is a single HPGe detector.

Measurements were performed to establish the uncertainties introduced to the data resulting from geometrical variations within the confines of a 1.27-cm thick by 8.255-cm square geometry. A 9.5-mm diameter ^{22}Na source was used on both the NaI(Tl) spectrometer and the HPGe detector since the triple coincidence afforded by ^{22}Na (the annihilation photons plus the 1274.5-keV gamma ray) offers a more stringent requirement than a simple coincidence such as offered

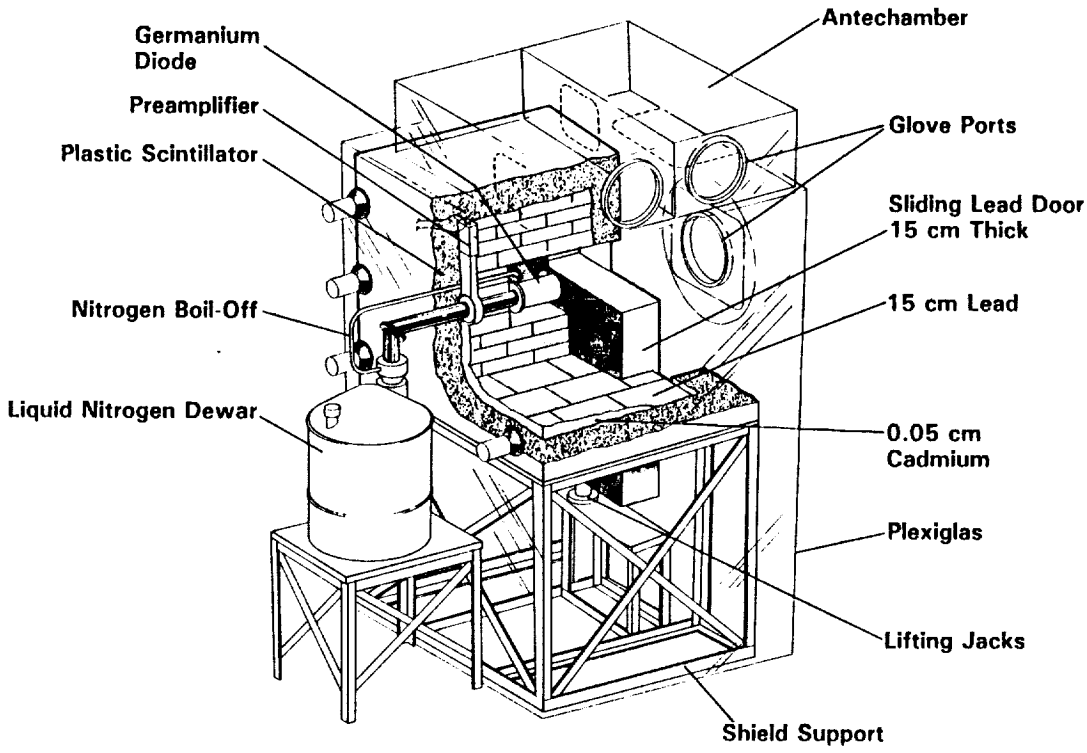

Figure 1. Anticosmic-shielded, above-ground, ultra-low-background 31.5% HPGe gamma-ray spectrometer.

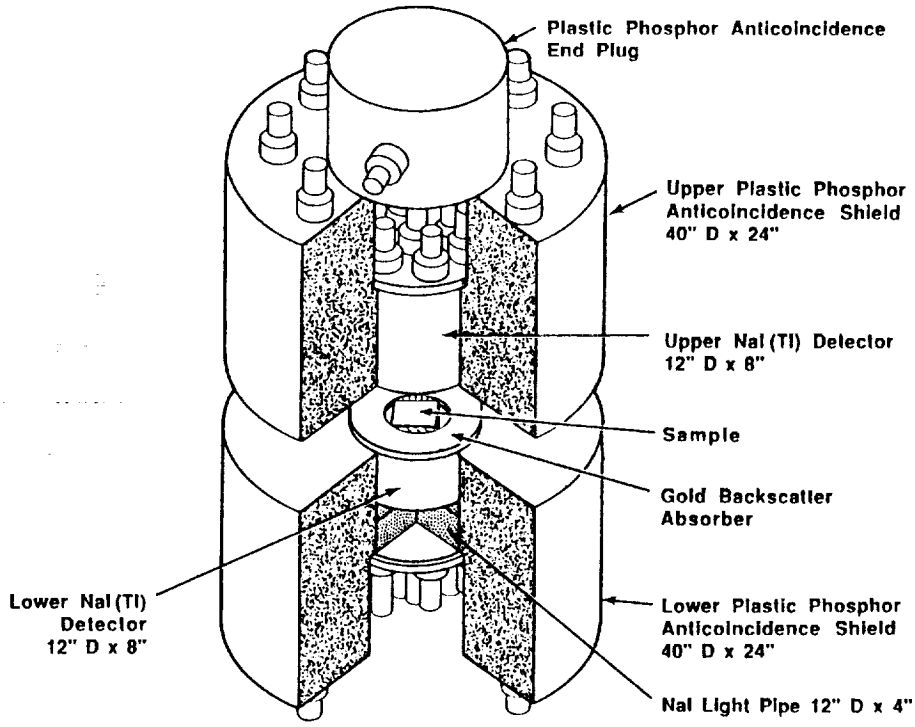

Figure 2. A large detector, anticoincidence shielded multidimensional nai(tl) gamma-ray spectrometer.

C- 2

Table 1. Comparison of Counting Efficiencies and System Backgrounds for NaI(Tl), 31.5% HPGe and 90% HPGe Spectrometers for ^{60}Co in 5.08-cm Square by 0.32-cm Thick Cobalt Metal Samples.

	NaI(Tl) System	31.5% HPGe System	90% HPGe System
Counting Efficiency (counts per gamma-ray)	0.133	0.030	0.097
System Background (counts per day)	34	6	14

Table 2. Activity of ^{60}Co in 5-cm Square Steel and Cobalt Samples.

	Identification	NaI(Tl) System (pCi/kg)	31.5% HPGe System (pCi/kg)
Cobalt			
	I-C9	33.9 ± 2.1	29.4 ± 2.9
	G12-A-1-F-N	34.1 ± 2.1	27.4 ± 2.7
	I-H12 (A+B)	208 ± 11.3	204 ± 20
Stainless Steel**			
	LHDS2	0.84 ± 0.30	0.9 ± 0.4
	LHDS3	1.3 ± 0.2	N/A
	LHDS5	1.2 ± 0.2	N/A
	LHDN2	1.3 ± 0.3	N/A
	LHDN3	1.3 ± 0.2	N/A

** For the stainless steel samples, the sample blank was derived from stock other than that used in the actual LDEF samples; low inherent ^{60}Co activity in the blank would result in an artificially high activity.

by ^{60}Co. For purposes of comparison, the same source positions are used relative to the center of the face of the end cap of the germanium detector and the center of the face of one NaI(Tl) detector. All measurements are normalized to 1.00 at this position for each detector system. The relative efficiencies are summarized in Table 3. In general, the absolute efficiency of the NaI(Tl) system is greater than that of the HPGe system.

Measurements for one set of data in Table 3 were taken with no absorbing material between the source and the detector and show the relative efficiency decrease as the source is moved away from the center of the HPGe detector end cap. The relative efficiency for the NaI(Tl) spectrometer also decreases as the source is moved away from the axial center of the crystals. The greatest efficiency for the HPGe spectrometer occurs when the source is centered on the face of the detector end cap, since the greatest solid angle is subtended at such a position. The relative counting efficiency with the HPGe detector is reduced by a factor of 2.7 with the source 1.27 cm away from the end cap and offset 5.08 cm laterally whereas the data in Table 3 indicate only minor variations of between 4 and 6% with the NaI(Tl).

Measurements for the second set of data in Table 3 were taken with an aluminum sample and show that the relative efficiency decreases more severely due solely to attenuation of the gamma rays by the aluminum as the source is moved away from the HPGe, up to a factor of 4 when the source is located 1.27 cm away and offset 5.08 cm; however, with the same offsets the relative efficiency of the NaI(Tl) spectrometer actually increases by 16% with the ^{22}Na source and by 2% with the ^{60}Co source. This increase in relative efficiency is due to an edge effect. When the source is located near the edge of the aluminum, more gamma rays can escape the source and be absorbed in the two NaI(Tl) crystals because they pass through only a very thin section of aluminum as shown in Figure 3.

EXPERIMENTAL RESULTS

The LDEF aluminum samples analyzed at PNL for ^{22}Na consisted of rectangular slabs of aluminum of various dimensions. The slabs were centered on the face of the lower NaI(Tl) crystal for counting (this geometry having been previously standardized for samples of similar sizes and composition). The counting times were typically several days. Uncertainties reported include counting statistical uncertainties plus 5% for the combination of absolute standardization uncertainty, geometrical parameters such as the edge effect, and weighing errors. The results are shown in Table 4.

Sample KP-6 was also counted on the HPGe system. The count rate for the 511-keV peak plus the 1274.5-keV peak was about half the count rate observed with the NaI(Tl) system. If only the 1274.5-keV peak were used, then the count rate would be about 5% that seen with the NaI(Tl) system.

DISCUSSION

Results from both detector systems, as shown in Table 2, indicate that the activity in cobalt sample I-H12 (A+B) is 6 times higher than the activity measured in the other cobalt samples. The higher activity is likely due to higher thermal-neutron fluence. Such a likelihood is further discussed by Alan Harmon in the proceedings of this symposium (ref. 5).

Table 3. Comparison of the Relative Efficiencies of HPGe vs. NaI(Tl) Spectrometers for a 9.5-mm Diameter Source Positioned in Various Locations Relative to a Sample 1.27-cm Thick By 8.255 cm Square.

Source Location (cm)		Relative Efficiency			
		No Absorber		Aluminum	
Distance from Surface	Radial Offset	31.5 % HPGe Diode	NaI(Tl) Spectrometer	31.5 % HPGe Diode	NaI(Tl) Spectrometer
0	0	1.00	1.00	1.00	1.00
0	2.54	0.80	0.99	0.80	1.01
0	5.08	0.40	0.94	0.40	1.13
1.27	0	0.70	1.02	0.56	1.03
1.27	2.54	0.58	0.99	0.46	1.04
1.27	5.08	0.38	0.96	0.25	1.16

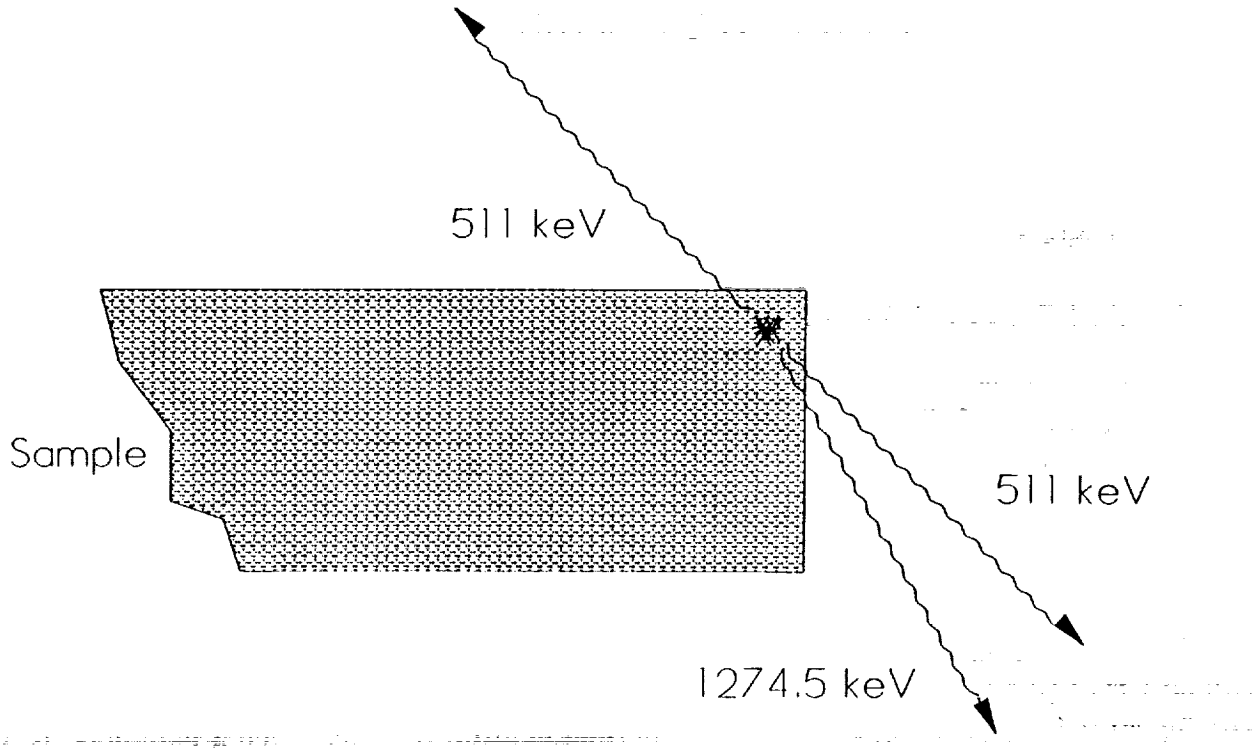

Figure 3. Schematic illustration of the edge effect for the decay of ^{22}Na.

Table 4. Activity of ^{22}Na in LDEF Aluminum Slabs as Determined Using a Large NaI(Tl) Detector Spectrometer.

Identification	Weight (kg)	Thickness (g/cm^2)	Counting Efficiency (%)	^{22}Na Activity (pCi/kg)	^{22}Na Activity Uncertainty (1σ)
KP-6	0.06533	2.532	18.81	129.0	6.6
KP-7	0.06533	2.532	18.81	120.2	6.2
CA-W-EAN-1	0.02203	0.535	21.98	106.3	5.7
CA-W-EAN-2	0.04994	1.261	21.10	95.4	4.9
CA-W-EAN-3	0.07078	1.938	19.86	82.6	4.4
CA-W-EAN-4	0.07748	2.527	18.81	78.7	4.0
CA-W-EAN-5	0.06715	2.376	19.07	70.3	3.7
CA-W-SPS-1	0.02117	0.514	22.03	101.5	5.9
CA-W-SPS-2	0.04949	1.254	21.11	89.8	4.6
CA-W-SPS-3	0.07034	1.926	19.88	83.2	4.4
CA-W-SPS-4	0.07590	2.476	18.89	74.7	3.9
CA-W-SPS-5	0.06532	2.501	18.85	68.8	3.7

HPGe detectors can be readily calibrated using homogeneous standards, even for radionuclides with coincident emissions, such as ^{22}Na which emits a 0.55-MeV β^+, but errors introduced from coincidence summing can be significant and some method of correction must be used (ref. 1). However, there is no reliable method for calibrating HPGe detectors for situations where the activity is not uniformly distributed throughout the sample. Furthermore, the range of the β^+ in the sample material will affect the location at which annihilation occurs, especially in thin samples. Since coincidence summing is actually used for the measurements with the NaI(Tl) system, and due to the low sensitivity to source position, errors are vastly reduced even for inhomogeneous samples.

Measurements on samples of varying shapes and sizes requiring high precision are sometimes required and uncertainties due to edge effect must be minimized. For homogeneous samples, efficiency calibration with standards of similar shape and surface density are sufficient. However, for highly inhomogeneous samples, a better method must be used. One such method is to include a small border of blank material around the perimeter of the sample. The correct thickness and extent of the border material can be determined from mathematical calculations of absorption parameters. Uncertainties from edge effect have little significance for large samples

counted on small HPGe detectors since the edge of the sample extends past the outer surface of the HPGe crystal. However, for the large HPGe detectors currently available, the edge effect may contribute a significant uncertainty for 1-cm thick by 5-cm square stainless steel samples or other relatively thick, high density samples.

SUMMARY

Large NaI(Tl) detector systems as described above are competitive with, and in many cases superlative to, even the largest low-background HPGe detector systems for measuring radionuclides which decay with coincident gamma rays of at least moderate energies. The combination of efficiency and system background are at least comparable to the best HPGe systems operating above ground. Large NaI(Tl) detector systems are especially advantageous for large inhomogeneous samples because of their low sensitivity to variable source position.

REFERENCES

1. Wogman, N. A.; Robertson, D. E.; and Perkins, R. W.: A Large Detector, Anticoincidence Shielded Multidimensional Gamma-Ray Spectrometer, *Nucl. Instrum. Methods*, vol. 50, 1967, pp. 1-10.
2. Reeves, J. H.; Hensley, W. K., III; and Brodzinski, R. L.: An Ultralow-Background Germanium Gamma-Ray Spectrometer Using Super-Clean Materials and Cosmic-Ray Anticoincidence, *IEEE Trans. Nucl. Sci.*, vol. 31, no. 1, Feb. 1984, pp. 697-700.
3. Arthur, R. J.; and Reeves, J. H.: Methods for Achieving Ultra-Low Backgrounds in Above-Ground Germanium-Detector Systems, *J. Radioanal. Nucl. Chem., Articles*, vol. 160, no. 2, Aug. 1992, pp. 297-304.
4. Winn, W. G.: Gamma-Ray Spectrometry of LDEF Samples, WSRC-RD-91-16, Feb. 1992.
5. Harmon, B. A.; Fishman, G. J.; Parnell, T. A.; and Laird, C. E.: Induced Activation Study of LDEF. Second LDEF Post-Retrieval Symposium, NASA CP-3194, 1993.

N93-29628

RADIOACTIVITIES INDUCED IN SOME LDEF SAMPLES*

Robert C. Reedy, Calvin E. Moss, S. George Bobias, and Jozef Masarik
Space Science and Technology Division
Los Alamos National Laboratory
Los Alamos, NM 87545
Phone: 505–667–5446, Fax: 505–665–3332

SUMMARY

Radioactivities induced in several LDEF samples were measured by low-level counting at Los Alamos and elsewhere. These radionuclides have activities similar to those observed in meteorites and lunar samples. Some trends were observed in these measurements in terms of profiles in trunnion layers and as a function of radionuclide half-life. Several existing computer codes were used to model the production by the protons trapped in the Earth's radiation belts and by the galactic cosmic rays of some of these radionuclides, ^{54}Mn and ^{57}Co in steel, ^{46}Sc in titanium, and ^{22}Na in alloys of titanium and aluminum. Production rates were also calculated for radionuclides possibly implanted in LDEF, ^{7}Be, ^{10}Be, and ^{14}C. Enhanced concentrations of induced isotopes in the surfaces of trunnion sections relative to their concentrations in the center are caused by the lower-energy protons in the trapped radiation. Secondary neutrons made by high-energy trapped protons and by galactic cosmic rays produce much of the observed radioactivities, especially deep in an object. Comparisons of the observed to calculated activities of several radionuclides with different half-lives indicate that the flux of trapped protons at LDEF decreased significantly at the end of the mission.

INTRODUCTION

Many structural pieces from the Long Duration Exposure Facility (LDEF) were measured using low-level gamma-ray spectroscopy by several research teams (*e.g.*, refs. 1,2.) Several radionuclides were observed, as was predicted on the basis of calculations done using the energetic-particle environment expected at LDEF (ref. 3). Two sources of energetic particles are expected to dominate the production of these induced radioactivities, energetic (E $\sim 10^2$–10^3 MeV) protons trapped in the Earth's radiation belt and the high-energy ($\gtrsim$ 4 GeV/nucleon) galactic-cosmic-ray particles that penetrate the Earth's magnetic field and reach LDEF in its 28.5° inclination orbit (ref. 3). There is very little experience with radionuclides made in material in a low-Earth orbit like LDEF's, which is what makes the induced radioactivities measured in LDE

* This research was supported by NASA's Marshall Space Flight Center and done under the auspices of the U.S. Department of Energy.

samples so unique and valuable. However, there is much experience with cosmic-ray-produced (cosmogenic) nuclides made by energetic particles in lunar samples (ref. 4), meteorites (ref. 5), and terrestrial samples (ref. 6). We compare our LDEF radioactivities with production rates of cosmogenic nuclides calculated with models developed for these other objects.

MEASURED RADIOACTIVITIES IN LDEF SAMPLES

At Los Alamos, we measured activity-versus-depth profiles in four sets of trunnion layers, six trunnion sections, five parts of aluminum alloy from end support retainer plates, two aluminum alloy keel plate pieces, and two titanium clips, and details on these measurements are in ref. 7. All activities are corrected to 20 January 1990. In the aluminum samples, we observed 2.6-year ^{22}Na with activities ranging from 3.8±0.6 becquerel (disintegrations per second) per kilogram of sample (Bq/kg) to 5.2±0.6 Bq/kg, in good agreement with the ^{22}Na activities of ref. 1 in aluminum tray clamps and of ref. 8 for other keel-plate samples.

As shown in ref. 1, our measured activities for 312-day ^{54}Mn in layers of the D trunnion section, 3–5 Bq/kg, are in good agreement with measurements in adjacent samples done by D. C. Camp at the Lawrence Livermore National Laboratory. A plot of our ^{54}Mn results for layers from the D section of the west trunnion is shown in figure 1, and shows the trend seen in all sets of trunnion layers of a decrease in radioactivity from the surface to the center of the trunnion.

In two titanium clip samples, which we received more than 200 days after LDEF was recovered, we observed low activities of ^{22}Na of 0.6±0.3 and 0.7±0.3 Bq/kg, many gamma rays from uranium and its daughter isotopes, but no clear signal for 84-day ^{46}Sc. Our 3-standard-deviation limits for ^{46}Sc were 3.3 and 4.1 Bq/kg. Our limits for ^{46}Sc are consistent with the activities of 1.1–1.5 Bq/kg estimated for other titanium clips in ref. 8. As ^{46}Sc is made from ^{48}Ti by the same reactions that make ^{54}Mn from ^{56}Fe, it is a little surprising that the measured radioactivity of ^{46}Sc is much lower (by a factor of ~3) than that of ^{54}Mn in the trunnion samples.

MODELS FOR PRODUCTION OF COSMOGENIC NUCLIDES

These radionuclides measured in LDEF pieces have activities that are at roughly the same levels as observed in lunar samples (ref. 4) and meteorites (ref. 5), which range from a few tenths of a becquerel per kilogram for high-energy products like ^{10}Be to ~5 Bq/kg for solar-proton-produced radionuclides like ^{26}Al and ^{22}Na in the very surfaces of lunar rocks. However, most samples from LDEF, like the titanium clips, are very different in composition from extraterrestrial objects, so direct comparisons are difficult to make. Several models have been developed and are well tested for cosmogenic nuclides in lunar samples and meteorites, and we apply two of these models, both from ref. 4, to our LDEF samples. One calculates production rates of nuclides by galactic-cosmic-ray particles. The other was designed for nuclides made by solar-energetic-

particles, which are often called solar-cosmic-ray (SCR) particles. We also used another computer code system to test the assumptions of the SCR model.

Radionuclide Production by Galactic-Cosmic-Ray Particles

Production of cosmogenic nuclides by the high-energy particles in the GCR have been well reproduced in lunar samples by the GCR model of Reedy and Arnold (ref. 4). This model has also been successfully extended to meteorites (cf., ref. 5). However, this model is not directly applicable to LDEF as the Earth and its magnetic field affect the fluxes of GCR particles reaching LDEF. Only GCR particles arriving from 2π steradians of space reach a point near the Earth, thus production rates calculated for meteorites need to be reduced by a factor of two to be applicable to LDEF, although calculated rates with the lunar model do not need this factor. The Earth's very strong magnetic field scatters away a large fraction of GCR particles for geomagnetic latitudes less than $\approx 60°$. This effect has been known for terrestrial cosmogenic nuclides, such as ^{14}C, and needs to be applied to nuclides made in-situ in surface samples. Production rates near the Earth's equator are about a factor of three lower than those near the geomagnetic poles, while those around a geomagnetic latitude of $\approx 30°$ are lower by a factor of about two (ref. 6). As LDEF's orbit had an inclination of 28.5°, this factor averaged over its orbit is estimated to be about 2.5.

The GCR particle-flux model of ref. 4 was used with the cross sections for the important reactions. Several fluxes for large meteorites and the Moon were used as LDEF pieces were usually on the main part of the spacecraft or, like the trunnions, were fairly thick. GCR production rates for the very surface or in a very small object would be lower as the leakage of particles or reduced production of secondary neutrons lower GCR production rates (refs. 4,5). As described in ref. 4, the cross sections used in this model are for neutrons at energies below a few hundred MeV and mainly for protons at higher energies. Most cross sections used here are similar to those in ref. 4.

The calculated production rates by GCR particles corrected to LDEF's orbit are given in the last column of table I for several materials in LDEF. Other radionuclides observed or being searched for in LDEF pieces include ^{7}Be, ^{10}Be, and ^{14}C; the latter two could be like ^{7}Be and implanted on the surfaces on LDEF's leading side (J. C. Gregory, G. F. Herzog, and A. J. T. Jull, priv. comm.). Production rates of these implanted radionuclides are also given in table I to help show that observed concentrations are more than those expected by GCR-induced nuclear reactions.

For the LDEF mission length of 69 months, all of these radionuclides except ^{22}Na, ^{10}Be, and ^{14}C should have their activities in equilibrium with their production rates. Thus the GCR contribution to the activity of ^{54}Mn in steel should be about 0.9 Bq/kg, which is much lower than the measured activities. The activity for ^{22}Na would be about 80% of its production rate, so its activity in aluminum pieces from the GCR is about 0.5 Bq/kg, again less than observed. The calculated production rate for the "implanted" isotope ^{7}Be is much lower than for those induced

"in-situ," like ^{54}Mn and ^{22}Na, consistent with the interpretation (ref. 9) that the ^{7}Be found on LDEF's leading surface was not produced in LDEF. Production rates for ^{10}Be and ^{14}C are lower than for ^{7}Be, and the calculated GCR production rates for these isotopes in iron are down by a factor of ~2 for ^{10}Be to ~10 for ^{14}C relative to their rates in aluminum.

Radionuclide Production by Trapped Protons

The energy spectra of the trapped protons near LDEF's orbit are estimated (ref. 10) to be fairly steeply dropping with energy with most protons having energies of 10^2 to 10^3 MeV. These spectra are similar to those of the energetic SCR protons (ref. 4), although there are relatively more higher-energy protons in the trapped radiation than in the SCR.

Protons with an energy of 100 MeV only have ranges in aluminum and most materials of $\approx$10 g/cm^2, which is a small fraction of their interaction lengths. The few particles that do interact before they are stopped make few secondary particles because of their relatively low energies. The primary particles themselves induce most reactions. Thus the most important interaction mechanism for such particles is slowing down (and stopping), which occur due to ionization losses along the particles' paths and is a well known process. A model is presented in ref. 4 that involves production of nuclides by particles with energies below a few hundred MeV by considering only ionization energy losses. This model has been successfully applied to many studies of the interactions of SCR protons and alpha particles in the Moon and meteorites (ref. 5).

The trapped protons at LDEF's orbit tend to have relatively more energy than those in the SCR, thus some of the assumptions made above are weakened. To test whether secondary particles made by trapped protons could be important, we used the pair of Monte Carlo codes in the LAHET Code System (LCS) to calculate the interaction of trapped protons with LDEF's trunnion. These codes are LAHET (ref. 11), the Los Alamos High Energy Transport code, and MCNP (ref. 12), the Monte Carlo Neutron Photon code. A solid sphere of radius 4.125 cm with density of 7.62 g/cm^3, the same as the LDEF trunnion, and with the composition of the trunnion 17-4PH steel was used in these codes with the trapped proton flux of ref. 10 for protons traveling in the direction of geographic east at an altitude of 500 km. This proton spectrum is harder than that for geographic west at 500 km or those at 300 km altitude.

The proton and neutron fluxes crossing a surface at a depth of 0.59 cm (4.5 g/cm^2) in this sphere is shown in figure 2. While there is a fairly strong flux of neutrons at lower energies, the flux of protons exceeds the flux of neutrons for energies above about 20 MeV. While the energy where the proton and neutron fluxes cross varies slightly with depth, being at lower energies at the surface and at somewhat higher energies in the center, the trend is similar throughout the trunnion. Using a cylinder instead of a sphere for the trunnion would tend to increase slightly this cross-over energy. These fluxes calculated with LCS show that for the trapped radiation, while secondary neutrons are not negligible, protons are the dominant particle inside a trunnion piece. A very similar conclusion was obtained by the calculations of ref. 3, which showed that production by the protons in the trapped radiation dominates production by neutrons until

depths of $\approx$25 g/cm^2.

The rates for the production of nuclides by trapped protons in LDEF samples were calculated with proton fluxes calculated inside an object with the SCR model in ref. 4 and cross sections for proton-induced reactions. As with the LCS calculations, the geographic-east flux at 500 km of ref. 10 was used. The ionization parameters used for slowing-down and stopping calculations are those for LDEF's trunnion steel. The SCR code in ref. 4 only considers slab and spherical geometries. Calculations were done using omnidirectional fluxes on solid spheres of radius 31.5 and 63 g/cm^2 and for a semi-infinite slab. The proton fluxes calculated with the slowing-down model of ref. 4 agree well with those from the LCS calculations. At the surface and at a depth of 15 g/cm^2 from the surface, the calculated production rates in the 31.5-g/cm^2 sphere and a slab differed by factors of $\approx$25% and 2.5, respectively, with the rates at these depths in the 63-g/cm^2-radius sphere intermediate. As a long, narrow piece, like a trunnion, is intermediate between a sphere and a slab, the results for a 63-g/cm^2 sphere are used for the trunnion and for the other geometries.

Most cross sections used for these calculations are similar to those in ref. 4. For two induced radionuclides of interest, ^{54}Mn in steel and ^{46}Sc in titanium, more recent measured cross sections for proton reactions with iron and titanium from refs. 13, 14, and 15 were used. Only cross sections for proton-induced reactions are used.

The flux at 500 km is too high, as LDEF never was that high (having started at 476 km and recovered at 332 km, ref. 16), and fluxes at lower orbits are lower (ref. 10). The calculated production rates for the geographic-west flux at 500 km and for the geographic-east flux at 300 km are about 3–5 and about 50–60 times lower, respectively, than for the geographic-east flux at 500 km. Thus LDEF probably was exposed to a flux of trapped protons that was a factor of several to an order of magnitude or more lower than used here. However, these calculated rates can be used to show that the measured radioactivities are consistent with production by trapped protons.

DISCUSSION

The radioactivities measured in LDEF are similar to those observed in meteorites and lunar samples. Production-rate models developed for extraterrestrial materials have been used to calculate the production rates of several radionuclides in samples of LDEF for particles in the galactic cosmic rays and for protons in the trapped radiation. These calculated production rates are consistent with the measured radioactivities.

Production rates were calculated for four radionuclides measured in three materials from LDEF and for three radionuclides that could have been implanted in LDEF's leading surface. The rates for these implanted isotopes, ^{7}Be, ^{10}Be, and ^{14}C, can be used to help show that they were not made "in-situ" by the GCR or trapped protons. As these three radionuclides are made mainly by high-energy particles, their depth-versus-activity profiles are fairly flat, as the calcu-

lated rates for trapped protons given in table I show. Thus a sample away from the surface of LDEF can be used to establish the production rate by "in-situ" nuclear reactions for an "implanted" species in LDEF.

The production rates estimated for the GCR are lower than the measured activities by factors of several, although there are a number of uncertainties in going from GCR interactions in meteorites or lunar samples to GCR-induced reactions in LDEF. The production rates by GCR particles vary slowly with depth (ref. 4), and production by GCR particles at depth in LDEF probably is important. The calculated GCR rates are less than the radioactivities measured in LDEF.

As noted above, the production rates calculated here for trapped protons are too high. As these calculated rates are also higher than the observed activities, then the lower fluxes of trapped protons that LDEF was exposed to would be adequate to make most of the induced radioactivity induced in LDEF. The measured radioactivities of ^{54}Mn in the trunnion layers dropped less than a factor of two in going from the surface to a depth of 15 g/cm^2 (a radius of 0.9 inches in figure 1), while the calculated production rates dropped a factor of three over this depth. Thus trapped protons by themselves probably can not account for all of the activity induced in the trunnion. However, the shape of the activity-versus-depth profile clearly shows a surface excess of radioactivity that is similar to that made by relatively-low energy particles.

The calculated production ratios for ^{54}Mn/^{57}Co made in steel by either trapped protons or the GCR are about 6 – 7, similar to their measured activity ratios. The calculated production ratios for ^{54}Mn in steel to ^{22}Na in the aluminum 6061-T6 alloy is about unity, again consistent with the measurements. The fact that these production ratios are similar for both trapped protons and the GCR means that the observed activity ratios can not be used to unfold relative contributions by these two types of incident radiations.

The calculated production ratios for ^{54}Mn in steel to ^{46}Sc in the titanium Ti-6Al-4V alloy is about unity, while the measured activity ratio is about 3 to 1. While shielding of the titanium by overlying material could affect this ratio, there does not appear to have been enough differences due to the locations and shielding of these samples to give a ratio of 3. Another explanation for the lower activity of ^{46}Sc is that it was made nearer to the end of LDEF's mission than was ^{54}Mn. LDEF's orbit was lower then (ref. 16), and the fluxes of trapped protons decrease rapidly in very low orbits (ref. 10).

The calculations present here, while not very detailed, show that the radioactivities induced in LDEF are consistent with our experience in meteorites and lunar samples. There is a component due to the relatively-low-energy protons in the trapped radiation that contributes the observed enhancement in activity at the surface of the trunnions. Another component involves higher-energy particles and their secondary neutrons that contributes a fairly flat profile and much of the production at depth. Calculated production ratios for all isotopes but ^{46}Sc are consistent with measured ratios. Activities of 84-day ^{46}Sc are probably low because of the lower fluxes of trapped protons near the end of LDEF's mission when LDEF was in a very low orbit.

ACKNOWLEDGMENTS

We thank Thomas Parnell, Gerald Fishman, and B. Alan Harmon for providing us with samples of LDEF, especially those pieces that stimulated this work, and all members of the Ionizing Radiation Special Interest Group for their discussions.

REFERENCES

1. Harmon, B. A.; Fishman, G. J.; Parnell, T. A.; Benton, E. V.; and Frank, A. L.: LDEF Radiation Measurements: Preliminary Results. *Nucl. Tracks Radiat. Meas.*, vol. 20, no. 1, 131–136, 1992.

2. Parnell, T. A.: Status of LDEF Ionizing Radiation Measurements and Analysis. *Second LDEF Post-Retrieval Symposium*, NASA CP-3194, 1993.

3. Armstrong, T. W.; and Colborn; B. L.: Predictions of Induced Radioactivity for Spacecraft in Low Earth Orbit. *Nucl. Tracks Radiat. Meas.*, vol. 20, no. 1, 101–130, 1992.

4. Reedy, R. C.; and Arnold, J. R.: Interaction of Solar and Galactic Cosmic-Ray Particles with the Moon. *J. Geophys. Res.*, vol. 77, no. 4, 537–555, 1972.

5. Reedy, R. C.: Predicting the Production Rates of Cosmogenic Nuclides in Extraterrestrial Matter. *Nucl. Instrum. Methods Phys. Res.*, vol. B29, 251–261, 1987.

6. Lal, D.: In Situ-Produced Cosmogenic Isotopes in Terrestrial Rocks. *Annu. Rev. Earth Planet. Sci.*, vol. 16, 355–388, 1988.

7. Moss, C. E.; and Reedy, R. C.: Measurements of Induced Radioactivities in Some LDEF Samples. *First LDEF Post-Retrieval Symposium*, NASA CP–3134, pp. 271–285, 1991.

8. Smith, A. R.; and Hurley, D. L.: Radioactivities of Long Duration Exposure Facility (LDEF) Materials: Baggage and Bonanzas. *First LDEF Post-Retrieval Symposium*, NASA CP–3134, pp. 257–270, 1991.

9. Fishman, G. J.; Harmon, B. A.; Gregory, J. C.; Parnell, T. A.; Peters, P.; Phillips, G. W.; King, S. E.; August, R. A.; Ritter, J. C.; Cutchin, J. H.; Haskins, P. S.; McKisson, J. E.; Ely, D. W.; Weisenberger, A. G.; Piercey, R. B.; and Dybler, T.: Observation of ^{7}Be on the Surface of LDEF Spacecraft. *Nature*, vol. 349, 678–680, 1991.

10. Watts, J. W.; Parnell, T. A.; and Heckman, H. H.: Approximate Angular Distribution and Spectra for Geomagnetically Trapped Protons in Low Earth Orbit. In: *High-Energy Ra-*

diation Background in Space, American Institute of Physics Conference Proceedings 186, pp. 75–85, 1989.

11. Prael, R. E.; and Lichtenstein, H.: User Guide to LCS: The LAHET Code System. Los Alamos National Laboratory document LA-UR-89-3014, September 1989.

12. Briesmeister, J. F., Ed.: MCNP – A General Monte Carlo Code for Neutron and Photon Transport. Los Alamos National Laboratory report LA-7396-M, September 1986.

13. Michel, R.; Brinkmann, G.; Weigel, H.; and Herr, W.: Proton-Induced Reactions on Titanium with Energies Between 13 and 45 MeV. *J. Inorg. Nucl. Chem.*, vol. 40, 1845–1851, 1978.

14. Michel, R.; Brinkmann, G.; Weigel, H.; and Herr, W.: Measurement and Hybrid-Model Analysis of Proton-Induced Reactions with V, Fe, and Co. *Nucl. Phys.*, vol. A322, 40–60, 1979.

15. Michel, R.; and Stück, R.: On the Production of Cosmogenic Nuclides in Meteorites by Primary Galactic Particles: Cross Sections and Model Calculations. *Proc. 14th Lunar Planet. Sci. Conf.*, in *J. Geophys. Res.*, vol. 89, suppl., pp. B673–B684, 1984.

16. Kinard, W. H.; and Martin, G. D.: Long Duration Exposure Facility (LDEF) Space Environments Overview. *First LDEF Post-Retrieval Symposium*, NASA CP–3134, pp. 49–60, 1991.

Table I. Calculated Production Rates in LDEF Samples.

The target is the material or alloy being considered, such as the titanium alloy used for clips. Rates are calculated for the indicated radionuclide in that target material. The first three rates are for production by trapped protons at different depths, and the last one is for production by GCR particles away from a surface. The incident omnidirectional flux for the trapped protons was the geographic-east 500-km one in ref. 10, and the target was modeled as a sphere of radius 63 g/cm^2. See text for details on the two sets of calculations. The calculated production rates are in units of atoms s^{-1} kg^{-1} for the composition of the indicated target.

Target	Nuclide	Surface	4.5 g/cm^2	15 g/cm^2	GCR
Steel	^{54}Mn	22.5	12.5	7.1	0.9
Steel	^{57}Co	4.5	2.1	1.2	0.13
Ti alloy	^{46}Sc	23.5	13.9	8.2	0.9
Ti alloy	^{22}Na	1.7	1.0	0.6	0.08
Al alloy	^{22}Na	24.7	14.5	8.5	0.7
Aluminum	^{7}Be	1.4	1.0	0.6	0.1
Aluminum	^{10}Be	0.2	0.15	0.1	0.03
Aluminum	^{14}C	0.2	0.15	0.1	0.07

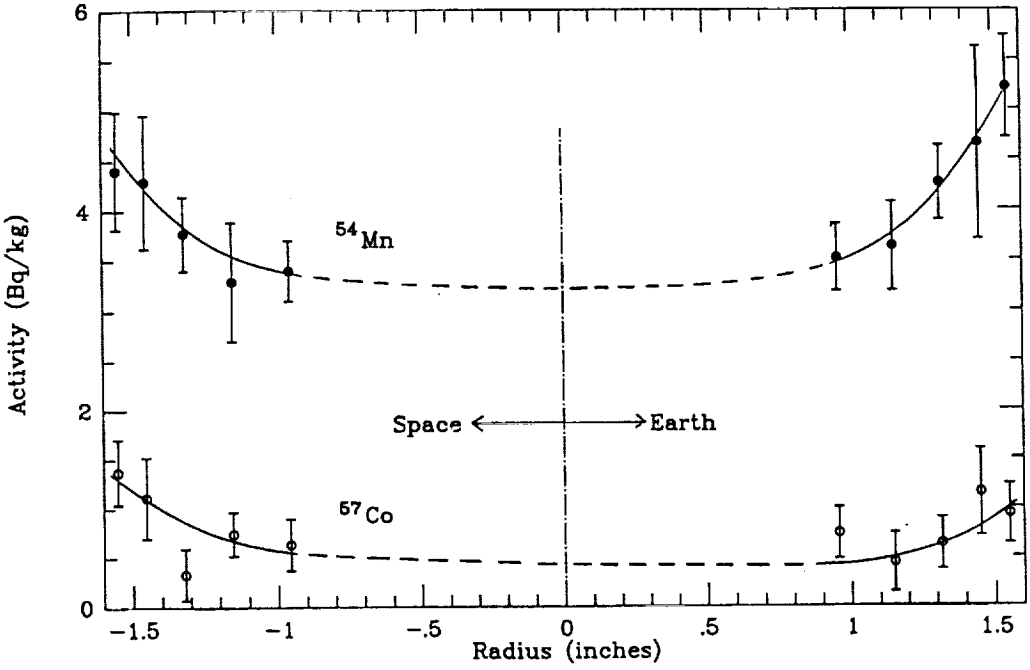

Figure 1. Induced radioactivity in section D of the left hand (west) trunnion. The curves are to guide the eye, especially to the enhanced activity near the surface and the flattening of the profile near the center.

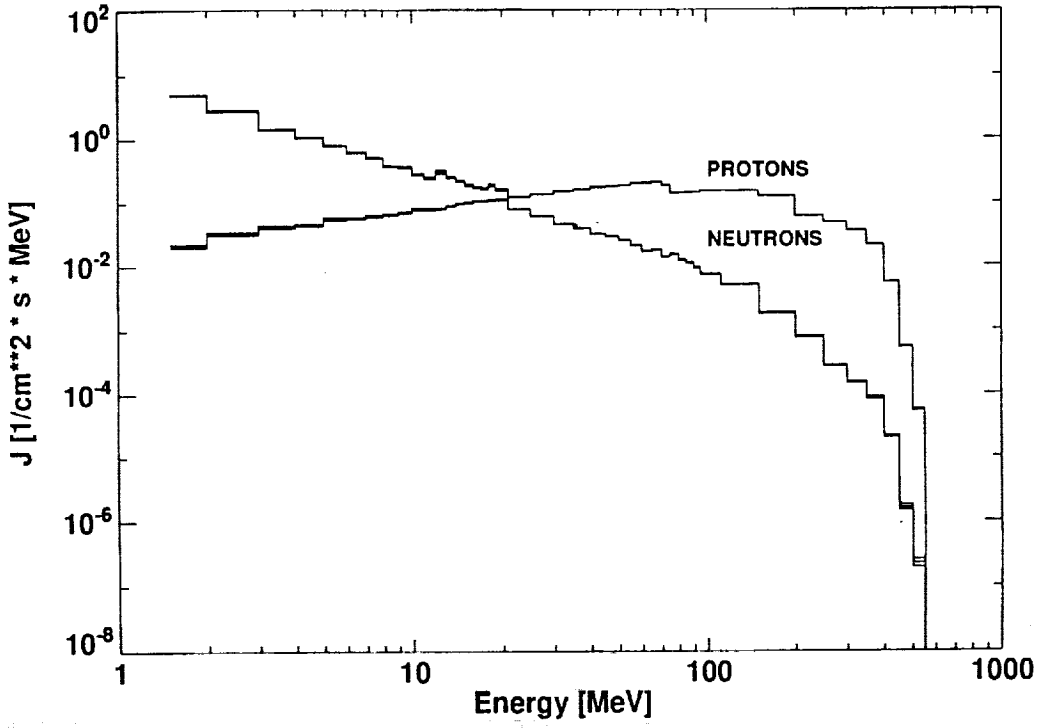

Figure 2. Proton and neutron fluxes calculated by the LAHET Code System as crossing a surface 0.59 cm (4.5 g/cm^2) deep in a steel sphere of radius 4.125 cm (31.5 g/cm^2). The incident flux was the geographic-east, 500-km trapped proton one from ref. 10. The fluxes of protons dominate except for energies below 20 MeV.

N93-29629

A PHOTON PHREAK DIGS THE LDEF HAPPENING

Alan R. Smith and Donna L. Hurley
Engineering Division
Lawrence Berkeley Laboratory
University of California
Berkeley, CA 94720
Phone (510) 486-5679 FAX (510) 486-5888

ABSTRACT

A year ago at the First LDEF Post-Retrieval Symposium, we reported detailed measurements on trunnion sections, as well as results from "intentional" samples (Co, Ni, In, Ta, and V) and spacecraft parts. For this year's Symposium we re-evaluate some of these findings in combination with more recent results, to cast a longer perspective on the LDEF experience, and to sketch some promising avenues toward more effective participation in future missions. The LDEF analysis effort has been a superb training exercise, from which lessons learned need to be applied to future missions - - right back to the early phases of mission planning.

INTRODUCTION

A dedicated group of experts in low-level gamma-ray spectrometry has worked diligently at a number of laboratories across the USA, to produce an impressive array of radiometric analyses on LDEF samples and spacecraft parts (refs. 1, 2). This effort was most intensive during the first few months of sample availability: the period March - August 1990.The LBL measurement program continued into calendar 1991 and 1992 at a reduced pace, and there remain selected samples to be counted for the first time at the Oroville Facility when our new "Merlin" detector arrives; these are samples that require long counting times in a very low-background environment. In addition, it may be worthwhile to re-examine some samples containing long-lived radionuclides in order to achieve higher precision, for example: the LDEF aluminum clamp plates, to produce more accurate Na-22 activity values for detailed comparison with model predictions.

It is a rare privilege, this participation in the LDEF analysis program, and we look forward to continuing with future LDEF sample analysis. We are in the midst of a major upgrading of the LBL Low Background Facilities, a process that has been strongly stimulated by our LDEF participation; consequently, we will be in a position to offer greatly expanded analysis capability to future space missions, be they of days-long or years-long duration.

In the following sections of this report we illustrate how our LDEF analysis efforts have led to recommendations for revising some procedures in order to enhance the value of radiometric analysis results from future missions. We also describe extensions of this technology which have the potential to provide useful data in the quest to understand the recent history of solar activity.

SAMPLE SIZE: BIGGER CAN BE MUCH BETTER

Results of our measurements of the North-to-South profile for Mn-54 activity in trunnion section LHG are shown on Table I. Also listed are the ranges of observed count rates in the 834 KeV peak, count times, and individual sample weights. Our aim was to produce data of good statistical quality (no greater than 3% standard deviation) so that small changes in profile shape could be identified, for example: the possible appearance of a broad "peak" in Mn-54 activity in the core region of the trunnion that would be associated with the buildup of secondaries generated by galactic cosmic ray interactions.

This work was supported by NASA under Marshall Flight Center Order No. H-06815D through U.S. Department of Energy under contract No. DE-AC03-76SF00098.

TABLE I

Profile of Mn-54 Activity vs depth in Trunnion Section LHG

Trunnion Slice		Mn-54 pCi/Kg	Mn-54 S.D.
LHG	N1	171.3	6.0
	N2	137.3	5.2
	N3	117.5	3.7
	N4	105.1	2.0
	N5	95.0	2.5
	N6	93.1	3.8
	N7	97.0	3.2
	Core		
	S7	82.6	2.6
	S6	73.4	2.8
	S5	69.3	2.1
	S4	68.4	2.8
	S3	75.8	2.4
	S2	88.2	2.7
	S1	107.3	4.7

Parameter Ranges
Count Rates: 0.074-0.470 c/min
Count Times: 2400-10100 min
Sample Weights: 30-70 grams

Although we generally achieved the goal of 3% statistical precision, some counting times of 10000 minutes (7 days) were required for these relatively small samples. Week-long count times severely constrain the number of samples that can be analyzed - -even when the facility is "dedicated" and the halflives are suitably long. Shorter counting times become imperative, when considering the need to measure short halflife isotopes that would dominate from shorter (days to weeks-long) Space Shuttle missions.

We are implementing significant improvement in this aspect at the LBL/ORO Facility, where an upgrade replacement for our "Merlin" detector will soon be in operation, providing an approximate 3-fold increase in detection efficiency. We expect count time reductions of a comparable factor without any sacrifice in measurement precision. Conversely, keeping to the long count times would enhance measurement precision for some of the nuclides which produced much smaller peaks in these trunnion samples, such as: Co-56, Co-57, Co-58, Co-60, Ti-44, and Na-22.

Further improvement in our ability to measure such minute activities can most reasonably come through an increase in sample size. Suppose the typical 50-gram sample is increased in weight to 1 Kg, a 20-fold increase. If the resultant peak count rates increased only half this ratio, we would achieve a 10-fold gain. Combining the gain in efficiency with this sample-size gain produces a 30-fold reduction in count time, while maintaining the original precision. A week-long count becomes a 6-hour count. That is progress!

This effect can be seen from the previously cited results for single trunnion slices, compared to a special "Merlin" run on a collection of these same samples. A group of 18 trunnion slices was arranged around the sides and at the end (standard position) of the detector endcap. Total sample weight was about 1 Kg, from which the week-long run produced a Mn-54 activity value with 1% standard deviation. A small portion of this spectral data is plotted on Fig. 1, where the feature of greatest interest is the prominent peak at 1274 KeV belonging to Na-22, measured here to a precision of about 10% This peak was either unobservable or so small as to be quantitatively useless in all data obtained from week-long

runs on single slices. The presence of Na-22 in these stainless steel samples signifies a reaction requiring an incident particle energy in the low hundreds of MeV, representing the highest-energy reaction documented in LDEF materials through observation of induced-activity radionuclides.

A short portion of the spectrum from a Pb ballast slice is displayed on Fig 2, which shows the presence of 38-year halflife Bi-207, which was produced mainly by a proton-specific reaction on Pb. This data was obtained in a week-long "Merlin" run on a 2"x2"x1/8" thick Pb sample. While the peak is small, it is quantitatively useful (about 10% S.D.), and could be much more easily and accurately assayed upon implementation of the previously described system improvements.

WHAT TO SHOOT AT: SELECTION OF TARGET MATERIALS

Target materials (elements) must be carefully selected to provide as much information about the radiation field as possible. The nuclear reaction products (induced-radioactivities) discussed here can all be assayed by gamma-ray spectrometry, the most convenient method for direct measurement on "thick" samples. Our emphasis is on radionuclides with halflives long enough to be suitable for monitoring missions of many months to years duration, but at the same time noting that there are nuclides with shorter halflives appropriate for similar monitoring functions on short duration missions.

It is desirable, but not necessary, that target elements are of the single stable isotope category, such as Be, Na, Al, V, Mn, Co, Nb, I, Ta, Au, and Bi. Also acceptable are elements in which one stable isotope dominates, such as B, C, O, Si, S, and Fe. Similarly acceptable are elements in which closely adjacent (one or two nucleons apart) isotopes are the dominant members, such as Cl, Ni, Cu, Zn, Ag, and Eu. In some cases elements with many stable isotopes may be selected because of certain important reactions, such as: Ti, for 47-year Ti-44; and Pb, for 38-year Bi-207. It is important to keep in mind that as the reaction product is further removed from the target element (more nucleons removed, which signifies higher threshold energies and multiple reaction paths) it becomes less important to start from a single-isotope target element.

A special category of target materials includes those elements which are major constituents of large-mass active detectors, such as: the inorganic scintillators NaI, CsI, and "BGO" (Bi and Ge), plastic scintillators (C), and the semiconductor detectors Si and Ge. Some induced-activity radionuclides (electron-capture decay) can be assayed internally by these detectors, others, by beta-gamma coincidence techniques involving the use of external detectors for the gamma-ray analysis.

A sampling of candidate radionuclides is given on Table II, which lists halflives along with prominent gamma-rays, and the materials in which some of these nuclides were detected in our LDEF samples. Neither target elements nor reaction paths are specified here, except that nuclides followed by an asterisk are slow-neutron capture products from adjacent high-abundance stable isotopes of the same element. Most of the rest are products of reactions requiring tens to hundreds of MeV incident particle energies, and can be initiated by either protons or neutrons or heavier particles.

There are a number of radionuclides with suitable halflives from which fluorescent X-rays are the only photons emitted at decay. These X-rays are of low energy, for example: the 5.9 KeV K-shell X-rays from decay of 2.7 year halflife Fe-55; they cannot be detected with reasonable efficiency from the "thick" samples upon which our gamma-ray technique is based. Consequently, no members of this class appear on Table II.

TABLE II

Some Medium Halflife Gamma-Emitters For Space Monitoring

Nuclide	Half-life Years	Prominent Gamma-rays	In LDEF Samples
Na-22	2.60	511,1274	Al,ss
Al- 26	7.2 E05	511,1809	
Ar- 42 (K-42)	33.	1525	
Ti- 44 (Sc-44)	47.	68,78,511,1157	Ti,ss
Mn-54	0.85	834	Co,Ni,ss
Co- 57	0.74	122	Co,Ni,ss
Fe- 60 (Co-60)	3.0 E05	1173,1332	
Co- 60 *	5.27	1173,1332	Co,Ni,ss,In
Zn-65 *	0.67	1116	
Kr-81	2.1 E05	276	
Nb-92	3.2 E07	560,934	
Nb-94 *	2.0 E04	703,871	
Tc-98	4.2 E06	652,745	
Rh-101	3.3	127,198	In
Rh-102	2.9	475,631,697	In
Ru-106 (Rh-106)	1.0	512,622	
Ag-108m *	127.	434,614,722	
Cd-109 *	1.2	88	
Ag-110m *	0.69	658,885,1384	In
Sb-125	2.7	428,600,636	
Sn-126 (Sb-126)	1.0 E05	415,666,695	
I-129	1.6 E07	40	
Ba-133	10.7	81,356	
Cs-134 *	2.06	605,796	
Cs-137 (Ba-137)	30.2	662	
Pm-143	0.73	742	
Ce-144 (Pr-144)	0.78	134,2185	
Pm-144	0.96	477,618,696	
Pm-146	5.5	454,736,747	
Pm-147	2.6	121	
Eu-150	36.	334,439,584	
Eu-152 *	13.3	122,344,1408	
Eu-154 *	8.5	123,723,1274	
Tb-158	150.	944,962	
Hf-172 (Lu-172)	1.87	181,810,1093	Ta
Lu-173	1.37	272	Ta
Hf-182 (Ta-182)	9.0 E06	68,1121,1221	Ta
Os-194 (Ir-194)	6.0	328	
Hg-194 (Au-194)	520.	328,1924,2044	
Pb-202 (Tl-202)	3.0 E05	440	
Bi-207	38.	570,1063,1770	Pb
Bi-208	3.7 E05	2614	

Measurement of the same isotope in a sequence of successively heavier target elements provides information about increasingly higher-energy components of the radiation field. For example, the reactions to produce Na-22 from Al, Si, S, Ti, and Fe have increasing energy thresholds ranging from a few tens of MeV up to a few hundreds of Mev. Reactions to produce 47-year halflife Ti-44 from Ti, Mn, Zn, and Ge encompasses a similar range of threshold energies. Suites of target elements that produce appropriately "short" halflife radionuclides can also be found to provide a similar range of energy spectral information from short missions. In either case, the enhanced system performance and increased sample size discussed earlier will be required if we are to extract the best quality radiometric information from returned samples.

A number of nuclides listed on Table II were not observed in our LDEF samples, but are attractive candidates in certain target elements were they placed aboard future missions; alternatively, some of these nuclides should be sought in machinery left on the lunar surface during the Apollo Program, when key parts of these items are returned to earth for their 30-year checkup. A valuable companion study should be done on key parts of long-dormant earth-orbit satellites - - retrievable during shuttle missions. Relevant materials include Al, Si, Ti, Fe, and any heavier elements such as Ag, Ta, W, and Pb - - provided they are available in large enough quantities.

HOW TO DO IT BETTER NEXT TIME

The radiometric sample analysis effort has identified a number of mission parameters that need revision if our performance is to be improved on future missions. Crucial among these is the time elapsed between spacecraft touchdown and sample availability. For "intentional" samples on short missions (days to weeks) this delay should be no more than a few hours. For example, from a shuttle landed at Edwards Air Force Base, counting at LBL could start within 6 hours if air transport is involved in shipment to Berkeley or Oroville, or within 10 to 12 hours if only surface transport is available. These brief delay times are essential to maximize the return from short-halflife (days to weeks) radionuclides - - the species most favorable for measurement from comparably short missions. Longer delay times might be appropriate for "intentional" samples from long missions, although longer than a week seems unnecessary. The availability of spacecraft pieces is a different matter, wherein considerably longer delays may be unavoidable. This circumstance is in itself a strong argument for inclusion of more "intentional" samples on future missions.

Sample size is also an extremely important parameter in determining the success of any gamma-spectrometry analysis effort, as we have already discussed. We mention again that increasing a sample from a typical 50-gram weight to a 1000-gram weight in "favorable" counting geometry should produce at least a 10-fold increase in peak count rates for most gamma-ray energies in most target materials. While recognizing the dramatic penalty paid to put additional weight into orbit, the few extra kilograms inferred here is a very small increment compared to the total weight of the Space Shuttle launch vehicle, the LDEF itself, or other large satellites.

Target materials (elements) for "intentional" samples must be carefully chosen, so as to maximize the information recovered from measurement of induced-activity radionuclides, as already mentioned. We note here that at least the elements Be, C, F, Na, Al, S, Si, Ca, Ti, Mn, Fe, Cu, Ge, Zr, Nb, Mo, Ag, Eu, W, Au, Pb and Bi should be considered as candidate "intentional" sample materials in addition to the LDEF suite (V, Co, Ni, In, Ta); further, that some elements from this list might be appropriate substitutes for the V and In samples that were aboard the LDEF satellite.

The radioactive content of ALL "intentional" samples sent aloft in the future must be known (measured) before launch. Although peaks from this "baggage" usually do not overlap peaks sought from space-induced activities, their presence at sufficient intensity can interfere with measurement of all peaks of interest which have lower energies than the strong interfering peaks. We documented such a case in last year's report: the presence of relatively high-intensity U-series gamma-peaks in spacecraft parts made of titanium Type 6-4 alloy. In cases where samples are intended for neutron monitoring by production of

slow-neutron capture radionuclides, it is crucial to check for the pre-launch content of these radionuclides, for example: Co-60 in cobalt "intentional" samples. This is especially important when long halflife nuclides are to be measured from short-duration missions, as is the case for Co-60 in cobalt

With improved detection efficiency, increased sample size, and a favorable sample recovery schedule, it is feasible to undertake "frequent flyer" missions on the Space Shuttle with 5- to 10-member sets of "intentional" samples. It is important to build a multi-mission database for this kind of information, initially to test its validity, but mainly to supply important information on characterization of the extra-terrestrial environment into which mankind is just beginning to venture in the context of long-term occupancy.

WHAT'S WITH THE SUN?

Comparisons of the radionuclide content of lunar-surface Apollo Mission machinery with the content of these same radionuclides in natural lunar surface "soil" can, in principle, provide valuable information concerning any changes in the level of solar activity during intervals on the same time scale as the radionuclide halflives. For example, the amount of Ti-44 in Apollo titanium could be compared to the fraction of Ti-44 in lunar surface material that is attributable to the Ti-content of the lunar material. Similar measurements could be made for the Ti-44 content of stainless steel, again comparing it to the Ti-44 in lunar material attributable to its Fe-content. This gives us the 50- to 100-year perspective, during which solar activity has been monitored from earth with some regularity. An even shorter view, a 5-year perspective, could be based on the comparison between the Na-22 content of Apollo aluminum and lunar surface material.

Upon validation of this approach for these time scales, a long-range possibility comes to view: the million-year perspective, afforded by measurement of the 720000-year halflife radionuclide Al-26, by direct counting of its decay. The Al-26 content of lunar surface material has been documented from Apollo Program samples (refs. 3, 4) at approximately 50 d/min-Kg, or about 20 pCi/Kg. One pCi in a kilogram sample is easily measurable with our present systems. The real challenge will be to get it right for the Al-26 in Apollo aluminum, where the 30-year lunar exposure has produced but a tiny fraction of the near-equilibrium Al-26 activity existing in lunar surface material. Simple calculations, based on the efficiency increase provided by New Merlin and the availability of optimum sample size, predict the measurement will be difficult but successful.

Measurement of the long-lived nuclides Na-22, Al-26, Ti-44, and Bi-207 in parts retrieved from dormant earth-orbit satellites can provide additional information regarding the near-earth effects of solar activity. The value of such analyses would be increased if they can be obtained from parts of satellites that have been in orbit for different lengths of time, and/or different orbits.

Another very promising and rapidly developing technique, accelerator-based mass spectrometry (AMS) (ref. 5), is amenable to some of the analytic needs discussed here, especially in regards measurement of the longer halflife nuclides, such as Al-26. In this technique, any of the parent atoms (ionized, accelerated, and magnetically separated) can be counted, instead of only those atoms which decay while the sample is being "watched". Much smaller samples can be analyzed, and in shorter analysis times. AMS becomes ever more suitable as halflives lengthen, and ever more necessary as sample size decreases. The proposed "solar history" measurement of Al-26 may best be accomplished through use of AMS on the lunar surface material and gamma-spectrometry on the Apollo aluminum.

These gamma-spectrometric methods, along with other radiometric techniques, AMS, and conventional mass spectrometry are among the major avenues (ref. 6) toward understanding the extent of solar output variability on the time scale relevant to critical decisions to be made regarding the specter of "global warming" that now confronts our civilization.

SUMMARY

The perspective for this discussion of the LDEF sample analysis effort is forward-looking: evaluation of our experience at obtaining the reported results in the context of improvements that can be implemented during future missions. Examples have been given to emphasize the need for larger samples, as well as more efficient (larger) detectors. Choices for target elements (intentional samples) have been discussed, as well as the schedules for sample retrieval after spacecraft touchdown. Finally, some applications are outlined for use of induced-activity analysis of materials returned to earth after various times in space, as one of the promising avenues toward identifying (any) temporal variations in solar output - - perhaps reaching back as far as a million years.

ACKNOWLEDGMENTS

We again express our deepest appreciation to all NASA personnel associated with the LDEF mission, in particular: the 1984 Challenger crew who launched the satellite and the 1990 Columbia crew who brought it back to earth; the LDEF mission primary team at Langley, headed by Dr. William Kinard; the Langley team headed by Dr. Arlene Levine, who again organized a very successful symposium; and the Special Investigation Group for radioactivity measurements, headed by Dr. Thomas Parnell and including Drs. Gerald Fishman and B. Alan Harmon. Special thanks are due Alan Harmon for his masterful handling of acquisition of samples and their distribution among participating laboratories on a timely schedule.

Our appreciation continues for the superb support in detector and electronics technology afforded by the LBL group formerly headed by Fred Goulding, particularly regarding creation of our MERLIN spectrometer system. And - - thanks again to Kevin Hurley of the U.C. Space Science Laboratory, whose phone call alerted us to this opportunity of a lifetime: participation in the LDEF analysis program.

We respectfully dedicate all our efforts in the LDEF analysis program to the last crew of the Challenger, lost at launch in early 1986, but long remembered in the annals of man's journey into space.

BIBLIOGRAPHY

1. Space Environments, Ionizing Radiation, First LDEF Post-Retrieval Symposium, NASA CP-3134, conference proceedings, pp 199-396, 1991.

2. Space Environments, Ionizing Radiation: Second LDEF Post-Retrieval Symposium, NASA CP-3194, 1993.

3. Reedy, R. C.; and Arnold, J. R.: Interaction of Solar and Galactic Cosmic-ray Particles with the Moon. J. Geophys. Res., vol. 77, no. 4, pp 537-555, 1972.

4. Vogt, S.; Herzog, G.G.; and Reedy, R.C: Cosmogenic Nuclides in Extraterrestrial Materials. Rev. Geophys., vol 28-3, pp 253-275, 1990.

5. Suter, M.: Accelerator Mass Spectrometry: State of the Art, 1990. Proceedings of Fifth International Conference on Accelerator Mass Spectrometry, Nucl. Instrum. Methods Phys. Res., pp 211-223, 1990.

6. Reedy, R.C.; Arnold, J.R.; and Lal, D.: Cosmic-Ray Record in Solar System Matter. Annual Reviews of Nuclear and Particle Science, vol. 33, pp 505-37, 1983.

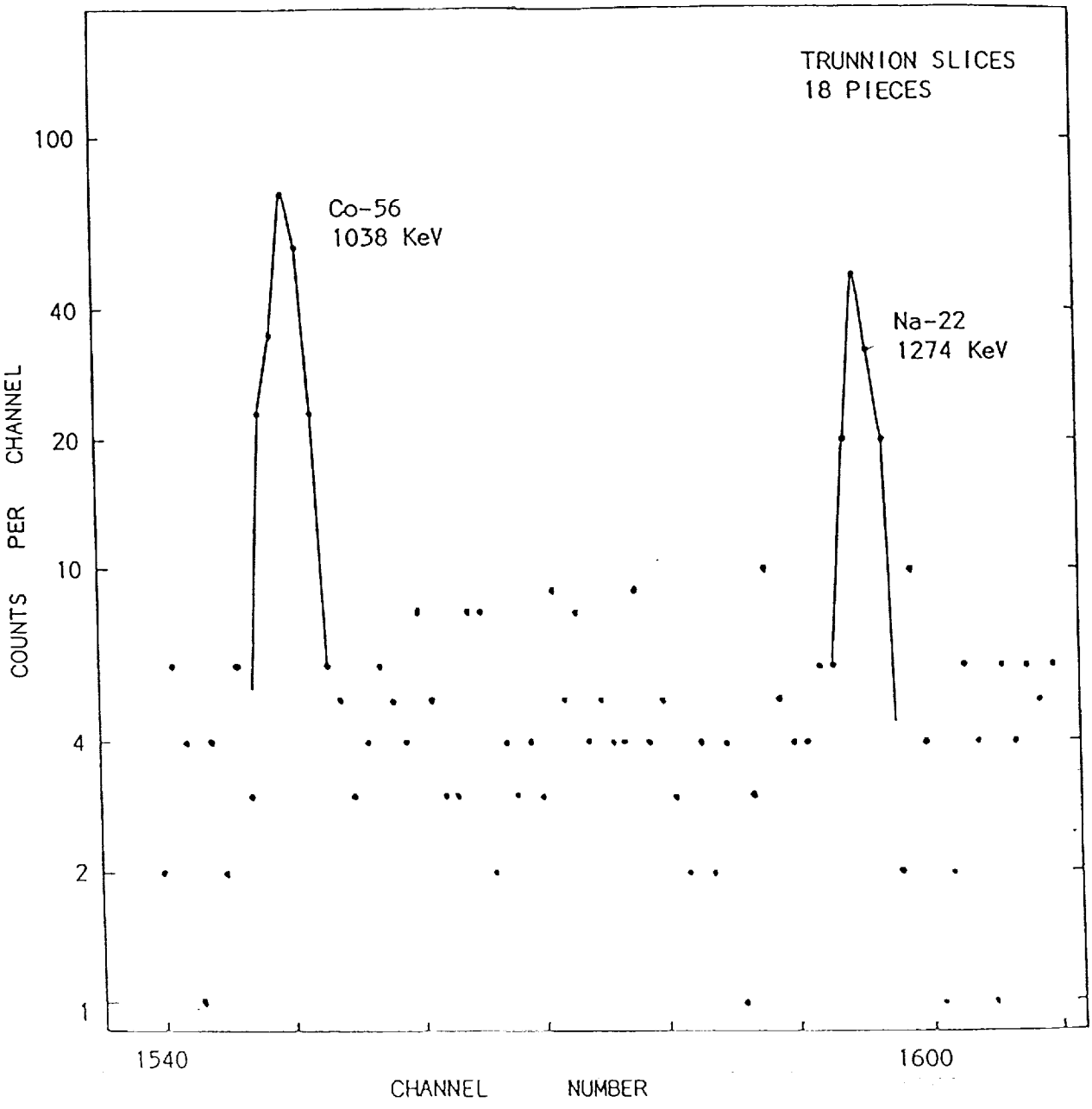

Figure 1. Spectral data from a week-long "Merlin" run on a group of trunnion slices; this interval features the 1274 KeV peak from Na-22.

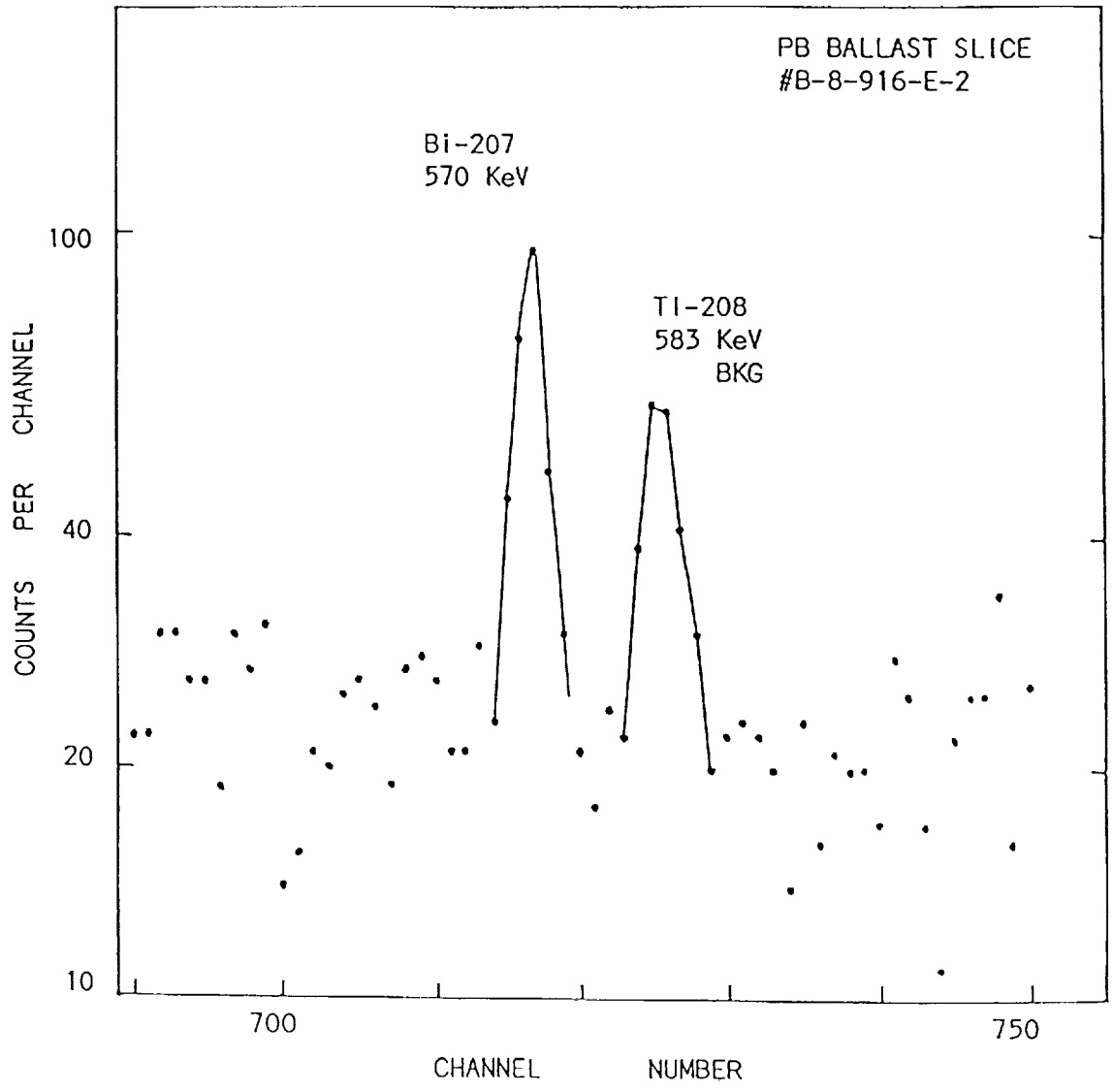

Figure 2. Spectral data from a week-long "Merlin" run on one Pb ballast slice; this interval features the 570 KeV peak from Bi-207, as well as a nearby TI-208 BKG peak, which has an intensity of 0.01 c/min.

CHARGED PARTICLE ACTIVATION STUDIES ON THE SURFACE OF LDEF SPACECRAFT

Ilhan Olmez
Massachusetts Institute of Technology
Nuclear Reactor Laboratory
138 Albany Street
Cambridge, MA 02139
Phone: 617/253-2995, Fax: 617/253-7300

Forest Burns and Paul Sagalyn
U.S. Army Materials Technology Laboratory
Watertown, MA 02172-0001
Phone: 617/923-5398, Fax: 617/923-5385

SUMMARY

High energy proton induced nuclear reaction products are examined using seven elements, namely, Aluminum, Silicon, Nickel, Copper, Zirconium, Tantalum, and Tungsten. The samples were in the form of plates, 2 x 2 x 1/8 inches. We detected activities due to ^{22}Na from Al, ^{56}Co and ^{57}Co from Ni, ^{58}Co from Cu, and ^{88}Y from Zr targets. No induced activity was observed in Si, Ta and W, most probably due to the long cooling times. Only the Zr sample contained a weak ^{7}Be peak, although Ta and W were also located at the leading edge of the spacecraft. Gamma-rays of individual isotopes were measured using high-resolution Ge(Li) solid state detector coupled to 4096-multichannel analyzer. Activities were calculated for ^{56}Co (846 keV) and Co-57 (122 and 136 keV's) at the time of the entry of the spacecraft and found to be 0.014 ± 0.005 c/sec. g, 0.018 ± 0.002 c/sec. g, and 0.0024 ± 0.0007 c/sec. g, respectively.

INTRODUCTION

A number of sample materials carried aboard the LDEF mission became weakly radioactive because of irradiation by high energy protons associated with the geomagnetically trapped, Van Allen radiation belt. Within the Van Allen belt, protons are present within an energy range of a few MeV up to about 700 MeV (ref. 1). In addition, radioactivity can be induced by irradiation from cosmic ray protons and heavier nuclei. These primary proton-material collisions may also produce secondary neutrons which in turn, could activate other materials.

In the present study, the activation product of interest was gamma radiation from radioactivities with half-lives of from 10's of days to a few years. Since the LDEF was in orbit for over 2000 days, it is expected that an induced activity will have reached equilibrium levels where any increase in the induced activity is offset by the decay process.

1. Watts, J. W., *LDEF Dose Predictions and Measurements,* LDEF Ionizing Radiation Special Investigation Group Meeting, NAIA/MSFC, July 1990.

RESULTS

Seven sample materials, Aluminum, Silicon, Nickel, Copper, Zirconium, Tantalum, and Tungsten, from the LDEF were analyzed for gamma emission by high resolution, high precision gamma ray spectroscopy techniques. The gamma ray spectroscopy equipment is based upon a Nuclear Data Corp. Genie 9900 system. Data acquisition, display, and processing are controlled by a DEC MicroVAX II computer. A Ge(Li) solid state detector was utilized to detect emitted gamma rays. The detector had an efficiency of approximately 20% with a resolution of approximately 1.9 keV (FWHM Co-1332 keV). The overall system operated as a 8192 multichannel analyzer. The gamma ray spectrum ranged from about 100 keV up to about 2 MeV.

Individual samples were counted for time periods ranging from 2 to 7 days. In all cases, samples were positioned about 2 cm away from the end cap of the detector. The detector-sample region was shielded with approximately 5 to 10 cm of lead.

Table I lists the target materials together with possible proton induced nuclear reactions, principal gamma ray emission line of the daughter radionuclide, half-life of the daughter radionuclide, and the relative position of the sample on the LDEF. As noted in the table, three samples, Si, Ta and W, exhibited no observable activity. This is probably due to the fact that only short half-life activities would have been produced with these elements.

For the four samples, Al, Ni, Cu, and Zr, which exhibited induced activities, Table II lists the calculated activities of these materials at the time of re-entry. These data confirm previous results with an additional ^{88}Y gamma emission from the Zr sample.

Also, the Zr sample exhibited a weak ^{7}Be peak at 477 keV. Since the exact shielding configuration of the LDEF is not known, it is not possible to make any conclusive statement as to the source of ^{7}Be. For instance, the ^{7}Be material could have occurred due to physical capture as the LDEF orbited at low altitude in the stratosphere. However, it should be noted that no ^{7}Be signatures were seen on the Ta or W samples although all three samples, Zr, Ta, and W, were located on the leading edge of the spacecraft.

Finally, the gamma ray spectroscopy results do not indicate any direct (n, γ) reactions. For example, no evidence for a ^{66}Cu (n, γ) or ^{67}Cu (n, γ) reaction was observed.

Table I. Target Materials

Target Material	Possible Induced Reaction	Gamma Energy (keV)	Half-Life	Location
Aluminum	^{27}Al (p, αd) ^{22}Na	1274	2.6y	Trailing Edge
Silicon	No Activity Observed			Earth End
Nickel	^{58}Ni (p, n2p) ^{56}Co	847	77.7d	Trailing Edge
	^{60}Ni (p, α) ^{57}Co	122	272d	Trailing Edge
		136		
Copper	^{63}Cu (p, αd) ^{58}Co	811	70.9d	Earth End
Zirconium	^{90}Zr (p, n2p) ^{88}Y	1836	107d	Leading Edge
Tantalum	No Activity Observed			Leading Edge
Tungsten	No Activity Observed			Leading Edge

Table II. Calculated Activities at Time of Re-Entry

Target Material	Elemental Constituent	Activity c/sec., gram
Nickel	^{58}Ni (846 keV)	0.014 ±0.005
	^{60}Ni (122 keV)	0.018 ±0.002
	(136 keV)	0.0024±0.0007

COLLECTION, ANALYSIS, AND ARCHIVAL OF LDEF ACTIVATION DATA*

C. E. Laird
Department of Physics and Astronomy
Eastern Kentucky University
Richmond, KY 40475

B.A. Harmon, G. J. Fishman, and T. A. Parnell
NASA Marshall Space Flight Center
Huntsville, AL 35812

SUMMARY

The study of the induced radioactivity of samples intentionally placed aboard the Long Duration Exposure Facility (LDEF) and samples obtained from the LDEF structure is reviewed. The eight laboratories involved in the gamma-ray counting are listed and the scientists and the associated counting facilities are described. Presently, most of the gamma-ray counting has been completed and the spectra are being analyzed and corrected for efficiency and self absorption. The acquired spectra are being collected at Eastern Kentucky University for future reference. The results of these analyses are being compiled and reviewed for possible inconsistencies as well as for comparison with model calculations. These model calculations are being revised to include the changes in trapped-proton flux caused by the onset of the period of maximum solar activity and the rapidly decreasing spacecraft orbit. Tentative plans are given for the storage of the approximately 1000 gamma-ray spectra acquired in this study and the related experimental data.

* Work supported by NASA contracts H-08071D and H-13029D.

INTRODUCTION

Samples intentionally placed aboard the Long Duration Exposure Facility (LDEF) and samples obtained from the LDEF structure have been studied at NASA Marshall Space Flight Center and seven national laboratories to determine the specific radioactivity produced in orbit. The gamma-ray spectra from these studies have provided information concerning the type and quantity of radioactive nuclei produced by various activating particles. The gamma-ray spectra, the resulting activation, and the experimental arrangements are being collected at Marshall Space Flight Center and Eastern Kentucky University for review, further analysis, and future archival. An overview of this process and the type of information that will be available for future reference will be given here. This information includes the samples studied, the location of the samples on LDEF, the amount and type of covering material, the types of detector systems, the format of the gamma-ray spectra and the corrections for geometry, self-absorption, detector efficiency and background needed to obtain accurate specific activities (activation per kilogram) of material. Tentative plans are given as to the archival of the data for such future reference and how other scientific investigators or spacecraft designers can access the data.

DATA COLLECTION

Approximately 400 samples[1] have been obtained from LDEF and most, if not all, have been studied for radioactivity at one or more of seven counting facilities. The LDEF activation samples include 20 elementally pure rectangular slabs of original 2" x 2" x 1/8" dimensions although some were cut to smaller dimensions for mounting. The slabs are made from the elements V, Ni, Co, In, and Ta. The first three elements (V,Ni,Co) represent materials having very well-known cross sections for proton-induced reactions up to 200 MeV[2] and fairly well known cross sections up to 1 GeV or higher.[3] The last two samples have well known large thermal neutron cross sections[4] and have recently been studied for incident protons up to 200 MeV[3] and for neutrons at 200 MeV[5].

The samples of opportunity, or "unintentional" samples, include aluminum clamp plates and trays, titanium clips, lead ballast, and the stainless-steel trunnions.* The trunnions have been cut into 1/2-2 inch sections and sections D, G and L have been layered by cutting at different radial distances from the center. (See Figure 1 in ref. 6). Except for the outer layer(layer number 1),

*Harmon, B. A.: Space Science Laboratory, NASA/MSFC, private communication.

these layers were carefully flattened to give an approximate rectangular slab geometry. The aluminum pieces are of various shapes and sizes. In addition, bolts were taken from the structure and have been studied.

These samples, mostly having rectangular slab geometries, have been studied for radioactivity at MSFC and six other counting facilities. These facilities are listed in Table 1 along with the collaborating scientists. These facilities could be categorized as being shielded, low-background, and ultra-low background. A shielded facility is one where shielding is used primarily to prevent contamination from other samples being counted in a multiple sample count facility. The TVA/Muscle Shoals facility might be considered such a facility. Low-background facilities would have several inches of shielding consisting of layers of lead, stainless-steel (or copper), and aluminum. The facility at the Space Science Laboratory at MSFC could be categorized amongst these. The ultra-low background facilities often have a low background facility placed in an underground location. The facilities used by Bill Winn at SRL[6] and by Al Smith at LBL[7] are ultra-low-background facilities.

At SRL the facility is located in a clean room 50 feet underground with the equivalent of 104 feet of water shielding. (See Figure 1, ref. 6). At LBL, or rather at their Oroville Dam facility, the facility is located inside the dam under 600 feet of bedrock. Such locations with low-background arrangements make excellent facilities for very low-activity samples.

The detectors used in these facilities consist of low resolution large volume NaI detectors and HPGe and Ge(Li) high resolution gamma-ray detectors which in some cases possess active shielding in addition to the passive shielding already described. The NaI(Tl) detectors include the 4π detector at JSC as well as the one at PNWL already mentioned by Jim Reeves in this conference. The germanium detectors are efficiency rated in relation to a 3" diameter, 3" long NaI(Tl) detector at a gamma-ray energy of 1332 keV. Those used in these studies have efficiencies ranging up to 90%. With shielding and electronics these are definitely state-of-the-art systems.

Analysis

Most radioactivity studies are done with very small, moderately active samples placed 10-25 cm from the detector. Such a sample is considered to be a point source and the determination of the activity is greatly simplified. However, the LDEF samples are quite large and must be counted in close proximity to the detectors to accurately determine gamma-ray yields. In order

to properly determine the activity, the efficiency of the detector for such an extended source must be determined and the correction for the self attenuation of the source must be made.

Each laboratory is responsible for determining the efficiency of their detectors and correcting for the self attenuation. The unique experimental arrangements of each laboratory prevent outside determination of these factors. However, to facilitate such corrections 2" x 2" mixed gamma-ray sources have been made by Charles Frederick of TVA and MSFC has prepared a stack of 2" x 2" stainless steel absorbers. These have been distributed to the counting laboratories to establish common reference data.

Figure 1 shows the efficiency of the HPGe detector at SSL/MSFC along with the fit found using an appropriate energy-dependent function:

$$\ln \varepsilon = a/E\gamma + b + c\,(\ln E\gamma) + d(\ln E\gamma)^2 + e(\ln E\gamma)^3.$$

Figure 3 of reference 6 shows similar efficiencies for the Los Alamos detectors at several different distances made with one of the 2" x 2" sources. These curves are typical of those obtained for HPGe detectors.

Since the absolute efficiency of these detectors decreases with distance between source and detector and with the increase of material between them, the absolute gamma-ray activities required a correction to the measured gamma-ray rate. Various laboratories have developed their own correction for efficiency and self attenuation. Bill Winn[6] has done a careful study of his systems and has developed an excellent model for these corrections. A similar model made for the MSFC detector has been incorporated into the inverse-square, self-absorption program EFFATN. This program was originally developed to correct spectra obtained from intentional samples activated with 200 MeV neutrons.[5] Figure 2(ref. 5) gives the activity of the 122 keV gamma rays from ^{57}Co taken through increasing thickness of stainless steel. The solid line is the predicted activity including inverse-square and self-absorption attenuation of this gamma ray. The plot was made using the average of the corrected activity through each absorber thickness. The "poor" fit at zero thickness may be due to incomplete correction for gamma-ray summing into the continuum. Such studies (results) indicate that these corrections can be accurately determined.

Table C-1.c of reference 7 from SRL shows an example of the exchange of samples. Consistent with the sharing of calibration sources and the exchange of samples is the goal of assuring that the results from the various counting laboratories are consistent. To date the data from the laboratories have been

very consistent. A few comparisons currently being studied are shown in figures 3-6. Alan Harmon will present additional results in the next paper.

To date, a large set of resultant specific activities have been reported. Primarily, these have been from SRL, LLNL and LANL. They have been compiled to a spreadsheet and are currently being reviewed. They are being correlated with the position on LDEF so that the effects of the surrounding material may be determined. The shielding provided by the covering material, the moderation of thermal neutrons and the production of secondary particles will be studied in relation to sample specific activity.

The specific activity of each LDEF sample depends on the flux of activating particles, on the half-life of the decaying nuclei, and on the production cross section for the particular nuclei. The sample activities, therefore, will be significantly different from those originally estimated. The most significant reason for this is the rapid lowering of the LDEF orbit in the last two years and the transition from a period of minimum solar activity to one of maximum solar activity. Figure 7 shows the trapped proton flux at a proton energy of 50 MeV for various times in the LDEF-1 mission.[8] Figure 8 shows the projected activation rate for ^{54}Mn for the same time period. Obviously, short-lived radioisotopes will significantly decay in the last few months in the orbit. A careful prediction of the activation taking into account these reduced fluxes must be made for activation comparisons.

Archival

As the counting of the samples is nearing completion, we are planning the archival of the specific activities and the spectra obtained at the counting laboratories. To be stored with the spectra is a directory containing the specific details of the activation study. These include sample material, shape, dimensions, mass, and location on the spacecraft as well as detector efficiencies, energy calibrations, and self-attenuation corrections.

Perhaps as many as 1000 spectra will be available for future review. The spectra in the original binary format will be stored on a convenient magnetic media in a specified computer center. A catalog will specify the data acquisition system(ADCAM, ND66, Canberra 100, etc.) and will give the data format. Programs to change from one format to another will be available as well as general procedures to change to other formats. Figure 9 shows a sample spectrum from SRL which has been changed from the original ADCAM

format to that for a Tennelec/Nucleus PCA-II system. Automatically analyzed peaks are indicated in the figures.

In addition, the spectra will be translated to a text format. Table 2 is a tentative sample of such a file from the SRL spectra. Included in the file is a channel number indicator in column 1 and a header giving the name of the original file and other pertinent details from the header of the spectrum file. Other data will be available in the overall directory.

Hopefully, if we can obtain the spectra and analysis from the counting laboratories in this calendar year(1992), then the archived spectra will be available during calendar year1993 for outside users. Then, scientists and engineers needing information concerning activation of spacecraft material in low-earth orbit will have a source of data that can greatly aid them in their individual projects.

REFERENCES

1. Harmon, B. A., Fishman, G. J., Parnell, T. A., and Laird, C. E. : Induced Radioactivity in LDEF Components, p. 301-311, part 1, First Post-Retrieval Symposium(1991).

2. Michel, R., Peiffer, F., and Stuck, R.: Nucl. Phys. A**441**, 617(1985): and references therein.

3. Laird, C. E.: Study of Proton and Neutron Activation of Metal Samples in Low-Earth Orbit, July, 1985, Final Technical Report, NASA Contract NAS8-35180.

4. ACTL82- a compilation of proton and neutron activation cross sections, Brookhaven National Laboratory(1982).

5. Laird, C. E.: Study of Activation of Metal Samples from LDEF-1 and Spacelab-2, July, 1991, Final Technical Report, NASA Contract NAS8-36649.

6. Winn, W. G.: Gamma-Ray Spectroscopy of LDEF Samples, USDOE SRS Report WSRC-RD-91-16 (February 19,1992).

7. Moss, C. E., and Reedy, R. C.:Measurements of Induced Radioactivity in some LDEF Samples, p. 271-285, part 1, First Post-Retrieval Symposium(1991) .

8. Watts, J. W., Jr.: Predictions of LDEF Fluxes and Dose Due to Geometrically Trapped Protons and Electrons, Nucl. Tracks Radiat. Meas. **20**, 85(1990).

Table 1. Counting Facilities
and Associated Scientists

Dr. Gerald Fishman
Dr. B. Alan Harmon
NASA/Marshall Space Flight Center(NASA/MSFC)

Dr. Ronald L. Brodzinski
Dr. James Reeves
Pacific Northwest Laboratory(PNWL)
Batelle Memorial Institute

Dr. Alan R. Smith
Donna L. Hurley
Lawrence Berkeley Laboratory(LBL)

Dr. Calvin E. Moss
Dr. Robert C. Reedy
Los Alamos National Laboratory(LANL)

Dr. David C. Camp
Lawrence Livermore National Laboratory(LLNL)

Mr. Charles Frederick
Tennessee Valley Authority(TVA)
Western Area Radiological Laboratory

Dr. David J. Lindstrom
NASA/Johnson Space Center(JSC)

Dr. Bill Winn
Westinghouse Corporation
Savannah River Laboratory(SRL)

Table 2. Sample Text File for Archived Gamma Ray Spectra

SPECTRUM FILE:1791NASA.PCA
SAMPLE COMPOSITION:ALUMINUM
START DATE:JAN 16, 1991
START TIME:10:23:00 am
REAL/CLOCK TIME: 254700 seconds
ELAPSED/LIVE TIME: 231216 seconds

CHANNEL	COUNTS							
1	0	0	0	0	0	0	0	0
9	0	0	0	0	0	0	0	0
17	0	0	0	0	0	0	0	21
25	133	141	136	132	136	122	131	127
33	145	132	125	121	117	146	103	117
41	104	100	98	114	102	95	116	127
49	138	118	123	117	122	99	109	106
57	105	104	106	98	115	117	96	108
65	103	99	101	119	87	91	89	97
73	105	107	102	102	90	90	90	81
81	114	94	100	103	87	103	101	122
89	109	106	90	96	101	123	102	79
97	88	93	84	95	92	93	87	76
105	115	88	92	123	112	88	106	94
113	112	88	91	103	99	91	112	105
121	107	93	109	95	105	113	164	207
129	195	149	82	90	100	98	88	99
137	116	102	101	120	124	97	101	102
145	122	101	127	126	106	125	164	190
153	136	113	139	170	155	133	100	130
161	112	107	102	112	113	108	114	127
169	137	138	186	165	160	123	125	148
177	178	136	125	127	131	124	111	119
185	122	215	374	369	245	153	121	107
193	98	113	108	108	98	107	122	118
201	126	96	110	109	110	113	131	91
209	123	105	115	120	117	123	119	111
217	114	115	107	117	119	132	115	130
225	133	124	130	142	121	135	124	107
233	110	130	125	120	108	119	116	121
241	112	131	121	134	132	108	124	134
249	128	116	113	131	123	133	129	136
257	153	118	139	125	126	144	133	107
265	132	136	140	123	126	131	129	130
273	121	140	123	149	133	136	140	122
281	121	137	152	138	137	166	106	148
289	139	166	184	189	160	140	133	152
297	135	156	154	125	144	141	128	136
305	136	143	131	152	148	124	179	158
313	164	138	154	161	159	153	126	139
321	146	146	161	154	137	167	139	138
329	155	134	186	172	177	143	168	162
337	148	148	134	172	147	178	158	157

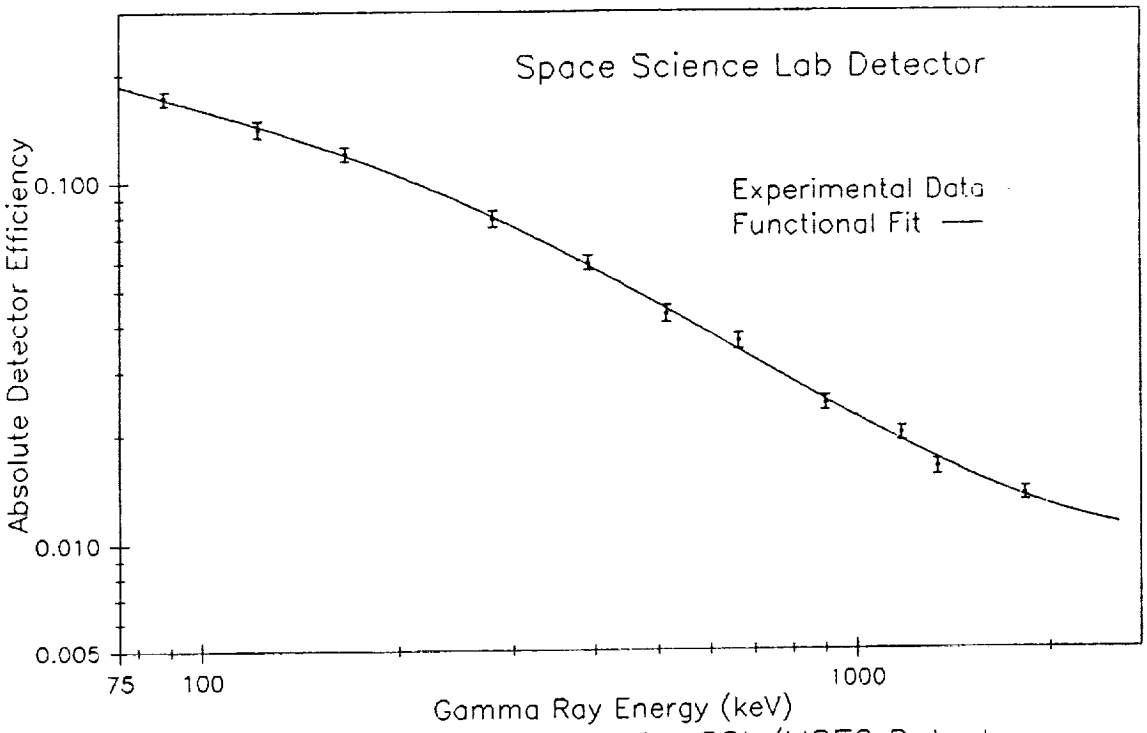

Figure 1. Efficiency Curve for SSL/MSFC Detector

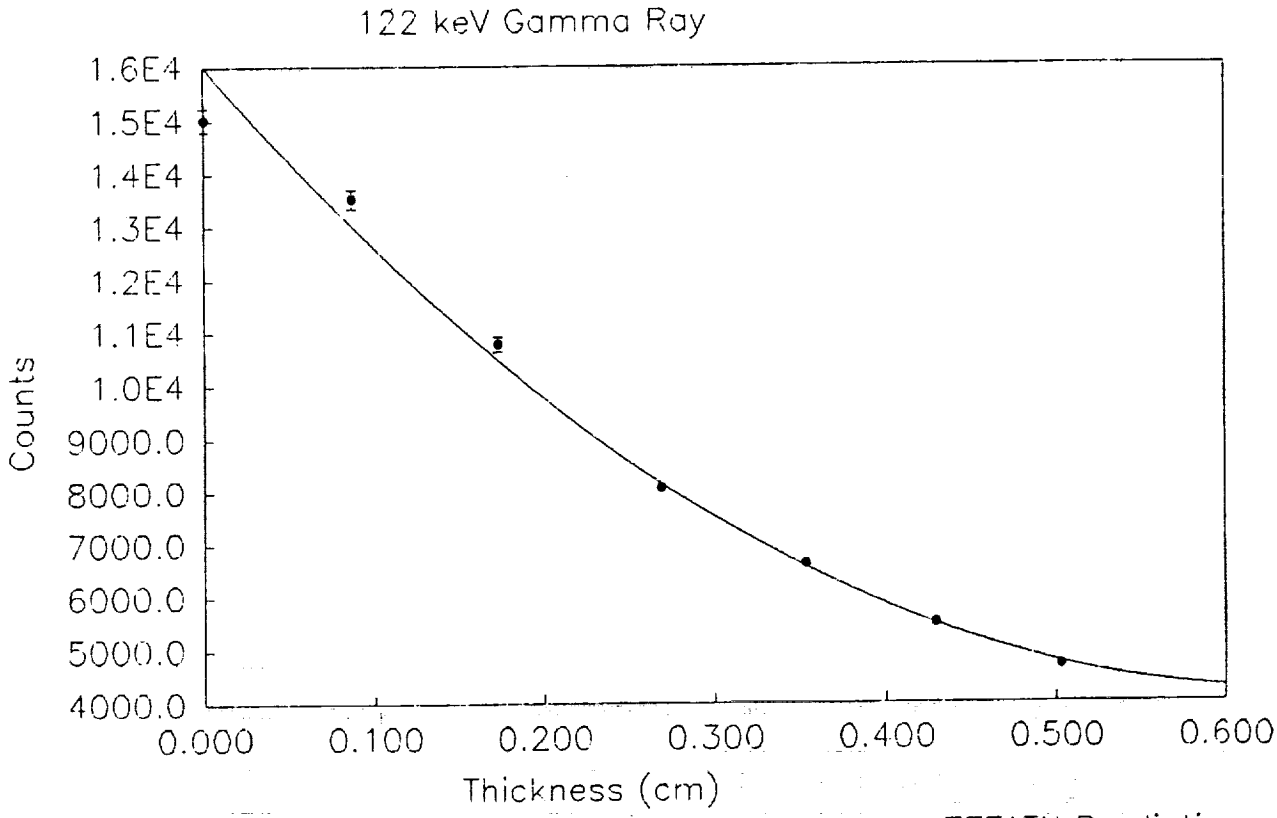

Figure 2. Yield of 122 keV Gamma Ray vs. EFFATN Prediction

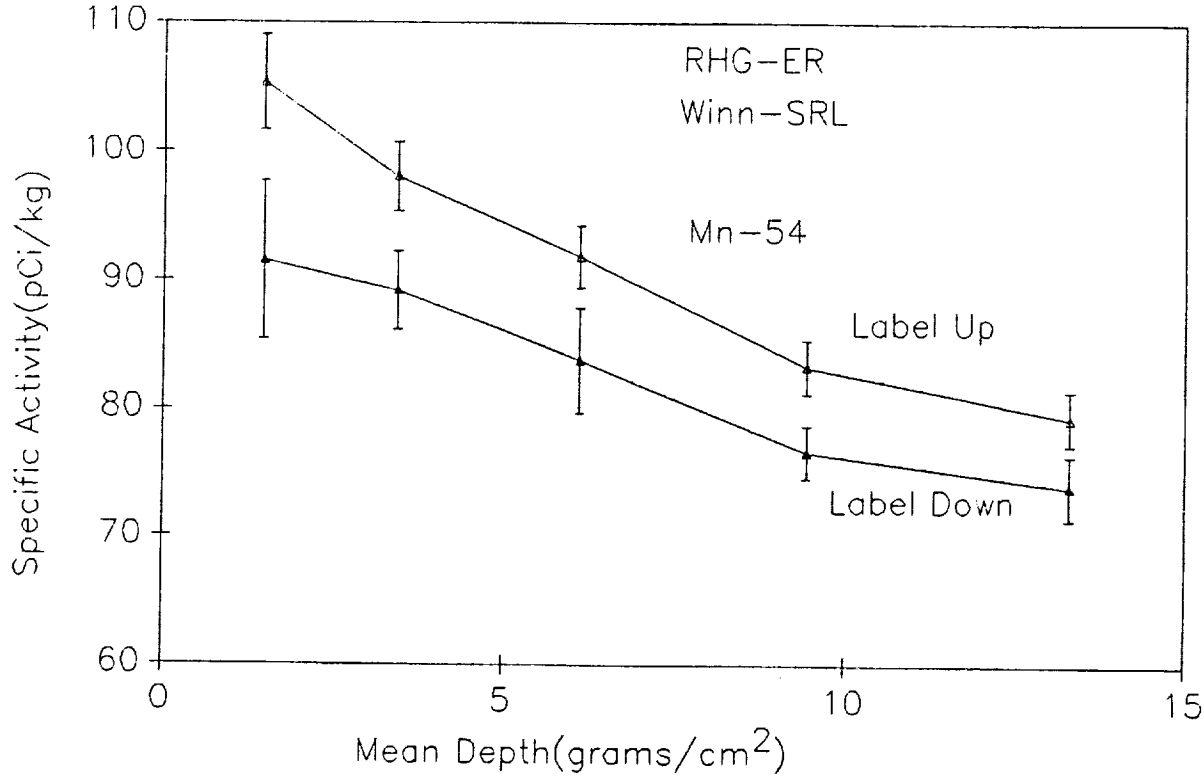

Figure 3. RHG Trunnion Layers(Earth End) Counted Face Up and Face Down.

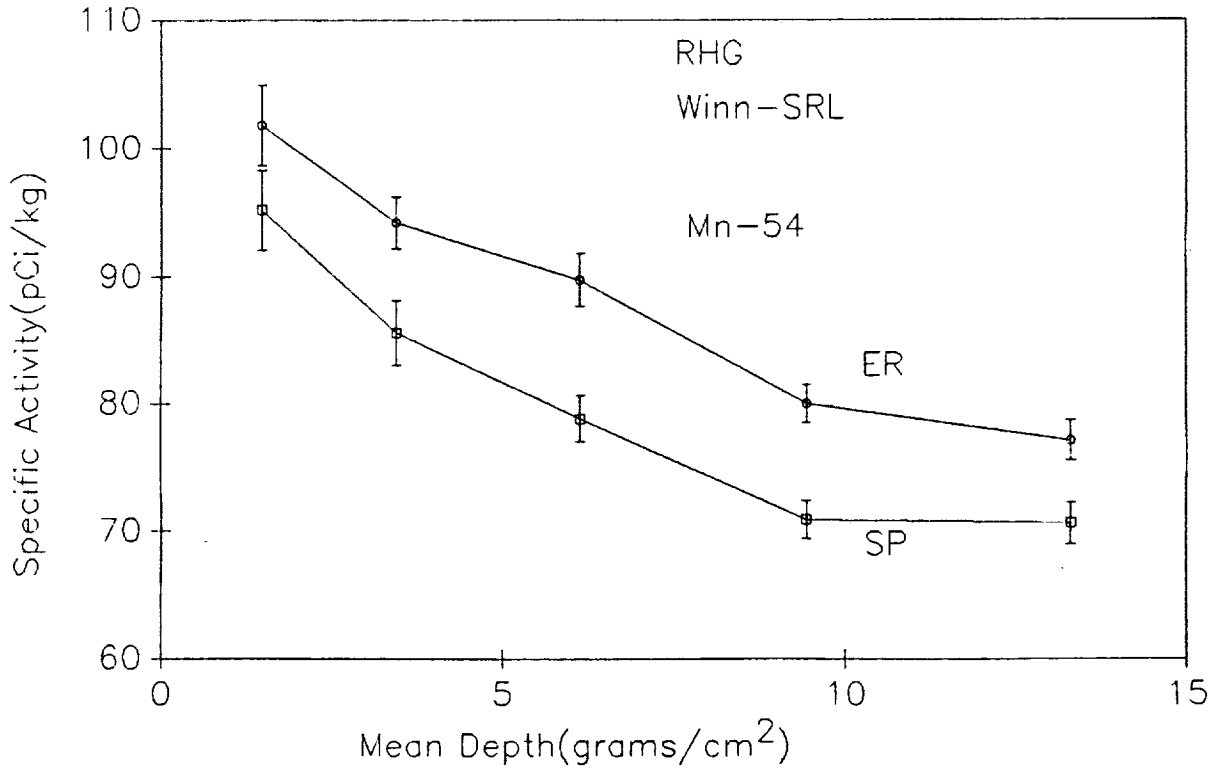

Figure 4. RHG Trunnion Layers: ER-Earth: SP-Space

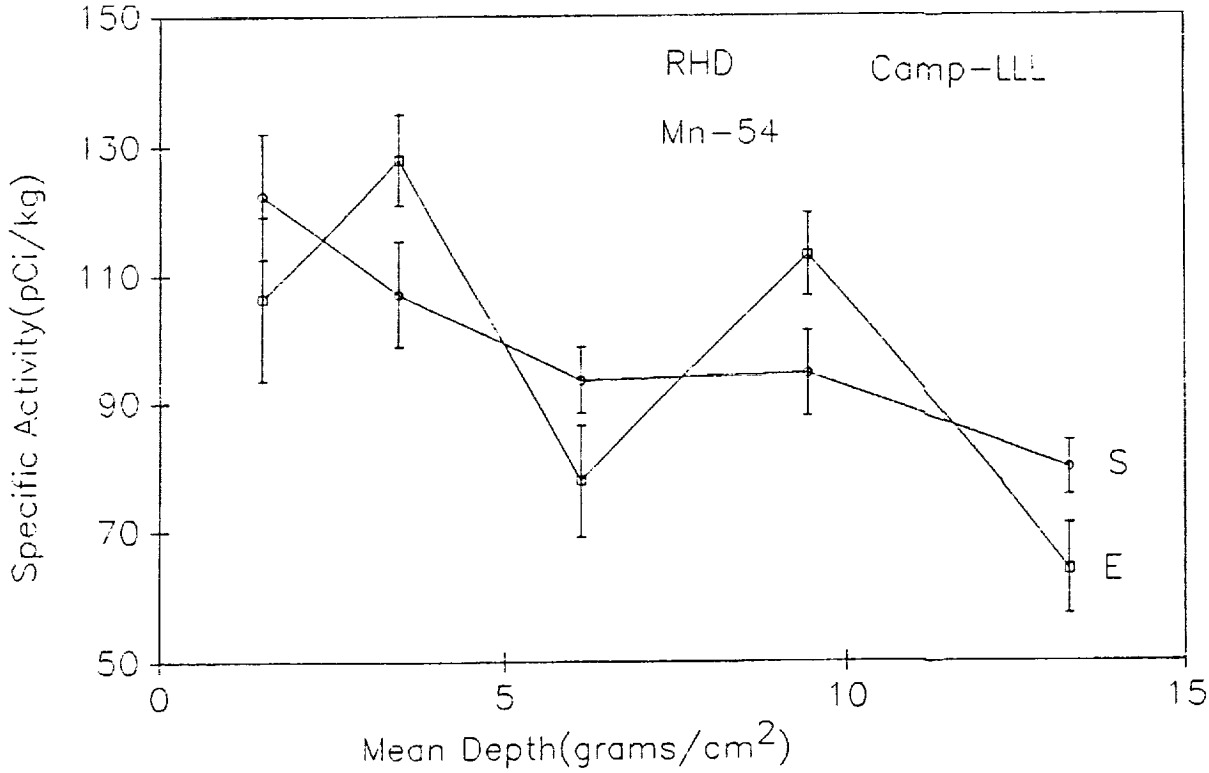

Figure 5. RHD Trunnion Layers: S-Space: E-Earth

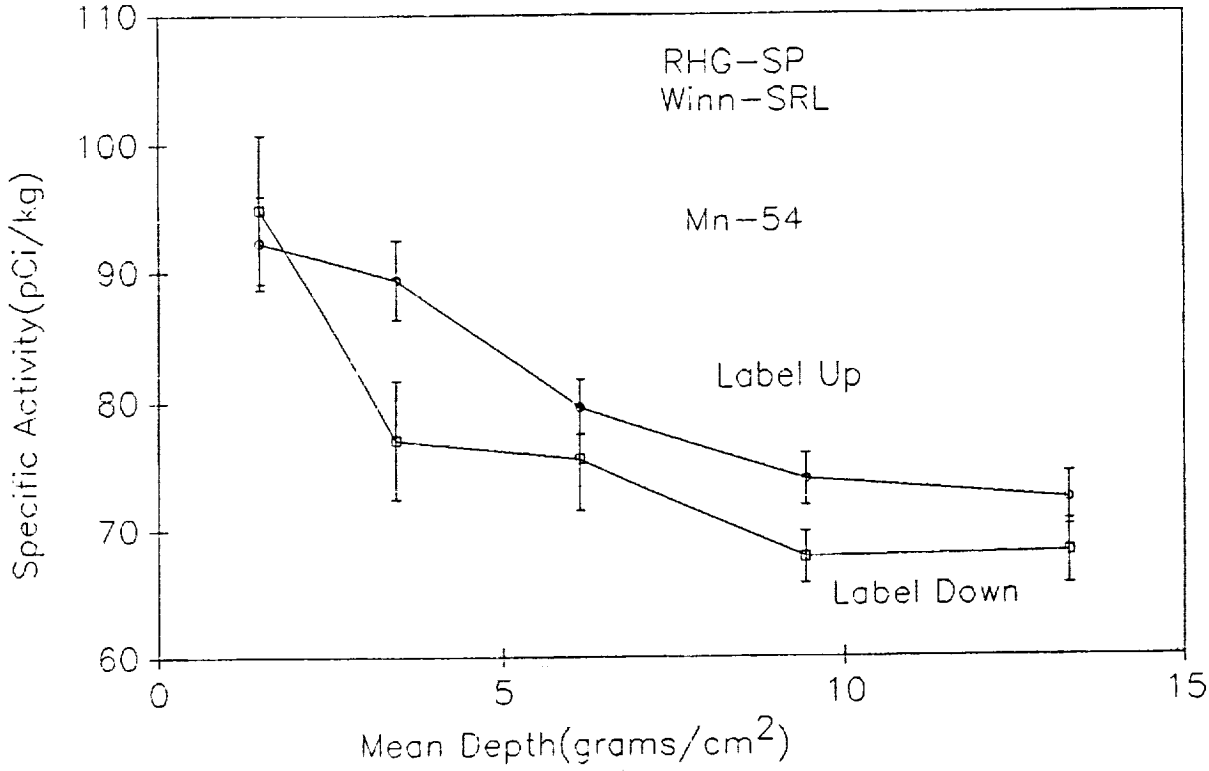

Figure 6. RHG Trunnion Layers-Space End.

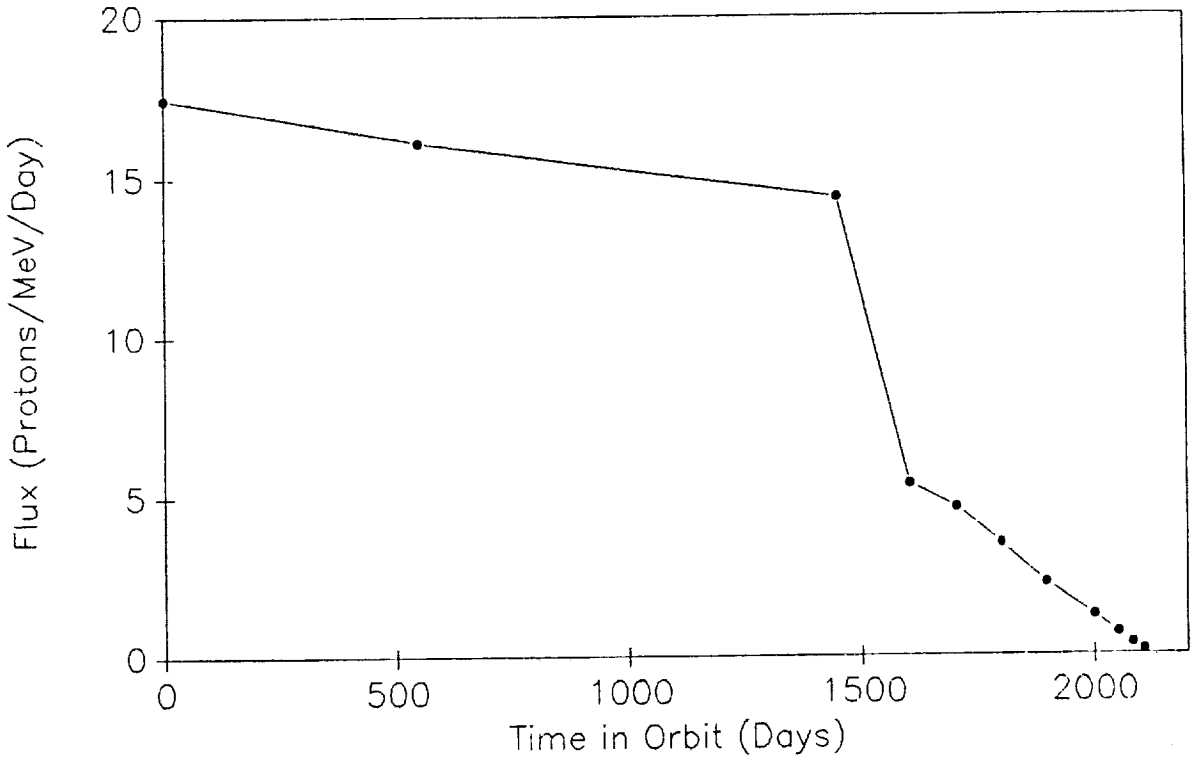

Figure 7. Proton Flux at 50 MeV as a Function of Time in Orbit

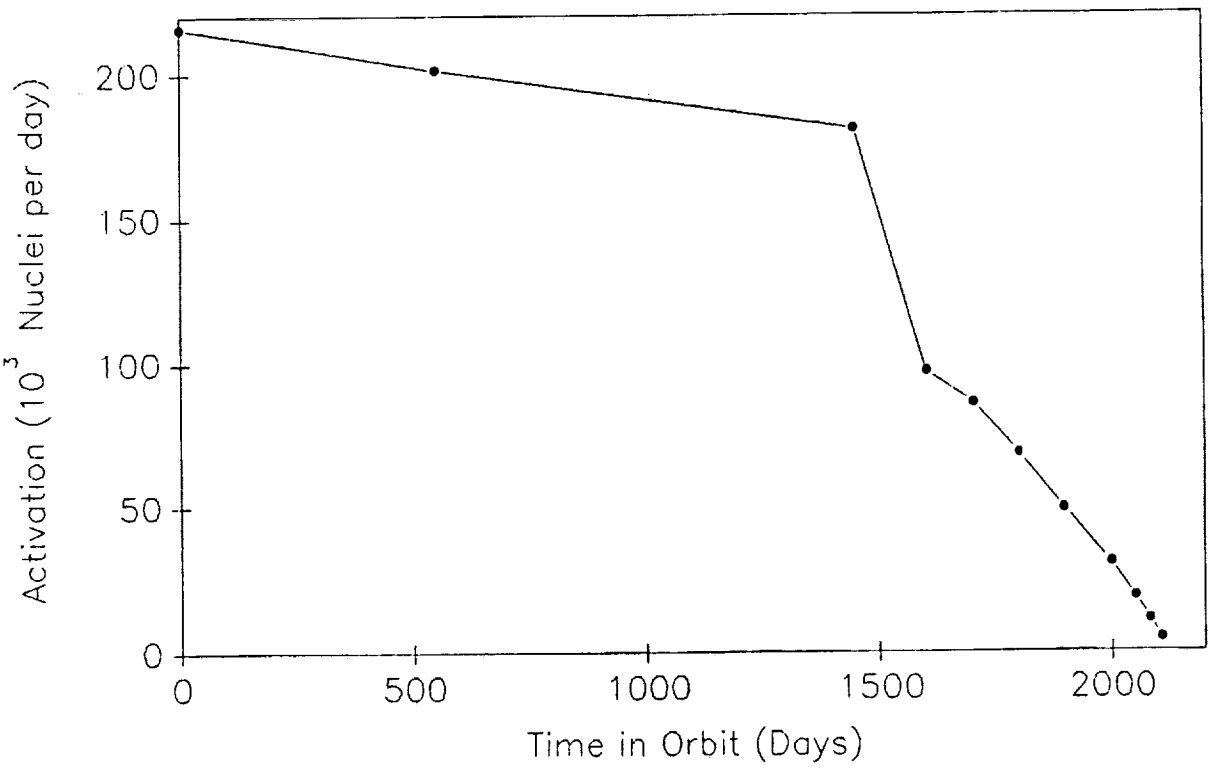

Figure 8. Production of Mn−54 as a Function of Time in Orbit

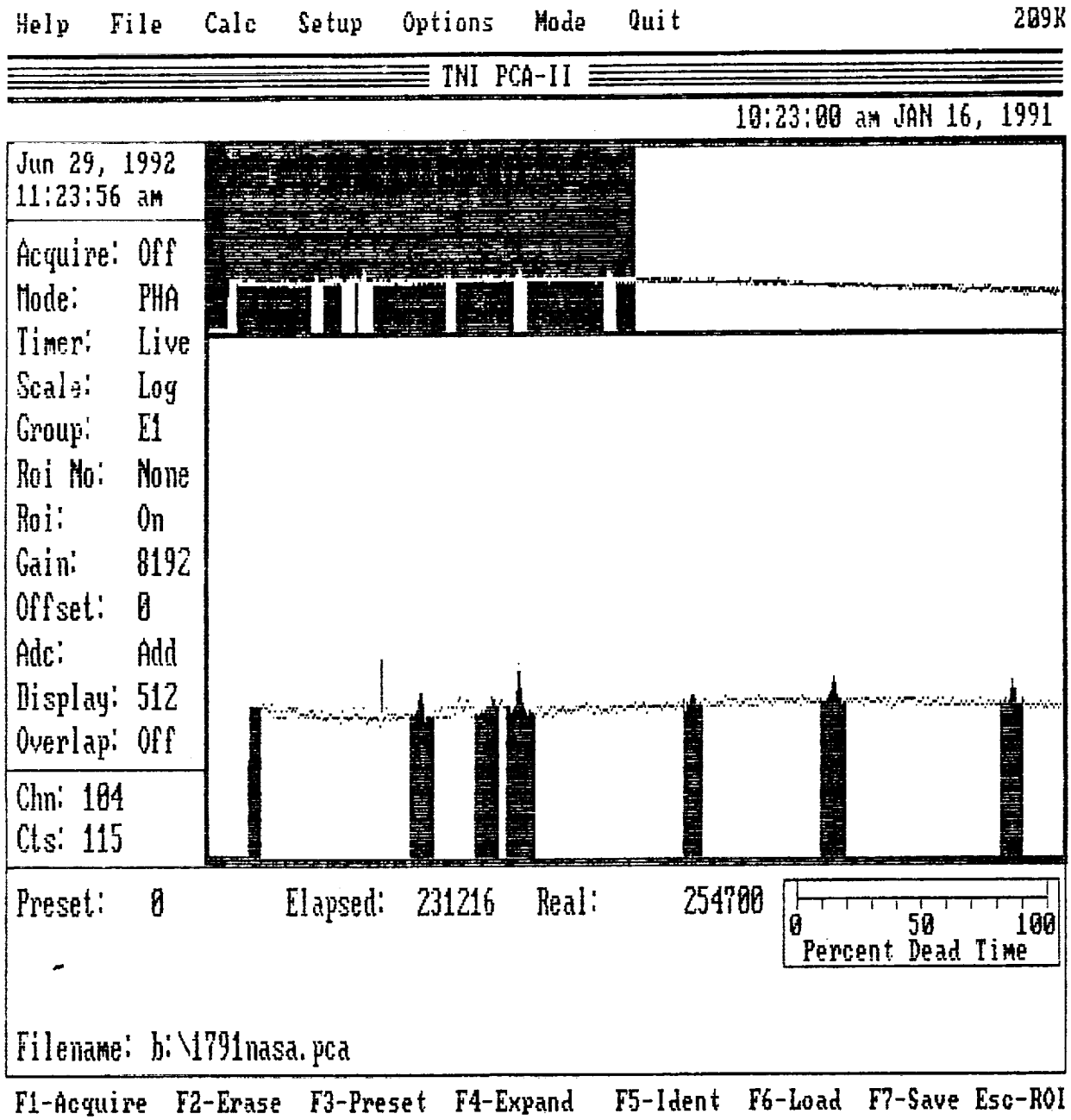

Figure 9. Sample of SRL Spectra converted to PCA-II Format.

INDUCED ACTIVATION STUDY OF LDEF

B. A. Harmon, G. J. Fishman, and T. A. Parnell
ES62 NASA/Marshall Space Flight Center
Huntsville, AL 35812
Phone: 205/544-4924, Fax: 205/544-7754

C. E. Laird
Department of Physics, Eastern Kentucky University
Richmond, KY 40475
Phone: 606/622-1526, Fax: 606/622-1020

SUMMARY

Analysis of the induced radioactivity of the Long Duration Exposure Facility (LDEF) is continuing with extraction of specific activities for various spacecraft materials. Data and results of activation measurements from eight facilities are being collected for interpretation at Eastern Kentucky University and NASA/Marshall Space Flight Center.

The major activation mechanism in LDEF components is the proton flux in the South Atlantic Anomaly (SAA). This flux is highly anisotropic, and could be sampled by taking advantage of the gravity-gradient stabilization of the LDEF. The directionally-dependent activation due to these protons has clearly been observed in the data from aluminum experiment tray clamps (reaction product ^{22}Na), steel trunnions (reaction product ^{54}Mn and others) and is also indicated by the presence of a variety of nuclides in other materials. A secondary production mechanism, thermal neutron capture, has been observed in cobalt, indium, and tantalum, which are known to have large capture cross sections. Experiments containing samples of these metals and significant amounts of thermalizing low atomic number (Z) material showed clear evidence of enhanced activation of ^{60}Co, ^{114m}In and ^{182}Ta. Other mechanisms which activate spacecraft material that are not as easily separable from SAA proton activation, such as galactic proton bombardment and secondary production by fast neutrons, are being investigated by comparison to radiation environmental calculations (Armstrong and Colborn, 1991, 1993). Deviations from one-dimensional radiation models indicate that these mechanisms are more important at greater shielding depths.

In this paper, we review the current status of the induced radioactivity measurements as of mid-year 1992. We present specific activities for a number of materials which show SAA effects and thermal neutron capture. We also examine the results for consistency by combining data from the participating institutions.

INTRODUCTION

In the First Post-Retrieval LDEF Symposium (Harmon, et al., 1991a), we discussed some of the major constituents of the space radiation environment which contributed to the activation of LDEF, and detailed a few of the measurements which illustrated their effects. A number of results were also presented by Smith and Hurley (1991), Moss and Reedy, and Winn from measurements made as a part of the cooperative effort to study the induced radioactivity of LDEF (Harmon, et al., 1991a,b). Further work by Smith and Hurley (1993), Reeves, et al., and Reedy, et al., can be found in these conference proceedings. Eight laboratories with low-level background detectors for gamma ray counting participated in a large scale study of LDEF radioactivity: Westinghouse/Savannah River Site (SRS), Pacific Northwest Laboratory/Battelle Memorial Institute (PNL), the Tennessee Valley Authority Western Area Radiological Laboratory (TVA), Lawrence Livermore National Laboratory (LLNL), Lawrence Berkeley Laboratory (LBL), Los Alamos National Laboratory (LANL), NASA/Johnson Space Center (JSC) and NASA/Marshall

Space Flight Center (MSFC). All received samples of spacecraft material following retrieval of LDEF in January 1990. Our efforts over the past year have been in collecting the results of induced radioactivity measurements from these laboratories, evaluating these results for consistency and quality, and extracting information about the radiation environment. Eventually all measurements will become part of a LDEF radiation database following evaluation. NASA/Marshall Space Flight Center and Eastern Kentucky University are primarily involved in a collaborative effort to produce this database and support a long-term archive. (Details can be found in the contribution by Laird, et al.) In this report, we attempt to bring together results from different laboratories and examine them in a coherent fashion. The data presented are, unavoidably, in various stages of completeness. While the measurement techniques are straightforward, extracting specific activities can be difficult for unusual sample geometries or samples which significantly attenuate the gamma rays of interest. In some cases, for identical geometries, different methods have been used to obtain the detector efficiency. (The efficiency relates the observed gamma-ray counting rate to the activity of the sample.) This can induce systematic uncertainties in the measured activity which can be larger than the statistical counting errors. We find systematic differences as large as 30% in some of the results reported here. We present these results with the caution that comparisons between measurements at different laboratories be regarded as preliminary until the evaluation is complete.

Materials obtained from LDEF in the months following retrieval are listed in Table I below. A detailed plan for analysis of these materials can be found in Harmon, et al., 1993. Further information and early results of the induced radioactivity investigations can be found in Harmon, et al., 1991b.

Table I. Analyzed Spacecraft Components

Aluminum	Experiment tray clamps and spacer plates, clamp assemblies, end support retainer plate, keel plate, scuff plate spacers, ballast covers, and end frame clamps
Titanium	Structural clips
Steel	End frame trunnions, tray clamp screws, and P0004/P0006 canister screws
Lead	Ballast plates
Other Samples	Vanadium, Nickel, Cobalt, Tantalum, and Indium (Exps. M0001, M0002, P0006, and A0114) Magnesium, Silver, Copper, Niobium, Molybdenum and Germanium (Exps. A0114 and A0171)

ALUMINUM

Many aluminum components (6061 alloy) at various shielding thicknesses were available from the spacecraft (see Table I). The most significant result from these was the mapping of the ^{22}Na activity (half-life 2.6 years, 511 and 1275 keV gamma rays) around the spacecraft using the experiment tray clamp plates (East, West, North and South directions) (Harmon, et al., 1991a,b). The activation was clearly peaked in the West direction, offset to the South, consistent with the expected angular distribution of the SAA proton flux (Watts, et al.). In order to obtain these results, about 50 clamp plates were counted at the Tennessee Valley Authority (TVA) Western

Area Radiological Laboratory. Several clamp plates have been counted at other laboratories to verify the extraction of the activities. In Table II, we present recent measurements from Winn (private comm.) at SRS and activities for the same clamp plates counted earlier by Frederick (private comm.) at TVA. All measurements presented have been decay-corrected to the date of LDEF return to Earth (January 20, 1990). Even though we are limited to only a common sample of six plates, comparison of these results shows that the trends are reasonably consistent between the two datasets. The computed differences between measurements also appear consistent with statistical error.

Table II. Comparison of Experiment Tray Clamp ^{22}Na Activities

Sample ID	Activity (SRS) (dis/sec/kg)	Activity (TVA) (dis/sec/kg)	Difference (dis/sec/kg)
B7-5	$4.61 \pm .19$	$4.46 \pm .38$	$-.15 \pm .42$
D7-2	$5.17 \pm .18$	$5.83 \pm .38$	$+.66 \pm .42$
G6-4	$5.34 \pm .22$	$6.26 \pm .81$	$+.92 \pm .84$
G6-10	$3.55 \pm .18$	$3.29 \pm .56$	$-.26 \pm .59$
H6-4	$4.80 \pm .20$	$4.55 \pm .64$	$-.25 \pm .67$
H9-12	$4.63 \pm .16$	$4.76 \pm .81$	$+.13 \pm .82$

Winn obtains the efficiency for thin samples such as the clamp plates via a model where the efficiency is separable into two factors for the area and thickness of the sample. Point-like calibration sources and aluminum attenuator blanks are used to map out the areal and depth dependences of the efficiency over a range of gamma-ray energies. Using parameters derived from the calibration, the total peak efficiency is calculated by integrating the model expression. In addition, because the measurements were made with a high efficiency 90% germanium detector, a summing correction is also required to the peak efficiency for ^{22}Na. This is due to mutiple emission of 511 keV (positron annihilation) and 1275 keV gamma radiation when ^{22}Na decays. The summing correction to the 1275 peak efficiency was measured to be 1.72 for the 90% detector (Winn, private comm.). Frederick at TVA (private comm.) used a mixed gamma source of the same area as the clamp plate (2" x 5") which eliminates the need for an area integral. The efficiency is then computed as a direct average of measurements of the calibration source placed in the front and back of the clamp plate. The lower efficiency germanium detectors at TVA (15%-30%) have a negligible summing correction for ^{22}Na. Mathematically, the only difference between the methods used by SRS and TVA is the treatment of the self-attenuation of the sample as an exponential in relating the "front" and "back" efficiency of the sample by Winn. This is critical for thick samples (see trunnion section studies below), but does not yield significantly different results from direct averaging for the thin clamp plates.

The experiment tray spacer plates, which were mounted beneath the clamp plates, also showed detectable ^{22}Na, mostly on the West side of the LDEF. These results have not been systematically analyzed, but show activities of 2-3 dis/sec/kg.

The keel plate (row 6, North side of LDEF) and the end support retainer plate (Earth end of LDEF) were both cut into samples roughly of 2"x2" area and individually counted at different laboratories. A composite representation of the ^{22}Na activities from LBL (Smith and Hurley, 1991), LANL (Moss and Reedy), and SRS (Winn) measurements is shown in Fig. 1. The keel plate was exposed to the westerly-peaked SAA flux and shows a correspondingly higher activity

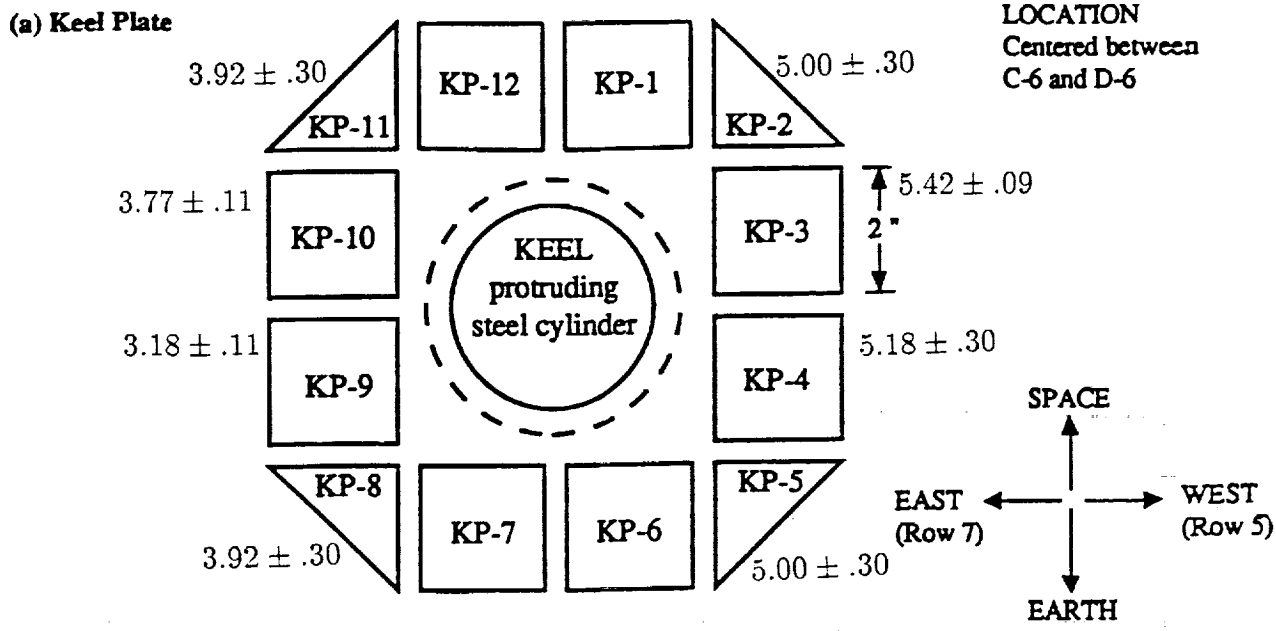

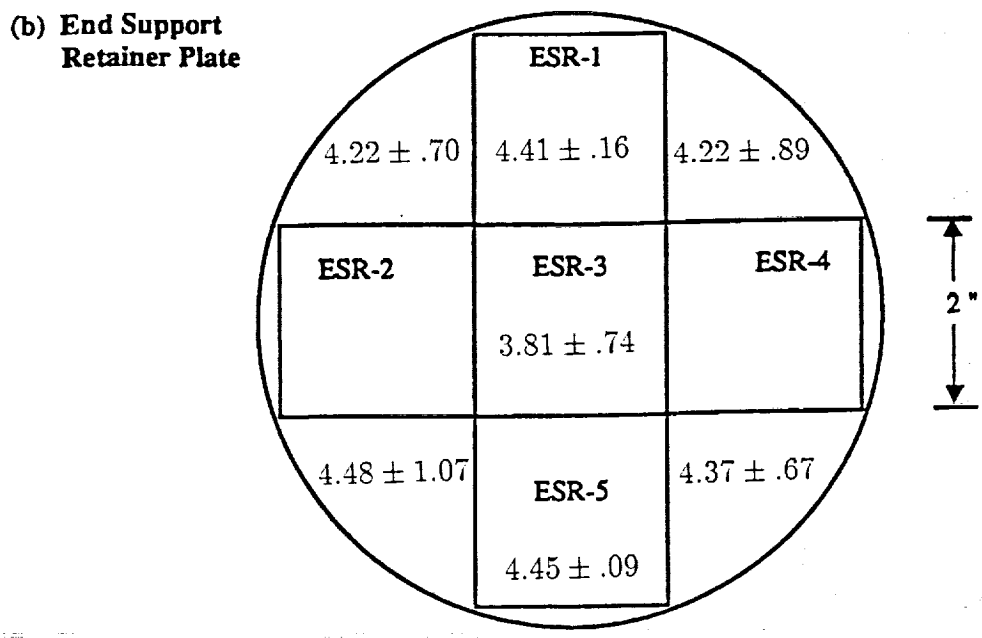

Figure 1. (a) Aluminum keel plate and (b) end support retainer plate showing the pattern in which samples were cut for activation analysis. ^{22}Na activities (dis/sec/kg) are shown for each sample. Activities for samples KP-1, 6, 7, and 12 and ESR-2 and 4 have not been reported.

in KP-2, 3, 4 and 5 (KP-2 and KP-5 were counted together) than KP-8, 9, 10, 11 (KP-8 and KP-11 were counted together). The retainer plate, which saw flux mainly from the Earth direction, has a much more uniform activation. The activity of the end support retainer plate should be compared to the earth end clamp plate data for G6-4 and G6-10 listed in Table II above.

The clamp assemblies, located behind the main (central) trunnion scuff plates, were the thickest samples of aluminum obtained from LDEF. These were large annular rings surrounding the main trunnions, which were cut and analyzed for directional and depth dependences, similar to the steel trunnions (see below). Some of the results for clamp assembly layers are given by Reeves and Frederick (private comm.); however, most of the measurements have not been reported. The scuff plate spacers and end frame clamps have also been counted; however, their geometry is too complex to extract specific activities easily. Both materials contained ^{22}Na and ^{7}Be activity. The ballast plate covers were rectangular plates mounted over the lead ballast on each end of LDEF. Some of the cover material was processed into normalizable 2"x2" squares and analyzed, but no activities have been reported.

TITANIUM

A number of titanium structural clips (6AL-4V alloy) were obtained from the internal frame of LDEF. The clips were mounted beneath the end intercostals, joining the intercostals to the longerons. Several groups Smith and Hurley (1991), Moss and Reedy, and Harmon report ^{46}Sc and ^{22}Na to be present in these samples. Obtaining specific activities are possible and appear to be in the range of 0.1-1 dis/sec/kg for ^{22}Na (Smith and Hurley, 1991) and about 0.5-1.5 dis/sec/kg for ^{46}Sc. The activation for ^{22}Na is considerably lower than that of the aluminum components, and is related to the heavier target (^{48}Ti, 73.7% natural abundance) and also the increased local shielding from the LDEF structure. The geometry of these samples (slanted parallelopiped cross section) will limit the accuracy of these measurements; nevertheless, these data are unique because of the atomic number Z being fairly well-removed from other analyzed materials (Z=13, 22 and 26 respectively for aluminum, titanium, and iron).

STEEL

^{54}Mn (half-life 312 days, 834 keV gamma ray) was expected to have the highest activity level in the steel trunnions (17-4PH alloy) based on the average energy of the trapped proton flux as well as the cross section for protons on iron (75% of 17-4PH). With an activity of 2-5 dis/sec/kg, it was possible to process the 20 in (50.8 cm) long by 3.25 in (8.26 cm) diameter cylinder into smaller cylindrical sections and concentric layers so that the ^{54}Mn activity could be mapped throughout the trunnion volume (Harmon, et al. 1991a,b). Directional and energy information about the activating particle fluxes could then be obtained. Figure 2 is a plot of the bulk ^{54}Mn activity in the two stainless steel trunnions from the Earth end of LDEF. The abscissa represents the distance along the trunnion axis measured from the end of the trunnion farthest from the spacecraft. Each point represents the average activity for one of the large cylindrical sections (3.25 in dia, from 0.5 to 1 in thickness). The space-exposed end of the "LH" trunnion was pointed West and offset to the North by the reported 8 degree yaw (Peters and Gregory), such that the axis of the trunnion was at an approximately 30 degree angle to the peak of the South Atlantic Anomaly proton flux angular distribution.

As indicated in Fig. 2, several counting groups have analyzed the large cylindrical sections. These have a large self-attenuation of 834 keV gamma rays (as much as 50%) which must be accurately assessed in order to extract a reliable specific activity. This becomes even more of a problem for ^{57}Co (122 keV) or ^{51}Cr (320 keV) activities, because of the rapid increase in attenuation for lower energy gamma rays. Winn has discussed in detail the required procedures for obtaining specific activities from these samples using point-like calibration sources. Frederick (private comm.), Lindstrom (private comm.), and Harmon have used a mixed gamma (planar)

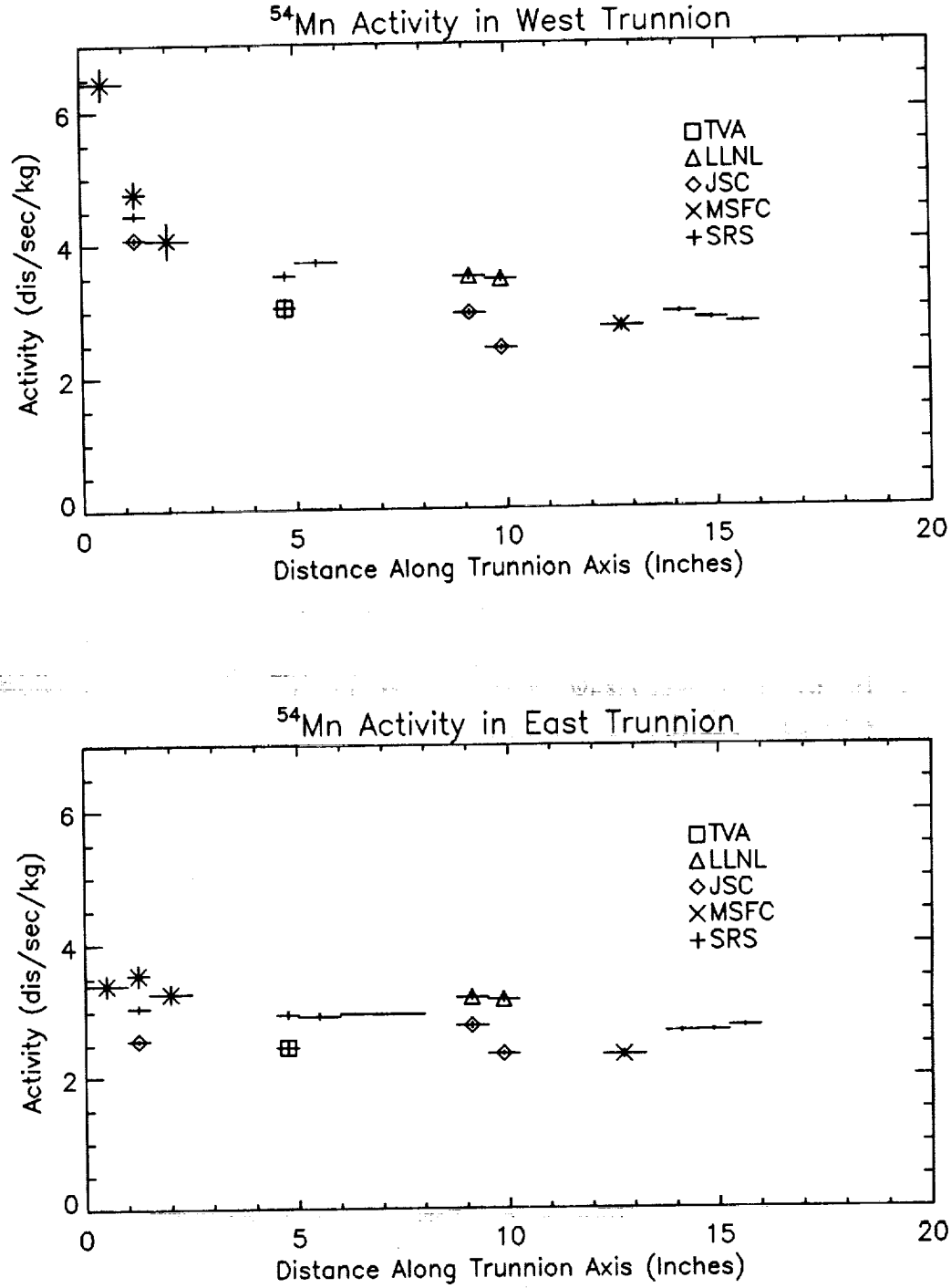

Figure 2. ^{54}Mn activities in the end frame steel trunnion as a function of distance along the trunnion center line. The origin of the horizontal axis represents the end of the trunnion farthest from the spacecraft.

grid source of the same diameter as the trunnion, which appears to give results comparable to the point source mapping technique. However, while the statistical error for several day counts of the large trunnion pieces is small as shown in Fig. 2, systematic differences in the activity at the 20-30% level are evidently present based on several measurements of the same sample (see activities measured at approximately 1, 5, 9 and 10 in in both East (RH) and West (LH) trunnions). The systematic differences also tend to be consistent between datasets. Both trunnions indicate a decreasing activity toward the spacecraft, with the SAA flux out of the West enhancing the activity considerably in the first two inches of the West trunnion. SAA protons are not energetic enough to penetrate the entire length of the trunnion and would not explain the more gradual decrease, which may be due to shielding from the spacecraft.

Three of the cylindrical sections from each of the two end trunnions were sliced into thin concentric layers about the trunnion axis, then quartered with a set of seven layers facing toward Earth, Space, North and South. The thinness and uniformity of the steel layer samples, coupled with the distribution of 2" x 2" mixed gamma standards to several of the counting laboratories, have made it much easier to extract activities from the layer samples than for the thick cylindrical sections discussed above. Results from each of the laboratories so far indicate reasonably consistent agreement with the trends and absolute magnitude of the activities as a function of direction and depth. Figure 3 shows the ^{54}Mn activity in trunnion layers from the LH (West) trunnion at a distance of approximately 7 inches from the end of the trunnion. These represent the most sensitive measurements to date of the steel layers. The observed differences in the North, South, Space and Earth directions are qualitatively similar to that in Harmon, et al., 1991b, where another layered section closer to the spaceward end of the trunnion was analyzed. The higher sensitivity measurements indicate a very significant difference in flux between North and South. The SAA exposure should produce an enhancement to the South (relative to North) due to the southwesterly peak of the proton flux. There is also a smaller Space-Earth asymmetry, which is at least partially attributable to shielding by the spacecraft on the space side of the trunnion (Armstrong and Colborn, 1991).

The only other steel components obtained from the LDEF were canister screws from experiments P0004 and P0006, and a large number of screws associated with the experiment tray clamps. These were generally too small to obtain sufficient statistics from counting of individual screws. Bulk counting by LLNL (Camp, private comm.) showed the presence of ^{54}Mn, ^{56}Co, ^{57}Co, ^{58}Co, ^{22}Na and ^{7}Be (surface deposition) with the ^{54}Mn/^{57}Co ratio being about 1.6-2.0 in the tray clamp screws, and a West/East ratio in the activities of 1.2-1.3. The ^{54}Mn/^{57}Co ratio appears to be quite different from the steel in the trunnions (^{54}Mn/^{57}Co = 8-12). The presence of significant amounts of ^{22}Na, which may be related to low mass impurities, was not expected, and is under investigation. Results for the P0004/P0006 screws have not been reported.

LEAD

Lead, taken from lead sheets used for ballast, was the highest atomic number (Z=82) material obtained for activation measurement. The lead ballast and associated aluminum cover plates were mounted on the end frame I-beams and were obtained several months following retrieval. Only ^{207}Bi at a very low activity has been reported by Smith and Hurley (1993) and Lindstrom (private comm.). No accurate activities have been obtained, but are estimated to be about 10^{-2} - 10^{-1} dis/sec/kg. Measured activities for both the aluminum and lead components are of interest due to the shielding effects from other parts of the spacecraft.

INTENTIONALLY-PLACED SAMPLES

Sets of vanadium, nickel, tantalum, indium, and cobalt metal samples, typically 2"x2" by 0.25" thick, were placed in four experiments (M0001, M0002, P0006 and A0114) on the LDEF. These constituted the original activation sub-experiment by Fishman (Harmon, et al., 1993)

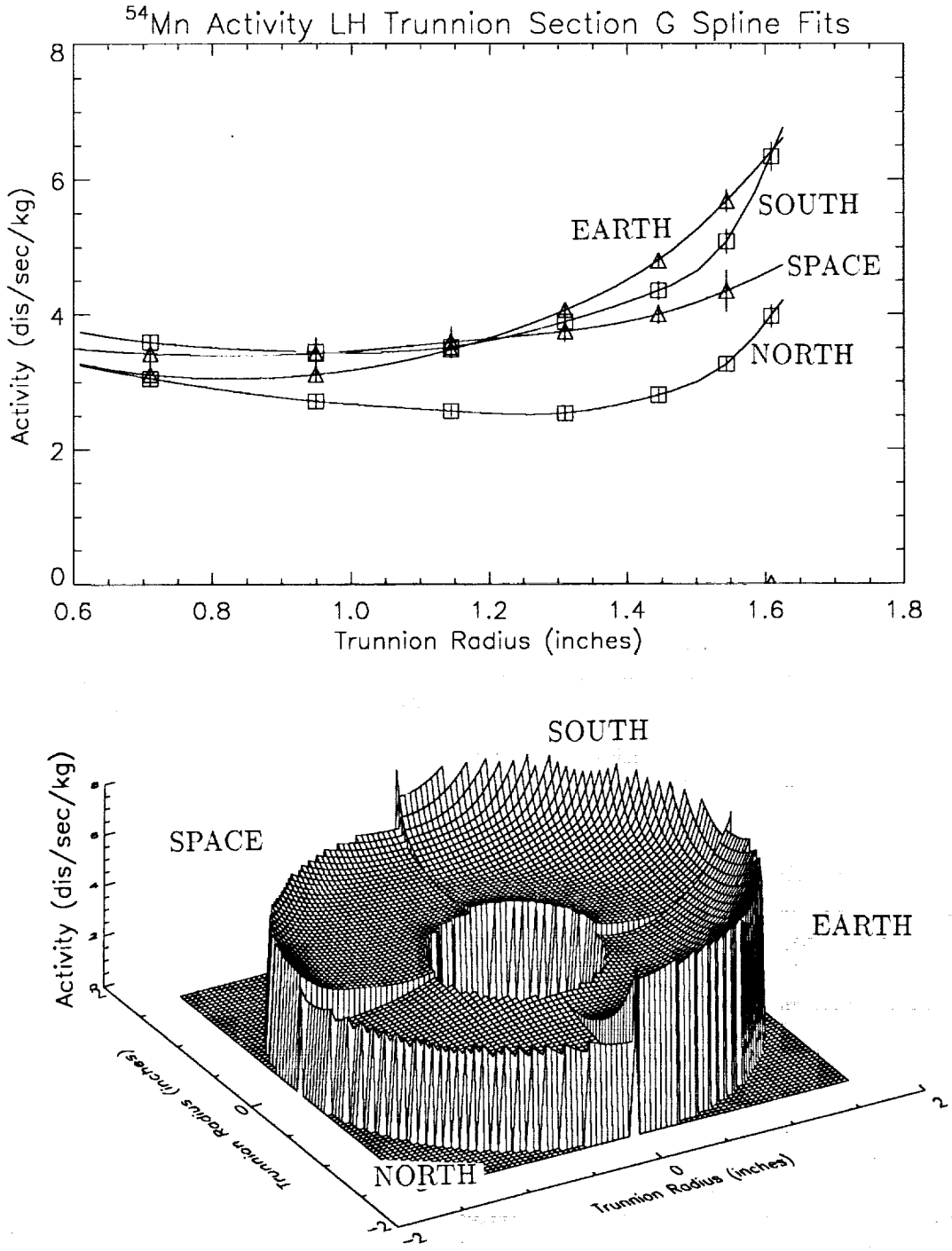

Figure 3. ^{54}Mn activity as a function of radius and direction for thin steel layers taken from the West (LH) trunnion. Top figure shows the activity profiles in the Earth, Space, North and South directions. Continuous curves represent a spline fit to the data. The spline fits were then used to create the bottom figure, which is an approximate two-dimensional representation of the activity throughout the cylindrical section. For clarity, no smoothing of the directional variation was performed.

for monitoring the on-orbit induced radioactivity. Many of these samples have been counted by different laboratories and provide a good basis for interlaboratory comparisons of absolute measurements. All of these materials, with the exception of nickel are monoisotopic or nearly so, which reduces the ambiguity of the reactions producing certain nuclides. Smith and Hurley (1991), Winn, Reeves, et al., and Camp (private comm.) have reported results for samples exchanged between laboratories. Table III gives a comparison of all activities for intentional samples which have been counted at more than one laboratory. Blanks indicate that no activity was detected. Recent measurements by Reeves, et al., of the G12 (M0002) cobalt with both an ultra low-level germanium and NaI coincidence system yields ^{60}Co activities of $1.01 \pm .10$ and $1.26 \pm .08$ dis/sec/kg, respectively. Generally the agreement is good for most nuclides, except for the ^{54}Mn and ^{57}Co in the G12 (M0002) cobalt, which is under investigation.

Table III. Comparison of Activities for LDEF Activation Foils

G12 (M0002)	Cobalt			G12 (M0002)	Indium
Nuclide	LLNL (dis/sec/kg)	LBL (dis/sec/kg)	Nuclide	LLNL (dis/sec/kg)	LBL (dis/sec/kg)
^{54}Mn	$3.38 \pm .14$	$2.31 \pm .05$	^{102}Rh	—	$.085 \pm .011$
^{56}Co	$0.82 \pm .14$	—	^{110m}Ag	—	$.085 \pm .011$
^{57}Co	$11.2 \pm .20$	$7.82 \pm .06$	^{113}Sn	$.80 \pm .14$	$.78 \pm .04$
^{58}Co	$4.30 \pm .73$	—	^{114m}In	—	$1.3 \pm .56$
^{60}Co	$0.97 \pm .08$	$0.85 \pm .03$	^{88}Zr	$.64 \pm .11$	—
G12 (M0002)	Vanadium			F2 (P0006)	Vanadium
	SRS	LLNL		SRS	LBL
^{46}Sc	$.59 \pm .05$	$.59 \pm .05$	^{46}Sc	$.72 \pm .08$	$.64 \pm .04$

Most of the radionuclides listed in Table III are products expected from proton-induced reactions. However, tantalum, indium, and cobalt also have high thermal neutron capture cross sections. These foils are activated by very low energy thermal and epithermal ($\geq .02eV$) neutrons that are moderated by low Z material on the LDEF. Only a few experiments carried significant amounts of plastic or organic compounds which slow energetic neutrons (some are made as secondary products from the proton-induced reactions, others may be atmospheric albedo neutrons). Reeves, et al., report an enhanced ^{60}Co (neutron capture on ^{59}Co) activity in the M0001 experiment (Adams, et al.), which contained plastic cosmic ray track detectors, relative to ^{60}Co activities in the other experiments. Similarly, the ^{182}Ta (neutron capture on ^{181}Ta) is higher in the M0001 experiment and the P0004/6 experiments (Benton, et al., and Alston) which contained plastic detectors and organic materials. A comparison of the neutron capture activities in the three foils is shown in Fig. 4, which represents a composite of data from LBL (Smith and Hurley, 1993), PNL (Reeves, et al.), and JSC (Lindstrom, private comm.). Neglecting formation and decay rates, the trends appear consistent between experiments. The only exception is experiment M0001, which apparently showed a lower tantalum activation than cobalt or indium. The ^{182}Ta (115 day half-life) activity will decrease relative to ^{60}Co (5.27 year half-life) due to the decrease in proton flux at the lower altitudes encountered in the later part of the mission. The activity of ^{114m}In (49.5 day half-life, neutron capture on ^{113}In (4.3% natural abundance)) is somewhat

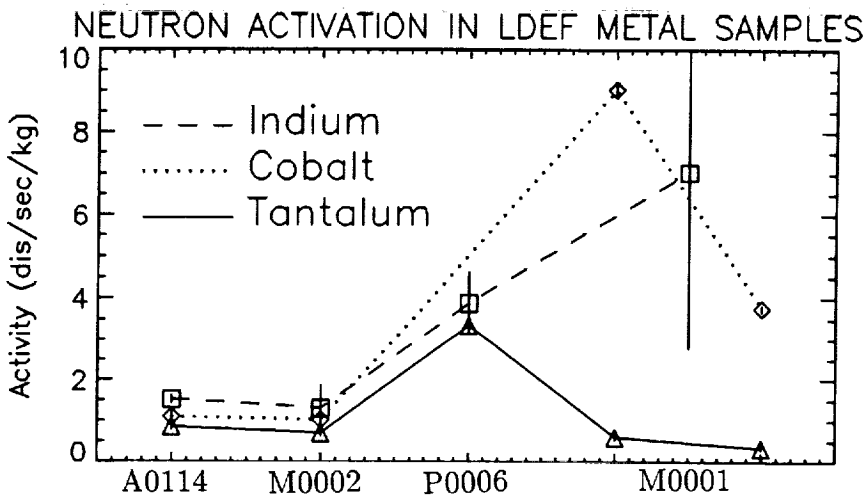

Figure 4. Neutron capture activities for indium, cobalt and tantalum metal samples from Exps. A0114, M0001, M0002 and P0006. Exp. M0001 had two samples of the same metal, one near the edge of the experiment tray and one near the center. (See text for further explanation.) Exp. P0006 did not contain a cobalt sample.

inconsistent with this picture, yet the indium could be a factor of 2-3 lower and still be within the large 1-sigma uncertainty. In addition, ^{114m}In includes a significant fraction of proton-induced activation from ^{115}In (95.7% abundance). The metal samples in Experiment M0001, which were delivered for integration in the standard 2"x2" geometry, had to be cut into two smaller pieces of approximately 2" x 3/4" for mounting on opposite sides of a subtray. The tantalum and cobalt were counted separately, and interestingly show a difference in activity between two sides of the tray. This is directly related to the amount of low Z material in proximity to the samples, which was greater on one side than the other. In the near future, it may be possible to deduce reasonably accurate local thermalized neutron fluxes from these measurements.

OTHER MATERIALS

A few small metal samples were obtained from other experiments (magnesium, silver, copper, niobium, molybdenum and germanium) several months after retrieval. Almost all had no detectable activity, at the 0.1-1 dis/sec/kg level or higher with the exceptions of magnesium (^{22}Na) and germanium (^{65}Zn). Olmez, et al., 1991, 1993, reported results for larger samples of copper and zirconium, which showed the presence of ^{58}Co and ^{88}Y, respectively, consistent with production by trapped SAA protons.

CONCLUSION

We have surveyed the overall status of the activation measurements performed on the LDEF spacecraft components. Although all samples have been counted, a significant fraction of the results have not been reported. Collection, analysis and evaluation of measurements are continuing. It is planned to complete these phases of the investigation by the end of 1993, and shift the effort toward developing a complete picture of the external radiation fluxes, secondary reactions and the shielding/geometric effects on the results. Complementary studies of LDEF dosimetric and activation data should sufficiently constrain calculations of the low earth orbit radiation environment and allow better prediction of radiation doses for future space missions.

REFERENCES

Adams, J. H., et al.: Preliminary Results from the Heavy Ions in Space Experiment. First Post-Retrieval LDEF Symposium, NASA CP-3134, 1991, p. 377.

Alston, J. A.: Seeds in Space Experiment. First Post-Retrieval LDEF Symposium, NASA CP-3134, 1991, p. 1625

Armstrong, T. W. and B. L. Colborn: Ionizing Radiation Calculations and Comparisons with LDEF Data. First Post-Retrieval LDEF Symposium, NASA CP-3134, 1991, p. 347.

Armstrong, T. W. and B. L. Colborn: Radiation Model Predictions and Validation Using LDEF Data. Second Post-Retrieval LDEF Symposium, NASA CP-3194, 1993.

Benton, E. V., et al.: Radiation Exposure of LDEF: Initial Results. First Post-Retrieval LDEF Symposium, NASA CP-3134, p. 325.

Harmon, B. A., et al.: Induced Radioactivity in LDEF Components. First Post-Retrieval LDEF Symposium, NASA CP-3134, 1991, p. 301.

Harmon, B. A., G. J. Fishman, T. A. Parnell, E. V. Benton and A. L. Frank: LDEF Radiation Measurements: Preliminary Results. Nucl. Tracks and Rad. Meas. **20**, No. 1, 1991, p. 131.

Harmon, B. A., G. J. Fishman, and T. A. Parnell: LDEF Induced Radioactivity Analysis Plan. NASA TM-103545, 1993.

Laird, C. E., et al.: Collection, Analysis, and Archival of LDEF Activation Data. Second Post-Retrieval LDEF Symposium, NASA CP- 3194, 1993.

Moss, C. E. and R. C. Reedy: Measurement of Induced Radioactivity in Some LDEF Samples.

First Post-Retrieval LDEF Symposium, NASA CP-3134, p. 271.
Olmez, I., et al.: Charged Particle Activation Studies on the Surface of LDEF Spacecraft. First Post-Retrieval LDEF Symposium, NASA CP-3134, 1991, p. 255.
Olmez, I., et al., Second Post-Retrieval LDEF Symposium, NASA **CP-3194, 1993.**
Peters, P. N. and J. C. Gregory: Pinhole Cameras as Sensors for Atomic Oxygen in Orbit; Application to Attitude Determination of the LDEF. First Post--Retrieval LDEF Symposium, NASA CP-3134, 1991, p. 61.
Reedy, R., et al.: Radioactivities Induced in Some LDEF Samples. Second Post-Retrieval LDEF Symposium, NASA **CP-3194, 1993.**
Reeves, J., et al.: Sensitivity of LDEF Foil Analyses Using Ultra- Low Background Germanium vs. Large NaI(Tl) Multidimensional Spectrometers. Second Post-Retrieval LDEF Symposium, NASA **CP-3194, 1993.**
Smith, A. R. and D. L. Hurley: Radioactivities of Long Duration Exposure Facility (LDEF) Materials: Baggage and Bonanzas. First Post-Retrieval LDEF Symposium, NASA CP-3134, 1991, p. 257.
Smith, A. R. and D. L. Hurley: A Photon-Phreak Digs the LDEF Happening. Second Post-Retrieval LDEF Symposium, NASA **CP-3194, 1993.**
Watts, J., et al.: Approximate Angular Distributions and Spectra for Geomagnetically-trapped Protons in Low-Earth Orbit. AIP Conf. Proc. **186**, High Energy Radiation Background in Space, Ed. by A. C. Rester and J. I. Trombka (AIP, New York), 1989, p. 75.
Winn, W. G.: Gamma-Ray Spectrometry of LDEF Samples at SRS. First Post-Retrieval LDEF Symposium, NASA CP-3134, 1991, p. 287.

REVISED PREDICTION OF LDEF EXPOSURE TO TRAPPED PROTONS

John W. Watts
ES62, NASA/Marshall Space Flight Center
AL 35812
Phone: 205/544-7696; Fax: 205/544-7754

T. W. Armstrong and B. L. Colborn
Science Applications International Corporation
Route 2, Prospect, TN 38477
Phone: 615/468-2603; Fax: 615/268-2676

SUMMARY

The LDEF spacecraft flew in a 28.5° inclination circular orbit with an altitude in the range from 319.4 to 478.7 km. For this orbital altitude and inclination two components contribute most of the penetrating charge particle radiation encountered--the galactic cosmic rays and the geomagnetically trapped Van Allen protons. Where shielding is less than 1.0 g/cm^2 geomagnetically trapped electrons make a significant contribution. The "Vette" models (refs. 1-3) together with the associated magnetic field models (ref. 4) and the solar conditions were used to obtain the trapped electron and proton omnidirectional fluences reported previously (ref. 5). Results for directional proton spectra using the MSFC anisotropy model for solar minimum and 463 km altitude (representative for the LDEF mission) were also reported (ref. 6). Here the directional trapped proton flux as a function of mission time is presented considering altitude and solar activity variation during the mission. These additional results represent an extension of previous calculations to provide a more definitive description of the LDEF trapped proton exposure.

INTRODUCTION

The LDEF spacecraft flew in a 28.5° inclination circular orbit with an altitude in the range from 319.4 to 478.7 km. It was gravity-gradient stabilized and oriented so that one side always pointed along the velocity vector. For this orbital altitude and inclination two components contribute most of the penetrating charge particle radiation encountered--the galactic cosmic rays and the geomagnetically trapped Van Allen protons. Where shielding is less than 1.0 g/cm^2 geomagnetically trapped electrons make a significant contribution. All three sources are strongly modulated by the Earth's magnetic field with the trapped flux being anisotropic with most of the flux arriving from a narrow band perpendicular to the local geomagnetic field direction. A model for predicting the trapped proton angular distribution has been developed (ref. 7) including both the pitch angle and east-west effects. Since trapped protons produce most of the spacecraft activation except at heavily shielded locations and almost all of the dose at most LDEF measurement locations, a large part of calculational effort (refs. 6 and 8) of the LDEF Ionizing Radiation Special Interest Group has been directed toward testing the predictions of this model and the Vette

omnidirectional flux model (ref. 1) against LDEF measurements (refs. 9-12). Here is presented further refinement of the trapped proton exposure over the LDEF mission. Improvements include detailed consideration of solar cycle modulation of the flux, improved time resolution near the mission end where the altitude was changing rapidly, directional flux calculations over the whole mission, and modification to the B and L calculations.

DISCUSSION

Previous predictions of the LDEF mission fluences (refs. 5 and 6) were obtained by calculating long-term average fluxes for five circular orbits at 478.7, 472.3, 462.8, 426.0, and 319.4 km altitudes which occurred on mission days 0, 550, 1450, 1950, and 2105, respectively, and performing a numerical integration over time assuming a straight line between time points. The solar $F_{10.7}$ cm radio flux which characterizes solar activity exceeded 150 about mission day 1540 (June 27, 1988). The environment models used for solar minimum (the first three times) were AP8MIN (ref. 1) and the magnetic field model was the IGRF 1965.0 80-term model (ref. 4) projected to 1964, the epoch of the environmental model. The environment models used for solar maximum (the last two times) were AP8MAX (ref. 1) and the magnetic field model was the Hurwitz USGS 1970 168-534M model (ref. 4) for 1970, the epoch of the environmental model. Both magnetic field calculations used a fixed constant magnetic moment of 0.311653 which was built into the ALLMAG package for calculating B and L magnetic parameters.

For low altitude orbits such as that of LDEF the flux retrieved from the Vette model is very sensitive to the input calculated B and L values. For the current calculation the constant magnetic moment in the ALLMAG package was replaced by a moment calculated from the magnetic model expansion coefficients at the epoch of the model. At the highest altitudes this change reduced the fluxes by about 5%. At the lowest altitudes near the mission end fluxes were reduced by a factor of 2.

The goals for improving the flux model were better representation of the solar cycle modulation and better time resolution near mission end. In Figure 1 solar activity as defined by the solar $F_{10.7}$ cm flux (ref. 13) and orbital altitude over the LDEF mission period are shown versus mission day. The LDEF mission began near the end of the last cycle and ended near the maximum of the current one with the orbital altitude changing slowly over the first 1500 days but rapidly during the last 500 days of the mission. From the data represented in Figure 1 the mean $F_{10.7}$ value at the last solar minimum F_{min} was 67 and the mean value at solar maximum F_{max} was 183. Rather than an abrupt switch from AP8MIN to AP8MAX a parameter

$$Alpha(t) = (F(t) - F_{min}) / (F_{max} - F_{min})$$

was defined where $F(t)$ is the $F_{10.7}$ flux at time t. Then the proton flux, $\phi(t)$ at time t, was given as a mixture

$$\phi(t) = \phi_{AP8MIN}(1 - Alpha(t)) + \phi_{AP8MAX} Alpha(t)$$

where ϕ_{AP8MIN} and ϕ_{AP8MAX} are the Vette model proton fluxes for solar minimum and solar maximum, respectively. Table 1 shows the mission times for the current model, the orbital altitude, the $F_{10.7}$ value, *Alpha* and the scale height parameter for solar minimum (min) and solar maximum (max) (used in the directional flux calculation).

Table 1. Model Inputs

Mission Day	Altitude (km)	$F_{10.7}$ Flux	*Alpha*	Scale Height (km)	
				min	max
0	478.7	95	0.24	116.6	127.2
300	475.8	67	0	115.7	---
1000	469.1	67	0	113.7	---
1300	466.2	87	0.17	112.8	123.4
1500	461.5	118	0.44	111.4	122.0
1700	449.5	158	0.78	108.0	118.5
1800	433.6	171	0.90	103.6	114.0
1900	412.8	183	1.00	---	108.4
2000	388.8	183	1.00	---	102.3
2050	368.0	183	1.00	---	97.2
2105	319.4	183	1.00	---	86.4

Note that about half the points are distributed during the last 500 days of the mission. In Figures 2 and 3 the current model flux is compared to the pure AP8MAX and AP8MIN model fluxes and the previous model fluxes, respectively, over the mission period. Note the transition near 1500 days in the previous model curve due to switching from AP8MIN to AP8MAX. In Figure 4 the predicted mission fluences from the current and previous model are compared. The current fluences are about 20% lower.

For the previously directional flux calculation the AP8MIN model and a fixed orbital altitude of 463 km were used. The current model has now been used to calculate directional fluxes at each of the time points in Table 1 as input for dose and activation calculations using a complex geometrical model of LDEF (ref. 14). In Figure 5 the cumulative mission fluence and the ratio of eastward to westward traveling flux are shown as a function of mission time. Note that the proton flux is much more directional near the mission end. Short half-life isotopes produced by activation might be expected to reflect this greater directionality by greater ratios in abundance on the west side versus the east side of LDEF.

CONCLUSIONS

Predictions of the LDEF mission's trapped proton exposure have been made using the currently accepted models with improved resolution near mission end and better modeling of solar cycle effects. Mission fluences are reduced by 20% from previously reported results. The LDEF experimental measurements are providing an opportunity to validate the model predictions.

REFERENCES

1. Sawyer, Donald M. and Vette, James I.: AP-8 Trapped Proton Environment for Solar Maximum and Solar Minimum. National Science Data Center, Goddard Space Flight Center, NSSDC/WDC-A-R&S 76-06, 1976.

2. Teague, Michael J. and Vette, James I: A Model of the Trapped Electron Population for Solar Minimum. National Science Data Center, Goddard Space Flight Center, NSSDC 74-03, 1974.

3. Vette, James I.: The AE8 Trapped Electron Model Environment. National Space Science Data Center, Goddard Space Flight Center, NSSDC/WDC-A-R&S 91-24, 1991.

4. Stassinopoulos, E. G. and Mead, Gilbert D.: ALLMAG, GDALMG, LINTRA: Computer Programs for Geomagnetic Field and Field-Line Calculations, National Space Science Data Center, Goddard Space Flight Center, NSSDC 72-12, 1972.

5. Watts, J. W.; Parnell, T. A.; Derrickson, J. H.; Armstrong, T. W.,: and Benton, E. V.: Prediction of LDEF Ionizing Radiation Environment. First LDEF Post-Retrieval Symposium, NASA CP-3134, 1991, pp. 213-224.

6. Armstrong, T. W.,; Colborn, B. L. and Watts, J. W.: Radiation Calculations and Comparisons with LDEF Data. First LDEF Post-Retrieval Symposium, NASA CP-3134, 1991, PP. 347-360.

7. Watts, J. W.; Parnell, T. A.; and Heckman, H. H.: Approximate Angular Distribution and Spectra for Geomagnetically Trapped Protons in Low-Earth Orbit. High Energy Radiation Background Space, Proceedings of AIP Conference, Sanibel Island, Florida, Vol. 186, 1989, pp. 75-85.

8. Armstrong, T. W. and Colborn, B. L.: Radiation Model Predictions and Validation Using LDEF Satellite Data. Second LDEF Post-Retrieval Symposium, NASA CP-3194, 1993.

9. Benton, E. V.; Frank, A. L.; Benton, E. R.; Csige, I.; Parnell, T. A. and Watts, J. W.: Radiation Exposure of LDEF: Initial Results. First LDEF Post-Retrieval Symposium, NASA CP-3134, 1991, pp. 325-338.

10. Frank, A. L.; Benton, E. V.; Armstrong, T., W. and Colborn, B. L.: Absorbed Dose and Predictions on LDEF. Second LDEF Post-Retrieval Symposium, NASA CP-3194, 1993.

11. Harmon, B. A.; Fishman, G. J.; Parnell, T. A.; and Laird, C. E.: Induced Radiaoactivity in LDEF Components. First LDEF Post-Retrieval Symposium, NASA CP-3134, 1991, pp. 301-312.

12. Harmon, B. A.; Fishman, G. J.; Parnell, T. A.; and Laird, C. E.: Induced Activation Study of LDEF. Second LDEF Post-Retrieval Symposium, NASA CP-3194, 1993.

13. Adjusted Ottawa 2800 MHz Solar Flux. Herzberg Astrophysics Institute, Ottawa, Ontario, Canada National Geophysical Data Center, Boulder, CO, 1991.

14. Colborn, B. L. and Armstrong, T. W.; Development and Application of a 3-D Geometry/Mass Model for LDEF Satellite Ionizing Radiation Assessments, Second LDEF Post-Retrieval Symposium, NASA CP-3194, 1993.

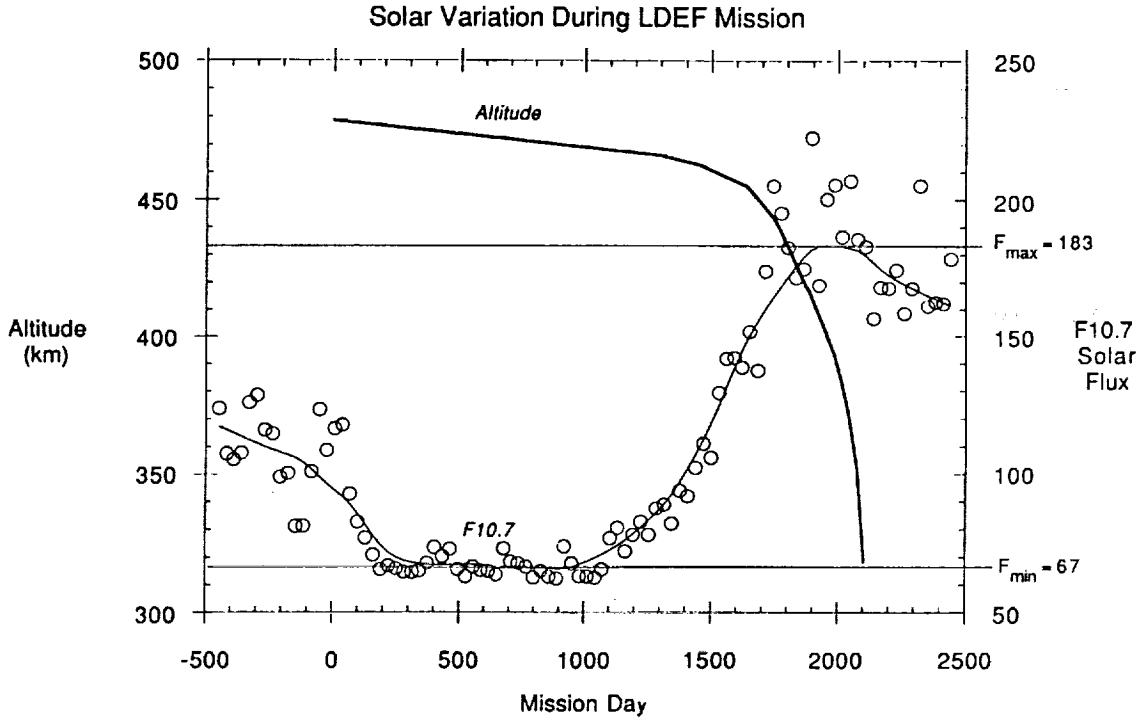

Figure 1. Variation of the solar $F_{10.7}$ cm flux (ref. 13) in units of 10^{-22}J/(s-m^2-Hz) and LDEF orbital altitude during the period of the LDEF mission.

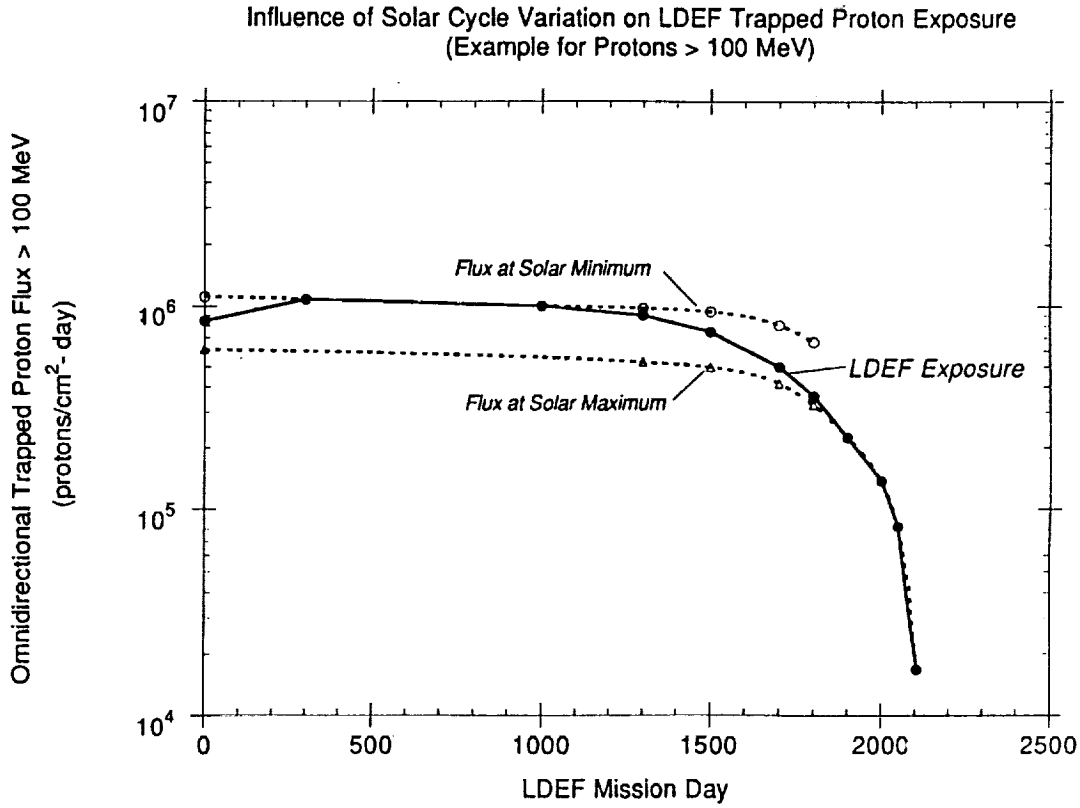

Figure 2. Current model proton flux > 100 MeV compared to APSMIN and APSMAX model predictions.

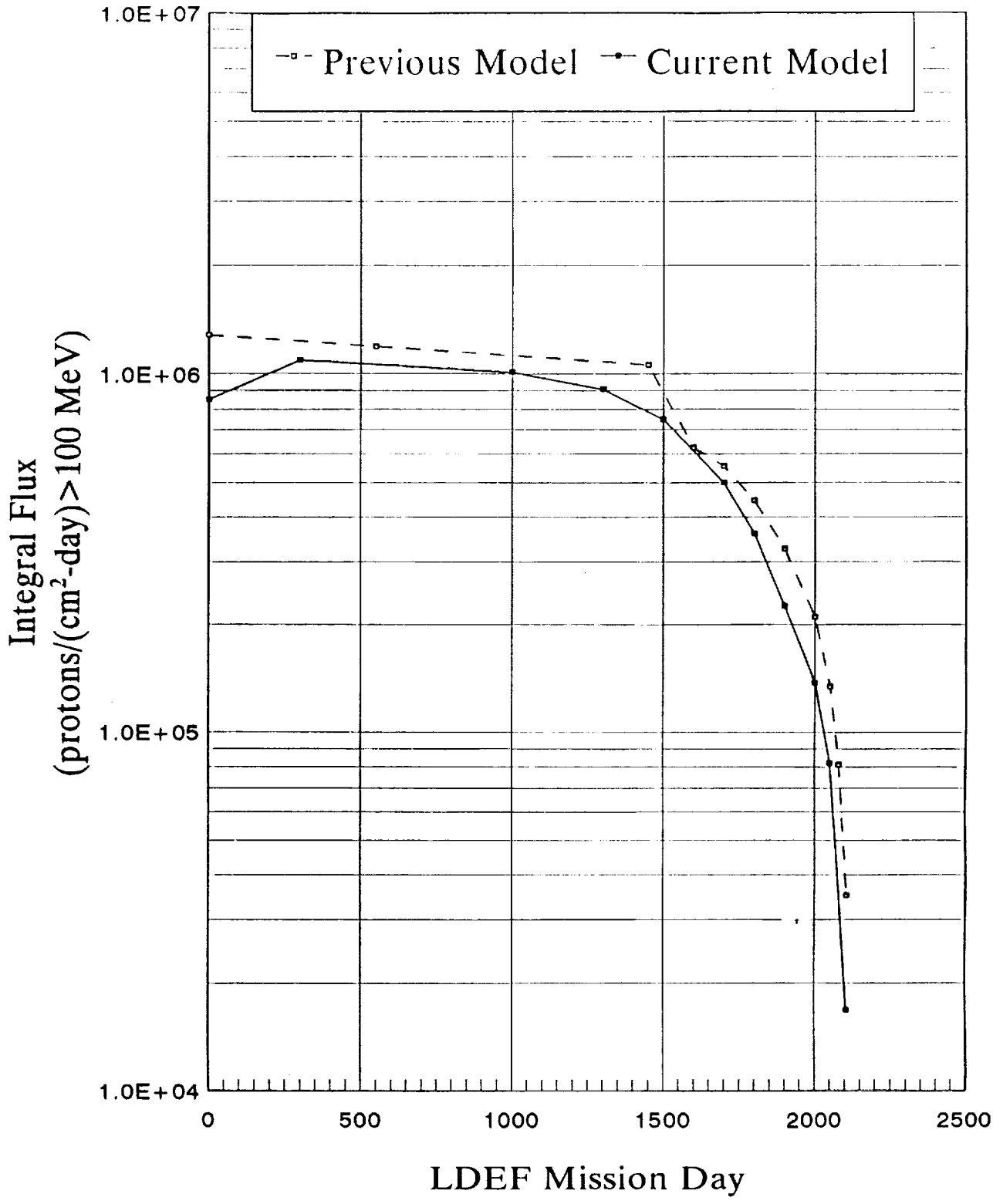

Figure 3. Current model proton flux > 100 MeV compared to previous model predictions (ref. 5).

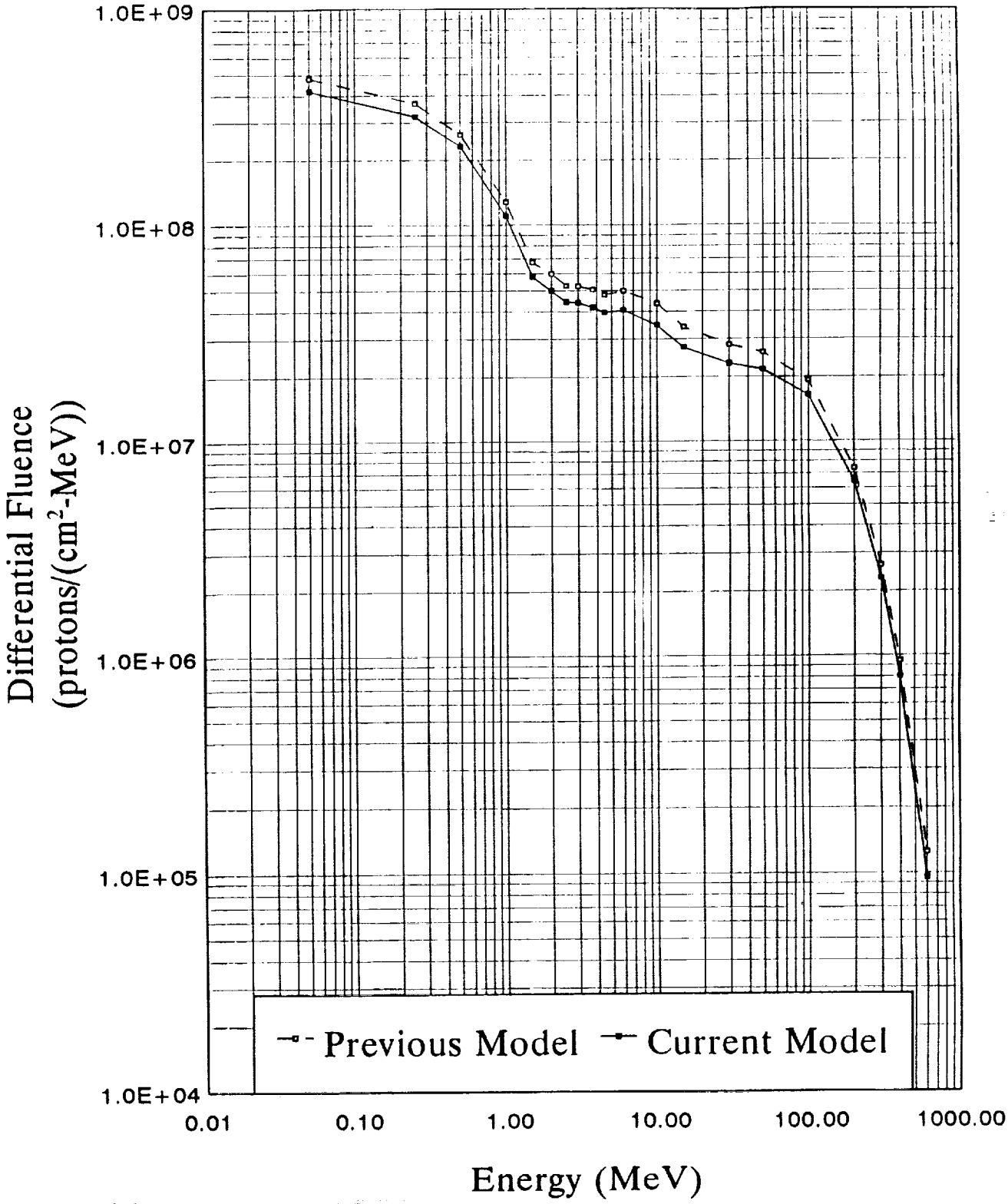

Figure 4. Current model proton mission fluence compared to previous model predictions (ref. 5).

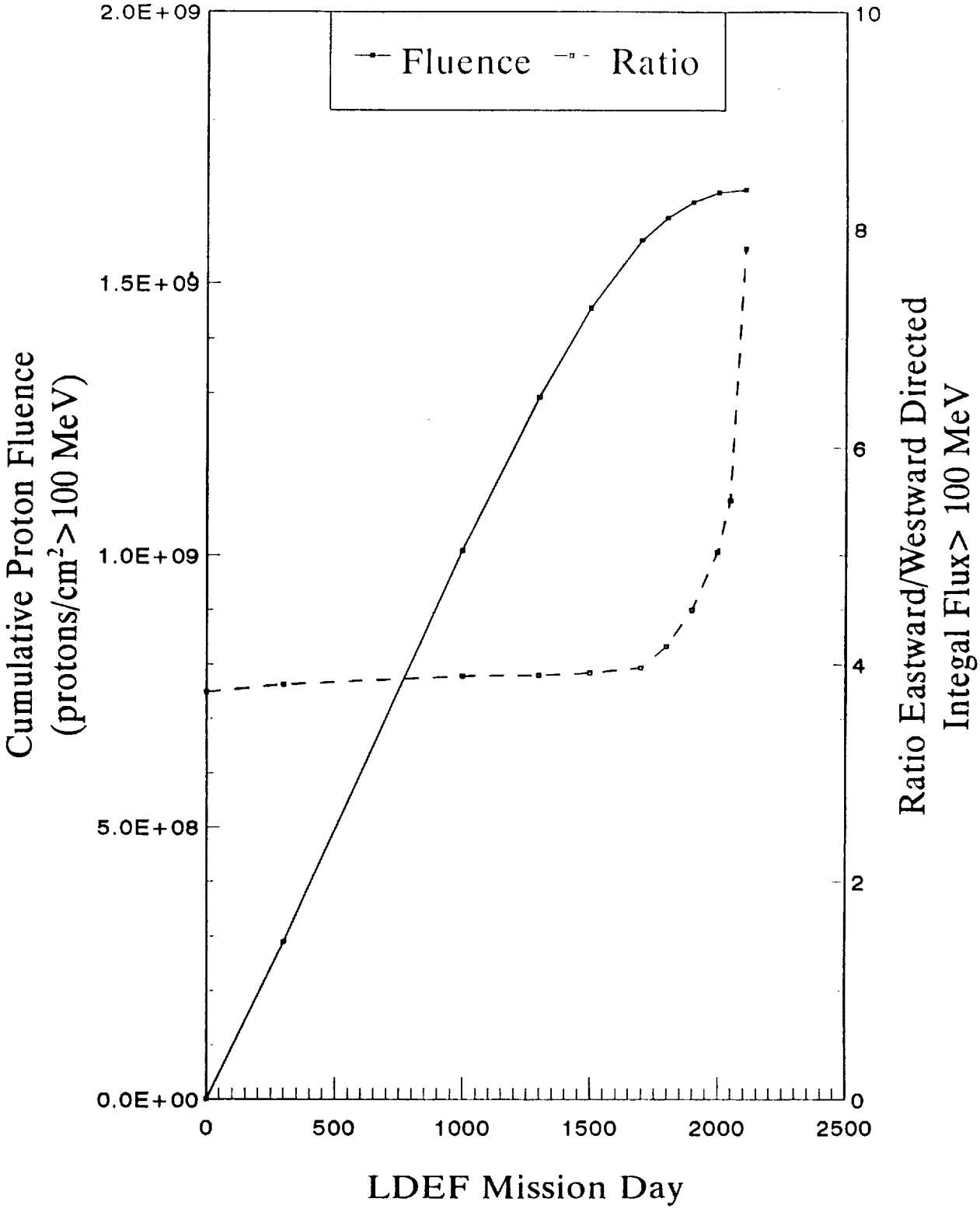

Figure 5. Cumulative mission fluence and ratio of eastward/westward directed integral flux > 100 MeV versus mission day.

A MEASUREMENT OF THE RADIATION DOSE TO LDEF BY PASSIVE DOSIMETRY

J. B. Blake and S. S. Imamoto
Space and Environment Technology Center
The Aerospace Corporation
Los Angeles, CA 90009

SUMMARY

The results from a pair of thermoluminescent dosimeter experiments flown aboard LDEF show an integrated dose several times smaller than that predicted by the NASA environmental models for shielding thicknesses much greater than 0.10 gm/cm^2 of aluminum. For thicknesses between 0.01 and 0.1 gm/cm^2, the measured dose was in agreement with predictions.

INTRODUCTION

The Space and Environment Technology Center of The Aerospace Corporation fielded two related experiments on LDEF to measure the energetic radiation dose by means of passive dosimetry. The sensors were LiF thermoluminescent dosimeters mounted behind various thicknesses of shielding. In this report, the details of the experiment are described first, followed by the results of the observations. A comparison is made with the predictions based upon the NASA environmental models and the actual mission profile flown by LDEF; conclusions follow.

EXPERIMENTS

The TLDs used in these two experiments were Harshaw TLD-100 LiF ribbon thermoluminescent dosimeters. Their size is 1/8" x 1/8" x .035". They were packaged at Harshaw on 10 October 1980, control number T-1409-S(1). A Harshaw Model 3000 was used for readout. The procedures recommended by Harshaw were followed carefully.

The configuration of the first experiment consisted of two identical packets of 16 TLDs arranged in planar arrays. One array was placed on the leading edge of the spacecraft, the other on the trailing edge. These arrays were installed in opaque packets of 1-mil aluminum foil and Kapton tape mounted behind an aluminum plate of 30-mil thickness. The aluminum shield and foil wrapping of the TLDs were approximately 0.22 gm/cm^2. In addition to the flight arrays, two control arrays were prepared that were kept with the flight

arrays as long as possible during experiment integration, and then stored in our laboratory. After recovery, the flight detectors were read out in groups of four, alternating with the control detectors.

The TLDs were calibrated before flight with a Co^{60} gamma source. The flight and control detectors were re-calibrated after the flight using a 55-MeV proton beam at the Lawrence Berkeley 88" Cyclotron. It was decided to use protons for the re-calibration because the flight data, discussed below, suggested that the majority of the dose observed in this first experiment was due to energetic protons that impinged upon LDEF in the region of the South Atlantic Magnetic Anomaly. The proton beam fluence was monitored using a plastic scintillator and an ion chamber. Figure 1 is a plot of the calibration data and a least-squares fit to these data. These new data are in good agreement with our earlier calibration data.

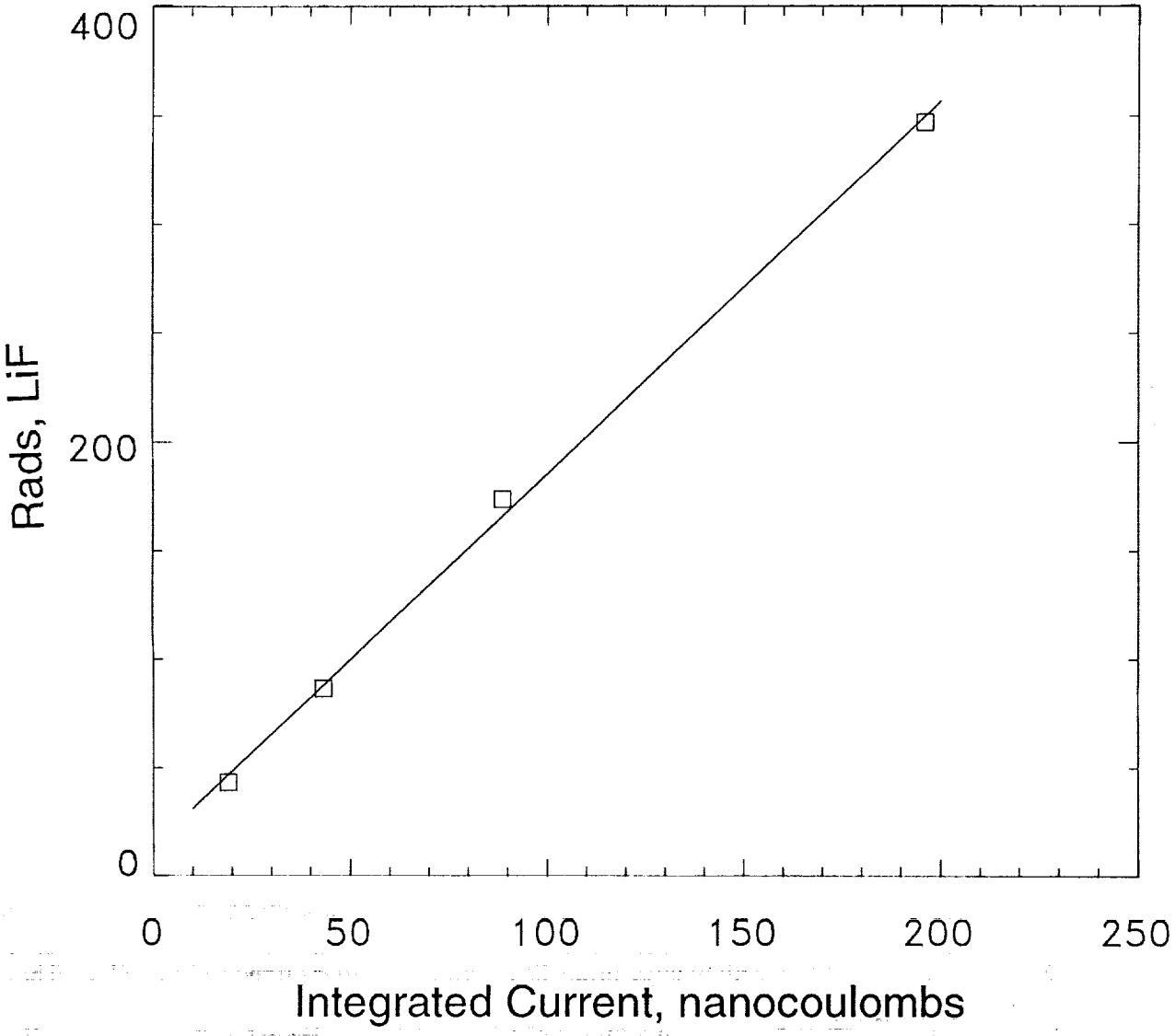

Figure 1. A plot of dose from 55-MeV protons vs integrated current as measured with the Harshaw 3000. The actual flight detectors were used in this calibration run.

The configuration of the second experiment consisted of 12 LiF TLDs, each mounted behind a different thickness of metal shield. Figure 2 is a photograph of the assembly; Table 1 gives the shield thicknesses and the shield material. Three of these assemblies were mounted on the leading edge of LDEF and exposed to the ambient radiation for the entire 69-month mission. A fourth assembly also was mounted on the leading edge, but was covered after 40 weeks with a shield of stainless steel almost 2 cm thick. Thus, during most of the LDEF mission, the dose received by the fourth assembly was determined by the much thicker cover. A fifth assembly was mounted on the trailing edge of LDEF and exposed for the entire mission while the sixth assembly also was on the trailing edge and recovered after 40 weeks. The assembly locations are summarized in Table 2.

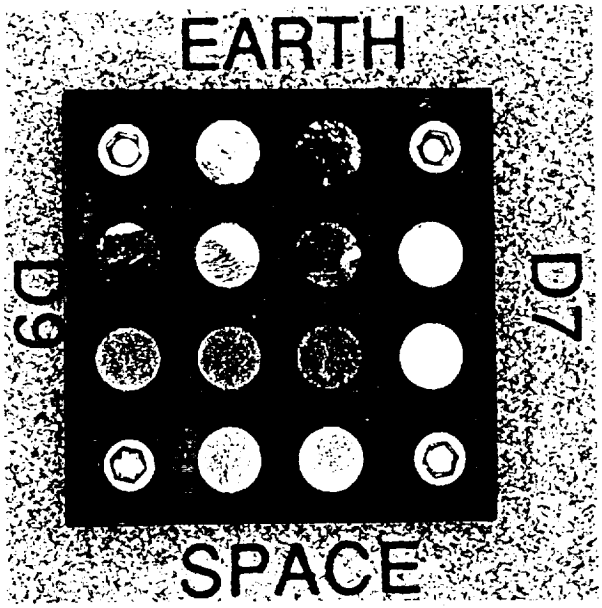

Figure 2. One of the flight assemblies used in Experiment 2.

Table 1. Shield Thicknesses

Shield Number	Material	Shield Thickness (mil)
1	Al	.0295
2	Ti	.096
3	Stainless steel	.20
4	Al	1.0
5	Stainless steel	.57
6	Stainless steel	.80
7	Stainless steel	1.0
8	Stainless steel	1.5
9	Stainless steel	2.2
10	Stainless steel	4.4
11	Stainless steel	8.0
12	Stainless steel	16

Table 2. Exposure Time and Location on LDEF

Assembly Number	Location on LDEF	Exposure Time
1	Leading edge	69 months
2	Leading edge	69 months
3	Leading edge	69 months
4	Leading edge	40 weeks
5	Trailing edge	69 months
6	Trailing edge	40 weeks

RESULTS

Experiment 1

Table 3 gives the results of the readout measurements for the flight and control arrays in nanocoulombs. These readings are shown in detail so the reader can get a feel for the scatter in the measurements.

It can be seen that the control dose is negligible. The LDEF flight doses were:

$$\text{Leading Edge} = 88.9 \pm 11.5 \text{ rads} \quad (1)$$

$$\text{Trailing Edge} = 147 \pm 21.1 \text{ rads} \quad (2)$$

$$\text{Dose Ratio} = 1.65 \pm 0.32 \quad (3)$$

Table 3. TLD Readings for LDEF Flight and Control Detectors

Sample #	Leading Edge (nC)	LE Control (nC)	Trailing Edge (nC)	TE Control (nC)
1	†	0.05 nC	70.87	0.03
2	42.54	0.02	89.02	0.02
3	37.62	0.02	83.43	0.03
4	39.09	0.02	85.88	0.02
5	46.76	0.03	73.62	0.02
6	42.41	0.03	62.95	0.02
7	42.14	0.03	78.85	0.02
8	50.55	0.02	67.43	0.02
9	38.14	0.02	76.46	0.02
10	46.00	0.03	76.91	0.03
11	42.84	0.02	95.53	0.02
12	50.22	0.03	82.07	0.02
13	37.24	0.03	62.80	0.02
14	40.36	0.03	71.97	0.02
15	38.08	0.03	61.22	0.03
16	56.19	0.02	96.88	0.03
	43.35 ± 5.59		77.24 ± 11.09	

† A malfunction in the readout apparatus interfered with the measurement of the first leading edge TLD.

Experiment 2

Experiment 2 differed from Experiment 1 in that it consisted of single LiF TLDs under a variety of shield thicknesses and materials rather than several TLDs under a single shield thickness. As a consequence, it is convenient to show the observations in graphical form. Figure 3 is a plot of the dose vs shielding thickness for the three arrays exposed on the leading edge of LDEF for 69 months. Three different symbols are used; the solid line shows the average value. The results for all shields are reduced to the equivalent gm/cm^2 of aluminum. It can be seen that the measured dose reaches an asymptotic value at about 0.01 gm/cm^2; a smaller shield thickness did not increase the measured dose.

Figure 4 shows the results for the leading-edge exposure of 40 weeks at the beginning of the LDEF mission. It can be seen that the depth-dose profile for the 40-week mission shows the same shape as for the 69-month mission. Figure 5 shows the ratio of the two exposures; the solid line is simply the ratio of 69 months to 40 weeks. The ratio of doses shown in Figure 5 clearly is not a simple function of shielding thickness. Figure 6 shows the measured and predicted dose on the leading edge for the 69-month mission. The predicted dose (ref. 1) is over 300,000 rads for zero shield thickness (not plotted).

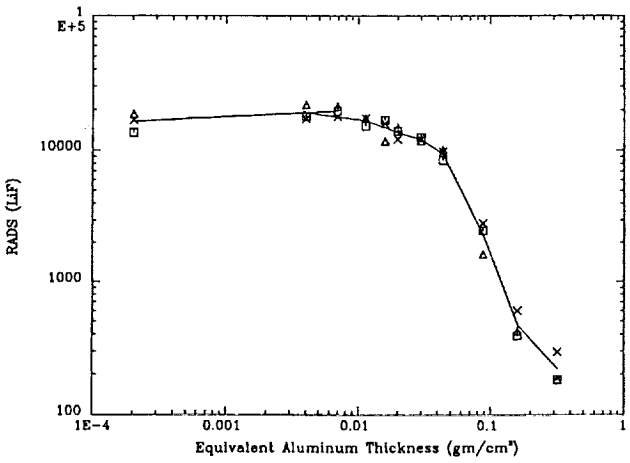

Figure 3. The measured dose vs shielding thickness for the three arrays exposed on the leading edge of LDEF for a 69-month period. The solid curve gives the average of the three measurements.

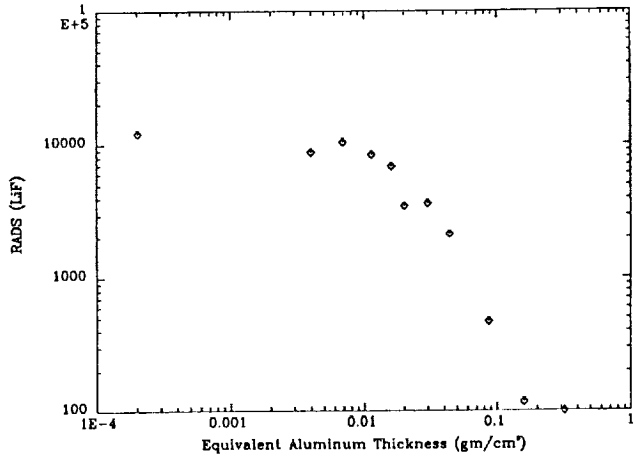

Figure 4. The depth-dose profile for the single leading edge exposure of 40 weeks.

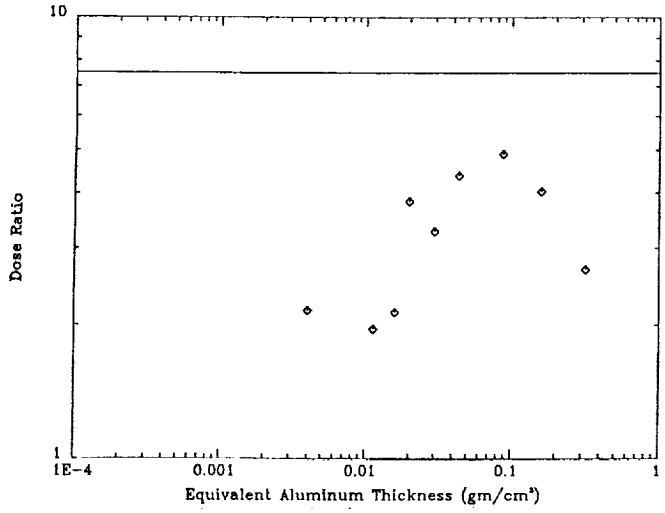

Figure 5. The ratio of the results given in Figures 3 and 4 are shown as well as the ratio of exposure times, solid curve.

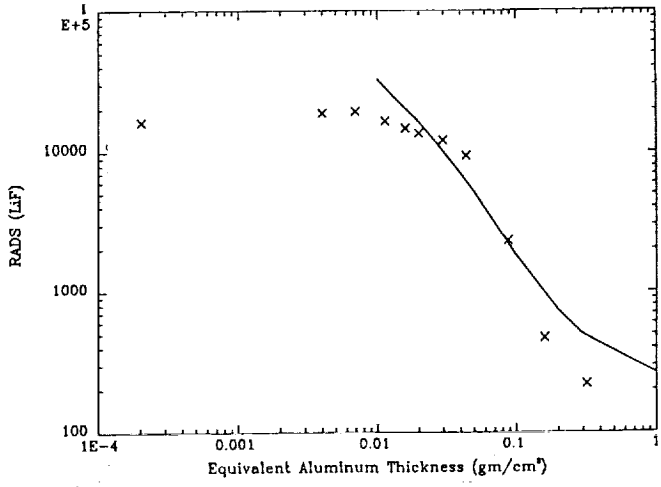

Figure 6. A comparison of the dose measured on the leading edge of LDEF and the predicted dose for the entire mission (69 months).

DISCUSSION

Experiment 1

A difference between the leading-edge and trailing-edge dose was expected, the so-called East-West effect, but was larger than expected. The predicted dose is about 690 rads with 380 rads due to protons and 310 rads due to electrons (ref. 1). Thus, the observed dose is of the order of 15% of the predicted value.

It has been suspected for some time that the NASA AE-8 model over-predicts the electron dose for modest shielding such as used in Experiment 1. Gussenhoven et al. (ref. 2) have shown from observations made aboard CRRES that this suspicion is correct, in general. A much smaller electron dose than the predicted 140 rads would mean that the dose observed in Experiment 1 was due almost entirely to protons. Support for this supposition is given by the observed East-West effect. The large observed value of 1.65 is in agreement with the predictions if the electron dose is negligible compared to the proton dose. The electrons, because of their small gyro-radii in the geomagnetic field, show no East-West effect and, thus, lessen the observed dose asymmetry.

Even if the measured dose were entirely due to protons, it was less than 40% of the predicted proton dose. However, the prediction used the NASA AE-8 model. This model is based upon data acquired in the late 1960s to early 1970s time period. The model contains two environments, one for solar minimum and one for solar maximum. The differences of course are based upon the magnitude of the solar-cycle effect during the time period of data acquisition. The increase in atmospheric density increases the drag upon the

protons as well as the spacecraft. The solar activity during the later part of the LDEF mission was substantially higher than during the solar maximum when the model data were acquired. Therefore, it is expected that the proton fluxes during the later part of the LDEF mission would have been significantly less than predicted by the AP-8 model.

Experiment 2

Figure 5 shows that the ratio of the dose received over 69 months of exposure to that experienced over the first 40 weeks of the LDEF mission is substantially less than the ratio of exposure times. Furthermore, Figure 6 shows that the measurements agree fairly well with the predictions for shielding thicknesses between $\approx .03$ gm/cm^2 and $\approx .10$ gm/cm^2. For thicknesses greater or less than this shielding range, the predicted dose is significantly higher than the observations. Note that both experiments show a substantially lower dose at 0.3 gm/cm^2 than given by the predictions. How could we explain these differences?

An obvious question is that of the linearity of the response of the TLD dosimeters over the long LDEF mission. The literature on LiF TLDs gives a large scatter in values for fading in LiF (refs. 3,4,5). Values range from several percent per month to a percent per year. The higher values would significantly affect the LDEF results. If, for example, the fade were 20% per year, the real dose would have been around twice the measured dose for the samples exposed over the entire mission. However, fading does not explain the results shown in Figures 4 and 5 unless one were to postulate that the fading is a complex function of radiation exposure. Other studies have indicated a supralinearity in the response of TLDs (ref. 6); such behavior would worsen the fit between predictions and measurements.

A second question is that of the useful range of absorbed dose for LiF. Bull (ref. 4) gives a range of 5×10^{-3} to 10^5 rads. This useful dose range covers the expected dose to the LDEF experiments. However, at low energy, the electrons and protons do not uniformly irradiate the entire TLD, but are absorbed in a small portion of the TLD that faces outboard. Saturation could have occurred in the near-surface region of a TLD without the entire device being adversely affected. A simple range estimate indicates that it takes on the order of 600 keV for an electron to penetrate a TLD-100 and 13 MeV for a proton. An accurate calculation of the depth-dose profile in a TLD-100 would require detailed knowledge of the electron and proton energy spectra, which are at best poorly known. The flattening in the observed dose occurs around 2×10^4 rads, which is 20% of the maximum useful range of LiF dosimeters (ref. 4); therefore, the hypothesis that saturation effects are at least a partial cause of the deviation between predictions and observations for the thin shields cannot be ruled out.

Figure 5 further supports the saturation hypothesis — the reason that the dose ratio below 0.01 gm/cm^2 is much less than the ratio of exposure times is due to the onset of saturation effects. Once saturation begins, the effectiveness of further exposure is reduced, and, eventually, more radiation has no further effect on the TLD response. The dose ratio never equals the ratio of exposure times of approximately 7.5.

However, since LDEF moved to a more benign environment at lower altitude as the mission progressed, the dose ratio would be expected to be less than the exposure time ratio.

The discussion of the results of Experiment 2 given above suggest that fading is not a major factor in these experiments. Thus, it is concluded that the radiation dose in the LDEF orbit resulting from higher energy particles is more benign than predicted by the NASA models. Furthermore, since the observed East-West effect is equal to that predicted for protons alone, it suggests that the electron dose is negligible compared to that from protons.

PRESENT CONCLUSIONS

The results of this experiment suggest that for the LDEF mission:

1) The dose due to electrons that can penetrate 0.22 gm/cm^2 or more was an order of magnitude lower than predicted.

2) The dose due to protons that can penetrate 0.22 gm/cm^2 or more was a factor of 3 lower than predicted.

3) The total dose for shielding thicknesses between $\approx$ 0.01 gm/cm^2 and 0.1 gm/cm^2 agreed well with the predictions based upon the NASA models.

4) For shielding thicknesses less than $\approx$ 0.01 gm/cm^2 no conclusion has been reached at the present time.

ONGOING WORK

Saturation and fading effects are being studied. In order to estimate the magnitude of fading in our TLDs, 20 were irradiated again at the Lawrence Berkeley Laboratory with a 55-MeV proton beam. They will be read out over a year or more to determine the magnitude of fading. We will study saturation effects by irradiating some TLDs with low-energy electron and proton beams. It should be possible to determine if the apparent dose saturation is really due to saturation effects or indicates an absence of very-low-energy electrons and protons in the LDEF orbit.

It should be noted that the data base used in generating the NASA models does not go down to zero energy. Thus, the predictions given for LDEF are extrapolations into the unknown as the shielding thickness goes to zero. The LDEF environment is expected to be different at the lowest energies from two earlier low-altitude dosimetric missions — COSMOS 1887 (ref. 7) and COSMOS 2044 (ref. 8). These two Soviet missions had inclinations of 82.3° and 62.8°, respectively, and thus regularly traversed auroral latitudes, whereas LDEF remained below and was not exposed to auroral particles.

It is hoped that the activation experiments will lead to a quantitative value for the integrated proton flux over the LDEF mission that can be compared with the TLD results.

ACKNOWLEDGEMENT

This work was supported at The Aerospace Corporation under Air Force Space Systems Division Contract FO4701-88-C-0089.

REFERENCES

1. Benton, E. V.; Heinrich, W.; Parnell, T. A.; Armstrong, T. W.; Derrickson, J. H.; Fishman, G. J.; Frink, A. L.; Watts, J. W., Jr.; and Wiegel, B.: Ionizing Radiation Exposure Of LDEF (Pre-Recovery Estimates), *Nucl. Tracks Radiat. Meas.* 20, 75-100, 1992.
2. Gussenhoven, M. S.; Mullen, E. G.; Brautigam, D. H.; Holeman,E.; Jordan, C.; Hanser, F.; and Dichter, B.: Preliminary Comparison Of Dose Measurements On CRRES To NASA Model Predictions, *IEEE Trans. Nuc. Sci.* 38, 1655-1662, 1991.
3. Piesch, E.; Burgkhardt, B.; and Vilgis, M: Photoluminescence Dosimetry: Progress And Present State Of Art, *Radiation Protection Dosimetry*, 33, 215-226, 1990.
4. Bull, R. K.: Thermoluminescence And Its Applications: An Introduction, *Nucl. Tracks Radiat. Meas.* 11, 105-113, 1986.
5. Horowitz,Y.: Editorial, *Radiation Protection Dosimetry*, 32, 147, 1990.
6. McKeever, S. W. S.: Modelling Supralinearity In Gamma Irradiated TL Dosemeters, *Radiation Protection Dosimetry*, 33, 83-89, 1990.
7. Reitz, G.; B*f*cker, H.; Facius, R.; Beaujean, R.; and Enge, W.: Dosimetry Results Of COSMOS 1887, *Nucl. Tracks Radiat. Meas.* 17, 99-104, 1990.
8. Reitz, G.; B*f*cker, H.; Facius, R.; Schäfer, M.; and Beaujean, R.: Dosimetric Results Of COSMOS 2044, *Nucl. Tracks Radiat. Meas.* 20, 161-165, 1992.

LDEF: DOSIMETRIC MEASUREMENT RESULTS (AO 138 - 7 EXPERIMENT)

J. Bourrieau
CERT-ONERA/DERTS
2 Avenue E. Belin
31055 Toulouse, France
Phone: (33) 61557113, Fax: (33) 61557169

SUMMARY

One of the objectives of the AO 138 - 7 experiment on board the LDEF was a total dose measurement with Thermo Luminescent Detectors (TLD 100).
Two identical packages, both of them including five TLDs inside various aluminum shields, are exposed to the space environment in order to obtain the absorbed dose profile.
Radiation fluence received during the total mission length has been computed, taking into account the trapped particles (AE8 and AP8 models during solar maximum and minimum periods) and the cosmic rays; due to the magnetospheric shielding the solar proton fluences are negligible on the LDEF orbit.

The total dose induced by these radiations inside a semi infinite plane shield of aluminum are computed with the radiation transport codes available at DERTS. The dose profile obtained is in good agreement with the evaluation by E.V. BENTON.

TLD readings are performed after flight; due to the mission duration increase a post flight calibration was necessary in order to cover the range of the in flight induced dose. The results obtained, similar (± 30%) for both packages, are compared with the dose profile computation.
For thick shields it seems that the measurements exceed the forecast (about 40%). That can be due to a cosmic ray and trapped proton contributions coming from the backside (assumed as perfectly shielded by the LDEF structure in the computation), or to an underestimate of the proton or cosmic ray fluences. A fine structural shielding analysis should be necessary in order to determine the origin of this slight discrepancy between forecast and in flight measurements.
For the less shielded dosimeters, mainly exposed to the trapped electron flux, a slight overestimation of the dose (less than 40%) appears. Due to the dispersion of the TLD's response, this cannot be confirmed.

In practice these results obtained on board LDEF, with less than a factor 1.4 between measurements and forecast, reinforce the validity of the computation methods and models used for the long term evaluation of the radiation levels (flux and dose) encountered in space on low inclination and altitude Earth orbits.

OBJECTIVE OF THE STUDY

AE8 and AP8 used for the computation of trapped particle fluences encountered in space are steady state models, and of course short term fluctuations cannot be obtained. They come, for the main part, from old measurements performed during the sixties and seventies. Dose evaluations on board STS point out that the use of an updated magnetic field model, taking into account the secular drift, leads to an overestimate of the trapped proton fluence forecast on LEO (ref.1).

The remarks above explain the uncertainties allowed by NASA (ref.2) for the long term forecast of the trapped particle fluence:

- a factor 2 (up and down) for protons,
- a factor 2-3 (up and down) for electrons in the inner zone,
- a factor up to ten for electrons in the outer belt.

An other concern is to define the rate of Single Event Effects (SEE) on electronic devices and the risk of an accute exposure induced by large solar flares during manned missions. For these computations the magnetospheric shielding during solar flares must be well known in order to define the level of transiting radiations, Galactic and Solar Cosmic Rays (GCR and SCR).

On the orbit of LDEF, with an inclination equal to 28.5 degrees and an altitude ranging between 480 km at the begining and 320 km at the end of the flight, the radiations encountered are mainly trapped particles. Due to the orbit inclination the magnetospheric shielding is very effective for the solar protons and the GCR. Concerning the heavy ions from solar events their state of charge is not well known and consequently the magnetospheric absorption cannot be defined.

Significant exposure on board LDEF comes from trapped protons and electrons and the absorbed dose induced by GCR and SCR are weak.

The objective of this study was the evaluation of the doses profiles induced during a mission of some months (mean term) on LEO. Due to the increase of the flight duration the results can be used for a comparison with the long term forecast including solar maximum and minimum periods.

EXPERIMENTAL METHOD

The AO 138 - 7 experiment was part of the FRECOPA tray developed by the Centre National d'Etudes Spatiales (CNES) and set on the row 3 (tray B) on board LDEF.

Dosimeters

Without data transmission, only passive dosimeters could be used. Ten lithium fluoride thermoluminescent dosimeters (TLD 100) were located inside two cases behind various aluminum plane shields (see figure 1)in order to obtain the dose profiles for thicknesses up to 1.08 g/sqcm (0.4 cm of aluminum).

The two dosimeter assemblies were located on the plate supporting the AO138 - 1 experiment ; they are directly exposed to the space environment during all the flight.

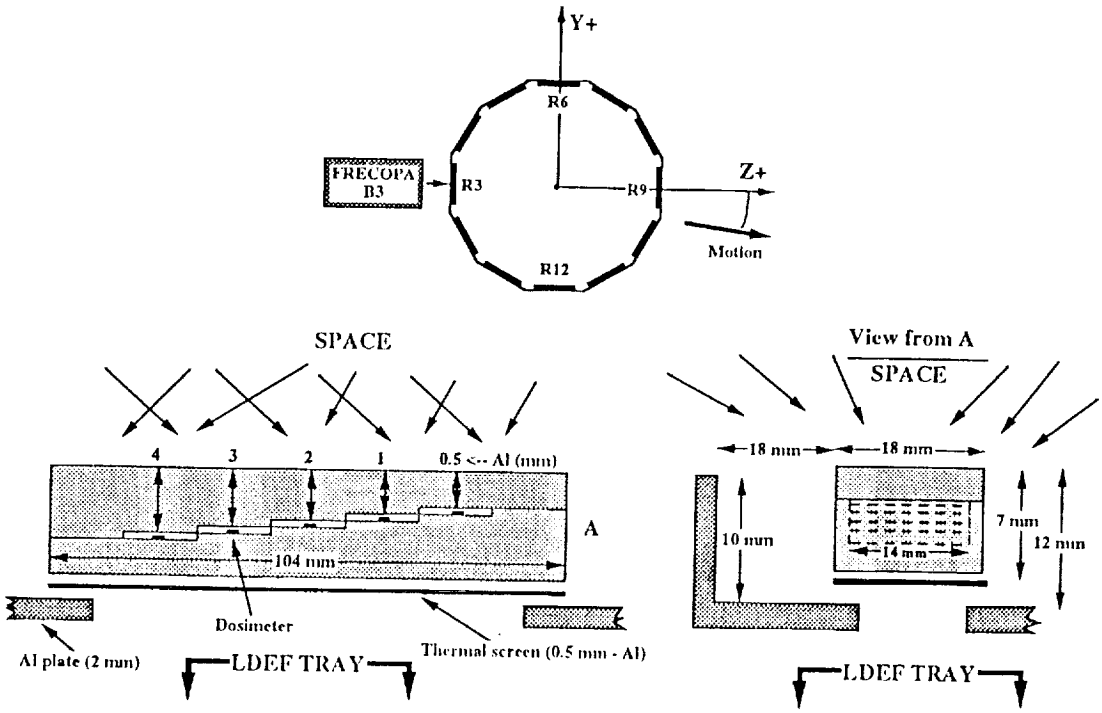

Figure 1 : FRECOPA location on board LDEF and dosimeter assembly

Calibration

The preflight calibration made with detectors of the same set of TLDs (on a range covering the dose expected during the planned mission) cannot be used because of the delayed retrieval of LDEF.

After the post-flight reading a new calibration was performed on all the TLDs used to control their sensitivity in the enlarged domain of dose obtained during the LDEF mission.

FLUX AND ABSORBED DOSE FORECAST

The flight of LDEF, from April 1984 to January1990, extends approximately over half part of a solar cycle, with a minimum of activity observed in September 1986.

GCR and trapped particle fluences are determined assuming that the first four year period was during solar minimum; the end of the flight (about 10 months) was during solar maximum.
The AP8 and AE8 environment models are used,with solar maximum and minimum conditions, for the evaluation of the trapped particle fluences. In the code available at DERTS for these computations (ref.3), following NASA recommendations, the magnetic field model is not updated and fits the conditions encountered at the epoch of the measurements.
Concerning GCR fluence evaluation, the models for solar minimum and maximum periods are those developed by DERTS from the data of JP. Meyer (ref.4). The magnetospheric shielding is included in the computation (DERTS code BLINMAG).

In order to take into account the altitude change during the mission the computations are performed for the inclination 28.5 degrees and four steps of altitude:

- 475 km, from the mission begining up to the day 1000,
- 470 km, from day 1000 to day 1500,
- 440 km, between day 1500 and 2000,
- 330 km, from day 2000 to the retrieval.

The absorbed dose profiles, D(x), induced by the trapped particles and the GCR , are computed at a point tissue sample at depth x inside an infinite plane shield of aluminum. Isotropic distributions are assumed for the radiations impinging the shield. Straight ahead approximation is used for protons and other ions; scattering is taken into account for electrons and the bremsstrahlung induced dose computed is negligible.
The dose profiles obtained with our codes (ref.5) for trapped protons and electrons (see figure 2) are similar to the results reported by EV. Benton (ref.6).
Due to the orbit inclination the protons from solar events (October 89 for instance) are unsignificant, and the doses due to GCR are negligible for the shield thicknesses studied.

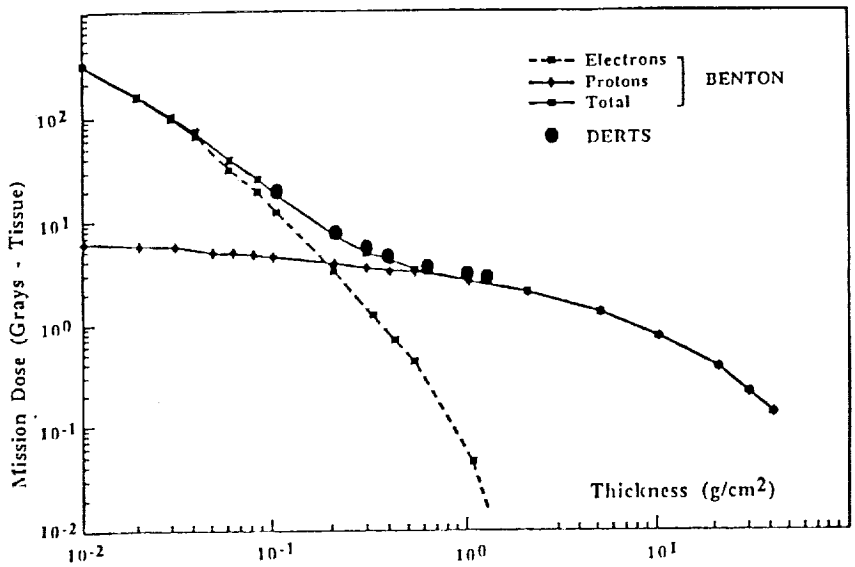

Figure 2 : Dose profile forecast, for tissue inside an infinite plane shield

LDEF MEASUREMENTS

The results obtained (see figure 3) on the FRECOPA tray agree with both dosimeter groups for shield thicknesses above 0.5 g/sqcm; due to energetic trapped protons the dose profile is then relatively flat (between 3 and 4 gray).

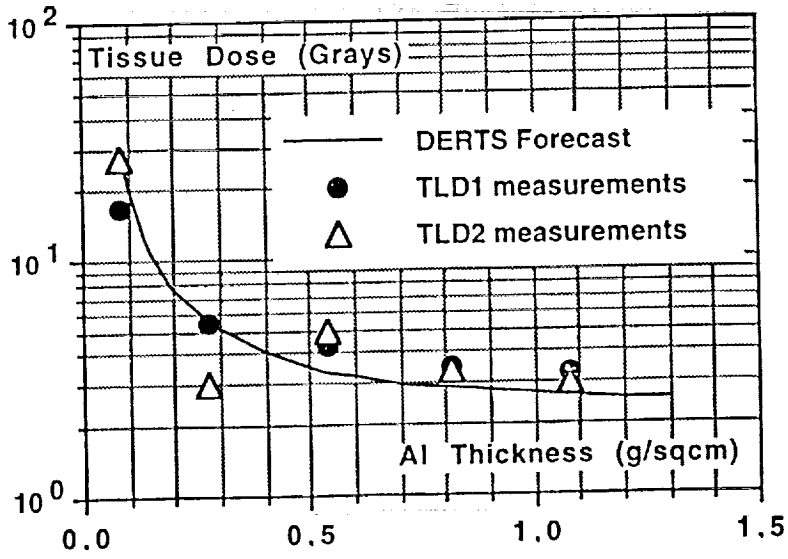

Figure 3 : TLD measurement results, comparison with the computation

A good agreement (difference about 20% for the point 0.7 g/sqcm) is observed with the measurements performed by G. REITZ (see figure 4) in the BIOSTACK unit (location: C2, near the FRECOPA tray).

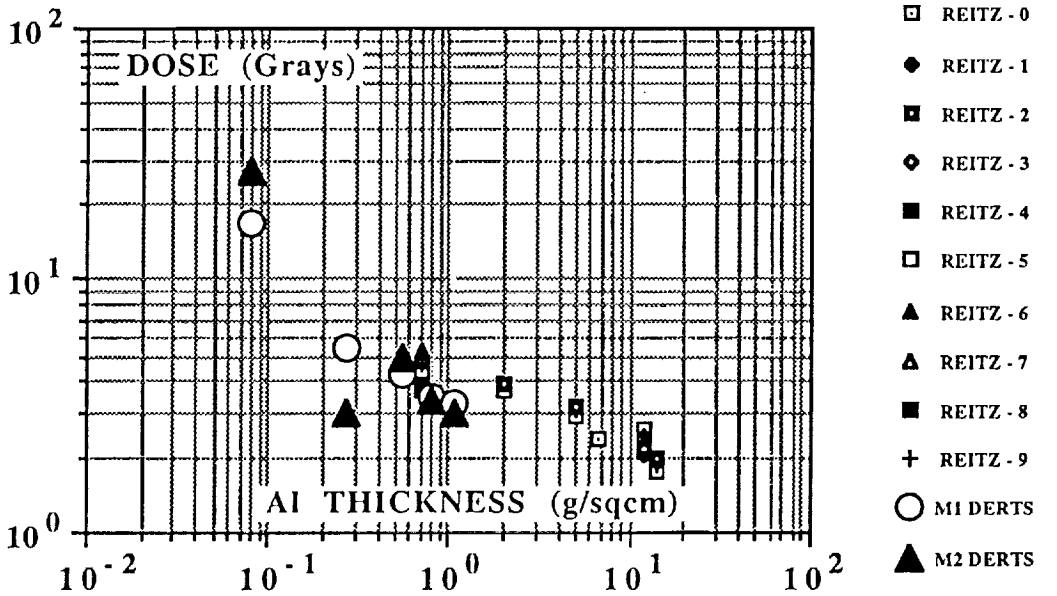

Figure 4 : In flight measurement, comparison with results reported by G. REITZ (ref.7)

For thin shields (0.081 and 0.27 g/sqcm) the dose is mainly induced by trapped electrons, and larger dispersions (20 and 30 %) are observed between the two groups of TLD of our experiment.

In spite of rough descriptions (two and four steps respectively) of solar activity change and altitude decrease during the mission, there is a general agreement between measurements and simple plane shield geometry calculation.

For thick shields (0.55, 0.81, and 1.08 g/sqcm) the differences between forecast and measured doses indicate an under-estimate (20 to 30%) of the computed values, that may be from the AP8 models, but in this case the unaccuracy announced by NASA (factor 2) appears as pessimistic. Increases of doses for thick shield can be also due to:

- primary particles from the lateral and back sides of the TLD case,
- secondaries (neutrons, protons, etc) produced in the structures,
- the anisotropy of the incident radiations (mirror points).

For thin shields (0.081 and 0.27 g/sqcm) the dispersion of the measurements (± 20 and 30 %) and the differences with previsions are of the same order of magnitude; however, it seems that computations overestimate (less than 50 %) the electron induced dose.

CONCLUSION

The part of the AO138-7 devoted to dosimetric measurements on the FRECOPA tray on board LDEF, with differences smaller than 50% between forecast and measurements, generally confirms the validity of:

- the NASA models AP8 and AE8 used for the computations of trapped particle fluences encountered in LEO during more than half of a solar cycle,

- the codes developed to simulate the particle transport in matter, and to determine the absorbed dose, at least for plane shield, and thicknesses smaller than 1.1 g/sqcm.

These conclusions concern long term missions on low altitude and weakly inclined orbits. They are not valid for many application satellites, particularly in GEO, where an overestimation of the electronic doses and an unexpected effect of the solar activity are evidenced (ref.8).

The LDEF mission demonstrates the interest of in-flight passive (if retrieval) or active dosimetry in order to study various unsolved problems as:

- the validity of the long term forecasting methods for inclined LEO and GEO (trapped particles, solar events and GCR),
- the consistency of the doses that can be computed and measured inside the complex structures of a space vehicle,
- the short term fluctuations of trapped particle populations linked with variations of geomagnetic activity, problem concerning mainly, as the solar flares, the manned space missions.

REFERENCES

1 - PD. McCORMACK : "Radiation Dose and Shielding for the Space Station"
paper n° IAF/IAA-86-38037th Congress of the IAF, Innsbruck, October 86.

2 - EG. STASSINOPOULOS et al : "The Space Radiation Environment for Electronics"
Proceeding of the IEEE, Vol.76, N) 11, November 88.

3 - J. BERRY et al : "Description of the Earth's Radiation Environment for Future European Manned Space Mission"
Pub.CERT-ONERA, TN 1001, ESA contract n° 6988/86/NL/PP (SC), March 87.

4 - JP. MEYER et al : "Cosmic Rays - Astronomy with Energetic Particles"
Phys. Today , p 23, 1974.

5 - J. BOURRIEAU et al : "Radiation Dose Calculation and Measurement for Manned Space Missions"
TN 1002, ESA contract n° 6988/NL/PP (SC), May 87.

6 - EV. BENTON et al : "Ionizing Radiation Exposure of LDEF (LDEF Pre-Recovery Estimates)"
USF - TR - 77, August 90.

7 - G. REITZ : "Preliminary Total Dose Measurements on LDEF"
LDEF 69 months in Space, first post-retrieval symposium, NASA Conf. Pub. 3134, part 3, p 1643, June91.

8 - A. HOLMES-SIEDLE et al : "The Meteosat-3 Dosimeter Experiment : Observation and Calibration of Radiation Surges in Geostationary Orbit"
ESA Space Environment Analysis Workshop,October 90.

ABSORBED DOSE MEASUREMENTS AND PREDICTIONS ON LDEF*

A. L. Frank and E. V. Benton
Eril Research, Inc., P. O. Box 150788
San Rafael, CA 94915-0788
Phone: 415/386-0254, Fax:415/666-2469

T. W. Armstrong and B. L. Colborn
Science Applications International Corporation
Route 2, Prospect, TN 38477
Phone: 615/468-2603, Fax: 615/468-2676

SUMMARY

The overall radiation environment of the Long Duration Exposure Facility (LDEF) was determined in part through the use of thermoluminescent detectors (TLDs) which were included in several experiments. The results given here are from four experiments (A0015 Biostack, M0004 Fiber Optics Data Link, P0004 Seeds in Space, and P0006 Linear Energy Transfer Spectrum Measurement) and represent a large fraction of existing absorbed dose data. The TLDs were located on the leading and the trailing edges and the Earth end of the spacecraft under various shielding depths (0.48 to 15.4 g/cm^2). The measured absorbed doses were found to reflect both directional dependence of incident trapped protons and shielding.

At the leading edge, doses ranged from 2.10 to 2.58 Gy under shielding of 2.90 to 1.37 g/cm^2 Al equivalent (M0004). At the trailing edge, doses varied from 3.04 to 4.49 Gy under shielding of 11.7 to 3.85 g/cm^2 (A0015), doses varied from 2.91 to 6.64 Gy under shielding of 11.1 to 0.48 g/cm^2 (P0004), and a dose range of 2.66 to 6.48 Gy was measured under shielding of 15.4 to 0.48 g/cm^2 (P0006). At the Earth end of the spacecraft, doses from 2.41 to 3.93 Gy were found under shielding of 10.0 to 1.66 g/cm^2 (A0015). The effect of the trapped proton anisotropy was such that the western side of LDEF received more than 2 times the dose of the eastern side at shielding depths of $\sim$1 g/cm^2. Calculations utilizing a directional model of trapped proton spectra predict smaller doses than those measured, being about 50% of measured values at the trailing edge and Earth end, and about 80% near the leading edge.

INTRODUCTION

Passive detector assemblies were included in four separate experiments on the LDEF satellite. The detectors included plastic nuclear track detectors of various sensitivities for heavy particle LET spectra

*Work partially supported by NASA Contract No. NAS8-38610 (NASA—Marshall Space Flight Center, Huntsville)

measurements, fission foil detectors and activation foils for neutron measurements and TLDs for total absorbed dose measurements. Only the TLD portion of the experiments is reported here.

The purpose of these measurements was to define the radiation environment, in some cases to determine the irradiation of experimental materials which accompanied the detectors, and in other cases to measure shielding and locational effects. All of the measurements are of use in the more general objectives of mapping the radiation environment and providing detailed measurements for intercomparison with calculations using modeling of the incident radiation and propagation through shielding. Preliminary calculations have been made using the Marshall Space Flight Center Proton Transport Code and detailed models of the experimental shielding materials.

EXPERIMENTS

The TLDs located in the four LDEF experiments which are discussed here were surrounded by diverse shielding materials and thicknesses and were located on different parts of the LDEF vehicle.

In the P0006 experiment, 18 TLD-700 chips were spread evenly in each of five layers within a large detector stack. The stack was chiefly composed of layers of different plastic types and of aluminum. The overall stack was 10.8 cm square (with $\sim$1.5 mm clipped from the corners) by 10 cm thick and was contained in an Al cylindrical canister with inner dimension of 15.2 cm diameter and 10 cm depth. It was located in Tray F2 near the trailing edge of the vehicle and positioned intermediately between four larger canisters of the P0004 experiment.

In the P0004 experiment, small plastic holders containing four TLD-700 chips were placed in six Al canisters carrying seeds (five canisters of tomato seeds, one canister with a variety of seeds). The canister interiors were 31 cm in diameter with average depths of about 12.5 cm, and they had rounded lids. They were arrayed, 3×2, in Tray F2. The TLDs were centered in the canisters, either at the top or bottom or at a position roughly centered within the seeds.

The M0004 experiment included two small Al canisters (interior dimensions of 4.8 cm diameter and 1.3 cm depth) containing two TLD plates each, which were separated by plastic stacks. Each plate contained either 3 or 4 TLD-700 chips. The canisters were mounted, canted 90° to each other, next to other flight components of the experiment in Tray F8 near the leading edge.

In the A0015 experiment, detector stacks containing TLD plates were included in three different Biostack canisters. The canisters were of Al with acrylic plastic liners. Interior dimensions were 9.7 cm diameter and 8.5 cm depth and the detector stacks were 7 cm square (with $\sim$1.5 mm clipped from the corners) and 8.5 cm thick. The stacks were mainly composed of layers of different plastic types and Al. Canister #1 was located at the Earth end of the vehicle and contained three TLD plates with 4 or 5 TLD-700 chips. Canister #2 was located in Tray C2 near the trailing edge and also contained three TLD plates with 4 or 5 TLD-700 chips. Canister #3 was also located in Tray C2 but was vented to space and only partially devoted to radiation detectors. It contained one TLD plate with 6 TLD-700 chips.

Table 1. P0006: LDEF Absorbed Dose Measurements With TLD-700

TLD Plate No.	Tissue Absorbed Dose (Gy)	Dose Rate (mGy/d)	Al Equivalent Shielding (g/cm^2)
1	6.48 ± 0.24	3.07 ± 0.11	0.48
2	3.92 ± 0.21	1.85 ± 0.10	4.10
3	3.16 ± 0.15	1.49 ± 0.07	8.34
4	2.76 ± 0.13	1.31 ± 0.06	12.2
5	2.66 ± 0.12	1.26 ± 0.06	15.4

The doses were approximately uniform over Plates 1 and 2 and were non-uniform over Plates 3, 4, and 5 (due to lesser shielding through the sides than through the top of the detector assembly for the deeper TLD plates). The minimum shielding to the side (for only the detector assembly) of the individual TLDs was 1.96 to 6.66 g/cm^2 Al equivalent. All shielding was converted to Al equivalent on the basis of the relative ranges of 100 MeV protons in the materials.

MEASUREMENTS

The TLD measurements from the four experiments are given in Tables 1-4. The highest doses are seen to be near the trailing edge under thin shielding. Doses are lower by more than a factor of two near the leading edge, taking shielding into account, and doses at the Earth end are intermediate between the leading and trailing edges. This distribution of doses is due to trapped proton anisotropy combined with the shielding from the LDEF vehicle, which together yield a dose maximum at the western side of the vehicle.

The distribution of doses within a given flight canister is also complex, as demonstrated from the P0006 measurements in Fig. 1. As vertical shielding thickness of the TLD plates increases, average dose decreases and the spread in doses across a plate increases. The spread is due to radiation entering through the sides of the canister. The solid line represents the distribution of smallest doses from the TLD plates, near the plate centers, where the effect of radiation entering through the sides of the canister is minimized. A comparable study of dose distribution cannot be done for the other three experiments where there were only a few TLDs per plate.

The doses measured in the A0015 Biostack canisters can be compared with other canister measurements reported by Reitz.[1] Table 5 shows an approximate agreement of measured doses at the trailing edge and at the Earth end, as functions of vertical shielding thickness. Only approximate agreement can be expected since the measurements are from different canisters with different contents, internal geometries and horizontal distributions of TLDs.

Table 2. P0004: LDEF Absorbed Dose Measurements with TLD-700.

Detector No.	Canister No.	Tissue Absorbed Dose (Gy)	Dose Rate (mGy/d)	Al Equivalent Shielding (g/cm^2)
1	6	6.64 ± 0.29	3.14 ± 0.14	0.48
2	6	2.91 ± 0.07	1.38 ± 0.03	11.1
3	6	3.88 ± 0.22	1.83 ± 0.10	~5
4	4	3.12 ± 0.08	1.48 ± 0.04	6.11
5	2	3.05 ± 0.08	1.44 ± 0.04	6.10
6	5	3.09 ± 0.08	1.46 ± 0.04	6.10
7	7	2.93 ± 0.10	1.39 ± 0.05	6.10
8	3	3.15 ± 0.08	1.49 ± 0.05	6.10
GC1		$3.2 \pm 0.2 \times 10^{-3}$	$1.3 \times 10^{-3*}$	
GC2		$3.2 \pm 0.2 \times 10^{-3}$	$1.3 \times 10^{-3*}$	

*For a total detector assembly time of 2418 days. The flight detectors are averaged over the LDEF orbital duration of 2115 days.
The minimum shielding to the side (for only the detector assembly) of the individual TLDs was ~12.4 g/cm^2 Al equivalent. All shielding was converted to Al equivalent on the basis of the relative ranges of 100 MeV protons in the materials. The proton range in the seed was assumed to be equal (in units of g/cm^2) to that of polycarbonate plastic.

Table 3. M0004: LDEF Absorbed Dose Measurements with TLD-700.

Detector No.	TLD Plate No.	Tissue Absorbed Dose (Gy)	Dose Rate (mGy/d)	Al Equivalent Shielding (g/cm^2)
1	1	2.10 ± 0.13	0.99 ± 0.06	2.90
	2	2.37 ± 0.10	1.12 ± 0.05	1.37
2	1	2.19 ± 0.12	1.04 ± 0.06	2.90
	2	2.58 ± 0.09	1.22 ± 0.04	1.37
3(GC)	1	$2.9 \pm 0.2 \times 10^{-3}$	$1.3 \pm 0.1 \times 10^{-3*}$	
	2	$3.2 \pm 0.2 \times 10^{-3}$	$1.4 \pm 0.1 \times 10^{-3*}$	
4(GC)	1	$2.9 \pm 0.2 \times 10^{-3}$	$1.3 \pm 0.1 \times 10^{-3*}$	
	2	$2.9 \pm 0.2 \times 10^{-3}$	$1.3 \pm 0.1 \times 10^{-3*}$	

*For a total detector assembly time of 2271 days. The flight detectors are averaged over the LDEF orbital duration of 2115 days.
All shielding materials were converted to Al equivalent on the basis of the relative ranges of 100 MeV protons in the materials.

Table 4. A0015: LDEF Absorbed Dose Measurements with TLD-700.

Canister No.*	TLD Plate No.	Tissue Absorbed Dose (Gy)	Dose Rate (mGy/d)	Al Equivalent Shielding (g/cm^2)
1	1	3.93 ± 0.08	1.86 ± 0.04	1.66
	2	2.74 ± 0.23	1.30 ± 0.11	6.23
	3	2.41 ± 0.18	1.14 ± 0.09	10.0
2	1	4.49 ± 0.11	2.12 ± 0.05	3.85
	2	3.29 ± 0.22	1.56 ± 0.10	7.83
	3	3.04 ± 0.32	1.44 ± 0.15	11.7
3	1	3.47 ± 0.22	1.64 ± 0.10	—

*Canister #1 was to Earthside.
*Canister #2 was at the trailing edge.
*Canister #3 was vented to space and at the trailing edge.
Minimum shielding to the side (for only the detector assembly) of the individual TLDs was 2.52 to 5.31 g/cm^2 Al equivalent.
All shielding materials were converted to Al equivalent on the basis of the relative ranges of 100 MeV protons in the materials.

Table 5. Comparison of LDEF A0015 Absorbed Doses from TLD-700.

Location	Laboratory	Tissue Absorbed Dose (Gy)	Vertical Shielding (g/cm^2)
Earthside	USF*	3.93 ± 0.08	1.66
	DLR**	3.79 ± 0.17	0.7
		3.89 ± 0.19	0.7
	USF	2.41 ± 0.18	10.
	DLR	2.22 ± 0.30	12.
		1.99 ± 0.25	14.
Trailing Edge	USF	4.49 ± 0.11	3.85
	DLR	4.73 ± 0.26	0.7
		3.88 ± 0.64	2.
	USF	3.04 ± 0.32	12.
	DLR	2.38 ± 0.22	12.
		2.46 ± 0.26	12.

*University of San Francisco
**DLR Institut für Flugmedizin (see 1 Reitz, G.: Preliminary Doses on LDEF. *Proc. XXVIII Plenary COSPAR Meeting, The Hague, 1990*)

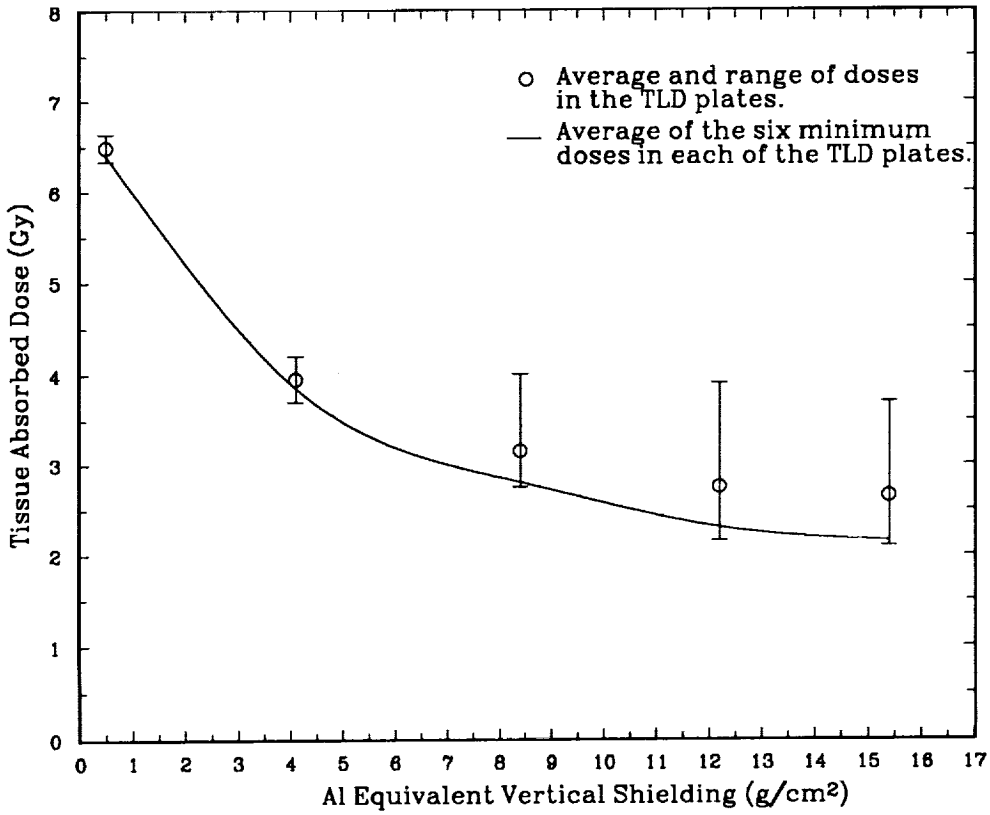

Figure 1: TLD-700 doses in the LDEF P0006 experiment.

COMPARISON OF MEASURED AND CALCULATED DOSES

The Marshall Space Flight Center Proton Transport Code, which utilizes directionally-dependent trapped proton spectra[2], has been used to calculate doses for comparison with measured values. The flight canister physical configurations were modeled for the calculations.[3] Comparisons with measurements are shown in Table 6. The ratio of calculated to measured doses is approximately 50% near the trailing edge and at the Earth end, and approximately 80% near the leading edge. The GCR contribution to dose is not included in the calculations but at the LDEF orbit this represents a small fraction of total dose.[4,5] The differences seen are representative of the present state of trapped proton models and calculational codes. The different dose ratios near the leading edge, as compared with other locations, are not presently understood.

CONCLUSIONS

TLD measurements in four LDEF experiments have yielded absorbed dose as a function of shielding thickness near the leading and trailing edges and at the Earth side of the LDEF vehicle. A consistent set of dose values is produced which defines much of the LDEF radiation environment and provides comparisons for dose calculations using advanced trapped proton predictions and transport codes. Dose rates up to 3.14 mGy/d (0.48 g/cm^2 shielding) and down to 1.26 mGy/d (15.4 g/cm^2 shielding) were found near the trailing edge. The dose rate range near the leading edge was 0.99-1.22 mGy/d (2.90-1.37 g/cm^2 shielding) and at the Earth end it was 1.14-1.86 mGy/d (10.0-1.66 g/cm^2 shielding). Calculations using directionally dependent trapped proton spectra produced doses less than those measured with ratios of about 50% for locations near the trailing edge and at the Earth end, and about 80% near the leading edge. Further refinement is needed in the trapped proton modeling. This goal may be advanced by results from other radiation detectors flown in the LDEF experiments which are still under analysis.

REFERENCES

1. Reitz, G.: Preliminary Total Dose Measurements on LDEF. *Proc. XXVIII Plenary COSPAR Meeting*, The Hague, June/July 1990.

2. Armstrong, T. W.; Colborn, B. L.; and Watts, J. W.: *Characteristics of Trapped Proton Anisotropy at Space Station Freedom Altitudes*. SAIC Report No. SAIC-90/1474, 1990.

3. Colborn, B. L.; and Armstrong, T. W.: *Geometry and mass model of ionizing radiation experiments on the LDEF satellite*. SAIC Report No. SAIC-TN-9202, 1992.

4. Benton, E. V.; Heinrich, W.; Parnell, T. A.; Armstrong, T. W.; Derrickson, J. H.; Fishman, G. J.; Frank, A. L.; Watts, J. W. Jr.; and Wiegel, B.: Ionizing Radiation Exposure of LDEF (Pre-recovery Estimates), *Nucl. Tracks Radiat. Meas.* Vol. 20, No. 1, 1992, pp.75-100.

5. Armstrong, T. W.; and Colborn, B. L.: *Scoping Estimates of the LDEF Satellite Induced Radioactivity*. SAIC Report No. SAIC-90/1462, 1990.

Table 6. LDEF Absorbed Dose Calculations: Comparison with TLD Measurements.

	Detector	Location	Shielding Min. Al. Equiv. (g/cm^2)	Absorbed Dose in Tissue (cGy) Measured	Calculated	Ratio: Calculated/ Measured
Exp. P0004	#1	Can. #6	0.48	664 ± 29	338	0.51
	#3	Can. #6	~5	388 ± 22	170(a)	0.44
	#4	Can. #4	6.1	312 ± 8	172	0.55
Tray F2	#5	Can. #2	6.1	305 ± 8	170	0.56
Near Trailing	#6	Can. #5	6.1	309 ± 8	172	0.56
Edge	#7	Can. #7	6.1	293 ± 10	167	0.57
	#8	Can. #3	6.1	315 ± 8	172	0.55
	#2	Can. #6	11.1	291 ± 7	141	0.48
Exp. P0006	TLD Plate #1		0.48	630(b)	327	0.52
	TLD Plate #2		4.1	367	182	0.50
Tray F2	TLD Plate #3		8.3	275	138	0.50
Near Trailing	TLD Plate #4		12.2	218	118	0.54
Edge	TLD Plate #5		15.4	208	110	0.53
Exp. M0004	#1	Plate #2	1.37	237 ± 10	198	0.84
Tray F8	#1	Plate #1	2.90	210 ± 13	168	0.80
Near Leading	#2	Plate #2	1.37	258 ± 9	207	0.80
Edge	#2	Plate #1	2.90	219 ± 12	180	0.82
Exp. A0015	TLD Plate #1		1.66	393 ± 8	205(c)	0.52
Tray G2	TLD Plate #2		6.23	274 ± 23	127	0.46
Earth End	TLD Plate #3		10	241 ± 18	113	0.47

(a) Calculated at 6.1 g/cm^2 depth.
(b) Measured values at middle TLD plate (i.e. minimum TLD value in plate), corresponding to location used in calculations.
(c) Detailed geometry description of Tray G2 not included in calculations.

LET SPECTRA MEASUREMENTS OF CHARGED PARTICLES IN THE P0006 EXPERIMENT ON LDEF*

E. V. Benton, I. Csige, K. Oda, R. P. Henke, A. L. Frank, E. R. Benton, and L. A. Frigo
Physics Department
University of San Francisco
2130 Fulton St. San Francisco, CA 94117-1080
Ph: 415-666-6281, Fax: 415-666-2469

T. A. Parnell, J. W. Watts, Jr., and J. H. Derrickson
ES-62, NASA-George C. Marshall Space Flight Center
Marshall Space Flight Center, AL 35812
Ph: 205-544-7690, Fax: 205-544-7754

SUMMARY

Measurements are under way of the charged particle radiation environment of the LDEF satellite using stacks of plastic nuclear track detectors (PNTDs) placed in different locations of the satellite. In the initial work the charge, energy and linear energy transfer (LET) spectra of charged particles were measured with CR-39 double layer PNTDs located on the west side of the satellite (Experiment P0006). Primary and secondary stopping heavy ions were measured separately from the more energetic particles. Both trapped and galactic cosmic ray (GCR) particles are included, with the latter component being dominated by relativistic iron particles.

The results from the P0006 experiment will be compared with similar measurements in other locations on LDEF with different orientation and shielding conditions.

The remarkably detailed investigation of the charged particle radiation environment of the LDEF satellite will lead to a better understanding of the radiation environment of the Space Station Freedom. It will enable more accurate prediction of single event upsets (SEUs) in microelectronics and, especially, more accurate assessment of the risk — contributed by different components of the radiation field (GCRs, trapped protons, secondaries and heavy recoils, etc.) — to the health and safety of crew members.

*Work partially supported by NASA Grant No. NAG8-168 NASA Marshall Space Flight Center, AL 35812

INTRODUCTION

Cosmic ray and trapped charged particles contribute to the health risk of crew members of manned space flight and produce single event upsets (SEUs) in microelectronics in space. Risk estimations are usually based on measurements of the charged particle radiation environment external to the spacecraft in space and using transport codes to calculate the radiation environment internal to the spacecraft. Measurements of the spacecraft radiation environment are also essential to validate transport codes based on three-dimensional mass models, and in some cases to provide direct data for risk estimation. Plastic nuclear track detectors (PNTDs) have been widely used to measure both external (charge and energy spectra of GCRs and trapped particles) and internal (LET spectra, charge and energy spectra of secondary particles) charged particle radiation environments.

PNTDs exposed as part of the LDEF P0006 experiment "Linear Energy Transfer Spectrum Measurement" are being analyzed in order to measure the charged particle radiation environment of the LDEF. Measurements are being made of the charge, energy and linear energy transfer (LET) spectra as functions of shielding and detector location and orientation on the LDEF. LET spectra measured from the P0006 experiment and from other LDEF experiments designed to measure the charged particle radiation environment of LDEF constitute a unique set of measurements not likely to be duplicated in the foreseeable future. Results from P0006 will be compared to other measurements made aboard the LDEF satellite and with model calculations.[1,2]

EXPERIMENTS

The P0006 experiment was located in the F2 tray near the trailing edge of the LDEF satellite. Tray F2 also contained the P0004 "Seeds" experiment. The P0006 consisted of nine modular stacks of passive ionizing radiation detectors assembled into a stack with detector layers oriented parallel to the plane of the experiment tray. Four side stack modules were placed on the sides of the main stack. The configuration of the P0006 is shown in Figure 1. Each detector module contained a variety of passive ionizing radiation detectors and a layer of aluminum separator. The P0006 stack was 4.5" by 4.5" square and 4.0" high. It was sealed in an aluminum canister and bolted to the F2 tray. Air pressure was maintained within the canister over the duration of the mission.

Measurements of the LET spectrum as a function of shielding and detector orientation are under way. In addition, detailed measurements of the high LET tail region of the LET spectra are being made. Preliminary results of these measurements are presented below.

C-3

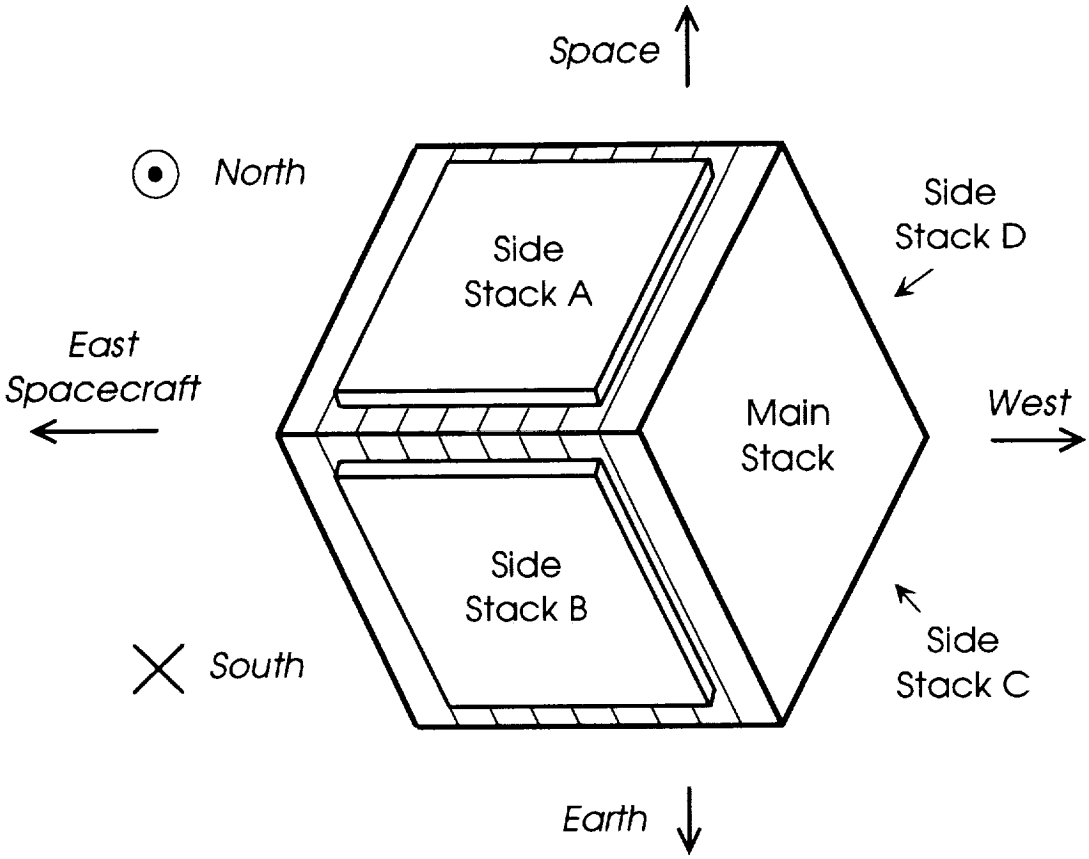

Figure 1: Configuration of LDEF P0006.

RESULTS

Dependence of LET Spectra on Shielding

LET spectra were measured in the main stack in CR-39 made with 1% DOP plasticizer under 6.5 and 9.5 g/cm^2 Al equivalent shielding. The CR-39/DOP detectors were at the center of the main stack and measurements were made in the same region of each detector. CR-39 with DOP is somewhat less sensitive than pure CR-39, but has a clearer surface making track location and measurement easier. The detectors were processed for 36 hours in 6.25 N NaOH at 50°C. Measurements were made using a double layer Track Coincidence Method. Two adjacent layers of CR-39 were etched and then reassembled into their flight configuration relative to one another on the microscope stage. Particle events were selected for measurement when two tracks produced by the same particle were found, one on each adjacent surface. Major and minor axes of the track were measured using a video micrometer. LET was calculated using a detector response function based on data from accelerator-exposed calibration samples. A further internal calibration was carried out by adjusting the spectrum with respect to the relativistic iron peak.

Figure 2 is the integral LET flux spectra for the two shielding configurations. Curve ○ was measured under 6.5 g/cm^2 and curve □ was measured under 9.5 g/cm^2. At low LET (<100 keV/μm) curve ○ lies a factor of 2 above curve □. This shows the attenuation of low LET particles, most likely trapped protons, as a function of shielding. There is good agreement between the two curves at high LET (>100 keV/μm). For the LDEF orbit (28.5° inclination) the major contribution to the high LET portion of the spectrum is from short range recoils. The good agreement between the two curves in the high LET region shows that the density of recoil tracks is not a steep function of shielding at these shielding depths. The shortest recoil track measured in this plot has a range of ~16 μm. Hence the shorter range recoil events are excluded from these LET flux spectra.

Dependence of LET Spectra on Detector Orientation

Four PNTD stacks were attached to the sides of the main stack. The exact orientation of the P0006 was based on comparison of experimental results with expected directional dependent effects and is represented in Figure 1. Side stack A was oriented toward the north and toward the space end of the satellite. Side stacks B and C were oriented toward the Earth end of the satellite. B was oriented toward the north while C was oriented toward the south. Measurements were made in CR-39/DOP. The self shielding of the P0006 experiment was 1.3 g/cm^2 in the locations where the side stack LET spectra were measured. The effect of the additional shielding from the P0004 experiment and from the LDEF satellite is not known at this time. The detectors were processed for 36 hours in 6.25 N NaOH at 50°C.

Figure 3 shows the integral LET flux spectra for side stacks A, B, and C. In the low LET region, there is good agreement between the measurements from B and C, while A rises above the other two by about a

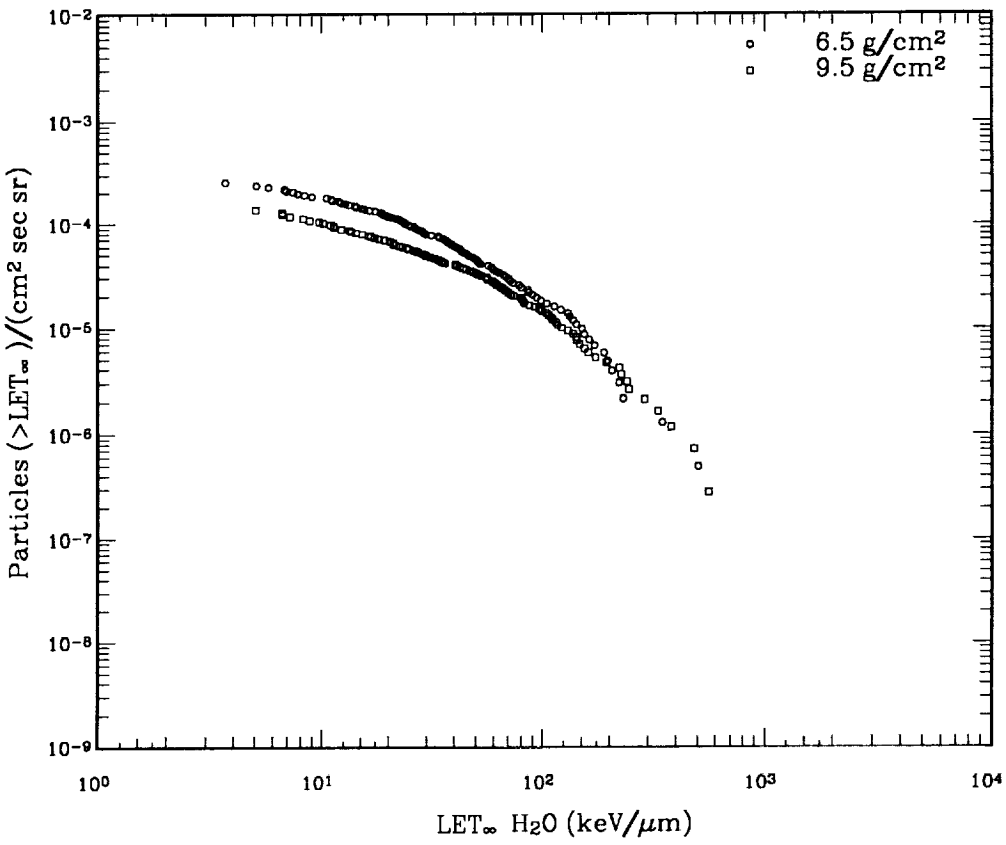

Figure 2: LET Spectra measured in the main stack beneath two shielding depths. Curve o was under 6.5 g/cm^2 and Curve □ was under 9.5 g/cm^2. Both spectra were measured in CR-39/DOP using the track coincidence method.

factor of two. Under the assumption that our interpretation of the experiment orientation is correct, this shows a higher flux of low LET particles from the space side of the satellite than from the Earth side. These low LET particles, most probably trapped protons, approach the experiment from the space/west side of the spacecraft. At higher LET, the reasons for the good agreement between A and B and their poor agreement with C are still not known.

High LET Tail

Sheffield Polycarbonate Measurements

Sheffield polycarbonate (PC) is a much less sensitive PNTD than CR-39, but has some advantages in measuring the high LET tail. Without ultraviolet (UV) sensitization, its LET threshold is about 300 keV/μm which means it cannot detect protons or alpha particles. Hence, the track densities in LDEF PC samples are much lower than in CR-39 samples and the overlapping of tracks is negligible. In the higher LET portion, PC has higher LET resolution than CR-39.

In a preliminary study, PC pairs were etched to remove about 10 μm from each surface. Overetched, bubble-like tracks were found on both surfaces which were identified as tracks from short range heavy recoil particles. To be able to use the track coincidence method, an even shorter etching time (12 hours in 6.25 N NaOH at 50°C) was used which removed about 3–4 μm from the layer surfaces. The range of the short range particles which can be identified as pairs using the track coincidence method is on the order of twice the thickness of the removed layer and was about 6-8 μm in this case.

The etch rate ratio was determined from the measured minor and major axes of the tracks using a constant etch ratio assumption. This approximation is very good if the residual range of the particle is significantly greater than the removed layer. In our case, the residual range of the majority of particles was on the order of the removed layer which means that some systematic error is present in the etch rate ratio estimation. This error depends on the range and on the dip angle of the particle and in most cases it was estimated to be within about 50%.

The LET of the particles was calculated from the etch rate ratios using an external calibration curve. The calibration curve was generated using tracks of stopping Ar ions obtained from the Bevalac (Berkeley). It also contains some known uncertainties which, together with the constant etch rate ratio approximation, makes the LET determination not better than about a factor of 2.

Finally, the LET spectra were generated using an assumed isotropic directional distribution of recoil particles. This assumption is also very questionable because of the known strong anisotropy of the high energy trapped proton environment by which these recoils were produced. In a calibration experiment with 200 MeV protons, we found that the directional distribution of heavy recoils reflects the directionality of the primary beam.[3]

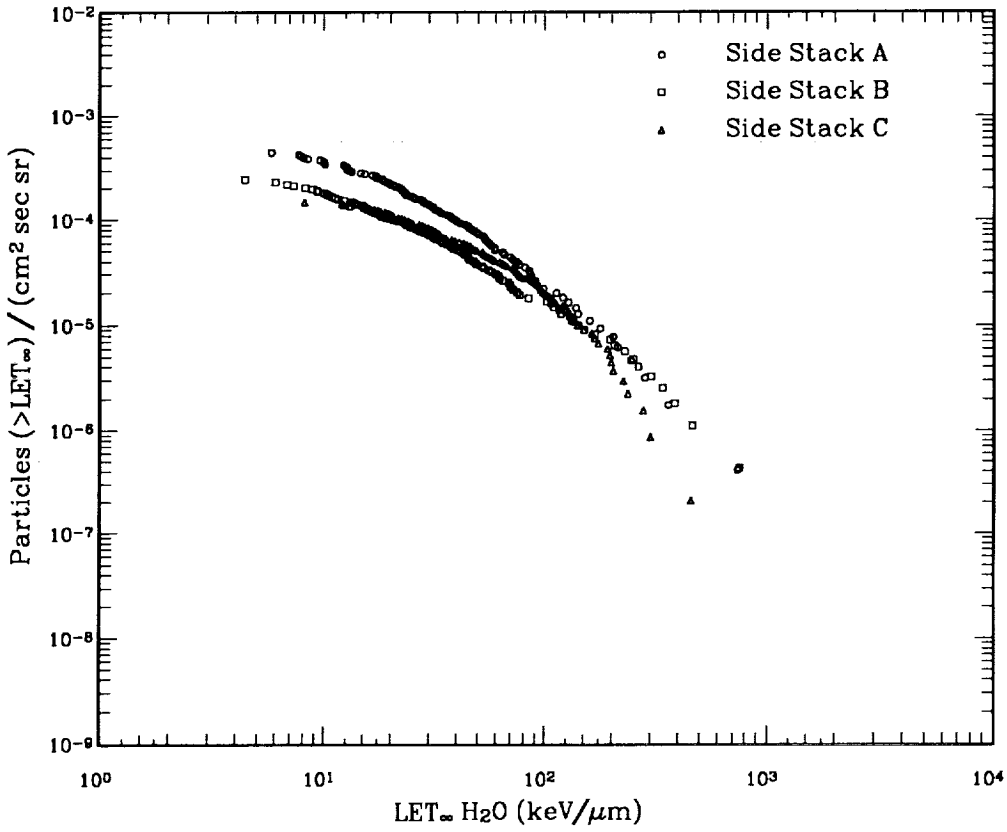

Figure 3: LET Spectra in side stacks showing effect of orientation of detectors. Curve ○ is from side stack A and faced toward space/north. Curve □ is from side stack B and faced Earth/north. Curve △ is from side stack C and faced Earth/south. All three spectra were measured in CR-39/DOP under a shielding of 1.3 g/cm^2.

The high LET tail was measured in CR-39(DOP) using a multiple-etch technique. After a short etching time only tracks of high LET particles are present. Tracks of low LET particles are not present because of the low etch rate ratio and a possible etch induction layer. High LET particles in CR-39 are mainly heavy recoils, but include stopping alpha particles, too. After longer etching times, the tracks of short-range recoils become overetched and they can no longer be recognized as pairs. At the same time, pairs of lower LET particles appear and become measurable. With this technique, a large portion of the high LET tail can be covered. Shortest range particles included in the spectra are determined by the shortest etching time, which is limited by the resolution of the microscope used to measure the track dimensions.

Figure 4 shows the LET spectra from the Sheffield polycarbonate under 7.5 g/cm^2 and the LET tail measured in CR-39(DOP) under 0.65 g/cm^2. The LET spectra in CR-39(DOP) under 6.5 g/cm^2 shielding measured by the track coincidence method are included for reference. The standard track coincidence method neglects short-range recoils as can be seen in the high LET portion of the spectrum as compared with the other measurements in this figure. The LET spectrum tail measured in polycarbonate lies to the left of the CR-39(DOP) multiple-etch spectrum. The minimum range of particles measured in the polycarbonate was 6—8 μm. While this is a significant improvement over the minimum range of measurements in the multiple-etch spectrum ($\sim$16 μm), it still excludes even shorter range recoils. The high LET tail measured by the multiple-etch technique in CR-39(DOP) under 0.65 g/cm^2 lies above and to the right of that for polycarbonate. The shortest range tracks measured are 2—3 μm in length. There is good agreement between the two polycarbonate measurements demonstrating that density of recoils in the high LET tail is not highly dependent on shielding. The high LET tail measured in CR-39(DOP) is considered to be more accurate than that in polycarbonate due to the shorter range particles included in the spectra, the more accurate determination of LET from measured track parameters in the CR-39 and to the inherent uncertainties in the polycarbonate measurements for the calibration and determination of LET. The multiple-etch LET measurement may also show an effect from the very low shielding (0.65 g/cm^2) of this CR-39 layer.

CONCLUSIONS

LET spectra have been measured for a number of detector layers in the P0006 main stack and side stacks. The dependence of the low LET region of the spectrum on shielding and detector orientation has been established. The major contribution to the high LET tail has been determined to be from short-range recoils. The density of short-range recoils, and hence the high LET tail, was found to be relatively independent of shielding up to several g/cm^2 for the LDEF orbit.

The high LET tail is being measured using the multiple-etch technique at different shielding depths in the main stack. These measurements will determine any dependence of the shorter range recoils on shielding. In addition, further etching and measurement of the CR-39 layer already measured will provide charge and energy spectra of the high LET tail and an internal calibration based on stopping protons and possibly stopping alpha particles. The internal calibration will improve the accuracy of the high LET tail measurement.

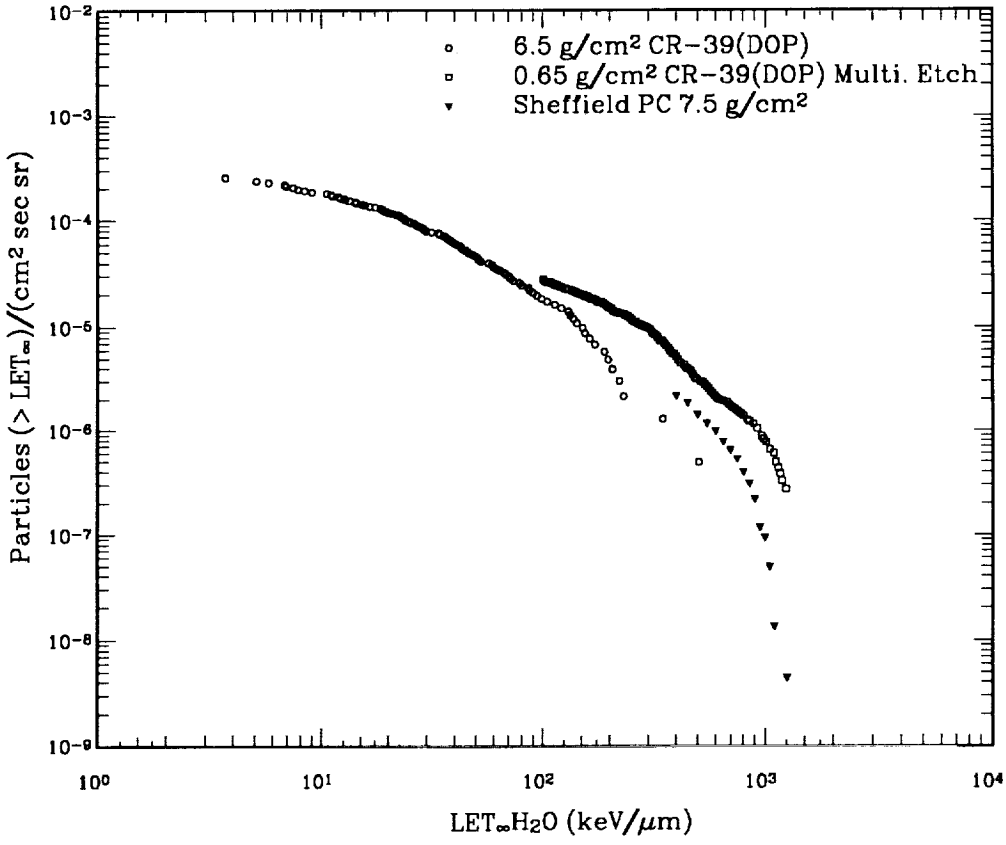

Figure 4: Measurements of the high LET tail in PC and CR-39(DOP).

REFERENCES

1. Armstrong, T.W. and Colborn, B.L. "Radiation Model Predictions and Validation Using LDEF DATA." Second LDEF Post-Retrieval Symposium, 1993, NASA CP-3194.

2. Benton, E.V.; Heinrich, W.; Parnell, T.A.; Armstrong, T.W.; Derrickson, J.H.; Fishman, G.J.; Frank, A.L.; Watts, J.W. and Wiegel, B. "Ionizing Radiation Exposure of LDEF: Pre-recovery Estimates." Nuclear Tracks and Radiation Measurements, Vol. 20, No. 1, 1992, pp. 75-100.

3. Csige, I.; Benton, E.V.; Soundararajan, S. and Benton, E.R. "Light-Heavy Ion Measurements in CR-39 Located on the Earth Side of LDEF." Second LDEF Post-Retrieval Symposium, 1993, NASA CP-3194.

LIGHT–HEAVY ION MEASUREMENTS IN CR–39 LOCATED ON THE EARTH SIDE OF LDEF *

I. Csige, E. V. Benton, S. Soundararajan and E. R. Benton
Eril Research Inc. P. O. Box 150788
San Rafael, CA 94915-0788
Phone: 415-666-2333, Fax: 415-454-4089

SUMMARY

The azimuthal angle distribution and the charge and energy spectra of selected light–heavy ($5 \leq Z \leq 8$) stopping particles were measured in a single layer of CR-39 plastic nuclear track detector (PNTD) from the stack of the A0015 experiment located on the Earth–end of the LDEF satellite. The directional incidence of the trapped protons is studied by comparing the azimuthal angle distribution of selected recoils, obtained in the LDEF detectors, to that obtained through calibrations of PNTDs with exposures performed with 200 MeV proton beams from different directions.

INTRODUCTION

The purpose of the A0015 Free Flyer Biostack experiment was to measure the total absorbed doses and particle LET spectra as a function of depth in shielding material at different positions on the surface of the LDEF satellite[1,2,3,4,5,6,7].

Cosmic ray charged particles contribute to the health risk of crew members and high LET particles can cause single event upsets (SEUs) in microelectronics. In the present study the charge and energy spectra of selected high LET particles (mostly heavy recoils) were measured in order to compare with model calculations. The contribution of high LET recoils to the LET spectra seems to be more significant than previously thought. Their flux in the inner radiation field is much higher than the flux of the high LET primary cosmic ray particles under the same shielding conditions. To measure the LET spectra, plastic nuclear track detectors are widely used. A standard technique is developed to measure the LET spectra in regular STS flight. This technique, however, has a range threshold about 30–40 μm, therefore recoil particles with a range shorter than that threshold could not be detected. Hence, short range recoils are not included in regular LET spectra measurements performed in STS flights. This range cut–off value, however, is proportional to the etching time which had to be much shorter in the case of the LDEF samples because of the expected high track density. Also, the fluence of these relatively long range recoils is much higher in the case of the LDEF samples because of the long duration exposure. Heavy recoils, satisfying

*Work partially supported by NASA contract No. NAS8-38610 (NASA–Marshall Space Flight Center, Huntsville).

certain selection criteria, can be identified in CR–39 PNTDs by measuring the geometrical parameters of their single–surface etched track. Detection efficiency of these particles can be calculated and experimental and theoretical results can be compared in the future. This gives a good opportunity to validate model calculations.

The directionality distribution of these particles was measured and compared with calibration measurements performed with 200 MeV proton beams. Some conclusions about the directionality of the primary trapped proton radiation environment are drawn.

EXPERIMENT

Detector stacks filled two Biostack containers and partially filled a third in the A0015 experiment. Detector stack No. 1 (Earth–side) and No. 2 (non–Earth–side) were positioned in the center of Al canisters. Each canister was sealed from the outside environment by means of an O–ring. The inner wall of each canister was covered by an acrylic layer.

Two layers of CR–39 from the Earth–side stack and two layers from the non–Earth–side stack were selected for analysis. The minimum shielding of these layers was 10.0 g/cm^2 for the Earth–side layers and 4.2 g/cm^2 for the non–Earth–side PNTDs. The layers were etched in a 6.25 N NaOH solution at 50 °C for 36 hours. A thickness of 8–10 μm was removed from each surface.

Measurement of Charge and Energy of "Energetic" Recoil Particles

A layer from the Earth–side stack was selected for these measurements of the charge and energy of selected energetic recoil particles. The minimum shielding distance (from the outer surface of the canister) for this layer was 10.3 g/cm^2. The surface of the layer was parallel with the surface of the Earth. That side of the layer nearest the satellite was scanned. The scanned area was 4.32 cm^2 and was located at the center of the layer. 400 undercut, rounded tracks were measured in the scanned area and 200 of these were selected for charge and energy determination. The range of the particles in the CR–39 layer and the reduced etch rate ratio ($V_T/V_B - 1$) along the particle's tracks were determined from track geometry measurements of etched tracks using the assumption of constant etch rate ratio. The particles were identified using an internal calibration technique and the REL (Restricted Energy Loss) model of track formation with a threshold energy of 200 eV. The internal calibration is based on the assumption that recoil particles with the highest charge are oxygen because there are no particles with larger charge in the composition of the CR–39 material. The corresponding charge distribution is shown in Figure 1.

The track selection criteria were determined in such a way as to ensure that only "energetic" recoil particles were measured, the range of which had to be greater than $\approx$ 15–20 μm depending on the charge of the particles. Currently, a detailed detection efficiency calculation is under way to convert this data into charge, energy and LET fluence spectra.

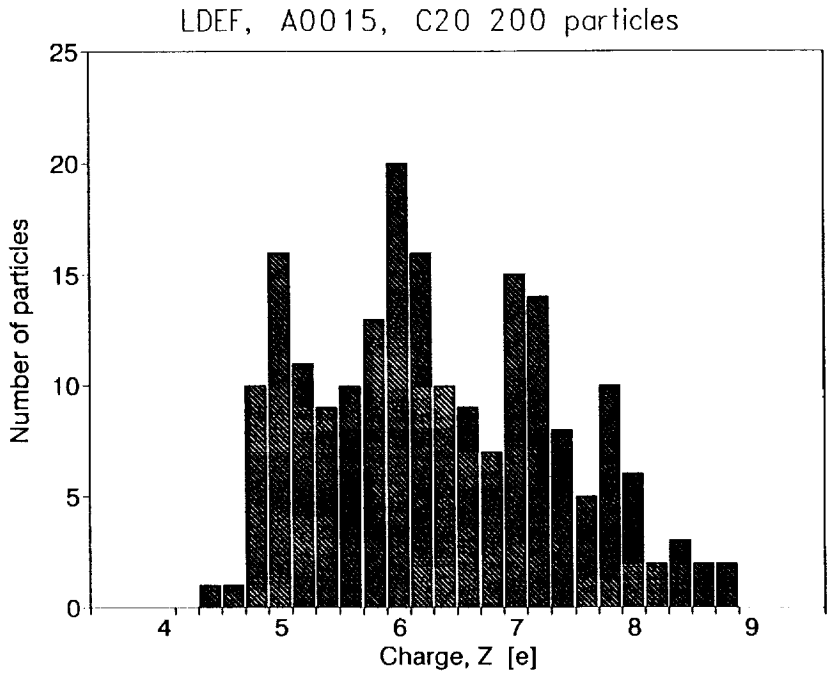

Figure 1: Number of energetic recoil particles as a function of charge measured in a CR-39 layer from the LDEF A0015 Earth–side stack.

Directionality of Recoil Particles

In addition to charge and energy spectra measurements, the directionality distribution of recoil particles was measured. Figure 2 shows the azimuthal angle distribution of the 400 measured tracks. The azimuthal angle in this case is the angle of the projection of the particle trajectory onto the detector surface measured from an arbitrary x–axis on the detector sheet.

Similar measurements have been performed on calibration samples of CR–39 exposed to 200 MeV protons at different angles of incidence. The corresponding azimuthal angle distributions are presented in Figure 3. The comparison of these distributions with that obtained from the LDEF sample confirm the anisotropic nature of the primary proton fluence by which these energetic heavy recoils were produced in the case of the LDEF.

CONCLUSIONS

Charge and energy spectra of selected energetic recoil particles can be measured in CR–39 samples with acceptable charged resolution in the case of the LDEF samples. Together with detailed detection efficiency calculations these spectra can be compared with theoretical results to validate model calculations.

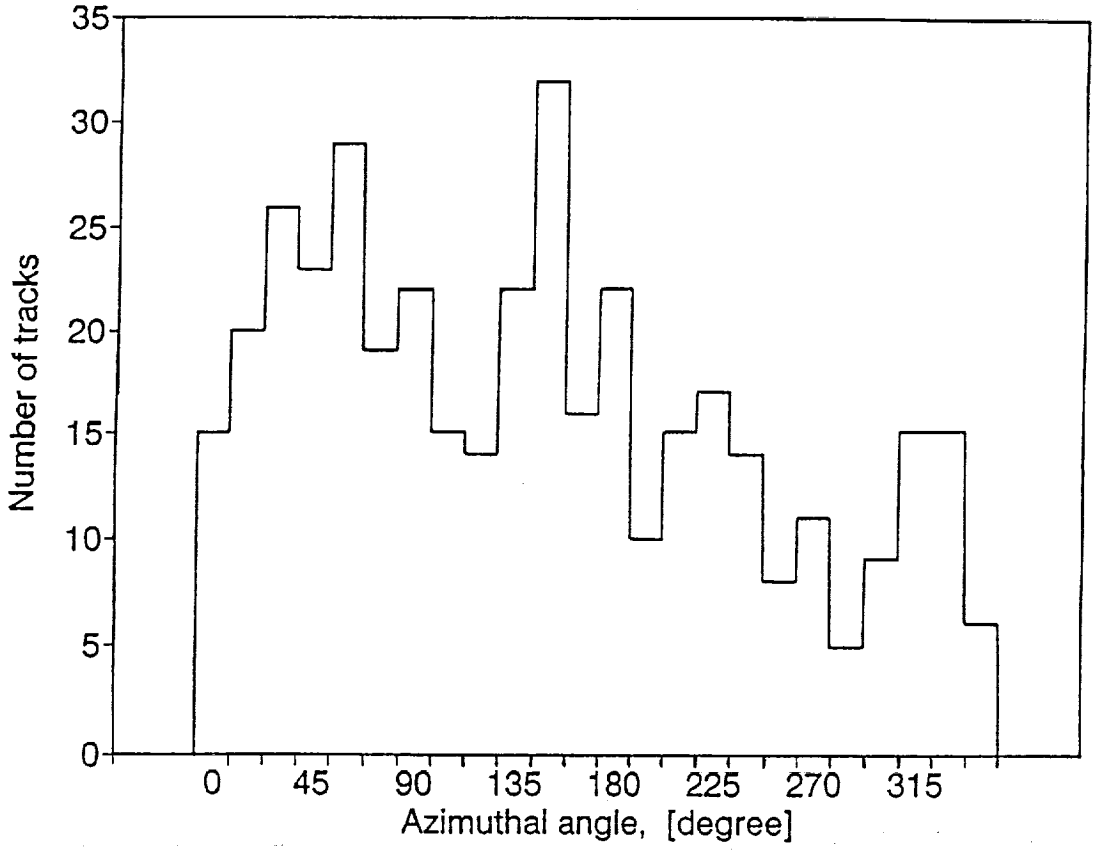

Figure 2: Azimuthal angle distribution of 400 tracks of energetic heavy recoils in a CR–39 layer from the LDEF A0015 Earth–side stack. The anisotropy reflects the anisotropy of the high energy trapped proton fluence by which these recoils were produced.

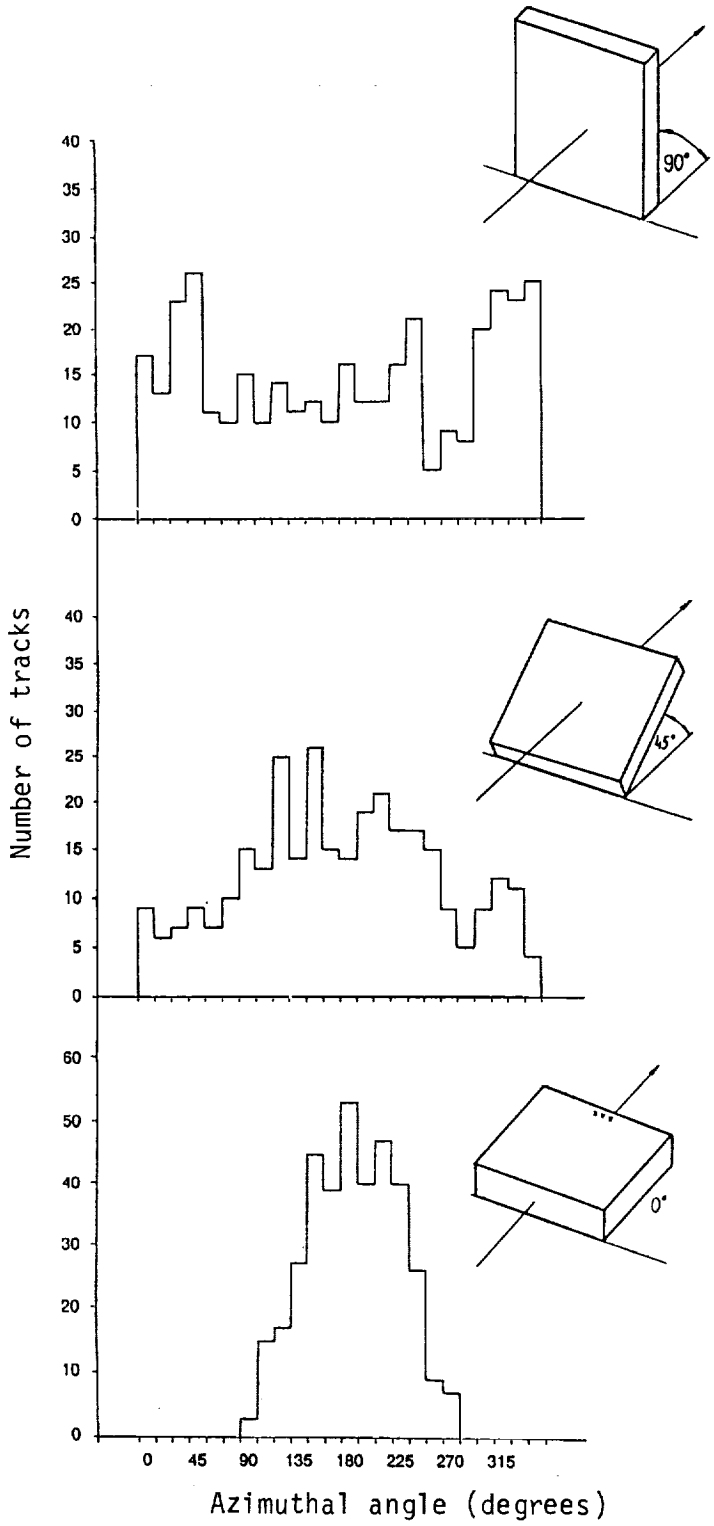

Figure 3: Azimuthal angle distributions of 300 energetic recoils produced by 200 MeV protons incident on CR–39 at various dip angles. Anisotropy of recoils show the directionality of the primary proton beam in the case of 45° and 0° dip angles.

It is found through calibration experiments that the directionality of energetic recoil particles reflects the directionality of the primary high energy proton beam by which the recoils were produced. The analysis of the azimuthal angle distribution of energetic recoils in an LDEF sample confirms the anisotropic nature of the high energy trapped proton fluence in the case of the LDEF.

Similar experiments are under way in a sample from the non–Earth–side stack to study the location dependence of the charge and energy spectra of energetic recoils. Also, a directionality study of energetic recoils is under way in samples with surfaces parallel with the East–West direction. The directionality of recoils in these samples is expected to be more definite as the majority of the trapped protons is expected to have arrived from the West direction. These experiments will be also used for validation of directionality of trapped proton radiation environment models.

REFERENCES

1. Armstrong, T. W.; and Colborn, B. L.: Radiation model predictions and validation using LDEF data. *Second LDEF Post-Retrieval Symposium*, NASA CP-3194, 1993.

2. Benton, E. V.; Heinrich, W., Parnell, T. A.; Armstrong, T. W.; Derrickson, J. H.; Fishman, G. J.; Frank, A. L.; Watts, J. W.; and Wiegel, B.: Ionizing radiation exposure of LDEF: Pre-recovery estimates. *Nuclear Tracks and Radiation Measurements*, Vol. 20, No. 1 1992, pp. 75-100.

3. Benton, E. V.; Frank, A. L.; Benton, E. R.; Csige, I.; Parnell, T. A.; and Watts, J. W. Jr.: Radiation exposure of LDEF: Initial Results. *LDEF–69 Months in Space: First Post-Retrieval Symposium*, NASA-CP 3134, Part 1, Washington DC, 1991, pp. 325-338.

4. Csige, I.; Benton, E. V.; Frank, A. L.; Frigo, L. A.; Benton, E. R.; Parnell, T. A.; and Watts, J. W. Jr.: Charged particle LET-spectra measurements aboard LDEF. *LDEF–69 Months in Space: First Post-Retrieval Symposium*, NASA-CP 3134, Part 1, Washington DC, 1991, pp. 339-346.

5. Harmon, B. A.; Fishman, G. J.; Parnell, T. A.; Benton, E. V.; and Frank, A. L.: LDEF radiation measurements: preliminary results. *Nuclear Tracks and Radiation Measurements*, Vol. 10, No. 1, 1992, pp. 131-136.

6. Watts, J. W. Jr.; Parnell, T. A.; Derrickson, H. J.; Armstrong, T. W.; and Benton, E. V.: Predictions of LDEF ionizing radiation environment. *LDEF–69 Months in Space: First Post-Retrieval Symposium*, NASA-CP 3134, Part 1, Washington DC, 1991, pp. 213-224.

7. Reitz, G.; Bücker, H.; Facius, R.; Horneck, G.; Schaefer, M.; Schott, J. U.; Bayonove, J.; Beaujean, R.; Benton, E. V.; Delpoux, M.; Heilmann, C.; Heinrich, W.; Kranz, A. R.; Planel, H.; Gasset, Y.; Gaubin, G.; Portal, G.; Graul, E. H.; Rüther, W.; Schopper, E.; Tobias, C. A.; and Yang, T. C. First biological and dosimetric results of the free flyer biostack experiment A0015 on LDEF. *LDEF–69 Months in Space: First Post-Retrieval Symposium*, NASA-CP 3134, Part 1, Washington DC, 1991, pp. 1639-1642.

THREE–DIMENSIONAL SHIELDING EFFECTS ON CHARGED PARTICLE FLUENCES MEASURED IN THE P0006 EXPERIMENT OF LDEF *

I. Csige, E. V. Benton and L. Frigo
Physics Department, University of San Francisco, 2130 Fulton St.
San Francisco, CA 94117-1080, USA
Phone: 415-666-2333, Fax: 415-666-2346

T. A. Parnell and J. W. Watts, Jr.
ES–62, NASA–Marshall Space Flight Center
George C. Marshall Space Flight Center, Al 35812, USA
Phone: 205-544-7690, Fax: 205-544-7754

T. W. Armstrong and B. L. Colborn
Science Applications International Corporation, Route 2
Prospect, TN 38477, USA
Phone: 615-68-2603, Fax: 15-468-2676

SUMMARY

Three-dimensional shielding effects on cosmic ray charged particle fluences were measured with plastic nuclear track detectors in the P0006 experiment on LDEF. The azimuthal and polar angle distributions of the galactic cosmic ray particles (mostly relativistic iron) were measured in the main stack and in four side stacks of the P0006 experiment, located on the west end of the LDEF satellite. A shadowing effect of the shielding of the LDEF satellite is found. Total fluence of stopping protons was measured as a function of the position in the main and side stacks of the P0006 experiment. Location dependence of total track density is explained by the three–dimensional shielding model of the P0006 stack. These results can be used to validate 3D mass model and transport code calculations and also for predictions of the outer radiation environment for the space station Freedom.

INTRODUCTION

Cosmic ray charged particles contribute to the health risk of crew members of manned flights and produce single event upsets (SEUs) in microelectronics in space. Risk estimations are usually based on measurements of the outer charged particle radiation environment and use three–dimensional mass

*Work partially supported by NASA grant No. NAG8-168 (NASA–Marshall Space Flight Center, Huntsville).

models and computer transport codes to calculate inner radiation fields. Measurements of the inner radiation environment are also essential to validate transport codes and in some cases to provide direct data for risk estimation. Plastic nuclear track detectors (PNTDs) have been widely used to measure both outer (charge and energy spectra of galactic cosmic rays (GCRs) and trapped particles) and inner (LET–spectra, charge and energy spectra of secondary particles) charged particle radiation fields[1,2,3,4,5,6,7].

A series of PNTD stacks were exposed on the LDEF (Long Duration Exposure Facility) satellite and the ongoing analysis of these stacks makes the cosmic ray charged particle experiments performed on LDEF probably the most comprehensive and, as of today, the most important ever conducted with PNTDs. Unique features of the LDEF satellite make this even more reasonable. The long duration, almost six years in space, makes it possible to study low abundant cosmic rays and measure the high LET-tail with good statistical accuracy. The gravity–stabilized orientation gives the possibility of studying the directionality distribution of cosmic ray charged particles. Also, a detailed mass model of LDEF is available, which makes it possible to compare the inner radiation field and activation measurements with model calculations.

"Outer radiation field measurements" usually actually means "inner radiation field measurements", taking into account the shadowing effects of shielding. This shadowing effect and the contribution of secondary particles to the primary particle fluxes makes a strong difference in the inner and outer radiation fluxes. Hence the understanding of three–dimensional shielding effects on charged particle fluences is essential when interpreting experimental data measured at different locations on LDEF under different shielding distributions. In the present paper we present data of the measurement of galactic cosmic ray Fe particles and stopping trapped proton particles in the main and four side stacks of the P0006 experiment flown on LDEF. The contribution of the three–dimensional shielding effects to the observed anisotropy of Fe particles and to the position dependence of total track density is discussed.

EXPERIMENTS AND RESULTS

The P0006 Experiment

The P0006 experiment on LDEF is a complex experiment to measure the inner and to a certain extent the outer radiation field of cosmic rays. It consisted of activation materials, neutron detectors, thermoluminescent detectors and plastic nuclear track detectors to obtain different kinds of information about the inner radiation field.

The P0006 experiment was located in the F2 tray of LDEF on the west end and close to the space end of the satellite. Its experimental unit consisted of a main and four side stacks as shown in Figure 1. The main stack consisted of 9 sub–stacks of PNTDs, the planes of which were perpendicular to the east–west direction. The side stacks were attached to the four sides of the main stack with the normal vectors pointing out from the main stack into space with the approximate directions as follows: north–space (side stack A), north–Earth (side stack B), Earth–south (side stack C) and south–space (side stack D). (The orientation of the side stacks is assumptive in the sense that experimental results obtained are in agreement with and only

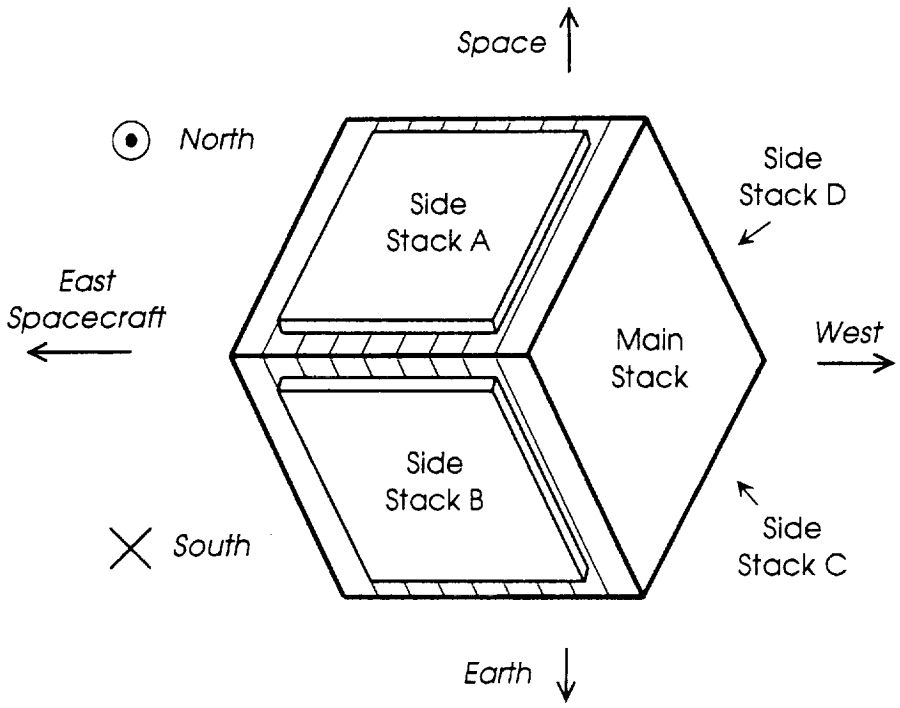

Figure 1: The P0006 experimental block on the LDEF satellite.

with this assumption. Unfortunately it was not possible to confirm the orientation of the side stacks from the data available about the disassembly of the LDEF satellite.)

The P0006 experimental block was placed in a sealed aluminum canister with 1 atmosphere normal air inside. In the surrounding of the P0006 experiment there were 4 other canisters of the P0004 corn seed experiment representing a significant amount of shielding from those directions.

Measurement of Relativistic Fe Particles

Two layers of CR-39 PNTDs were selected from the center of the main stack (6.5 g/cm^2 shielding from the top of the canister) and from the side stacks (1.3 g/cm^2 shielding) for scanning and measuring. The central area of each layer was scanned for tracks in coincidence at the adjacent surfaces. Track pairs were further investigated as to whether they have corresponding tracks on the top surface of the top layer and on the bottom surface of the bottom layer (4–surface tracks). Comparing the size of the tracks at all four surfaces to each other we found that the size of the tracks did not change within experimental errors which means that these tracks were produced by high energy particles. Comparing the differential LET–spectra of 4–surface tracks found in LDEF samples to a differential LET–spectra of 4–surface tracks found in a sample flown on a shuttle flight with similar altitude and inclination to LDEF, we found that practically all 4–surface tracks measured in LDEF samples must be produced by relativistic energy Fe particles. In the case of the sample from the shuttle flight other galactic cosmic ray particles are also included in the differential LET–spectra and the peak of the relativistic Fe particles can clearly be seen because of the

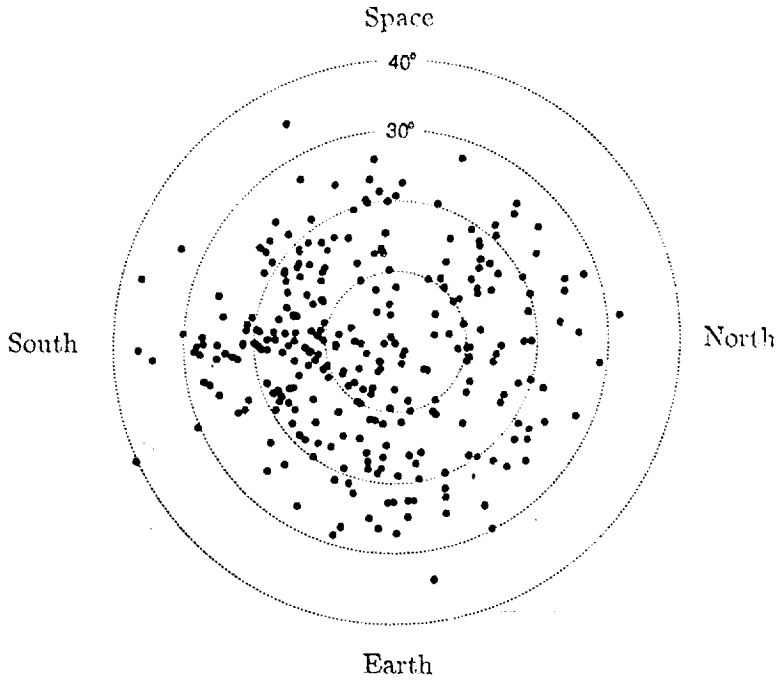

Figure 2: Arriving directions of GCR Fe particles with relativistic energies looking to the west direction from the center of the P0006 experiment on LDEF. Particles with dip angle greater than 40° could not be measured because of the critical angle cut–off of the detector.

relatively high abundance of these particles to the neighboring elements. Lighter than iron relativistic particles could not be seen in the case of the LDEF samples because of the short etching time needed.

300 particles in the main stack and 100 particles in each side stack were identified as relativistic galactic cosmic ray Fe particles in the present experiment. The azimuthal and dip angle distributions of the particles were measured. Since the moving direction along the particle trajectory could not be measured we assumed that all the particles measured arrived from the west direction and moved toward the east direction. Experimental data in the side stacks are consistent with this assumption.

Figure 2 shows from which directions 300 GCR Fe particles arrived to the center of the main stack of the P0006 experiment. No particles could be detected with dip angle (measured from the normal of the detector layer) greater than about 40° because of the dip angle cut–off of the detector. Scanning efficiency close to the cut–off dip angle was also significantly less than 100% due to the difficulty of finding corresponding tracks on the first and fourth surfaces of the CR-39 doublet. Figure 2 shows that arriving directions of particles from the west are very isotropic with some extra particles coming from the south-west, parallel with the Earth's surface.

In Figure 3, empty circles show the arriving directions; filled circles show the leaving directions of 100 particles in each side stack. The shielding of the LDEF satellite is the east side and the shielding of the P0004 canisters are at the center of the graphs. It seems that these large (about 40–150 g/cm^2) shieldings

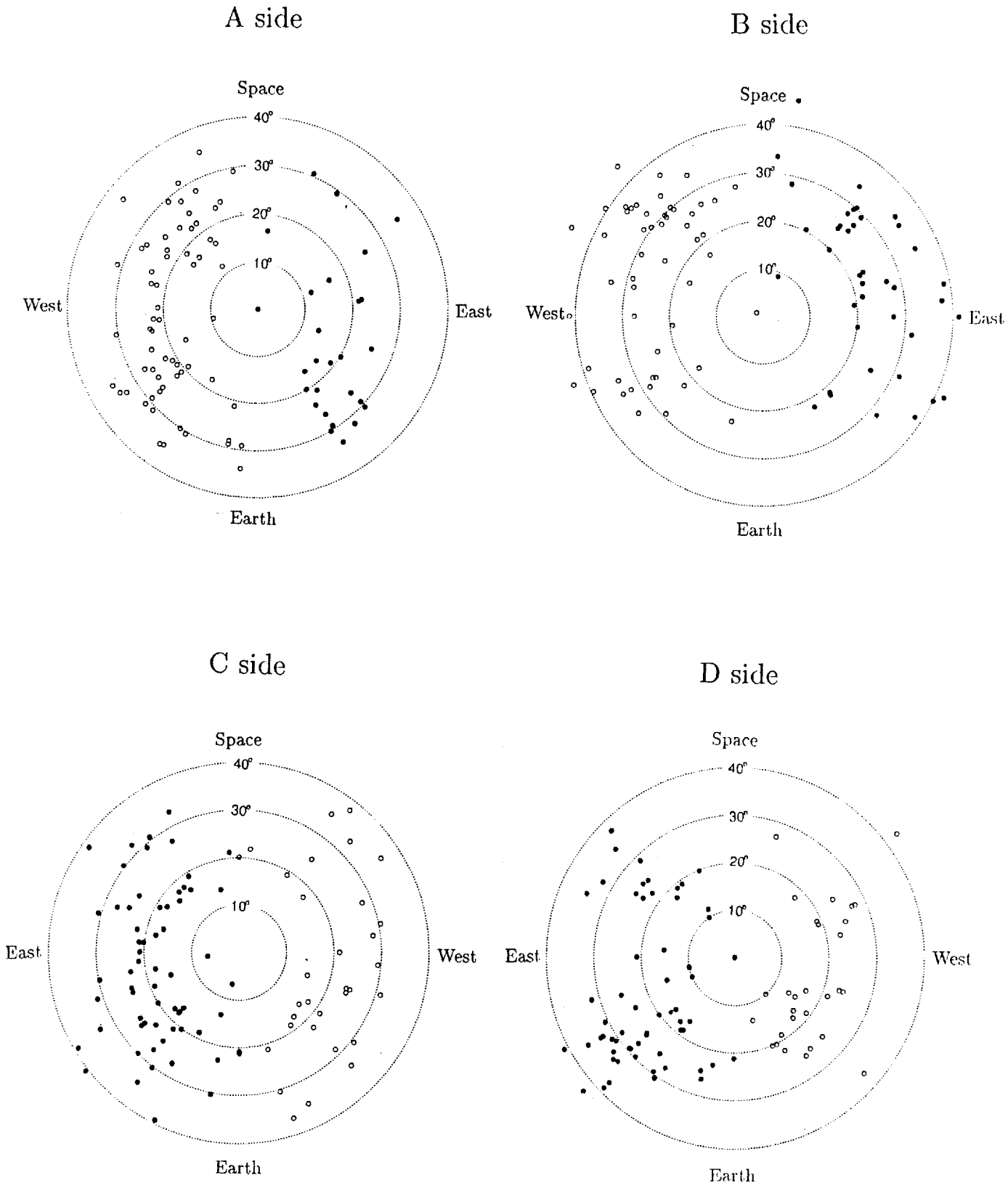

Figure 3: Arriving directions of GCR Fe particles with relativistic energies in the side stacks of the P0006 experiment.

can absorb relativistic Fe particles and only a very few percent can penetrate them. However, some anisotropy of the GCR Fe particles cannot be related to shielding effects, hence we believe there is an anisotropy in the flux of the primary GCR Fe particles.

Total Track Density Measurements

We have measured two–dimensional total track density profiles in each side stack using an image analyzer. The image analyzer was able to pick up tracks darker than a certain brightness threshold and having contrast high enough to detect edges. Track size criteria were also applied in the counting. Overlapping tracks were separated by the software with very high efficiency. Total track density measurements were also performed by manual scanning and counting and the results were used to calibrate the automatic system. A reasonably good agreement between manual and automatic scanning has been established.

Total track density in CR-39 consists of tracks of different particles. At low shielding, such as the case for the side stacks, a large contribution is due to stopping primary trapped protons. A significant contribution is due to secondary stopping particles and recoils and also from GCR Fe particles. At higher shielding depths, these particles dominate the total track density as the high flux of low energy trapped protons is absorbed in the shielding.

On the other hand, not all of the particles can be detected by CR-39. A stopping proton can be detected with very high efficiency if the particle stops in the upper layer of the detector, which has a thickness comparable with the layer removed by the chemical etching of the detector. This thickness was about 8–10 μm in our samples. The critical angle for the detection of a proton in this case is about 70° measured from the normal of the detector surface. This critical angle decreases rapidly with the residual range of the proton if the particle stopped below the post–etched surface which, we found, is usually the case for proton tracks. A detailed detection efficiency calculation is in progress taking into account a variable track etch rate ratio model for stopping particles. Internal calibration will also be performed using tracks of stopping proton particles.

Detection efficiency for other than proton particles is almost 100% if the particle stops in the removed layer, which means that CR-39 can detect practically all heavy recoils that have a part of their trajectories in the removed layer thickness. Relativistic Fe particles, on the other hand, are detected only from a small field angle around the normal of the detector with a critical angle of about 40°.

Trapped protons are expected to have a strong directionality. In the case of the P0006 stack they are expected to arrive from the west direction, mostly parallel with the Earth's surface and with the surfaces of the CR-39 layers in the side stacks. It means that the track density of stopping primary trapped protons is expected to decrease with the depth in the main stack as the low energy trapped protons and their secondaries are absorbed in it. The secondaries of the high energy trapped protons, however, are not expected to show strong shielding effects because they can penetrate the whole stack with approximately constant interaction cross sections. Hence, a strong location dependence of total track density is expected at low shieldings and some relatively smooth track density profiles at higher protected areas.

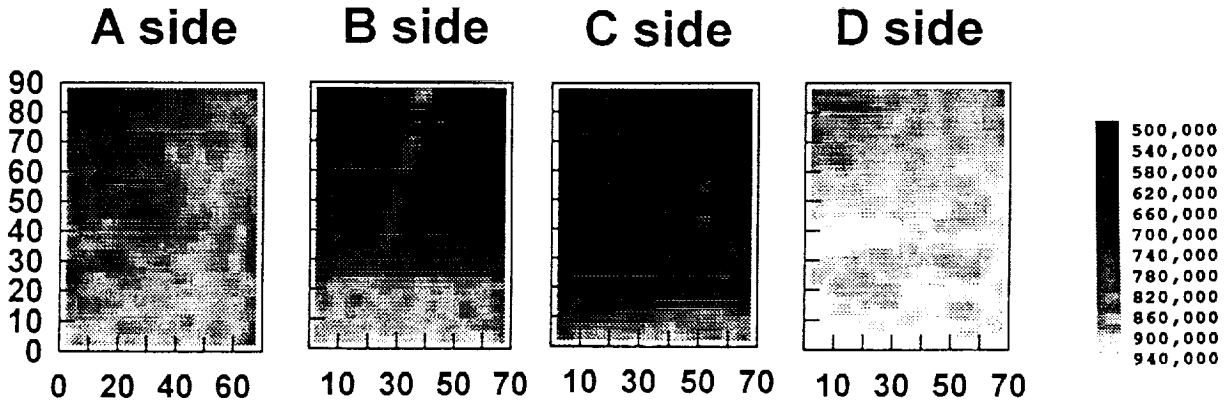

Figure 4: 2D total track density profiles in CR-39 from the side stacks of P0006. Bottom edges of the layers are the space side edges.

Figure 4 shows some preliminary 2D total track density profiles measured in the side stack CR-39 samples. The total track density varied between 0.6 and 1.3 million tracks/cm^2. Side stacks A and D had significantly higher track densities than side stacks B and C facing toward the Earth. On the side stacks facing toward space the side stack D has higher track density than side stack A, indicating more particles from the south–west than from the north–west direction. This observation is in good agreement with the Al activation measurements around the LDEF satellite which also show a maximum in the south-west direction.

On each sample the track density is highest at the space edge of the sample and decreases toward the LDEF satellite. This is especially demonstrated on side stacks B and C. The sudden drop of track density moving from the space edge toward the satellite probably reflects the absorption of low energy trapped protons arriving from the west–space direction and slowing down as they penetrate the main stack. The dominance of the trapped protons from the west–south–space direction is also suggested by the relatively uniform track density on the side stack D which has practically no shielding from this direction.

CONCLUSIONS

It is demonstrated that the three–dimensional shielding effect has to be taken into account when cosmic ray charged particle fluences are measured under different shielding conditions. The shadowing effect of the LDEF satellite on the relativistic GCR Fe particles was found. Additional observed anisotropy

in the fluence of these particles is assumed due to the anisotropic directional distribution of the particles which has to be explained by propagation codes.

The variation of total track density as a result of self shielding of the P0006 stack was also observed. The strong location dependence of the track density was found to be in good agreement with the anisotropic trapped proton environment and 3D geometrical considerations of the P0006 experimental block.

These experiments clearly indicate the need for detailed mass model calculations together with which they may provide an excellent opportunity to validate model calculations and help update flux data of the outer radiation environment.

REFERENCES

1. Armstrong, T. W.; and Colborn, B. L.: Radiation model predictions and validation using LDEF data. *Second LDEF Post-Retrieval Symposium*, NASA CP-3194, 1993.

2. Benton, E. V.; Heinrich, W., Parnell, T. A.; Armstrong, T. W.; Derrickson, J. H.; Fishman, G. J.; Frank, A. L.; Watts, J. W.; and Wiegel, B.: Ionizing radiation exposure of LDEF: Pre-recovery estimates. *Nuclear Tracks and Radiation Measurements*, Vol. 20, No. 1 1992, pp. 75-100.

3. Benton, E. V.; Frank, A. L.; Benton, E. R.; Csige, I.; Parnell, T. A.; and Watts, J. W. Jr.: Radiation exposure of LDEF: Initial Results. *LDEF–69 Months in Space: First Post-Retrieval Symposium*, NASA-CP 3134, Part 1, Washington DC, 1991, pp. 325-338.

4. Csige, I.; Benton, E. V.; Frank, A. L.; Frigo, L. A.; Benton, E. R.; Parnell, T. A.; and Watts, J. W. Jr.: Charged particle LET-spectra measurements aboard LDEF. *LDEF–69 Months in Space: First Post-Retrieval Symposium*, NASA-CP 3134, Part 1, Washington DC, 1991, pp. 339-346.

5. Harmon, B. A.; Fishman, G. J.; Parnell, T. A.; Benton, E. V.; and Frank, A. L.: LDEF radiation measurements: preliminary results. *Nuclear Tracks and Radiation Measurements*, Vol. 10, No. 1, 1992, pp. 131-136.

6. Watts, J. W. Jr.; Parnell, T. A.; Derrickson, H. J.; Armstrong, T. W.; and Benton, E. V.: Predictions of LDEF ionizing radiation environment. *LDEF–69 Months in Space: First Post-Retrieval Symposium*, NASA-CP 3134, Part 1, Washington DC, 1991, pp. 213-224.

7. Reitz, G.; Bücker, H.; Facius, R.; Horneck, G.; Schaefer, M.; Schott, J. U.; Bayonove, J.; Beaujean, R.; Benton, E. V.; Delpoux, M.; Heilmann, C.; Heinrich, W.; Kranz, A. R.; Planel, H.; Gasset, Y.; Gaubin, G.; Portal, G.; Graul, E. H.; Rüther, W.; Schopper, E.; Tobias, C. A.; and Yang, T. C. First biological and dosimetric results of the free flyer biostack experiment A0015 on LDEF. *LDEF–69 Months in Space: First Post-Retrieval Symposium*, NASA-CP 3134, Part 1, Washington DC, 1991, pp. 1639-1642.

DEVELOPMENT AND APPLICATION OF A 3-D GEOMETRY/MASS MODEL FOR LDEF SATELLITE IONIZING RADIATION ASSESSMENTS*

B. L. Colborn and T. W. Armstrong
Science Applications International Corporation
Route 2, Prospect, TN 38477
Phone: 615/468-2603, Fax: 615/468-2676

SUMMARY

A three-dimensional geometry and mass model of the LDEF spacecraft and experiment trays has been developed for use in predictions and data interpretation related to ionizing radiation measurements. The modeling approach, level of detailed incorporated, example models for specific experiments and radiation dosimeters, and example applications of the model are described.

INTRODUCTION

Measurements of the ionizing radiation and effects on the Long Duration Exposure Facility (LDEF) satellite provide new data important to attaining a more accurate definition of the space radiation environment. An important issue in interpreting the LDEF radiation dosimetry data, and in performing definitive predictions to compare with the data, is the influence of material shielding effects. For example, data for the absorbed dose from geomagnetically trapped protons indicate a strong anisotropy for measurements made at different locations on LDEF (ref. 1), and measured LET (linear energy transfer) spectra from galactic cosmic rays also exhibit a directional response (ref. 2). A question in interpreting these results is to what extent this angular response is due to the directionality of the space radiation environment, which would be common to other spacecraft having orbit parameters similar to LDEF, as opposed to the influence of shielding variations particular to the LDEF experiment/spacecraft configuration.

The purpose of the present work is to provide a geometry and mass model of LDEF incorporating sufficient detail that it can be applied in determining the influence of material shielding on ionizing radiation measurements and predictions. The model can be utilized as an aid in data interpretation by "unfolding" shielding effects from the LDEF radiation dosimeter responses.

*Work supported by NASA Marshall Space Flight Center, Huntsville, AL, Contracts NAS8-38121 and NAS8-39386.

MODELING APPROACH

Initial work on the development of a LDEF geometry/mass model, which included the spacecraft structure and individual experiment trays but provide no detailed modeling of the tray contents, has been reported earlier (ref. 3). The model has now been extended to include a detailed description of the contents of several trays (F2, F8, H3, and H12).

The rationale of this tray selection for detailed modeling is as follows: Tray F2 (containing Exps. P0004 and P0006) and Tray F8 (containing Exp. M0004) are located near the trailing and leading edges of LDEF, respectively, and contain radiation dosimeters important to assessing the directionality of the trapped proton exposure (ref. 1). Furthermore, other measurements from the P0006 experiment in Tray F2 show a directional dependence of the spectra from heavy ions in galactic cosmic rays (ref. 2), and shielding variations around this experiment are needed in interpreting the data. Preliminary data from Exp. M0001 in Trays H3 and H12 indicate a higher heavy ion flux than expected entering the detector from the direction of the interior of the LDEF spacecraft (ref. 4), and the influence of shielding on relating the observed ion spectra to the incident space spectra is of interest in interpreting these data.

Methodology

The LDEF geometry/mass model has been programmed in FORTRAN using the combinatorial geometry methodology of describing complex three-dimensional configurations. The computer version of the geometry module used here has been operated for many years in radiation transport applications, and is the geometry module commonly used with the HETC radiation transport code (ref. 5).

The combinatorial geometry method describes three-dimensional material configurations by applying logical operators to form unions, differences, and intersections in combining simple solid bodies (spheres, boxes, cylinders, etc.) to form a complex geometry. Material properties are assigned to each zone defined by these operators, and ray-tracing algorithms are included to provide the pathlength and material identifier for each zone traversed. This material identifier is used as an index to retrieve information (density, atomic compositions, etc.) from a materials properties table. As an aid in debugging, we have used the SABRINA code (ref. 6) to obtain a graphical output of the geometry input data.

Input Data Sources

Input data for constructing the LDEF model has been obtained from engineering drawings, preflight reports from experimenters describing component layouts, dimensions, and materials for individual

experiments, and pre- and post-flight photographs, all kindly provided by the LDEF Project Science Office.[1] Key modeling input was the weight of individual experiment trays and all spacecraft structural components provided by NASA LaRC from pre-flight center-of-mass and flight dynamics analyses.[2] Dimensions for the experiment trays and descriptions of certain electronics and data storage components common to various experiments were obtained from the LDEF Experimenter Users Handbook (ref. 7). General descriptions and photographs of individual experiments from Clark, et al. (ref. 8) were also helpful.

Information needed for the detailed modeling of Exps. P0004, P0006, and M0004 was provided by Benton and Frank,[3] and a detailed description of Exp. M0001 was provided by Tylka and Adams.[4]

Level of Detail Incorporated

The LDEF spacecraft is considered to be comprised of the following general categories for modeling purposes: spacecraft structure, miscellaneous spacecraft components, and experiments, which include the experiment trays and components (Tables I-III). The 84 experiment trays on LDEF can be further divided into four subcategories: (a) space debris experiments (26 trays), for which the tray contents can be adequately modeled as an aluminum plate; (b) ultra-heavy cosmic ray experiments (16 trays), for which the contents can be simply modeled as aluminum plus plastic; (c) trays containing ionizing radiation dosimeters (13 trays), for which some detailed modeling of the tray components is desirable, and (d) all other experiments (29 trays), for which the tray is considered to be filled with aluminum having a reduced density such that the individual tray weight is preserved. Thus, each individual experiment tray is modeled, with the actual weights of the trays and contents included, but only the contents of selected trays are modeled in detail for assessing shielding effects on the radiation dosimeter responses. Of the 13 trays indicated in Table III as containing ionizing radiation dosimetry, four trays (F2, F8, H3 and H12) are modeled in detail.

Experiment Models

Some of the geometry models of the LDEF ionizing radiation experiments are shown here as examples; other models and details of the modeling procedure are given in ref. 9. Fig. 1 shows a view of the LDEF spacecraft model with experiment trays, including the four experiment trays in which the contents are modeled in detail.

Fig. 2 shows the component layout in tray F2 and the corresponding combinatorial geometry model. This tray contains the six canisters of tomato seeds (SEEDS experiment) with the thermoluminescent

dosimeters (TLDs) of Exp. P0004 for measuring radiation dose at various positions in the seed canisters. This tray also contains the Exp. P0006 detector stack, which includes several types of radiation detectors: TLDs, plastic nuclear track detectors (PNTDs), activation materials, and neutron detection foils. The Exp. P0006 detector model is shown in more detail in Fig. 3.

The layout and geometry model of tray F8 containing Exp. M0004 on space environment effects on fiber optics is shown in Fig. 4. This tray contains two radiation dosimetry packets in each of two canisters, with each packet containing both TLDs and PNTDs.

The modeling assumptions for these and other trays in terms of geometry and material simplifications are detailed in ref. 9.

APPLICATIONS

The LDEF geometry module program can be applied in several operational modes: (a) as a stand-alone program, material thicknesses along rays emanating from specified spatial points and a specified angular grid can be generated to provide three-dimensional shielding variations around various dosimetry components; (b) such shielding distributions can also be used as input to one-dimensional transport codes which use solid angle sectoring to approximate three-dimensional radiation transport; and (c) the geometry module can be interface with detailed three-dimensional Monte Carlo radiation transport codes (e.g., HETC).

The geometry/mass model is currently being utilized in several studies related to predictions and comparisons with LDEF radiation dosimetry data and in the interpretation of LDEF radiation measurements. The model has been used with radiation transport calculations to predict the directionality of the radiation dose measured on LDEF (ref. 10), which showed that 3-D shielding effects were very important in comparing with the dosimetry data, and the model has been used by NRL[4] in analyzing results from the Exp. M0001 heavy ion experiment.

Shielding calculations using the LDEF geometry/mass model are also being made to investigate the directionality of protons and heavy ions observed (ref. 2) in Exp. P0006 plastic nuclear track detectors. An example model application (stand-alone mode) is given in Fig. 5, which shows the shielding distribution in a horizontal plane around one of the PNTD side modules of Exp. P0006. Here a local coordinate system is used with the angle α measured in a plane parallel to the tray top. The "dips" in the shielding distribution designated as (a), (b), and (c) occur for directions between the seed canisters, with the large peak in the distribution (d) corresponding to directions going through lower trays (toward earth-end) and through the center ring of the spacecraft structure. The other P0006 side modules see a similar horizontal shielding

distribution but displaced by 90°. Such shielding variations can have an important influence on the observed radiation environment.

REFERENCES

1. Frank, A. L.; Benton, E. V.; Armstrong, T. W. and Colborn, B. L.: Absorbed Dose Measurements and Predictions on LDEF. Second LDEF Post-Retrieval Symposium, NASA CP-3194, 1993.

2. Csige, I.; Benton, E. V.; Frigo, L.; Parnell, T. A.; Watts, J. W. Jr.; Armstrong, T. W. and Colborn, B. L.: Three Dimensional Shielding Effects on Charged Particle Fluences Measured in the P0006 Experiment on LDEF. Second LDEF Post-Retrieval Symposium, NASA CP-3194, 1993.

3. Colborn, B. L. and Armstrong, T. W.: LDEF Geometry/Mass Model for Radiation Analyses. First LDEF Post-Retrieval Symposium, NASA CP-3134, 1992.

4. Adams, James H. Jr.; Beahm, Lorraine P. and Tylka, Allan J.: Preliminary Results from the Heavy Ions in Space Experiment. First LDEF Post-Retrieval Symposium, NASA CP- 3134, 1992.

5. Armstrong, T. W. and Colborn, B. L.: HETC/LHI, A Thick Target Radiation Transport Code for Low-Mass Heavy Ions Beams. *Nucl. Instr. Meth.* 169, 161 (1980).

6. West, James T.: SABRINA: An Interactive Three-Dimensional Geometry-Modeling Program for MCNP. Los Alamos National Laboratory, LA-10688-M, October 1986.

7. Long Duration Exposure Facility (LDEF) Experimenter Users Handbook, LDEF Project Office Report No. 840-2 (Change No. 3), NASA Langley Research Center, October 3, 1980.

8. Clark, Lenwood G.; Kinard, William H.; Carter, David J. Jr. and Jones, James L. (Eds): The Long Duration Exposure Facility (LDEF): Mission 1 Experiments, NASA SP-473, 1984.

9. Colborn, B. L. and Armstrong, T. W.: Geometry and Mass Model of Ionizing Radiation Experiments on the LDEF Satellite. Science Applications International Corporation (NASA MSFC Contract NAS8-39121 Final Report), SAIC-TN-9202, April 1992.

10. Armstrong, T. W., and Colborn, B. L.: Radiation Model Predictions and Validation Using LDEF Satellite Data. Second LDEF Post-Retrieval Symposium, NASA CP-3194, 1993.

Footnotes

1. Jones, J., LDEF Project Science Office, NASA Langley Research Center, pri. comm., 1991.

2. Shearer, R., NASA Langley Research Center, pri. comm., 1991.

3. Benton, E. V. and Frank, A. L., University of San Francisco, pri. comm., 1992.

4. Adams, J. H., Jr. and Tylka, A. J., Naval Research Laboratory, pri. comm., 1992.

Table I. Level of Detail for Modeling LDEF Spacecraft

Category	Component	No. Places	Weight (lbs.)	Weight %	Modeling Approach
STRUCTURE	Center Ring	1	2,073	9.7%	Modeled as individual component.
	Longerons	24	2,280	10.7%	Modeled as individual components.
	End Frames	2	1,374	6.4%	Modeled as individual components.
	Diagonal Tubes	8	926	4.3%	Modeled as individual components.
	Intercostal Rings	72	758	3.5%	Modeled as individual components.
	Trunions,Pins,Scuff Plts	10	501	2.3%	Modeled as individual components.
	End Support Beams	5	285	1.3%	Modeled as individual components.
	TOTAL STRUCTURE:		8,197	38.3%	
MISCELLANEOUS	Batteries	2	100	0.5%	Included as part of earth-end support beam.
	Initiate Electronics	1	105	0.5%	Included as part of center ring weight.
	Wiring	-	100	0.5%	Included as part of center ring weight.
	Nuts and Bolts	-	200	0.9%	Included as part of center ring weight.
	Damper Assembly	1	62	0.3%	Modeled as individual component.
	Thermal Covers (Ends)	12	154	0.7%	Modeled as individual components.
	Ballast Plates	11	365	1.7%	Included as part of end frames.
	TOTAL MISCELLANEOUS:		1,086	5.1%	
EXPERIMENTS	Experiment Components and Trays	84	12,110	56.6%	Modeled each experiment tray separately, with individual experiment weights preserved. Modeling for components varies with experiment type.
	TOTAL LDEF WEIGHT:		21,393	100.0%	

Table II. Level of Detail for Modeling Experiments

No. Trays	Model	Experiments
26	Al plate	S0001: Space Debris (LaRC)
16	Al+plastic plates	A0178: Ultra-heavy Cosmic-Ray Expt. (Dublin Inst., ESTEC)
13	"detailed"	Selected experiments containing ionizing radiation dosimetry.
29	homogenized Al	(all others)

Table III. Trays Containing Ionizing Radiation Dosimetry

Tray Bay-Row	Experiment No.	Experiment	Dosimetry
C-2, G-2	A-0015	Biostack (DFVLR)	TLD's, PNTD's
C-3, C-9	A-0114	Atomic Oxygen (UAH, MSFC)	Activation Samples
B-3	A-0138	Optical Fibers (CERT/ONERA - DERTS)	TLD'S
H-3, H-12	M0001	Heavy Ions (NRL)	PNTD's
D-3,D-9,G-12	M0002-1	Trapped Proton Spect. (AFGPL,MSFC, et al.)	PNTD's,TLD's,Act.
E-6	M0002-2	Heavy Cosmic-Ray Nuclei (U. Keil)	PNTD's
D-3,D-8,D-9	M0003	Space Envr. Effects on Matls. (Aerospace)	TLD's
F-8	M0004	Space Envr. Effects on Optics (AFWL)	TLD's, PNTD's
C-2	M0006	Space Envr. Effects (AFTAC, Grumman)	TLD's
F-2	P0004	SEEDS (Univ. SF)	TLD's, PNTD's
F-2	P0006	LET Spectrum Meas. (Univ. SF, MSFC)	TLD's, PNTD's, Fiss. & Act. Samples

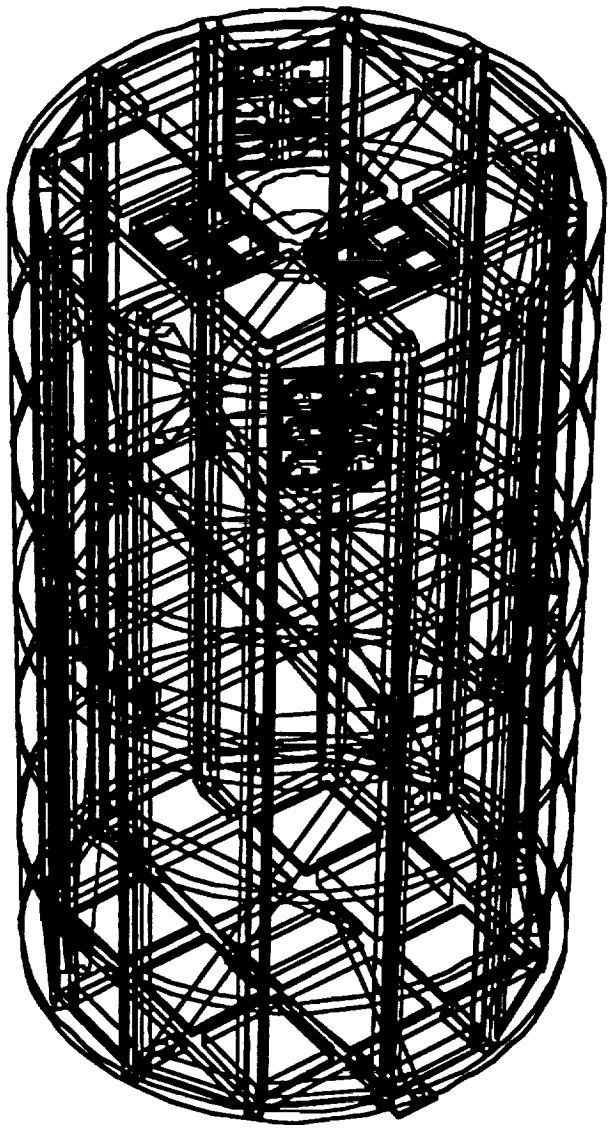

Figure 1. Combinatorial geometry model of LDEF spacecraft with the four experiment trays (F2, F8, H3, and H12) containing radiation dosimeters which have been modeled in detail.

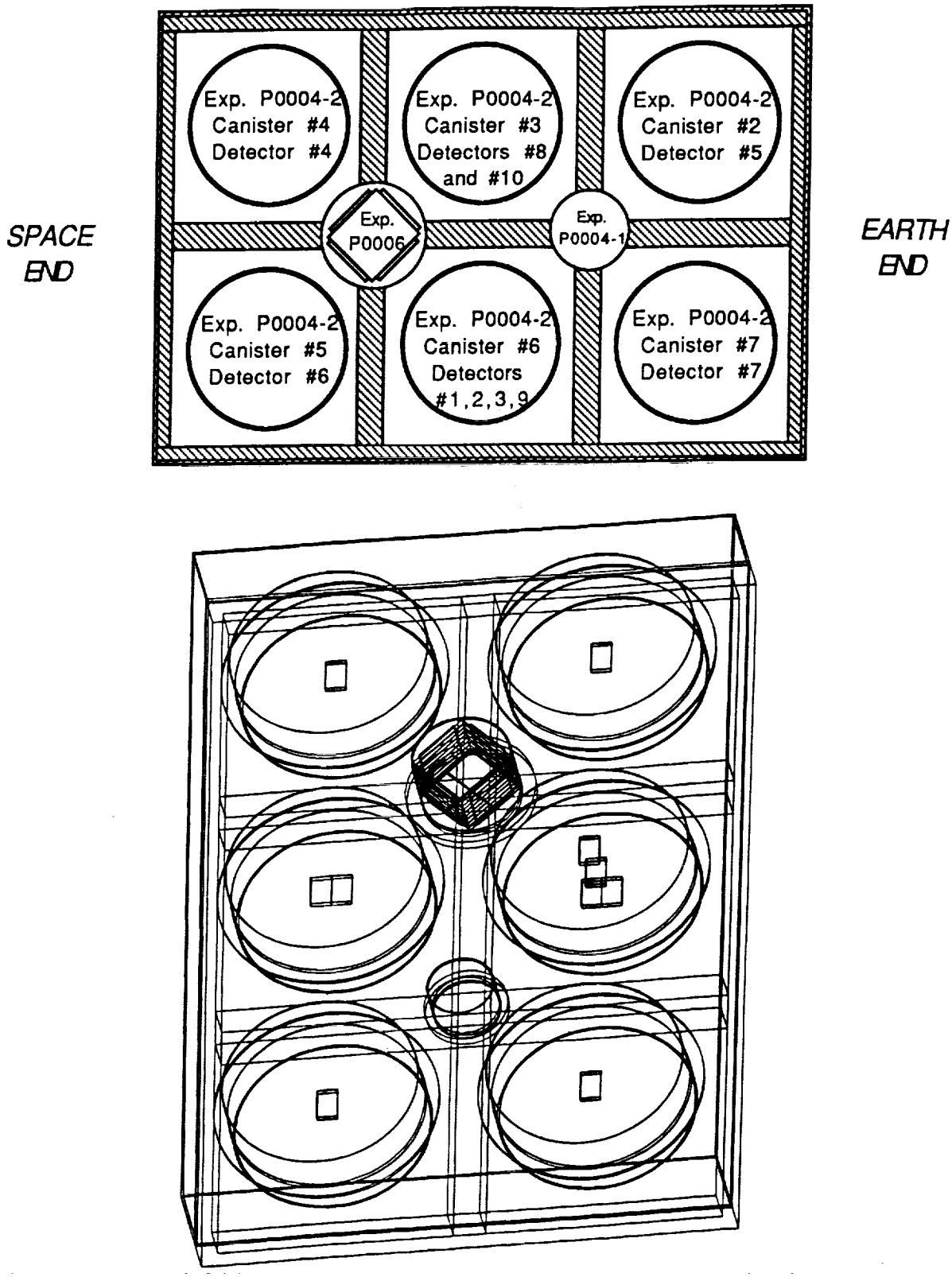

Figure 2. Layout of components in LDEF experiment tray F2 containing radiation dosimetry (top) and combinatorial geometry model (bottom), showing TLD packets (Exp. P0004) in the seed canisters and the Exp. P0006 detector stack.

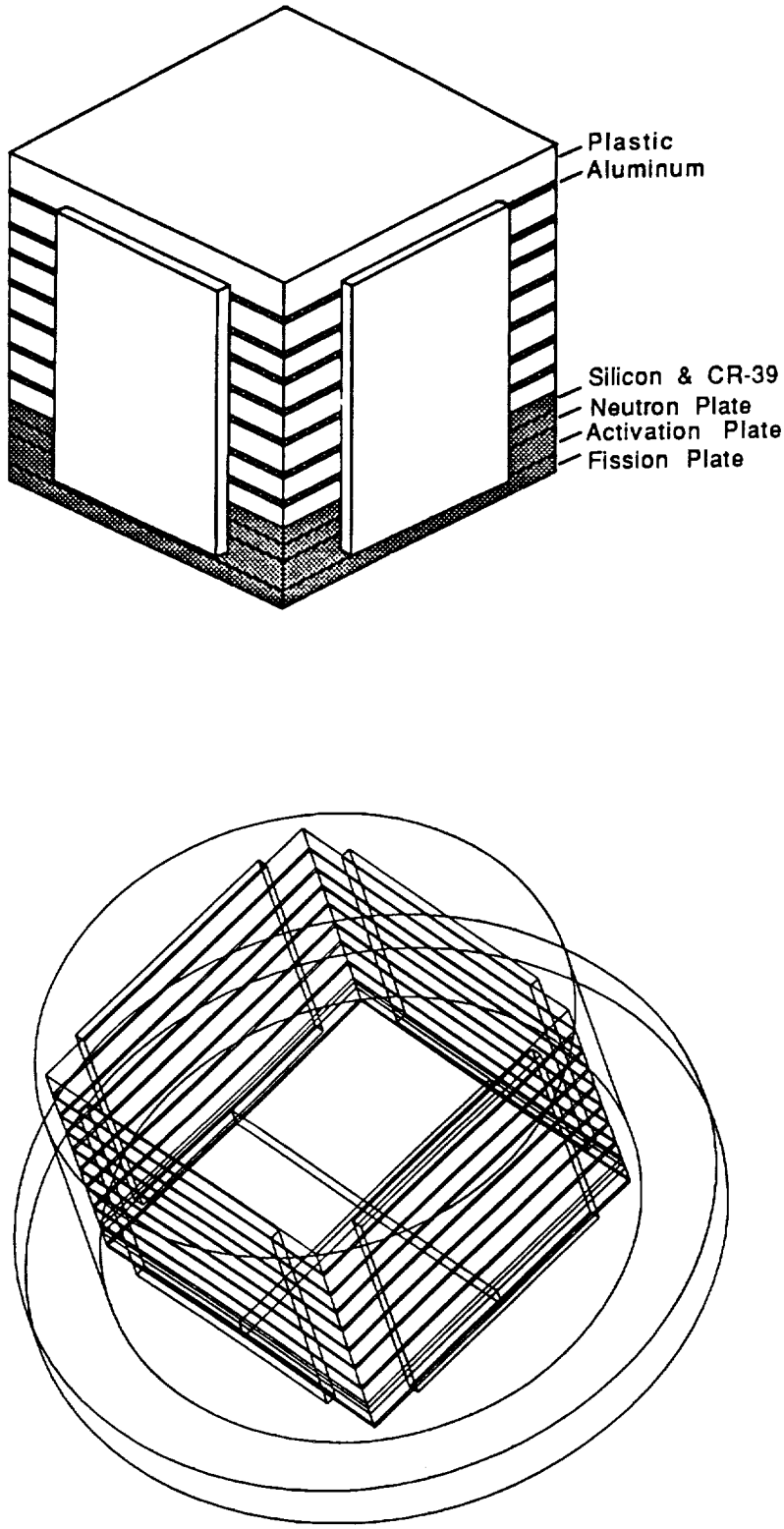

Figure 3. Material layers modeled in the Exp. P0006 detector stack (top) and corrresponding combinatorial geometry model of detector and canisters (bottom).

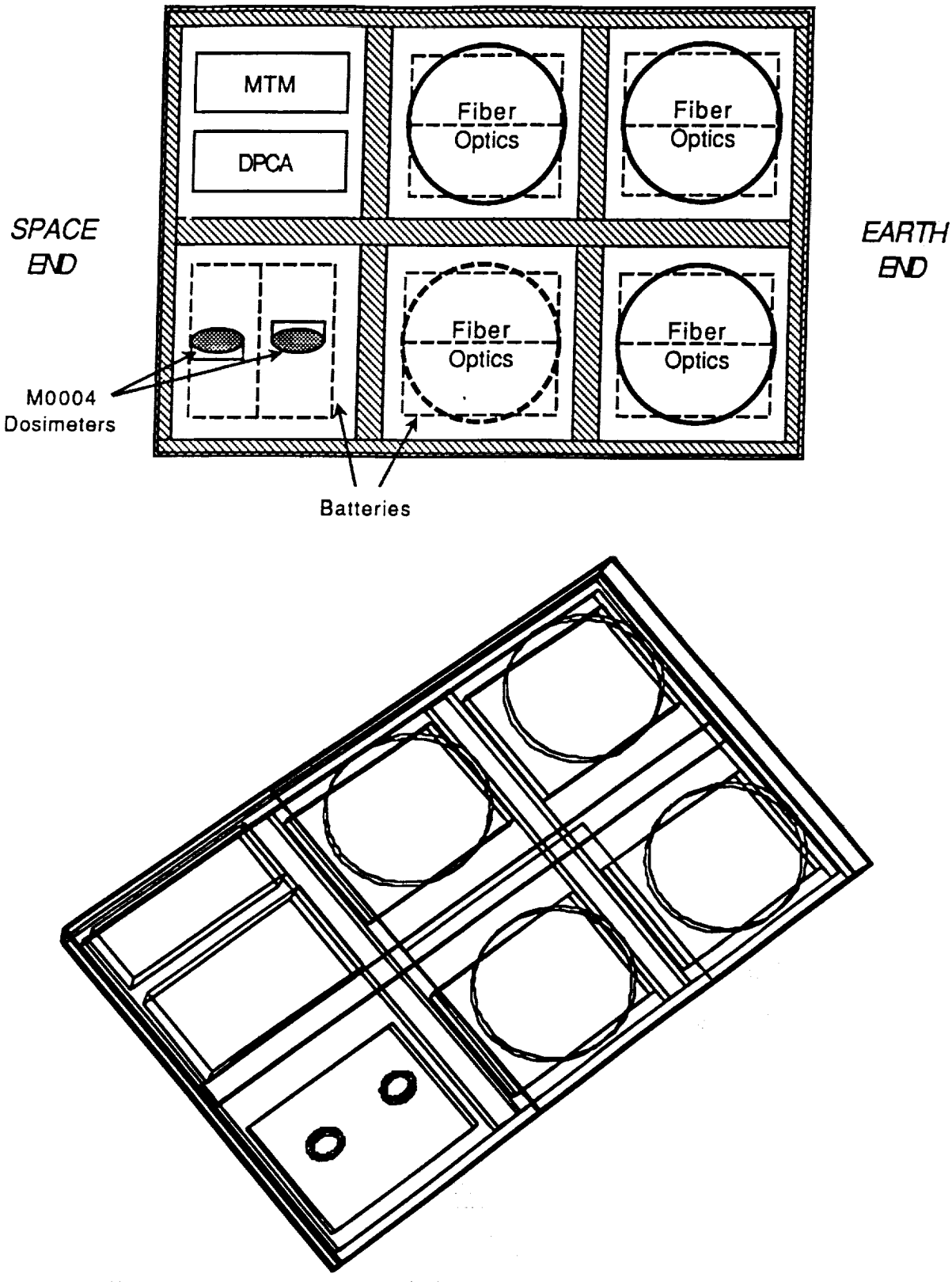

Figure 4. Layout of LDEF tray F8 containing Exp. M0004 radiation dosimeters (top) and corresponding geometry model (bottom).

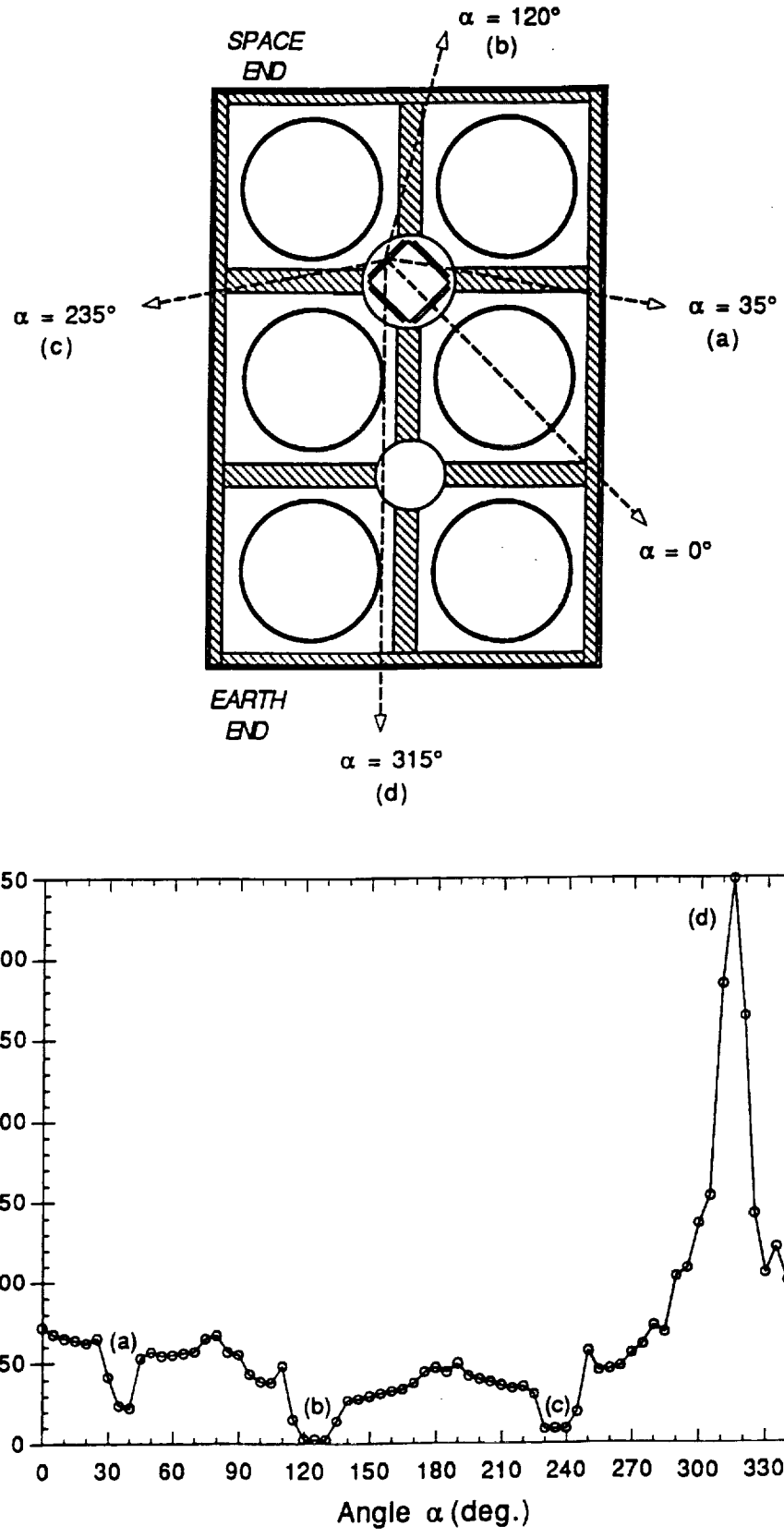

Figure 5. Shielding distribution in horizontal plane for a point on the surface of the detector module of Exp. P0006.

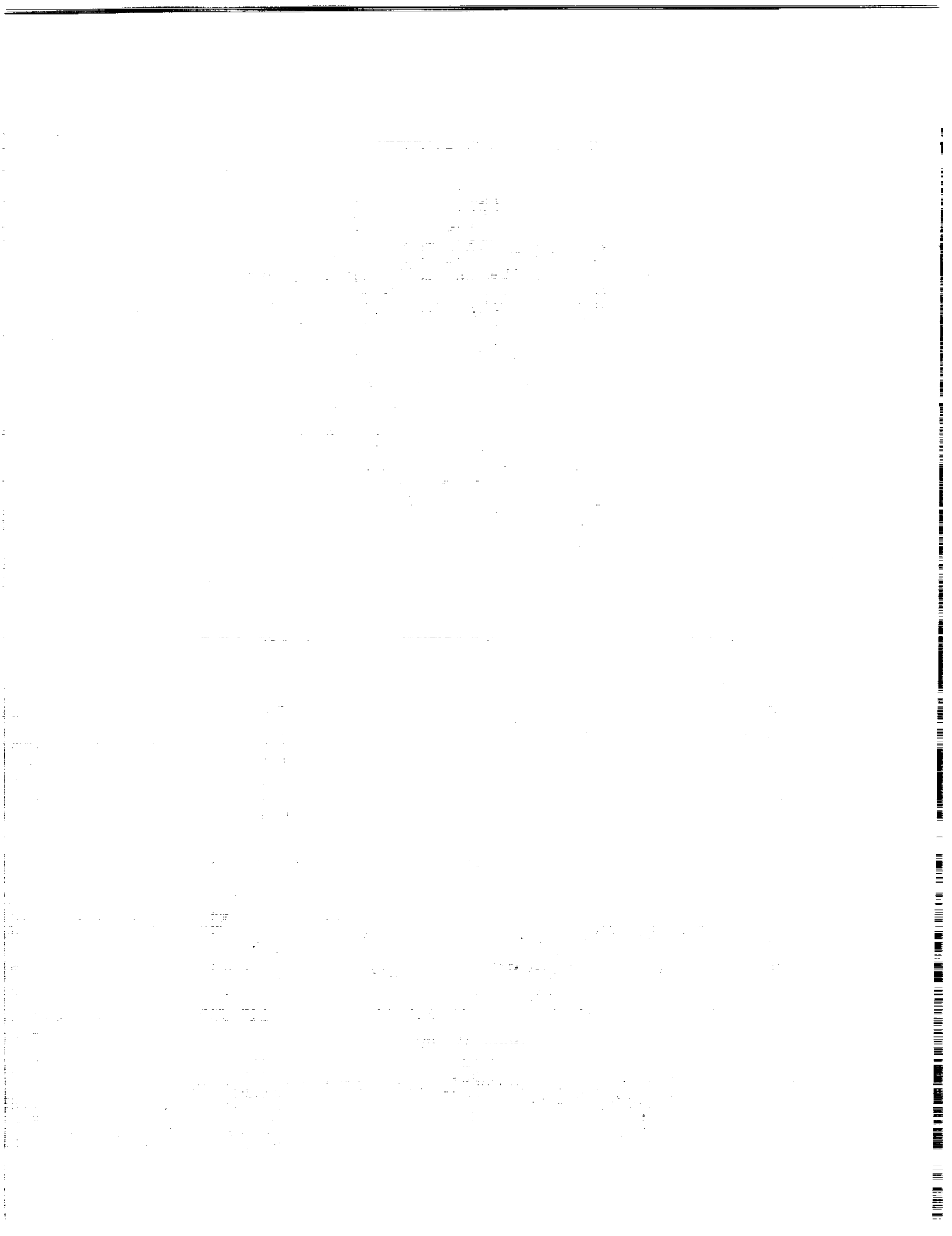

RADIATION MODEL PREDICTIONS AND VALIDATION USING LDEF SATELLITE DATA*

T. W. Armstrong and B. L. Colborn
Science Applications International Corporation
Route 2, Prospect, TN 38477
Phone: 615/468-2603, Fax: 615/468-2676

SUMMARY

Predictions and comparisons with the radiation dose measurements on LDEF by thermoluminescent dosimeters have been made to evaluate the accuracy of models currently used in defining the ionizing radiation environment for low Earth orbit missions. The calculations include a detailed simulation of the radiation exposure (altitude and solar cycle variations, directional dependence) and shielding effects (three-dimensional LDEF geometry model) so that differences in the predicted and observed doses can be attributed to environment model uncertainties. The LDEF dose data are utilized to assess the accuracy of models describing the trapped proton flux, the trapped proton directionality, and the trapped electron flux.

INTRODUCTION

Radiation dosimetry data from the Long Duration Exposure Facility (LDEF) mission are being utilized to evaluate the accuracy of current ionizing radiation environment models and to identify model improvements needed for future mission applications in low Earth orbit. A calculational program is in progress to compare model predictions with the different types of LDEF ionizing radiation measurements (dose, activation, LET spectra, secondary particles, etc.), and the status of this work is summarized in a companion paper (ref. 1).

The scope of the present paper is restricted to model predictions and comparisons with LDEF thermoluminescent dosimetry (TLD) measurements of the radiation dose. These TLD measurements provide one set of data for evaluating the accuracy of environment models describing the trapped proton flux, the trapped proton directionality, and the trapped electron flux. Assessments of trapped radiation models utilizing other LDEF data sets from plastic nuclear track detectors and activation sample measurements of induced radioactivity are in progress.

*Work supported by NASA Marshall Space Flight Center, Huntsville, AL, Contracts NAS8-38770 and NAS8-39386.

CALCULATIONAL METHOD

Environment Model -- Results from the calculations of Watts, et al. (ref. 2) are used to model the LDEF exposure to trapped protons. These calculations are based on the standard AP8 omnidirectional proton flux model (ref. 3), with altitude and solar cycle variations during the LDEF mission included, and with the MSFC anisotropy model (ref. 4) applied to determine the trapped proton directionality. In the calculations here, the directionality was taken into account by using different incident energy spectra along directions defined by a 3-D angular grid of 720 equal solid angle intervals about the dose point. Example spectra are shown in Fig. 1.

Spacecraft Model -- The LDEF radiation dosimetry data is influenced by material shielding effects due to the dosimeter itself, nearby components and experiments, and the spacecraft structure. It is necessary to isolate shielding effects particular to the LDEF spacecraft so that the evaluated model uncertainties can be attributed to the ambient radiation environment and so that the results have applicability to other missions with different spacecraft configurations. To help ensure that differences between predictions and measurements are due to the external radiation environment and not shielding effects, a detailed three-dimensional geometry/mass model of the LDEF spacecraft and selected experiment trays has been developed (ref. 5), and this 3-D model has been used to take into account shielding effects for the dose predictions here.

Radiation Transport -- Three-dimensional radiation transport calculations were performed using the 3-D LDEF geometry/mass model and the solid angle sectoring approximation, in which the solid angle around each dose point is divided into small sectors and the shielding attenuation along "ray" directions through each sector is computed. Transport calculations using different trapped proton energy spectra for each direction were carried out using the MSFC code written by Burrell (ref. 6), which employs the straightahead approximation together with fits to stopping power and range relations to obtain an analytical solution of the transport equation. The attenuation is computed for material along each ray direction representing a solid angle sector, the attenuated fluence spectrum is folded with the stopping power for tissue, and the results summed for all rays to obtain the tissue dose.

An example TLD shielding distribution used in computing the radiation attenuation is shown in Fig. 2. Shown are areal densities (aluminum equivalent) along rays emanating at the midpoints of 720 equal solid angle bins surrounding the TLD. The TLD in this case is located in one of the canisters containing tomato seeds in tray F2 (SEEDS experiment, Exp. No. P0004). The outward directed TLD normal is at $\varphi = 240°$ and $\theta = 90°$, where $+\varphi$ is measured from south (row 6) and $+\theta$ from the zenith direction. Also indicated in Fig. 2 is the constant shielding corresponding to a spherical geometry model having a radius equal to the vertical (minimum) TLD shielding, which is the simple geometry model assumed for some of the scoping

estimates in the LDEF pre-recovery dose predictions (ref. 7). As evident, the spherical geometry model substantially underestimates the dosimetry shielding.

RESULTS

TLD measurements were made at various locations on the LDEF spacecraft and at various shielding depths in the experiment trays. Fig. 3 summarizes the TLD data presently available at the larger shielding depths ($\geq$ 0.5 g/cm^2) where trapped protons dominate the dose contribution. The data shown are from dosimeters located: (a) on the trailing (west) side of the spacecraft, consisting of the measurements by Frank, et al. (ref. 8) for TLDs located in experiment tray F2 (Exps. P0004 and P0006), measurements by Frank, et al. (ref. 8) and Reitz (ref. 9) in tray C2 (Exp. A0015), and measurements by Bourrieau (ref. 10) in tray B3 (Exp. A0138-7); (b) on the earth-end of the spacecraft, consisting of measurements by Frank, et al. (ref. 8) and Reitz (ref. 9) in tray G2 (Exp. A0015); and (c) on the leading (east) side, consisting of measurements by Frank, et al. (ref. 8) in tray F8 (Exp. M0004) and by Blake and Imamoto (ref. 11) in tray D9 (Exp. M0003). In two cases, the Exp. M0006 measurements of Chang, et al. (ref. 12) and some of the Exp. M0003 measurements of Blake and Imamoto (ref. 11), TLD assemblies were located in drawers of the experiment trays which were closed 40 weeks into the mission. Thus, the shielding changed during flight in these cases, and results from these measurements are not included in Fig. 3.

The doses in Fig. 3, and in subsequent graphs of this type, are plotted as a function of the "vertical" shielding thickness in g/cm^2 of aluminum equivalent material (based on equivalent ranges for 100-MeV protons), where the vertical direction is along the normal from the TLD face outward from the LDEF interior. This vertical direction generally corresponds to the direction of minimum shielding, although there are exceptions, such as for the TLDs located near the edge of the thick detector stack in Exp. P0006.

Predicted doses and comparisons with the data of Fig. 3 are given below with the objective being to evaluate the accuracy of models describing the magnitude of the trapped proton flux and its angular dependence. Subsequent comparisons using previous predictions (ref. 7) are then made with the TLD data at thin shielding depths where the dose contribution is dominated by incident electrons to assess the accuracy of trapped electron flux models.

Trapped Proton Dose

Figs. 4-6 compare predicted and measured doses for TLDs in LDEF experiment trays located on the trailing edge, earth end, and leading edge of the spacecraft, respectively. Predictions for Exps. P0004 and P0006 located in tray F2 and Exp. M0004 in tray F8 are based on a detailed geometry modeling of the tray

contents (ref. 4); for other cases (trays B3, C2, and G2) the tray contents were modeled as a single homogenized material (aluminum) with reduced density, so the dosimetry shielding is approximate for these cases. For the TLDs located in the Exp. P0006 detector stack, both measurements and calculations show appreciable variation of the dose for different locations within the TLD array for the same vertical shielding depth; the computed doses shown for P0006 are for a point in the middle of the array, and the measured values are the minimum values observed (ref. 9) across the array. The values shown for the Reitz measurements in Exp. A0015 are averages of the reported data (ref. 8) for TLD types 100 and 700.

A summary of the predicted and measured doses is given in Fig. 7. These results show that the AP8 trapped proton flux model gives a lower dose than observed from TLD measurements aboard LDEF for all spacecraft locations and shielding depths, with the predictions usually about a factor of two lower than measured. The predicted-to-measured dose ratios are practically constant with shielding depth, indicating that the trapped proton model environment is too low by about the same factor over a wide range of proton energies. Since the total mission dose is accumulated during the early high-altitude portion of the flight, which occurred predominately during the solar minimum phase of the solar cycle (ref. 2), these conclusions refer to the solar minimum version (AP8MIN) of the AP8 trapped proton model. (Model comparisons with available LDEF induced radioactivity measurements, ref. 13, for relatively short half-life radioisotopes should enable a check of the AP8MAX model since the latter part of the flight took place during solar maximum.)

The present dose predictions based on a detailed LDEF geometry model and an anisotropic trapped proton environment differ from early scoping estimates (ref. 7) made as part of the LDEF pre-recovery predictions in which simple geometry models (sphere and planar) and an omnidirectional trapped proton environment model were used. The difference is illustrated in Fig. 8 for comparisons with the TLD data of Exps. P0004 and P0006. While the omnidirectional, spherical geometry calculations (fortuitously) agree with the data, the more accurate models give doses about a factor two lower than the measurements. This illustrates that directional effects and a reasonably detailed spacecraft geometry model are needed in utilizing LDEF data for definitive assessments of uncertainties in the radiation environment.

Trapped Proton Anisotropy

For the low inclination (28.5°) of LDEF orbits, the dose from galactic cosmic rays is very small due to geomagnetic shielding, and, except for near-surface shielding depths where the trapped electron environment is important, the absorbed dose measurements on LDEF are due almost entirely to the trapped proton exposure during passes through the South Atlantic Anomaly (SAA). In the SAA region at LDEF altitudes, protons are "mirroring" in the geomagnetic field, with trajectories confined mainly in planes perpendicular to the local magnetic field direction and with in-plane asymmetry due to the east-west effect.

Since LDEF had a very stable orientation during the entire mission, measurements at various positions around the spacecraft provide data for evaluating the proton anisotropy model used.

In several cases TLD dosimeters at similar shielding depths were located near the trailing (row 3) and leading (row 9) edges of the spacecraft. These data and predictions in terms of the ratio of trailing-to-leading edge doses are shown in Fig. 9. The measured anisotropy is generally higher than predicted by the MSFC anisotropy model; e.g., the measured anisotropy for Exps. P0004/M0004 and Exps. P0006/M0004 is a factor of ≈ 2.4, whereas the calculated anisotropy factor for these cases is ≈ 1.4.

To further investigate the difference found between measured and predicted trapped proton directionality, several calculations were performed to determine the influence of spacecraft geometry on the predicted anisotropy. Fig. 10 shows the angular variation of dose at a particular depth (4 g/cm^2) for three assumed geometries: (a) the curve labeled "LDEF" was computed using the three-dimensional LDEF spacecraft model, (b) the curve labeled "Cylinder" was computed for a cylindrical spacecraft geometry having the same diameter, length, and total mass as LDEF but with the mass uniformly distributed within the cylinder, and (c) the "Plane" curve is for a planar shielding geometry with infinite backing and lateral dimensions and with the plane normal vector pointed in the plotted direction. These results for different model geometries show significantly different characteristic shapes for the angular variation of the dose. The detailed 3-D spacecraft model exhibits a local enhancement of the dose on the east side of the spacecraft, which is not present for the homogeneous cylinder or planar models. This dose "bump" on the east side is due to the fact that the interior of LDEF underneath the experiment trays contains relatively little mass, so the high flux incident on the west side "streams" through the hollow interior and contributes to the dose on the east side. This radiation streaming through the interior of LDEF can also influence the anisotropy observed at different shielding depths because at deeper depths on the east side the west-side flux contribution becomes larger. This is illustrated in Fig. 11 where the dose at various depths is calculated around the center ring of the spacecraft structure using the 3-D LDEF model. At small depths (e.g., 0.5 g/cm^2) the west side dose is higher, at about 10 g/cm^2 depth the west and east side doses are about the same, and at larger depths (e.g., 14 g/cm^2), corresponding roughly to the bottom of most of the experiment trays, the east side dose is higher.

While these calculations on geometry effects do not fully explain the difference found between the measured and predicted dose anisotropy, they do indicate that the observed anisotropy can be substantially influenced by the spacecraft configuration and that a realistic spacecraft geometry model is necessary in interpreting the measurements and in applying the data to other spacecraft configurations for future missions.

Trapped Electron Dose

Two experiments on LDEF contained TLDs with sufficiently thin shielding that the response is dominated by incident electrons. Measured TLD doses for these cases have been reported by Blake and Imamoto (ref. 11) for Exp. M0003 and by Bourrieau (ref. 10) for Exp. A0138-7. Results from these measurements are plotted in Fig. 12 together with the pre-recovery predictions made by Watts (ref. 7) using the AE8MIN and AE8MAX trapped electron environment models (ref. 14). The predictions are for a planar shield with infinite backing, which is expected to be an adequate geometry approximation in this case because of the shallow shielding penetration of the electrons and secondary bremsstrahlung. The M0003 results reported by Blake and Imamoto for dose in the TLD lithium fluoride have been multiplied by 1.25, the stopping power ratio of water to lithium fluoride for electrons in the applicable energy range, to compare with the calculated results in terms of tissue dose. M0003 measurements were also made for thinner shielding than shown in Fig. 12, but these data points are not included here because, as discussed by Blake and Imamoto, the results are suspect at present due to possible TLD saturation effects.

Fig. 12 shows that for small shielding depths where the incident electron flux is predicted to clearly dominate the dose ($\lesssim 0.1$ g/cm^2, corresponding to $\lesssim 15$ mils of aluminum shielding), there is general agreement between the predictions and measurements. The largest difference is at a shielding depth of about 0.04 g/cm^2, where the predicted dose is lower than measured by a factor of two; near 0.01 g/cm^2, the predicted dose is higher by a factor of 1.5. Blake and Imamoto (ref. 11) point out that the flattening of the measured dose profile near 2×10^4 rads for very thin shielding may be due to TLD saturation effects caused by very high doses in a thin layer of the TLD near the outboard surface and by the steep dose gradient within the TLD thickness. Thus, this may account for at least part of the difference between measurements and predictions in the thin shielding region $\lesssim 3 \times 10^{-2}$ g/cm^2 of Fig. 12 rather than environment modeling uncertainties.

CONCLUSIONS

Based on the radiation dose measurements by thermoluminescent dosimeters on LDEF, the AP8 proton model at solar minimum (AP8MIN) underpredicts the trapped proton flux in low Earth orbit by about a factor of two. This difference between measurement and prediction is not totally unexpected since a factor of two uncertainty is often associated with the AP8 model, but the difference here is larger than indicated by some Shuttle measurements (e.g., ref. 15). The higher radiation dose observed for TLDs on the trailing edge of the spacecraft is in agreement with calculations using the MSFC model for describing the angular dependence of the trapped proton environment, although the measured dose anisotropy, based on the relatively few trailing-to-leading edge TLD positions onboard at common shielding depths, is somewhat

higher than predicted. For thin shielding where incident electrons dominate the dose, predictions based on the AE8MIN trapped electron flux model are in general agreement with the TLD measurements (within a factor of two). Some of this difference may be due to saturation effects in the TLDs, which is still under investigation (ref. 11).

These conclusions should be regarded as tentative since additional calculations and comparisons with other LDEF radiation data are still in progress. For example, measurements of the induced radioactivity in various metal samples, some located in close proximity to the TLDs, provide additional data for evaluating the trapped proton flux model and will allow a cross-check of the conclusions here based on model comparisons with TLD data. Also, a more detailed mapping of the proton anisotropy is available from activation measurements, and these data are expected to provide a more definitive test of the trapped proton anisotropy model. These and other model comparisons with the LDEF ionizing radiation data are underway.

REFERENCES

1. Armstrong, T. W. and Colborn, B. L.: Future Directions for LDEF Ionizing Radiation Modeling and Assessments. Second LDEF Post-Retrieval Symposium, NASA CP-3194, 1993.

2. Watts, J. W.; Armstrong, T. W. and Colborn, B. L.: Revised Predictions of LDEF Exposure to Trapped Protons. Second LDEF Post-Retrieval Symposium, NASA CP-3194, 1993.

3. Sawyer, Donald W. and Vette, James I.: AP-8 Trapped Proton Environment for Solar Maximum and Solar Minimum. National Science Data Center, Goddard Space Flight Center, NSSDC/WDC-A-R&S 76-06, Dec. 1976.

4. Watts, J. W., Jr.; Parnell, T. A. and Heckman, H. H.: Approximate Angular Distribution and Spectra for Geomagnetically Trapped Protons in Low-Earth Orbit, in: *High Energy Radiation Background in Space,* Proc. AIP Conf., Vol. 186, pp. 75-85, American Institute of Physics, New York, 1989.

5. Colborn, B. L. and Armstrong, T. W.: Development and Application of a 3-D Geometry /Mass Model for LDEF Satellite Ionizing Radiation Assessments. Second LDEF Post-Retrieval Symposium, NASA CP-3194, 1993.

6. Burrell, M. O.: The Calculation of Proton Penetration and Dose Rates, George C. Marshall Space Flight Center, Huntsville, AL., NASA TM X-53063, August 1964.

7. Watts, J. W., Jr.: Predictions of LDEF Fluxes and Dose Due to Geomagnetically Trapped Protons and Electrons, in: Ionizing Radiation Exposure of LDEF (Pre-Recovery Estimates), E. V. Benton, et al., *Nucl. Tracks Radiat. Meas.* 20, 75 (1992).

8. Frank, A. L.; Benton, E. V.; Armstrong, T. W. and Colborn, B. L.: Absorbed Dose Measurements and Predictions on LDEF. Second LDEF Post-Retrieval Symposium, NASA CP-3194, 1993.

9. Reitz, G.: Preliminary Total Dose Measurements on LDEF. *Adv. Space Res.*, 12, No. 2, 369 (1992).

10. Bourrieau, J.: LDEF Dosimetric Measurement Results (AO 138-7 Experiment). Second LDEF Post-Retrieval Symposium, NASA CP-3194, 1993.

11. Blake, J. B. and Imamoto, S. S.: A Measurement of the Radiation Dose to LDEF by Passive Dosimetry. Second LDEF Post-Retrieval Symposium, NASA CP-3194, 1993.

12. Chang, J. Y.; Giangano, D.; Kantorcik, T.; Stauber, M. and Snead, M.: Thermoluminescent Dosimetry for LDEF Experiment M0006. First LDEF Post Retrieval Symposium, NASA CP-3134, 1992.

13. Harmon, B. A.; Fishman, G. J.; Parnell, T. A. and Laird, C. E.: Induced Activation Study of LDEF. Second LDEF Post-Retrieval Symposium, NASA CP-3194, 1993.

14. Vette, James I.: The AE-8 Trapped Electron Model Environment. National Space Science Data Center, Goddard Space Flight Center, NSSDC/WDC-A-R&S 91-24, Nov. 1991.

15. Richmond, R. G.; Badhwar, G. D.; Cash, B. and Atwell, W.: Measurement of Differential Proton Spectra Onboard the Space Shuttle Using a Thermoluminescent Dosimetry System, *Nucl. Instr. Meth.* A256, 393 (1987).

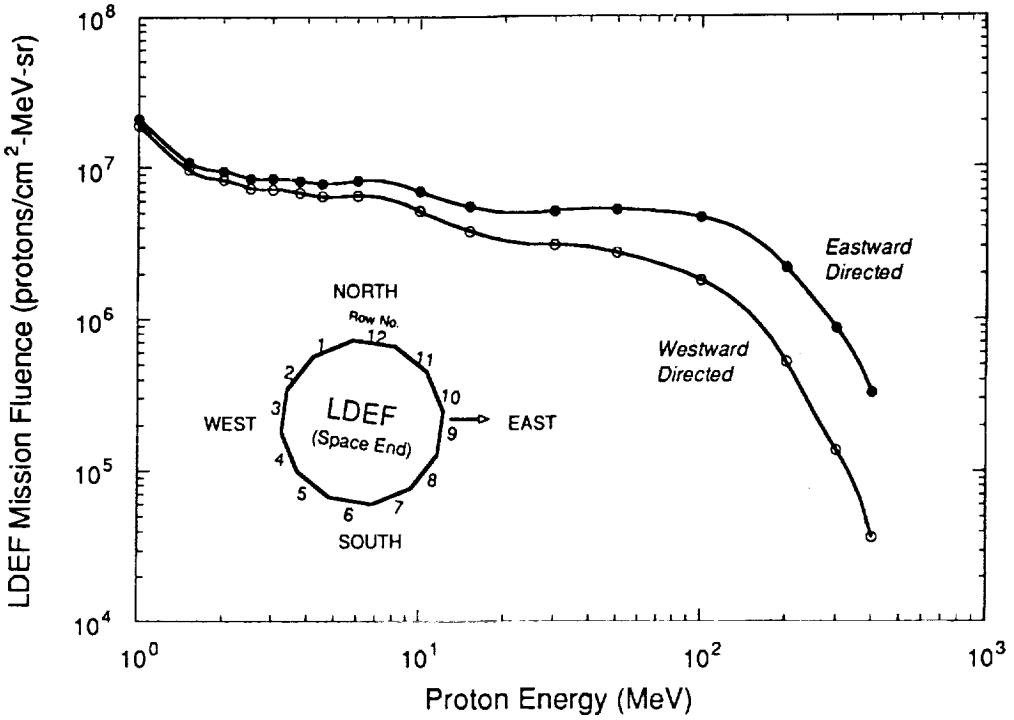

Figure 1. Directionality of LDEF radiation exposure to trapped proton environment. Example fluence spectra are shown for only two directions, the eastward-directed fluence (incident on west side of LDEF) and the westward-directed fluence.

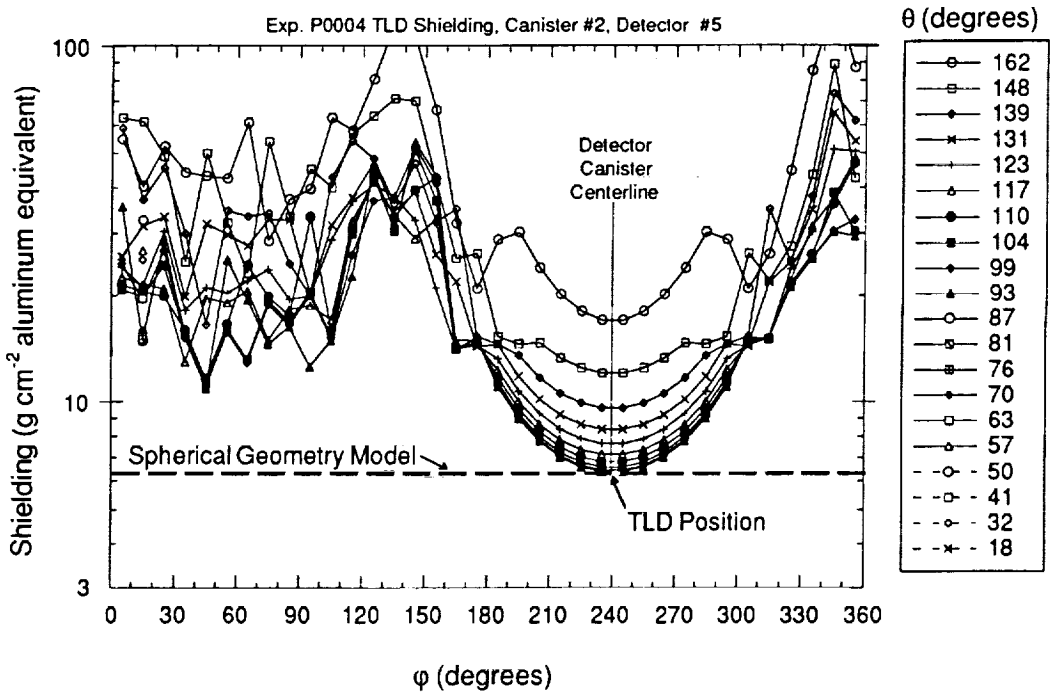

Figure 2. Example of shielding distributions generated using the 3-D spacecraft geometry model in predicting LDEF thermoluminescent dosimetry (TLD) response. Shown are areal densities along rays specified by the angles φ and θ (defined in text) emanating from a particular TLD location in the SEEDS experiment canister (Exp. P0004). The constant shielding for a simple 1-D spherical geometry model (used in some LDEF pre-recovery dose estimates) is shown for comparison.

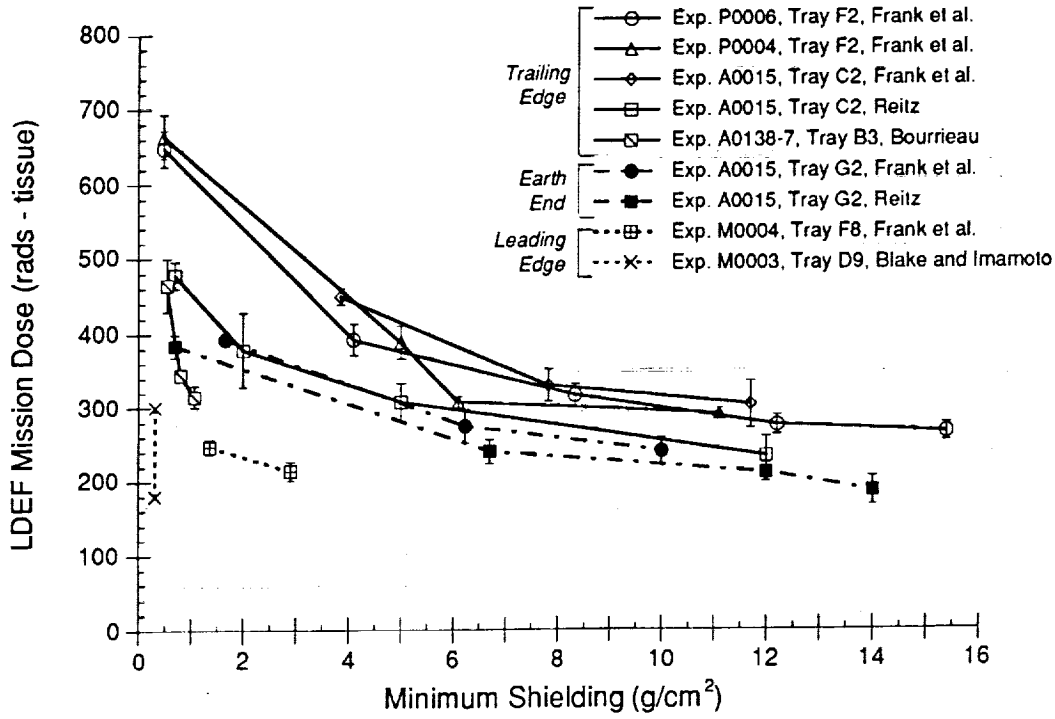

Figure 3. Summary of ionizing radiation dose measurements made on LDEF by thermoluminescent dosimeters (TLDs) at shielding depths where the dose is dominated by trapped protons.

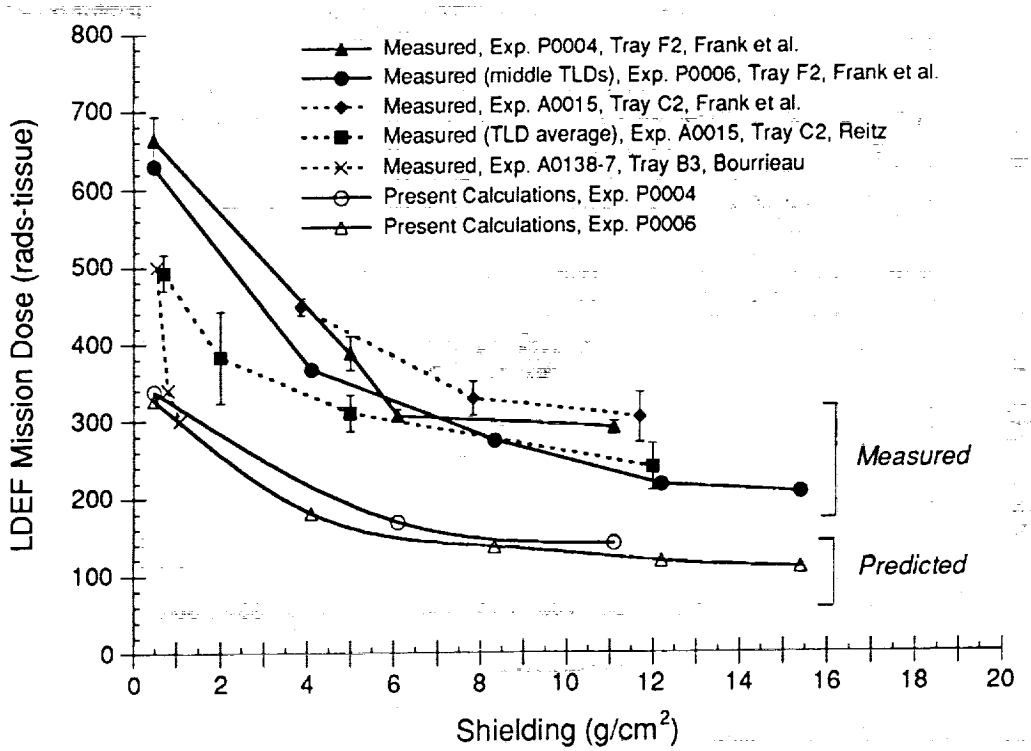

Figure 4. Predicted vs. measured radiation dose due to trapped proton environment for LDEF experiments on trailing (west) side of spacecraft.

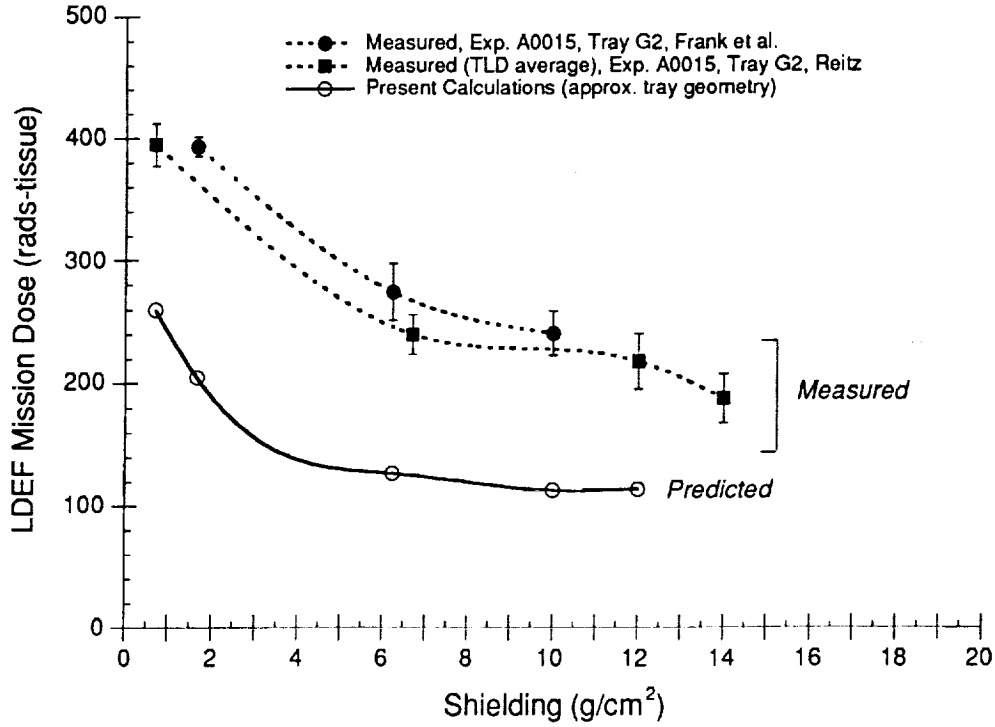

Figure 5. Predicted vs. measured radiation dose due to trapped proton environment for LDEF experiments on earth end of spacecraft.

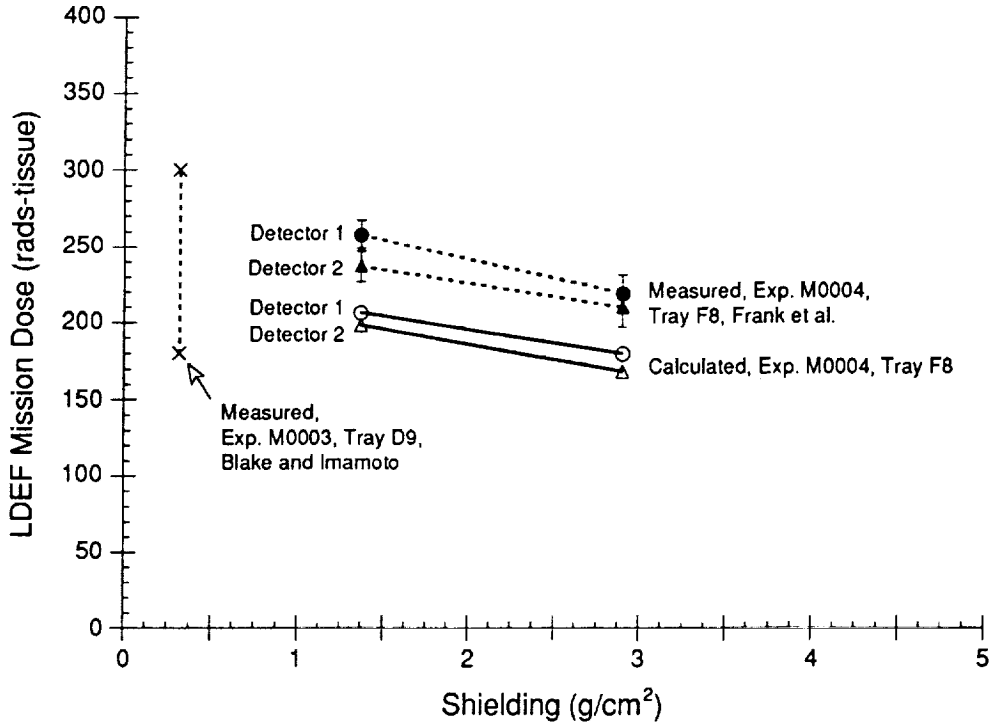

Figure 6. Predicted vs. measured radiation dose due to trapped proton environment for LDEF experiments on leading (east) side of spacecraft.

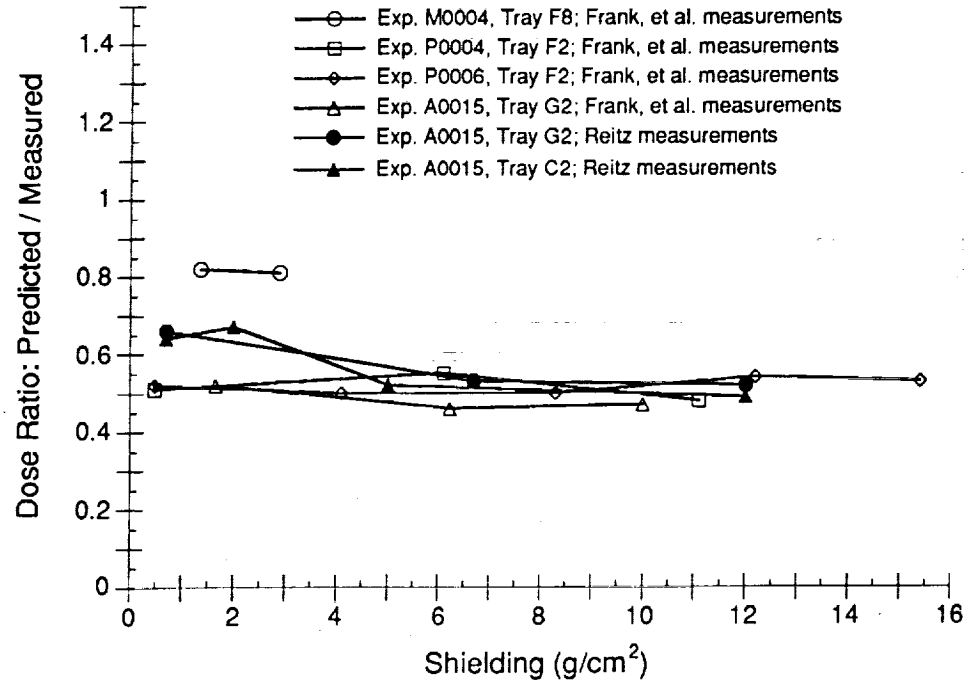

Figure 7. Ratio of predicted-to-measured radiation dose (in tissue) due to trapped proton environment based on LDEF data from thermoluminescent dosimeters.

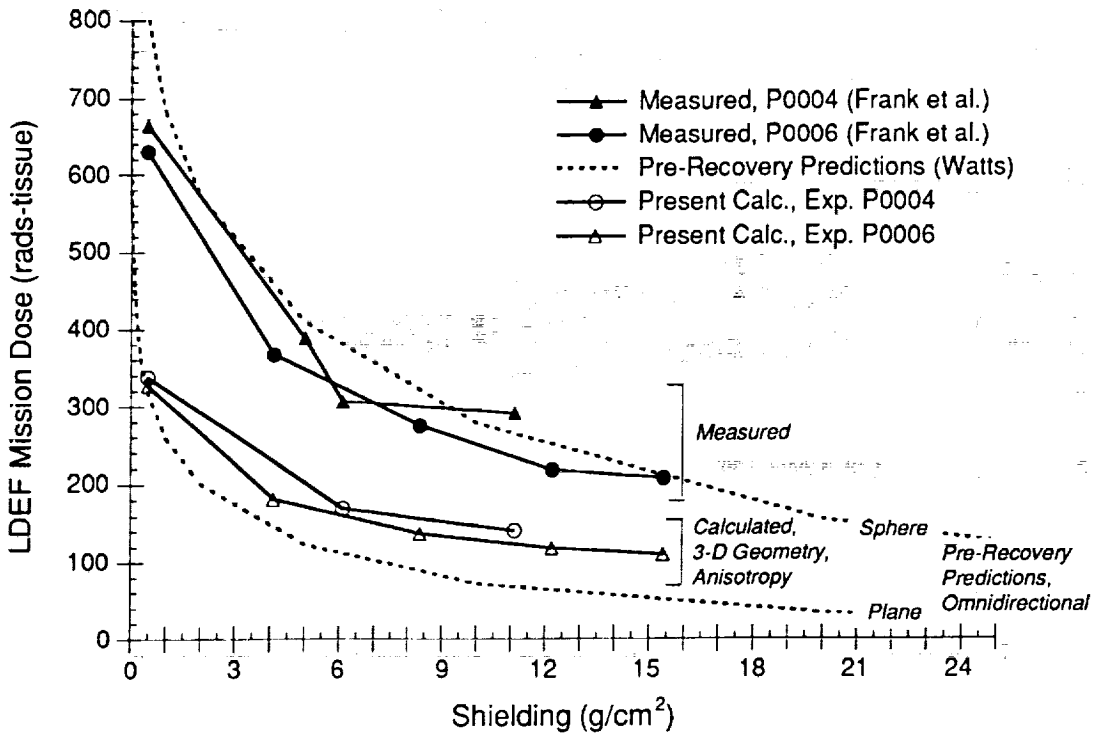

Figure 8. Influence of geomery model and environment anisotropy on predicting LDEF dose from trapped protons.

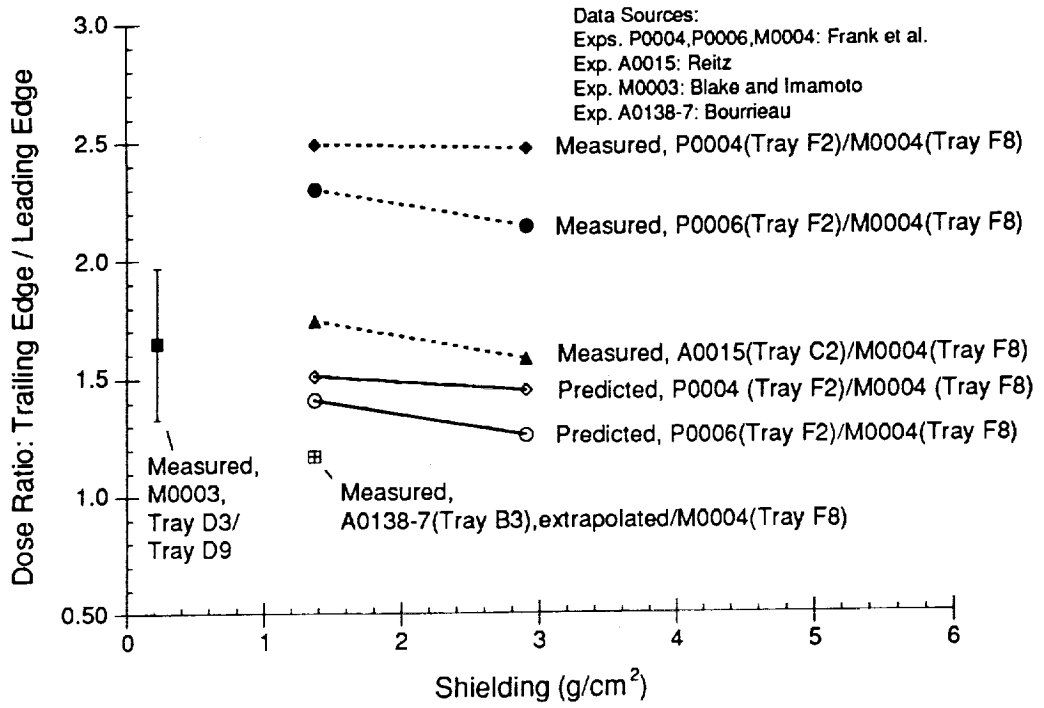

Figure 9. Radiation dose anisotropy on LDEF due to the directionality of the trapped proton environment. Shown are predicted and measured values of the ratio for the dose on the trailing (west) side LDEF to the dose on leading (east) side.

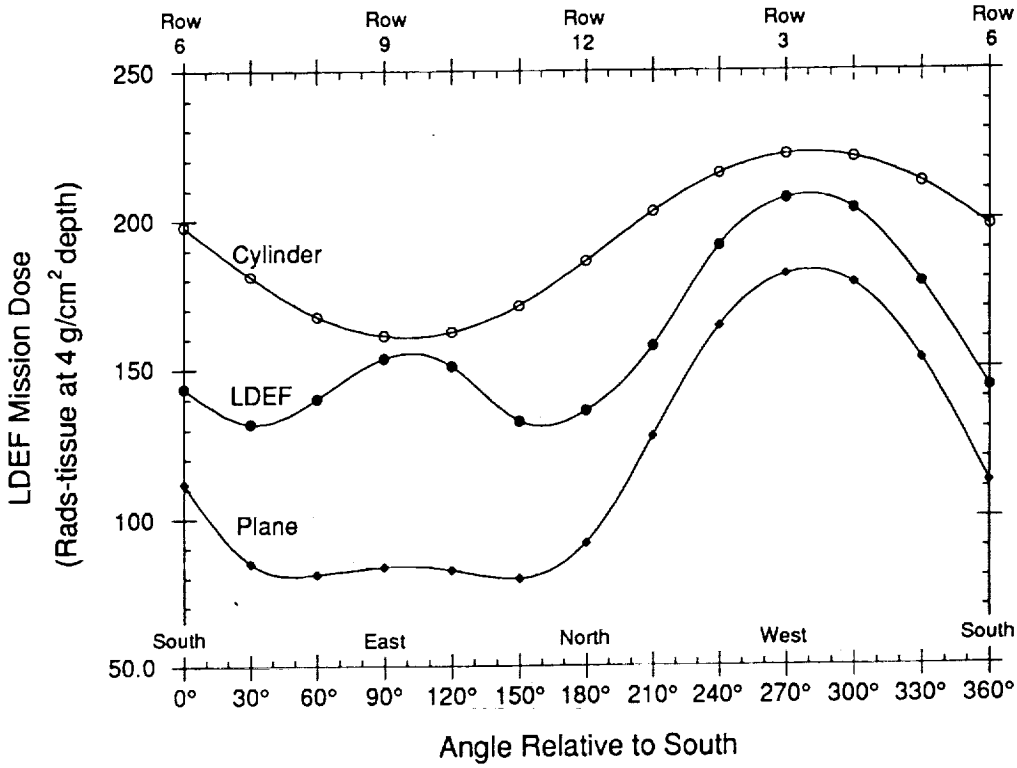

Figure 10. Influence of geomery model on predicted directionality of absorbed dose for LDEF mission due to trapped proton exposure.

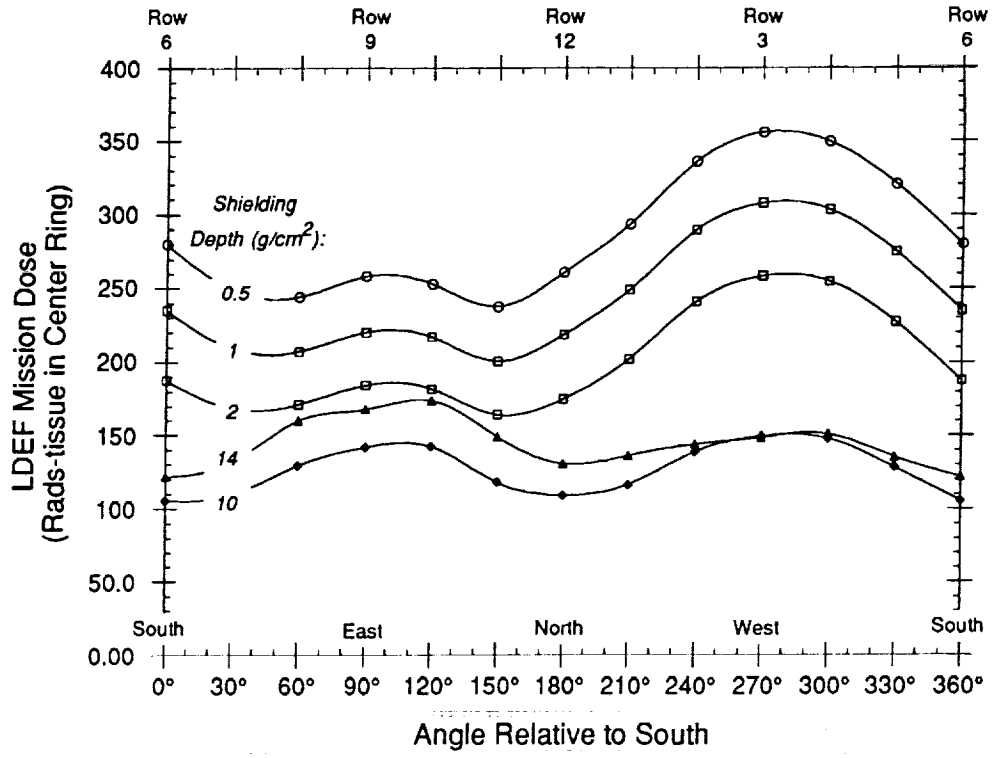

Figure 11. Influence of shielding depth on predicted directionality of absorbed dose from trapped protons. The dose is calculated in the center ring of the LDEF spacecraft using a 3-D geometry/mass model.

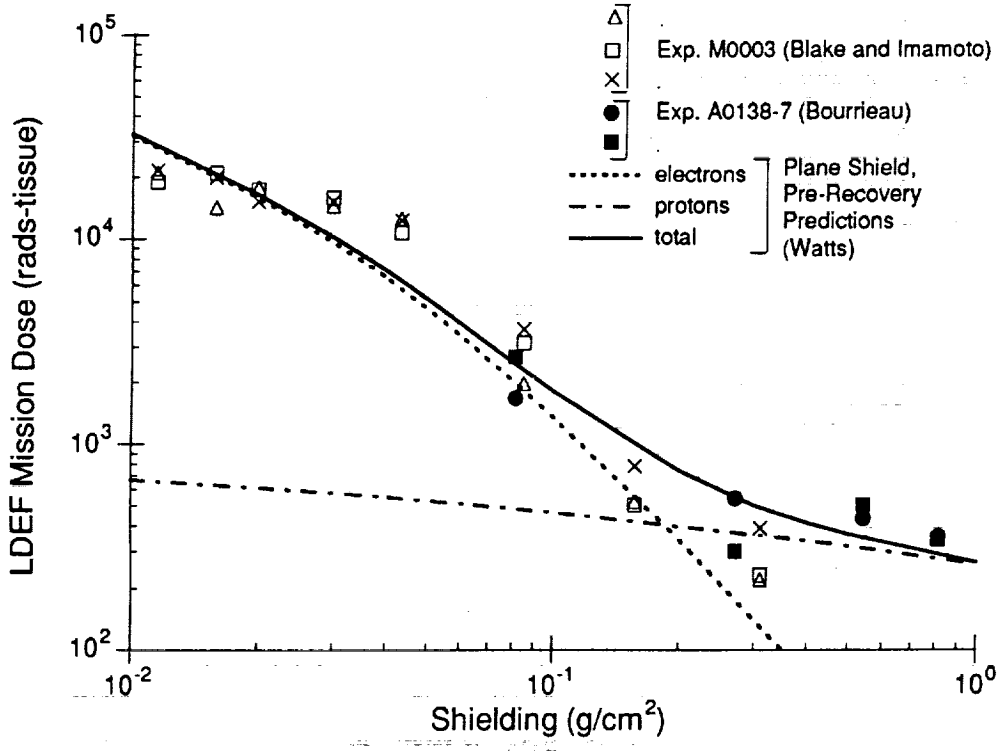

Figure 12. Comparison of measured and predicted absorbed dose for thermoluminescent dosimeters on LDEF having thin shielding where the dose is due to the trapped electron environment.

FUTURE DIRECTIONS FOR LDEF IONIZING RADIATION MODELING AND ASSESSMENTS*

T. W. Armstrong and B. L. Colborn
Science Applications International Corporation
Route 2, Prospect, TN 38477
Phone: 615/468-2603, Fax: 615/468-2676

SUMMARY

A calculational program utilizing data from radiation dosimetry measurements aboard the LDEF satellite to reduce the uncertainties in current models defining the ionizing radiation environment is in progress. Most of the effort to date has been on using LDEF radiation dose measurements to evaluate models defining the geomagnetically trapped radiation, which has provided results applicable to radiation design assessments being performed for Space Station Freedom. Plans for future data comparisons, model evaluations, and assessments using additional LDEF data sets (LET spectra, induced radioactivity, and particle spectra) are discussed.

INTRODUCTION

Ionizing radiation measurements on the Long Duration Exposure Facility (LDEF) satellite provide a unique opportunity for reducing present uncertainties in models used in defining the space radiation environment. The LDEF mission had several features particularly important to radiation model validation -- e.g., various types of radiation detectors were aboard, providing an extensive data set; because of the long mission duration, the data have unparalleled statistical accuracy; and, the LDEF spacecraft had a very stable orientation during the flight, allowing unprecedented data to be obtained on the directionality of the space environment. The radiation measurements performed and key results from analyses to date are summarized in refs. 1 and 2.

A calculational program is in progress as part of the LDEF ionizing radiation investigations. The scope of the program includes model predictions in support of data analysis and interpretation, calculations for data comparisons and model accuracy assessments, and model updates. The overall objective is to utilize the LDEF data to provide models that give a more accurate definition of the ionizing radiation environment. This will enable more accurate radiation designs and design margin assessments for future missions in low Earth orbit which in turn will help reduce risk and cost. Specific models which can be improved utilizing LDEF data and their importance in addressing particular radiation issues for planned missions are discussed in ref. 3.

*Work supported by NASA Marshall Space Flight Center, Huntsville, AL, Contract NAS8-39386.

The purpose of the present paper is to summarize the current status and future emphasis of the LDEF ionizing radiation modeling work. The next section gives an overview of the calculations made to date, followed by summaries of the status in terms of specific tasks and in terms of comparisons which have been made with different measurement data sets. The emphasis of planned radiation modeling work and related assessments is discussed in the last section.

OVERVIEW

Calculations made to date for LDEF ionizing radiation assessments and for model comparisons with dosimetry data can be categorized as follows:

Phase 0: Pre-Recovery Predictions -- To aid in the planning and interpretation of radiation dosimetry data analyses, pre-recovery estimates were made to characterize the expected radiation environment experienced by LDEF and the general features and magnitude of the induced environment and radiation effects expected to be observed (ref. 4). This work included estimates of the expected radiation environment (refs. 5,6) absorbed dose (ref. 5), LET spectra (ref. 7), and induced radioactivity (ref. 6). These calculations were of a scoping nature and included numerous approximations -- e.g., the directionality of the environment was ignored and shielding calculations were based on simple one-dimensional geometries.

Phase 1: Preliminary Calculations and Data Comparisons -- Several approximate calculations were carried out to obtain some quick comparisons with the initial data analysis results (e.g., ref. 8). This included preliminary comparisons of model predictions with absorbed dose and activation data, which were reported at the First LDEF Symposium (refs. 9, 10). Various approximations were made in the calculations to obtain these quick-look comparisons -- e.g., one-dimensional geometries were assumed, and the environment definition was incomplete, with anisotropy and orbit altitude variations neglected in most cases.

Phase 2: Definitive Modeling and Data Comparisons -- To obtain more accurate modeling and definitive comparisons with the more complete data becoming available, basic calculational work was needed in two areas: (a) a complete definition of the LDEF trapped proton exposure, taking into account directionality, altitude variation and solar cycle dependence, and (b) a realistic (three-dimensional) geometry/mass model of the LDEF spacecraft and dosimetry experiments in order to adequately account for shielding effects. This work has been completed and reported at this symposium (refs. 11, 12). These improved models have been initially applied for 3-D dose predictions and data comparisons, with results reported at this symposium (refs. 13, 14).

Future Work -- The emphasis of future calculations is on using the revised environment definitions and 3-D geometry/mass model to make definitive predictions and comparisons with other LDEF radiation data (LET spectra, induced radioactivity, secondary particles, etc.) as it becomes available. Specific predictions and planned data comparisons are outlined in the next two sections.

STATUS

In this section a breakdown of the completed and planned calculational tasks is given with the status of each task indicated.

Most of the work on assessing LDEF exposure to the radiation environment has been completed (Table I). Initial estimates (refs. 5,6) of the exposure were made to determine the importance of all sources (trapped protons, trapped electrons, galactic cosmic rays, earth albedo neutrons, and albedo protons) to different radiation effects. Initial work on the definition of the trapped proton environment was incomplete in that the altitude and solar cycle dependence of directional trapped proton spectra were not determined, but revised estimates using the MSFC anisotropy model (ref. 15) to obtain vector fluxes have now been completed (ref. 11). An input parameter to the MSFC trapped proton anisotropy model is the effective scale height of the atmosphere, which represents an average over proton trajectories and is difficult to estimate from first principles. LDEF data provide a basis for investigating appropriate scale height values for model input, and such studies are planned. Measurements of the LET spectra from heavy ions in the galactic cosmic ray (GCR) spectra indicate strong directionality (ref. 16). While this observed directionality is expected to be influenced by shielding variations, there are indications that the directionality of the external environment is a factor also (ref. 16). Thus, some additional environment definition work to estimate the angular dependence of the GCR heavy ion exposure may be needed for definitive comparisons with the observed LET directionality.

Key to obtaining definitive model predictions for data comparisons is a realistic treatment of shielding effects. As indicated in Table II, work on development of a detailed, 3-D geometry/mass model of LDEF is now completed (refs. 12, 17), and this model is currently being used in radiation transport calculations and other shielding assessments.

With the work on revised trapped proton environment calculations and 3-D geometry modeling completed, definitive predictions with state-of-the-art modeling accuracy can be performed to compare with the LDEF radiation dosimetry data. Initial calculations using these models have been made for the absorbed dose and comparisons made with the LDEF measurements (refs. 13. 18-20) using thermoluminescent dosimeters (TLDs), as indicated in Table III. These comparisons, which are complete except for some revisions that may be needed when results from final data analyses become available, provide a test of the accuracy of current trapped proton flux models (ref. 21) for low Earth orbit missions and provide partial data needed to check models describing the directionality of the environment.

Several experiments on LDEF contained plastic nuclear track detectors (PNDTs) that measured the linear energy transfer (LET) spectra (Table IV, ref. 1). Model predictions and comparisons with these data are important because LET has a key role in estimating various radiation effects, and because preliminary LET measurement results (ref. 22) indicate a high-LET component which is not predicted by pre-recovery

estimates (Fig. 1), but which may have important practical significance. LET calculational tasks involve several steps (Table IV), including 3-D transport calculations to account for shielding variations and the directionality of the environment, influence of secondaries from heavy ion fragmentation, and an extension of present calculational methods to account for target recoils and fragments, which is needed to compare with the unique data from LDEF on the high-LET tail of the spectrum. For definitive comparisons with the LET measurements, the calculations should, as suggested by the USF group (footnote 1), include the response function of the track detectors, which involves including energy and angular-dependent relations for track detection from observations for different track etch rates and from calibration experiments using accelerator beams.

Several measurements of the secondary neutron fluence were made on LDEF using ^{6}LiF foils (ref. 23) and activation samples (ref. 24). These data provide an opportunity to evaluate the accuracy of nuclear models and radiation transport techniques for predicting secondary neutron spectra in spacecraft, which is of interest in mission radiation assessments because such secondary particles contribute to biological damage, radiation backgrounds to sensitive instrumentation, and radiation damage to electronics. Planned calculations related to this are listed in Table V. Since the ^{6}LiF measurements may be influenced by the high proton fluence present, some initial calculations delineating the neutron vs. proton response are needed for the particular radiation environment experience by LDEF. To obtain a definitive estimate of the neutron fluence for data comparisons, a detailed transport calculation using Monte Carlo methods (HETC code) and the 3-D geometry/mass model of LDEF is planned with trapped , galactic, and albedo environment sources included. Intercomparisons using the two data sets from ^{6}LiF and activation will provide a check on the consistency of the neutron measurement methods.

Preliminary data on high-energy neutron and proton spectra are available (refs. 23, 25) from various fission foil measurements (Table V). Since fission is induced by both neutrons and protons, the relative contribution to the fission data will first need to be investigated. Of particular interest is the data from tantalum foils, where the fission threshold is above the energy of trapped protons, so the activation in this case is a measure of the galactic fluence only.

Induced radioactivity measurements are available from both metal samples placed aboard LDEF and from the analysis of various spacecraft components (refs. 24, 26-29), as summarized in Table VI. The activation of samples placed in the P0006 experiment, which also contained TLDs for dose measurements, is of particular interest for model comparisons because this will provide a cross-check on the differences found between measured and predicted doses. The activation samples also included some elements (Co, Ta) where the activation for particular isotopes is only from neutron-induced reactions, providing a cross-check on the ^{6}LiF neutron measurements and related calculations.

Several approximate calculations (ref. 10) were made to get some early preliminary comparisons with the activation measurements on spacecraft components (Table VI). Planned are more definitive calculations that remove the early approximations indicated in Table VI. Calculations to compare with the tray clamp activation data are of special interest because these measurements provide a detailed mapping of the

directional effects of trapped protons, providing a test of the accuracy of the MSFC anisotropy model. Data on the production of various radioisotopes in the LDEF spacecraft trunnions is of interest for model validation because it provides a measure of directional and secondary particle effects and contains contributions from both trapped and galactic sources. Measurements for other spacecraft components, such as the keel and end plates, provide additional directional data for model validation and confirmation.

DATA AVAILABLE FOR MODEL VALIDATION

In this section the status of work on radiation model validation is given in terms of the data available and comparisons which have been made.

Essentially all of the data on absorbed dose measurements using TLDs is available (Table VII), and the results of model comparisons are given in ref. 14. Initial results for measured LET spectra from PNTDs are available (Table VIII) but much data analysis remains, and LET model predictions to compare with the PNTD data are TBD (To Be Done).

Preliminary data on neutron and proton fluence and spectra from fission and ^{6}LiF foil measurements are available (Table IX), but results from some recent accelerator calibration tests need to be incorporated to complete the data analysis (footnote 1). Thus, only very preliminary model comparisons have been made to compare with this data.

The counting of intentionally placed activation samples on LDEF for the case of neutron measurements (Co and Ta samples) has been completed (Table X), but analyses to determine absolute neutron fluences are still in progress (footnote 2). Measurements for the other activation sample materials (Table X) are essentially complete, with intercomparisons and final data analyses nearing completion. Data available from induced radioactivity measurements in spacecraft components, and the status of calculations and comparisons, are summarized in Table XI.

FUTURE WORK

As indicated above, to date calculations have been made to compare with only a portion of the LDEF radiation dosimetry data. Preliminary evaluations have been made of environment models defining the trapped proton flux, the directionality of trapped protons, and the trapped electron flux. Interim results based on these early comparisons indicate that the proton flux model (ref. 21) underpredicts the observed dose by about a factor of two (ref. 14). The basic validity of the MSFC trapped proton anisotropy model (ref. 15) has been verified (ref. 14). However, preliminary results indicate that the observed directionality is somewhat stronger than predicted, and additional data comparisons are needed to resolve this issue. The results to date indicate that accuracy of electron flux environment models (ref. 30) for LDEF-type orbits is

about a factor of two (ref. 14). These findings, while only tentative at present, have already been important in establishing realistic radiation design margins for Space Station Freedom, and additional model environment accuracy assessments utilizing the full set of LDEF radiation dosimetry data (outlined below) are expected to provide important input for upcoming Space Station Freedom radiation design verification evaluations.

The emphasis of future radiation modeling work and related assessments is summarized below.

Calculations and Data Comparisons

Work to date has concentrated on model comparisons with the LDEF absorbed dose data. Subsequent work will emphasize data comparisons and model evaluations for the other measured data sets, with general priorities as discussed below. These planned comparisons will provide a test of modeling accuracies for predicting not only the ambient environment but the induced environment inside spacecraft and instrument packages as well. Furthermore, these additional data comparisons provide more stringent tests of predictive capabilities in that the model evaluations will include more detailed comparisons with differential data (LET and particle spectra), in contrast to the integral-type data (dose) comparisons made to date.

LET Spectra -- Modeling and data comparisons for LET spectra are of high priority for future work for several reasons: Accurate predictive capabilities for LET spectra are of practical significance for mission applications due to the fundamental role of LET in assessing various radiation effects, such as biological damage, electronics upset, and sensor noise. Also, the LET data from LDEF are unique due to their high-statistical accuracy and the data show features at high LET that are not accounted for in present models (Fig. 1). Updated models that take into account the LDEF observations are of practical importance in radiation assessments for spacecraft in orbits similar to LDEF, such as those planned for Space Station Freedom.

Activation -- Planned model comparisons with the activation data from induced radioactivity measurements are important in evaluating models for predicting both ambient and induced environments. Of high priority here are comparisons with the experiment tray clamp activation data, which will allow detailed anisotropy model evaluations, and comparisons with the Exp. P0006 activation samples, which will provide a check of the present tentative conclusions on the accuracy of trapped proton flux models based on absorbed dose comparisons.

Secondaries and Particle Spectra -- Model comparisons with fission foil data, measurements of certain radioisotopes in activation samples, and ^{6}LiF data will allow evaluation of models and transport methods for predicting secondary particle fluences inside spacecraft. Coarse spectral information for protons and neutrons is also available from these data. Also of interest here are model comparisons with the tantalum foil measurements, which will provide a check of model predictions for the GCR proton fluence at the geomagnetic cutoff of low inclination (28.5°) orbits.

From the calculations and data comparisons outlined above, intercomparisons taking into account all of the LDEF radiation dosimetry data sets are planned, including consistency checks comparing LDEF results where possible with previous flights. Quantitative assessments of model uncertainties will be performed and model improvements made, with documentation and dissemination of the updated models, data bases, and related computer codes provided for future mission applications.

Thus, the product goal of this planned work is improved models for predicting the ambient and induced ionizing radiation environments. While measurements of radiation effects for some of the newer component technologies (e.g., radiation sensitive microelectronics and sensors) were not included on LDEF, the improved radiation environment definitions from LDEF, together with ground-based measurements of component radiation susceptibilities, will enable improved radiation effects predictions for future missions and evolving component technologies despite the lack of LDEF radiation effects data for specific components. In this way, the LDEF radiation modeling results can have a significant impact on radiation assessments for future missions by reducing risk and cost associated with radiation designs and tests.

REFERENCES

1. Parnell, T. A.: Summary of Ionizing Radiation Analysis on the Long Duration Exposure Facility. First LDEF Post-Retrieval Symposium, NASA CP-3134, 1992.

2. Parnell, T. A.: Status of LDEF Ionizing Radiation Measurements and Analyses. Second LDEF Post-Retrieval Symposium, NASA CP-3194, 1993.

3. Armstrong, T. W. and Colborn, B. L.: Ionizing Radiation Calculations and Comparisons with LDEF Data. First LDEF Post-Retrieval Symposium, NASA CP-3134, 1992.

4. Benton, E. V.; Heinrich, W.; Parnell, T. A.; Armstrong, T. W.; Derrickson, J. H.; Fishman, G. J.; Frank, A. L.; Watts, J. W., Jr. and Wiegel, B.: Ionizing Radiation Exposure of LDEF: Pre-recovery Estimates. *Nucl. Tracks. Radiat. Meas.* 20, 75 (1992).

5. Watts, J. W., Jr.: Predictions of LDEF Fluxes and Dose Due to Geomagnetically Trapped Protons and Electrons. In: Ionizing Radiation Exposure of LDEF: Pre-recovery Predictions (E.V. Benton, et al.), *Nucl. Tracks. Radiat. Meas.* 20, 75 (1992).

6. Armstrong, T. W. and Colborn, B. L.: Predictions of Induced Radoactivity for Spacecraft in Low Earth Orbit. *Nucl. Tracks Radiat. Meas.* 20, 101 (1992).

7. Derrickson, J. H.: Linear Energy Transfer Spectra for the LDEF Mission. In: Ionizing Radiation Exposure of LDEF: Pre-recovery Predictions (E.V. Benton, et al.), *Nucl. Tracks. Radiat. Meas.* 20, 75 (1992).

8. Harmon, B. A.; Fishman, G. J.; Parnell, T. A.; Benton, E. V. and Frank, A. L.: LDEF Radiation Measurements: Preliminary Results. *Nucl. Tracks Radiat. Meas.* 20, 131 (1992).

9. Watts, John W.; Parnell, T. A.; Derrickson, James H.; Armstrong, T. W. and Benton, E. V.: Predictions of LDEF Ionizing Radiation Environment. First LDEF Post-Retrieval Symposium, NASA CP-3134, 1992.

10. Armstrong, T. W.; Colborn, B. L. and Watts, J. W., Jr.: Ionizing Radiation Calculations and Comparisons with LDEF Data. First LDEF Post-Retrieval Symposium, NASA CP-3134, 1992.

11. Watts, J. W. Jr.; Armstrong, T. W. and Colborn, B. L.: Revised Predictions of LDEF Exposure to Trapped Protons. Second LDEF Post-Retrieval Symposium, NASA CP-3194, 1993.

12. Colborn, B. L. and Armstrong, T. W.: Development and Application of a 3-D Geometry/Mass Model for LDEF Satellite Ionizing Radiation Assessments. Second LDEF Post-Retrieval Symposium, NASA CP-3194, 1993.

13. Frank, A. L.; Benton, E. V.; Armstrong, T. W. and Colborn, B. L.: Absorbed Dose Measurements and Predictions on LDEF. Second LDEF Post Retrieval Symposium, NASA CP-3194, 1993.

14. Armstrong, T. W. and Colborn, B. L.: Radiation Model Predictions and Validation Using LDEF Satellite Data. Second LDEF Post-Retrieval Symposium, NASA CP-3194, 1993.

15. Watts, J. W., Jr.; Parnell, T. A. and Heckman, H. H.: Approximate Angular Distribution and Spectra for Geomagnetically Trapped Protons in Low-Earth Orbit. In: *High Energy Radiation Background in Space*, Proc. AIP Conf., Vol. 186, pp. 75-85, American Institute of Physics, New York, 1989.

16. Csige, I.; Benton, E. V.; Frigo, L.; Parnell, T. A.; Watts, J. W. Jr.; Armstrong, T. W. and Colborn, B. L.: Three-Dimensional Shielding Effects on Charged Particle Fluences Measured in the P0006 Experiment on LDEF. Second LDEF Post-Retrieval Symposium, NASA CP-3194, 1993.

17. Colborn, B. L. and Armstrong, T. W.: LDEF Geometry/Mass Model for Radiation Analyses. First LDEF Post-Retrieval, NASA CP-3134, 1992.

18. Reitz, G.: Preliminary Total Dose Measurements on LDEF. *Adv. Space Res.*, 12, No. 2, 369, (1992).

19. Bourrieau, J.: LDEF Dosimetric Measurement Results (AO 138-7 Experiment). Second LDEF Post-Retrieval Symposium, NASA CP-3194, 1993.

20. Blake, J. B. and Imamoto, S. S.: A Measurement of the Radiation Dose to LDEF by Passive Dosimetry. Second LDEF Post-Retrieval Symposium, NASA CP-3194, 1993.

21. Sawyer, Donald M. and Vette, James I.: AP-8 Traped Proton Environment for Solar Maximum and Solar Minimum. Goddard Space Flight Center, National Science Data Center, NSSDC/WDC-A-R&S 76-06 (1976).

22. Benton, E. V.; Csige, I.; Oda, K.; Henke, R. P.; Frank, A. L.; Benton, E. R.; Frigo, L. A.; Parnell, T. A.; Watts, J. W. Jr. and Derrickson, J. H.: LET Spectra Measurements of Charged Particles in the P0006 Experiment on LDEF. Second LDEF Post-Retrieval Symposium, NASA CP-3194, 1993.

23. Benton, E. V.; Frank, A. L.; Benton, E. R.; Csige, I.; Parnell, T. A.; and Watts, J. W., Jr.: Radiation Exposure of LDEF: Initial Results. First LDEF Post-Retrieval Symposium, NASA CP-3134, 1992.

24. Harmon, B. A.; Fishman, G. J.; Parnell, T. A. and Laird, C. E.: Induced Activation Study of LDEF. Second LDEF Post-Retrieval Symposium, NASA CP-3194, 1993.

25. LDEF Experiment P0006 Linear Energy Transfer Spectrum Measurement (LETSME), Quick Look Report. Eril Research, Inc. NASA MSFC Contractor Final Report NAS8-38188, Dec. 1990.

26. Reedy, Robert C.; Moss, Calvin E.; Bobias, George S. and Masarik, Jozef: Radioactivities Induced in Some LDEF Samples. Second LDEF Post-Retrieval Symposium, NASA CP-3194, 1993.

27. Winn, W. G.: Gamma-Ray Spectrometry of LDEF Samples. Westinghouse Savannah River Company, WSRC-RD-91-16, February 1992.

28. Smith, Alan R. and Hurley, Donna L.: A Photon-Phreak Digs the LDEF Happening. Second LDEF Post-Retrieval Symposium, NASA CP-3194, 1993.

29. Reeves, James H.; Arthur, Richard J. and Brodzinski, Ronald L.: Sensitivity of LDEF Foil Analyses Using Ultra-Low Background Germanium and Large NaI (Tl) Multidimensional Spectrometers. Second LDEF Post-Retrieval Symposium, NASA CP-3194, 1993.

30. Vette, James I.: The AE-8 Trapped Electron Model Environment. National Space Science Data Center, Goddard Space Flight Center, NSSDC/WDC-A-R&S 91-24, Nov. 1991.

31. Adams, James H. Jr.: Cosmic Ray Effects on Microelectronics, Part IV. Naval Research Laboratory, NRL Memorandum Report 5901, December 1986.

FOOTNOTES

1. Benton, E. V. and Csige, I., Univ. San Francisco, priv. comm., 1992.

2. B. A. Harmon, NASA Marshall Space Flight Center, priv. comm., 1992.

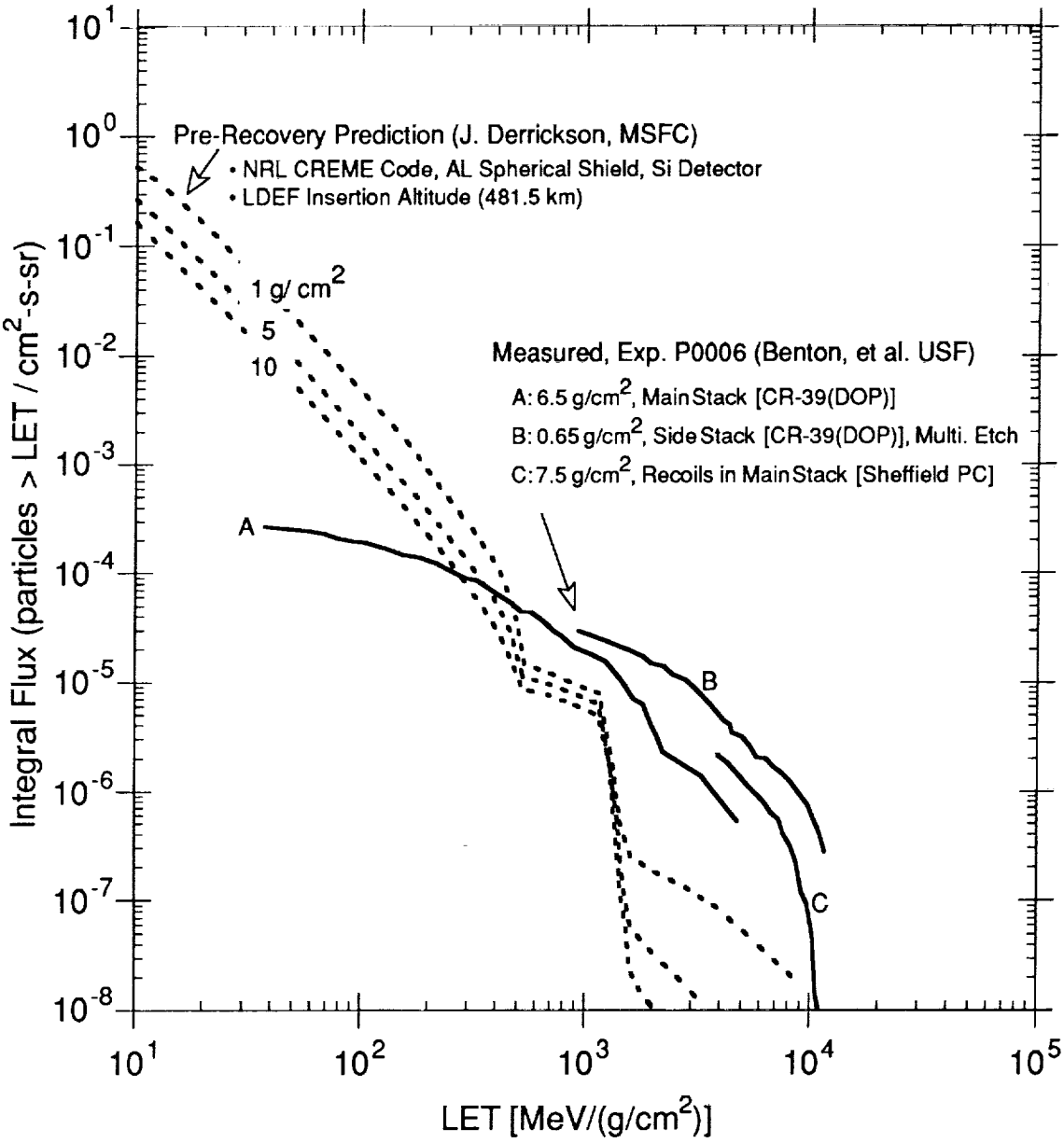

Figure 1. Comparison of LDEF pre-recovery predictions of linear energy transfer (LET) spectra (ref. 7) with interim results from measured spectra in Exp. P0006 (ref. 22). The predictions were made using the CREME code (ref. 31) and 1-D spherical shielding.

COSMOGENIC RADIONUCLIDES ON LDEF: AN UNEXPECTED ^{10}Be RESULT

J. C. Gregory
The University of Alabama in Huntsville
Department of Chemistry
Huntsville, AL 35899-2900
Phone: 205/895-6028, Fax: 205/895-6349

A. Albrecht and G. Herzog
Rutgers University
Department of Chemistry
New Brunswick, NJ 08901
Phone: 908/932-3955, Fax: 908/932-5312

J. Klein, R. Middleton and B. Dezfouly-Arjomandy
University of Pennsylvania
Physics Department
Philadelphia, PA 19104-6396
Phone: 215/898-8832, Fax: 215/898-2010

B.A. Harmon
NASA, Marshall Space Flight Center
Space Science Laboratory, ES62
Huntsville, AL 35812
Phone: 205/544-4924, Fax: 205/544-7754

SUMMARY

Following the discovery of the atmospheric derived cosmogenic radionuclide ^{7}Be on the LDEF[1], we began a search for other known nuclides produced by similar mechanisms. None of the others have the narrow gamma-ray line emission of ^{7}Be decay which enabled its rapid detection and quantification. This paper describes a search for ^{10}Be atoms on LDEF clamp plates using accelerator mass spectrometry. An unexpected result was obtained.

INTRODUCTION

During the first few weeks after return of LDEF to the Kennedy Space Center, the presence of ^{7}Be was discovered during surveys of the spacecraft for cosmic-ray-produced radionuclides. It was clear from those results that there was more of the isotope on the leading side than on the trailing. From further experiments at the Marshall Space Flight Center the activity of ^{7}Be was found to be 6 ($\pm$ 2) x 10^{5} atoms per cm^{2} (corrected to date of the orbital retrieval in January, 1990) on a variety of leading edge metal surfaces including stainless steel and aluminum.[1)] The activity associated with similar substrates from the trailing edge was of the order of 100 times less. The hypothesis proposed in the *Nature* article attributed the production of ^{7}Be to cosmic-ray proton and secondary neutron induced spallation of atmospheric oxygen and nitrogen nuclei throughout the entire upper atmosphere and subsequent transport of the Be upwards to orbital altitudes. The *in situ* production of Be from oxygen at orbital altitudes is too low by three or four orders of magnitude. The Be atoms then stuck to the LDEF surfaces until they decayed ($t_{1/2}$ for ^{7}Be is 53 days).

We have subsequently described[2)] a mechanism by which Be species are transported upwards as positive ions (at least above 100km). By analogy with meteoritic metal ion chemistry in the upper atmosphere, Be^{+} is the most probable form in that environment, rather than Be, BeO, or BeO^{+}. Simple diffusion of mass 7 particles (without invoking electrostatic effects) from the turbopause to 300km has been shown[3)] to be adequate to explain the ^{7}Be observation in a general way.

The front surfaces of stabilized vehicles like LDEF are scoured clean of hydrocarbon contamination by the ambient atomic oxygen. Surfaces of aluminum and stainless steel are covered with a thin layer of oxide; Al_2O_3, Cr_2O_3, Fe_2O_3, etc., which may be modified in some cases by the presence of SiO_2. In all cases these are ionic lattices into which an 8 km s^{-1} Be^{+} ion could easily be absorbed. The sticking probability at present is unknown, but because the areal densities of ^{7}Be on stainless steel and aluminum were found to be similar, we have assumed it to be 1.

Nuclear spallation is an indiscriminate shattering of a target nucleus by a high-energy projectile (usually a proton or neutron). Fragments from the breakup can be any smaller nucleus (a nucleus where Z or A or both are reduced relative to the target nucleus). The relative abundances of the products are generally known from accelerator measurements. Both stable and radioactive products result, but normally only the radioactive products are detectable because the pre-existing levels of stable nuclei in the target material due to chemical contamination are generally several orders of magnitude larger than the levels of these nuclei produced by spallation. Typical chemical ion purities are in the ppb to ppm range (roughly 10^{13} to 10^{16} atoms/g). Production rates of nuclei via spallation reactions by cosmic rays, for example in meteorites, are rarely greater than 10^{7} atoms/g/year, and more usually ~10^{4} atoms/g/year. In general, the concentrations of nuclei produced by spallation are too low to measure by ordinary chemical techniques. Radioactive nuclei can be detected by measuring their rate of decay (as in the case of ^{7}Be), but for the longer-lived nuclei and those not emitting very narrow line-width gamma-rays, even this process is often not sensitive enough. The technique of accelerator mass spectrometry (AMS) offers the highest sensitivity for detection of the unstable nuclei produced by spallation, including ^{14}C, ^{7}Be, and ^{10}Be from nitrogen and oxygen, and ^{26}Al and ^{36}Cl from argon. Other unstable nuclei, notably the noble gases ^{3}He and ^{37}Ar and ^{39}Ar, cannot be measured using this technique.

^{10}Be was chosen for our present study because of its chemical similarity to ^{7}Be. Source functions for both ^{7}Be and ^{10}Be in the atmosphere are known. We expected that the surface densities of these two nuclides on LDEF would directly reflect differences in the steady-state concentrations at orbital altitudes. These differences should depend on known production factors, mass dependence in atmospheric transport, and half-life of the two isotopes, while differences in chemical behavior, including atmospheric oxidation

or ionization characteristics or surface reaction with the satellite, should be eliminated. Thus we expected that a measurement of ^{10}Be would be a useful check on models of atmospheric diffusion at these altitudes.

EXPERIMENTAL APPROACH

Accelerator Mass Spectrometry (AMS)

^{10}Be concentrations were measured using carrier dilution and the dedicated AMS beam-line at the Tandem Van de Graaf accelerator in the physics department at the University of Pennsylvania. The accelerator (an HVEC FN) has been upgraded with a Pelletron charging system and Dowlish acceleration tubes. Details of the method are described elsewhere [3], but a brief description is given here. ^{10}Be is measured in a combination ΔE-E (gas-silicon surface barrier) telescope and boron-ion chamber. The ΔE-E telescope allows positive identification of each ion as it enters the detector, and the boron ion chamber provides a means of tuning the beam transport system on ^{10}B, which has exactly the same transport characteristics as ^{10}Be. The ^{10}Be is stopped before entering the ΔE-E telescope by a series of absorber foils located between the ion chamber and the ΔE-E telescope. The absorber foils completely eliminate the ^{10}Be while allowing all the ^{10}Be through.

Samples are prepared by adding 1 to 2 mg of ^{9}Be carrier (known to be free of ^{10}Be) to the sample during dissolution. Most materials contain less than a few ppm of Be so the Be in solution is dominated by the added carrier. Concentrations of ^{10}Be in the original material are determined from the measured $^{10}Be/^{9}Be$ ratios (determined by AMS), multiplied by the amount of carrier added, and divided by weight of the sample dissolved. The principal advantage of the carrier addition method is that after the addition of carrier, results are independent of chemical yields and losses during sample processing.

Typical background levels for ^{10}Be in measurements at Penn are $\sim 3 \times 10^{-15}$ (ratio of $^{10}Be/^{9}Be$). Currents of $^{9}BeO^-$ are typically 10 to 20μA, and transmissions through the accelerator are ~18%. Overall detection efficiency (including formation of BeO^-) is about 0.1%, and precisions range from ~3% to 7%. A typical measurement takes about 40 minutes. For the LDEF samples, the detected $^{10}Be/^{9}Be$ ratio ranged from 1×10^{-11} to 1.5×10^{-10} and a minimum of 700 atoms of ^{10}Be were detected in each sample. The blank, taken through the wet-chemistry procedures, contributed less than 5% to the ^{10}Be measured in the LDEF samples.

Preparation of the Samples (Rutgers University)

AMS samples are normally in the form of a few milligrams of metal oxide which is placed into the Cu cathode of the AMS ionization source. They are obtained by dissolving rock or mineral samples in suitable acids, extracting the Be, and precipitating the hydroxide. In this case, it was necessary to remove a thin layer of the surface of the LDEF material sample by chemical means. The samples available to us were anodized aluminum tray clamps. Since about 10^7 atoms of ^{10}Be are required per sample by the AMS technique, and since the cross-section for ^{10}Be production from O or N is similar (somewhat less) than that for ^{7}Be, we calculated we would need ca. 100 cm^2 of surface area per sample. This is based on the measured density of ^{7}Be. Since $t_{1/2}$ for ^{10}Be decay is 1.5 million years, corrections for decay since LDEF retrieval are unnecessary.

Each tray clamp was made of anodized aluminum alloy, of dimensions 2 in x 5 in x 0.125 in, providing about 60 cm^2 of surface area on the exposed side. Clamps used were from LDEF locations F-9, A-10, B-2 and F-4 (9 and 10 being leading edge rows and the others close to the trailing edge). All surfaces of each clamp which were not to be etched were coated with Petropoxy 154 epoxy cement and cured for a few minutes at 150°C. The first plate (B2) was etched with a few mL of 3:1 v/v solution of 9M HCl and 20% HNO_3 (high purity). Pre-existing scratches were attacked vigorously but most of the surface did not appear to react. We were concerned that a thin layer of Si O_2 a few nm thick, formed in orbit, may have been protecting the Al surface from attack. This Si 0_2 layer may also contain some of the ^{10}Be of interest. We abraded the surface with 5μm $Al_2 O_3$ powder and later with stainless steel wool. ^7Be carrier solution containing 1.484 mg Be mL^{-1} was added. The other plates were treated with steel wool and a mixture of acids including HF. Two successive etchings were performed on each of the last three plates and these samples, each of volume 40 to 80 mL, were then processed and analyzed separately. The steps in this processing were:

1. Evaporation of solution to dryness; redissolution in 9M HCl and filtering of solid residue.
2. Removal of Fe and Co using Dowex 1-X8 ion exchange column.
3. Removal of Al in a large ion-exchange column (Dowex 50W - X8). Elution of Be with 300 mL 1N HCl.
4. Precipitation of $Be(OH)_2$, and some residual Al $(OH)_3$, using ammonium chloride solution; washing of the precipitate.
5. Redissolution and passage through cation exchange column.
6. Redissolution and precipitation of $Be(OH)_2$ with NH_4OH.
7. Calcining of $Be(OH)_2$ in quartz crucibles at 850°C.
8. Loading of Be oxide into copper cathodes.

RESULTS

The results of these assays are shown in Table 1. In terms of areal density it may be seen that the absolute numbers cm^{-2} for ^{10}Be are of the order of 10^6, a reasonable value in light of the ^7Be number densities. However, there is clearly no ram/wake effect and a second etch of both ram (A-10) and wake (F4) plates produced similar values. These results are inconsistent with our hypothesis of atmospheric origin.

TABLE 1

Clamp	Plate No.	No. Be-10 atoms/cm^2
F9-7	(1st etch)	0.53 x 10^6
A10-1	(1st etch)	0.96 x 10^6
	(2nd etch)	0.91 x 10^6
B2-3	(1st etch)	7.1 x 10^6
F4-2	(1st etch)	1.2 x 10^6
	(2nd etch)	2.2 x 10^6

Table 1. Measured ^{10}Be densities on LDEF clamp plates. Data are presented as area density of ^{10}Be atoms cm^{-2} of exposed side of clamp plate. Note that plate B2-3 was etched more deeply than the others. Etch depth was not controlled and could not be accurately measured.

DISCUSSION

We have considered the following explanations for the result:

Laboratory contamination with ^{10}Be

These assays were performed in laboratories familiar with the risk of ambient contamination (the isotope is normally present in surface soil in concentration of ~ 10^8 atoms g^{-1}). Controls are used in various ways to catch the presence of such contamination. It was not considered a plausible cause for the result.

Production in orbit by spallation of Al with energetic protons

$$^{10}Be_{\ g^{-1}Al} = \int_{100MeV}^{600MeV} \phi(E) \bullet t \bullet \frac{N_A}{A} \bullet \sigma(E) \bullet dE$$

for t(flight) « $t_{1/2}$ (^{10}Be)

where: Φ (E) t is the mission proton fluence given by Watts[4], N_A is Avogadro's no., A=27, and σ (E) is the energy dependent cross-section for the reaction:

$$p + {}^{27}Al \rightarrow {}^{10}Be + \ldots.$$

This approximate calculation gave the LDEF mission production as:

n(mission) ^{10}Be ~ 1.3 x 10^5 atoms/g Al

The mechanism is clearly incapable of explaining our measurements.

^{10}Be is naturally present in industrial aluminum

It is clear that all the results are explained if this is the case. This was not known to us, and is quite unexpected. The results in Table 1 may be converted to ^{10}Be atoms g^{-1} Al, if we know the amount of Al removed in each etch. Etching could not be controlled nor measured very precisely. If we assume a mean etch of 100-200μm (about 1g Al) we obtain a mean value of 5-10 x 10^7 atoms ^{10}Be g^{-1} Al with a dispersion of at least a factor of 2 in this value.

Note added after the San Diego Conference

In the weeks following the conference, we have had the opportunity to test whether ^{10}Be might have existed in the clamps flown on LDEF prior to their exposure in space. For this purpose, we measured four samples: 1) the back surface of a clamp (9-7) whose front surface we had measured previously; 2) a clamp from the same lot as those used on LDEF, but which was not flown on the satellite; 3) a piece of ordinary Al foil; and 4) an aliquot of an Al standard solution used in normalizing atomic-absorption measurements. Table 2 summarizes the results of these measurements.

TABLE 2

Sample	weight (mg of Al)	$^{10}Be/^{9}Be$ (atom/atom)	^{10}Be (atoms/g Al)	uncertainty
LDEF 9-7 back	219.7	0.102×10^{-12}	6.4×10^{7}	5%
LDEF not flown	256.7	0.122×10^{-12}	7.5×10^{7}	5%
AL foil	327.3	0.102×10^{-12}	4.1×10^{7}	6%
Al (AA soln)	140	0.063×10^{-12}	6.1×10^{7}	6%

All of these samples contain appreciable concentrations of ^{10}Be. The average value for the ^{10}Be contained in these samples of Al is ~6×10^{7} atoms/g. This confirms that clamps flown on LDEF contained appreciable concentrations of ^{10}Be before flight. Unfortunately, it is not possible to subtract the contribution of this contamination from the values we have measured for LDEF clamps for two reasons: 1) we are not sure how variable the concentration of ^{10}Be is in these clamps (there is a 16% difference between the concentrations in the clamp that did not fly and in the back of LDEF 9-7); and 2) when we made the initial measurements, we did not weigh the amount of material etched, as we were initially interested in the surface density of ^{10}Be, not in its bulk concentration.

In retrospect, we should not be too surprised that Al contains ^{10}Be. Most Al is derived from bauxite, a thoroughly weathered product of many different rock types. It is often found in association with clay, and normally quite near the surface where it may be contaminated with ^{10}Be from rainwater. We can estimate an upper limit for the expected concentration of ^{10}Be in bauxite in the following manner: For a precipitation rate of 100 cm of rain/year, with an average concentration of 20,000 atoms of ^{10}Be/g or rain[7]), the saturation areal density of ^{10}Be in the soil (assuming no horizontal transport) is ~4×10^{12} atoms/cm^2. If the entire ^{10}Be inventory is contained within the bauxite deposit, a bauxite layer 20m thick, with an Al concentration of 30%, would have a ^{10}Be concentration/g of Al-metal of ~3×10^{9} atoms/g. The ^{10}Be concentrations that we actually measure in Al metal are only a few percent of this value. Consequently, we anticipate the ^{10}Be concentrations in various bauxites, and in Al derived from them, will vary appreciably.

We are currently planning to measure ^{10}Be on stainless steel and copper surfaces flown on LDEF.

REFERENCES

1. Fishman, G.J.; Harmon, B.A.; Gregory, J.C.; Parnell, T.A.; Peters, P.N.; Phillips, G.W.; King, S.E.; August, R.A.; Ritter, J.C.; Cutchin, J.H.; Haskins, P.S.; McKisson, J.E.; Ely, D.W.; Weisenberger, A.G.; Piercey, R.B.; and Dybler, T.: Observation of Be-7 on the Surface of LDEF Spacecraft. *Nature*, Vol.349, 1991, pp. 678-680.

2. Gregory, J.C.; Fishman, G.J.; Harmon, B.A.; Parnell, T.A.: The Interaction of Atmospheric Cosmogenic Radionuclides with Spacecraft Surfaces, The LDEF First Post-retrieval Symposium, Orlando, FL; NASA CP-3134, 1991.

3. G.W. Petty, Geophysical Research Letters 18 (a), 1687, (1991).

4) John W. Watts, T.W. Armstrong and B.L. Colborn, "Revised Prediction of LDEF Exposure To Trapped Protons", The LDEF Second Post-retrieval Symposium, San Diego, CA, 1992. NASA CP-3194, 1993.

5) Klein, J., Middleton, R. & Tang, H.-Q. *Nucl. Inst. Meth.* **193**, 601-616 (1982).

6) Middleton, R. & Klein, J. *Workshop on Techniques in Accelerator Mass Spectrometry* eds. Hedges, R.E.M., Hall, T., 76-81 (Oxford, England, 1987).

7) Brown, L., Stensland, G.J., Klein, J. & Middleton, R. *Geochimica et Cosmochimica Acta* **53**, 135-142 (1988).

HEAVY ION MEASUREMENT ON LDEF

D. Jonathal, R. Beaujean and W. Enge
Institut für Reine und Angewandte Kernphysik
Christian-Albrechts-Universität zu Kiel, D-2300 Kiel, FRG
Phone: (0)431/880-2544, Fax: (0)431/880-1647

SUMMARY

Heavy ions with nuclear charge Z=6 to Z=26 are detected in a stack of plastic track detectors. The measured energies in the range 10-240 MeV/nuc are well below the geomagnetic cutoff value of the LDEF orbit. The arrival directions of the low energy particles (Z=6-26, E<40 MeV/nuc) are consistent with a trapped component incident in the South Atlantic Anomaly.

INTRODUCTION

The Kiel experiment M0002 on tray E6 was designed to measure the charge and the arrival direction of heavy ions in the energy range 10-1000 MeV/nuc with nuclear charge equal to or greater than 3. To complement the arrival direction measurement, two additional stacks were integrated in subunits of the Biostack A0015 (DLR Cologne) on trays C2 and G2.

CR-39 and Kodak CN foils are used as visual track detectors with an excellent spatial resolution. These detectors remained sensitive throughout the whole LDEF mission. The scientific data are stored in latent tracks and are revealed in the laboratory after recovery. For a description of the detector arrangement see Beaujean et al. (1991a).

The extended LDEF mission time of $1.8 \cdot 10^8$ sec increased the number of collected particles without deterioration of the detector system. The objectives of the experiment are achieved and this progress report contains our present results on trapped radiation and geomagnetically forbidden particles.

CALIBRATION OF THE DETECTOR

The specific response of a plastic track detector is given by the variation of the track etching rate with respect to the energy loss of the heavy ion. For a postflight calibration the CR-39 detector of M0002 was exposed to 200 MeV/nuc Ar^{40} ions with a 90^0 angle of incidence at the Saclay accelerator. Etching of the CR-39 was done in 6n NaOH at 70^0 C for 10 hours. At this etching time the heavy ion tracks can be clearly separated from the small etch pits which were probably produced by secondaries from proton interactions.

The measured surface area of the Ar^{40} etch cones indicates a variation of the bulk etching rate. This variation is mainly due to the nonuniform CR-39 material. The influence of track aging and fading during the mission is included in the internal flight calibration using the cosmic rays particles themselves. Fig. 1 shows the result of 113 stopping heavy ions. Individual cones along a specific track are marked by the same identification number. 48 of these ions penetrated LDEF and stopped in the detector unit coming from backward direction.

Similar to our Spacelab-1 (Sl-1) measurement (Krause, 1986b), the data show a densely populated band with a sharp intensity drop to more ionizing particles. This edge can be allocated to Fe particles based on the knowledge of the cosmic ray elemental abundances.

The calculated track etching rate deduced from this inflight calibration shows a slightly reduced sensitivity compared to the CR-39 in Sl-1. The overall low sensitivity of the CR-39 detector flown in Sl-1 and LDEF is due the low oxygen concentration within the stack containers during space flight. According to Fig. 1 the registration probability for ions with $Z < 20$ is strongly decreased with decreasing nuclear charge Z.

The calibration of the Kodak CN, integrated in the A0015 subunits, is in progress. The preliminary analysis indicates a higher sensitivity compared to the CR-39 and we expect a high registration probability of nuclear charges $Z \geq 6$ in these foils.

EXPERIMENTAL RESULTS

54 particles from Fig. 1 arrived from unshielded free space and have a nuclear charge $Z \geq 20$. Using a geometric factor of $1.2 \cdot 0.03$ sr·m^2 and a preliminary corrected particle number of 75, the mission averaged flux of the detected particles with $Z \geq 20$ in the energy interval 40-240 MeV/nuc is

$$J(Z \geq 20) = (6 \pm 2) \cdot 10^{-8} / m^2 \cdot sec \cdot sr \cdot MeV/nuc. \qquad (E = 40 - 240 \text{ MeV/nuc})$$

The energy spectrum in this interval is found to be almost constant.

Using the CR-39 calibration, the analysis on the arrival direction measurements of low energy particles (Beaujean et al., 1991b) is extended to a charge identification. From Fig. 1 we conclude that completly etched stopping ends with conelength L > 150 μm are produced by stopping ions with Z ≥ 20.

In the topmost foil of M0002 24 stopping particles are detected on 100 cm^2 with a conelength L = 150 - 350 μm. All 24 particles arrived from unshielded space direction having energies 18 - 25 MeV/nuc. A similar analysis yielded 3 particles with L > 150 μm on 16 cm^2, stopping in the upper CR-39 foil of A0015 on tray C2 and arriving from unshielded earth direction.

The ions with Z ≥ 20 are part of the low energy particle population, which shows a cylindrical geometry in the arrival direction. To calculate the flux, 11 particles out of 24 are used having a conelength 150 - 200 μm (the corresponding energy is 18 - 20 MeV/nuc). Stopping ends with L > 200 μm are not considered, because particles with Z = 20 may be less represented due to the detector response. Assuming a trapped origin of these particles, the collecting time within the SAA is taken as 1% of the mission time. Using a geometric factor of 1.2·0.01 $m^2 \cdot sr$, the flux of the detected particles with Z ≥ 20 in the energy interval 18 - 20 MeV/nuc is

$$J(Z \geq 20) = (2.5 \pm {}^{2}_{1}) \cdot 10^{-4} / m^2 \cdot sec \cdot sr \cdot MeV/nuc. \qquad (E = 18 - 20 \text{ MeV/nuc})$$

The Kodak CN material integrated in A0015 is used to complement the arrival direction measurements including lower charged particles. Fig. 2 shows the result for 205 particles, penetrating the topmost Kodak CN foil on C2. Due to the higher sensitivity of this material we expect that particles with Z ≥ 6 are included in this distribution.

Note that the particles arrive from earth direction (but not from space direction). This distribution again gives a strong evidence for a cylindrical geometry and the arrival directions of all detected low energy particles follow a plane perpendicular to the magnetic field line at the northern edge of the SAA.

DISCUSSION

The detected iron/subiron particles have rigidities well below the geomagnetic cutoff value for the LDEF orbit assuming fully stripped ions. Fig. 3 shows rigidity versus kinetic energy for some ions with different (charge to mass) ratios and a rough transmission function for the LDEF orbit using vertical cutoff rigidities. From this figure we conclude that the detected iron/subiron particles in the energy range 40 to 240 MeV/nuc must have a charge state well below 14 to arrive at the LDEF orbit from outside the magnetosphere. In case the detected particles enter from interplanetary space, the given flux is a lower limit, as the ions are mainly admitted during the high latitude portions of the orbit.

Early measurements of geomagnetically forbidden particles at balloon altitude were reported by Blanford et al. (1972) and Friedlander et al. (1977), who explained them as return-albedo particles. Krause et al. (1986a) reported on 100 MeV/nuc particles below cutoff rigidity detected in the Spacelab-1 orbit (57^0 inclination, 250 km altitude). Adams et al. (1991) detected 600 MeV/nuc iron/subiron particles below cutoff rigidity in the LDEF orbit. Further investigations are in progress to analyse the published data and identify the source of the geomagnetically forbidden particles.

Because LDEF maintained a constant orientation during the mission, trapped heavy ions arrive at characteristic angles, thereby making them distinguishable from other particles. The arrival direction and the rigidity (Fig. 3) of the low energy particles ($E < 40$ MeV/nuc) indicate an origin from a trapped population. Oschlies et al. (1989) and Grigorov et al. (1991) reported on oxygen particles of magnetospheric origin. According to Grigorov et al. (1991) the trapped oxygen flux within the SAA at $2 < L < 3$ showed a strong time dependence with a peak value of about $5 \cdot 10^{-6}$ particles/$m^2 \cdot$sec in the energy range 5 - 30 MeV/nuc.

Our measurement in Kodak CN includes oxygen particles. From the preliminary analysis we deduce as $Z \geq 6$ particles per cm^2 the numbers (52 ± 4) and (34 ± 3) in the energy interval 21 - 25 MeV/nuc and 27 - 32 MeV/nuc respectively (Beaujean et al., 1991b). According to the measurements of Grigorov et al. (1991) on Cosmos satellites these particles are mainly oxygen, collected within one year from 1986 to 1987. In our measurement a definite charge identification is not yet done. Assuming again a detection in the SAA during 1% of the mission, we deduce a flux of

$$J(Z \geq 6) = (0.4 \pm 0.1)/m^2 \cdot sec \cdot MeV/nuc \qquad (E = 21 - 25 \text{ MeV/nuc})$$

as an average during $3 \cdot 10^5$ sec mission time in the SAA region with $1.2 < L < 1.3$. The measured mean flux on the LDEF is about 4% of the corresponding flux of

$$J(Z = 8)_{Cosmos} \approx 10/m^2 \cdot sec \cdot MeV/nuc \qquad (E = 5 - 30 \text{ MeV/nuc})$$

on the Cosmos satellite (averaged over one year during the maximum period).

If we assume a similar time dependence for the oxygen and subiron/iron particle flux in the SAA, the detected integral fluence of particles yields a preliminary relative abundance. Taking 52 particles/cm^2 ($Z \geq 6$, E = 21 - 25 MeV/nuc) and 0.11 particles/cm^2 ($Z \geq 20$, E = 18 - 20 MeV/nuc), the ratio is

$$N(Z \geq 6) \,/\, N(Z \geq 20) = 236 \pm^{140}_{80} \qquad (E \approx 20 \text{ MeV/nuc})$$

This preliminary ratio is about three times the ratio measured by Chan and Price (1975) on Skylab. Final relative abundances will be given after completion of the detector calibration.

This work was financially supported by the "Bundesministerium für Forschung und Technologie" under grant 01 QV 297 and 50 OS 9001.

REFERENCES

Adams, J., Beahm, L. and Tylka, A.: *Preliminary results from the heavy ions in space experiment,* NASA conference publication 3134, part 1, 377, 1991.

Beaujean, R., Jonathal, D. and Enge, W.: *Heavy ion measurement on LDEF,* NASA conference publication 3134, part 1, 393, 1991a.

Beaujean, R., Jonathal, D. and Enge, W.: *Heavy ion measurement on LDEF,* 22nd ICRC, Dublin, Vol. 3, 617, 1991b.

Blanford, G.E., Friedlander, M.W., Klarmann, J., Pomeroy, S.S., Walker, R.M. and Wefel, J.P.: *Observation of low-energy geomagnetically forbidden particles,* Journal of Geophysical Research, Vol. 77, No. 31, 6037, 1972.

Chan, J.H., and Price, P.B.: *Composition and Energy spectra of heavy nuclei of unknown origin detected on Skylab,* Phys. Rev. Lett. Vol. 35, #8, 539, 1975.

Friedlander, M.W., and Hoppe, M.: *Further observations of geomagnetically forbidden cosmic ray nuclei,* Journal of Geophysical Research, Vol. 82, No. 4, 734, 1977.

Grigorov, N.L., Kondratyeva, M.A., Panasyuk, M.I., Tretyakova, Ch.A., Adams, J.H., Blake, J.B., Schulz, M., Mewaldt, R.A. and Tylka, A.J.: *Evidence for trapped anomalous cosmic ray oxygen ions in the inner magnetosphere,* Geophysical Research Letters, Vol. 18, No. 11, 1959, 1991.

Krause, J., Beaujean, R. Enge, W.: *CR-39 used for cosmic ray measurements aboard Spacelab-1,* Nuclear Tracks, Vol. 12, Nos 1-6, 419, 1986a.

Krause, J.: *Magnetisch verbotene Teilchen mittlerer Energie bei der Spacelab-1 Mission,* Ph. D. Thesis, Institut für Reine und Angewandte Kernphysik, Universität Kiel, Germany, 1986b.

Oschlies, K., Beaujean, R. and Enge, W.: *On the charge state of anomalous oxygen,* The Astrophysical Journal, **345,** 776, 1989.

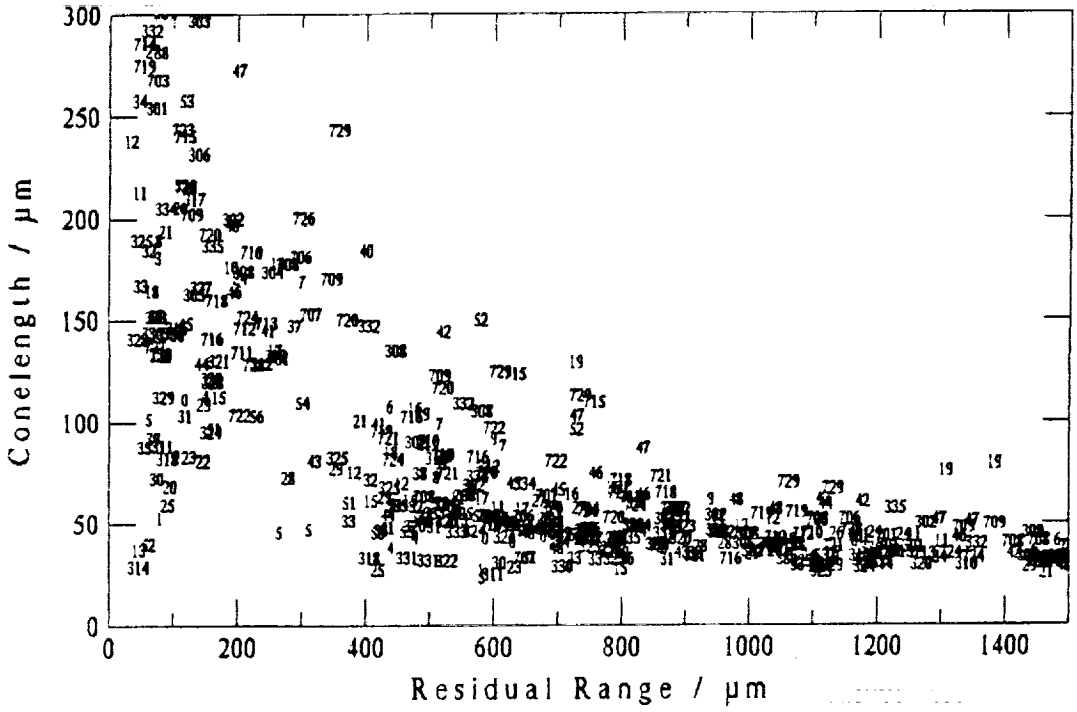

Fig. 1: Conelength-range diagram of 113 tracks in CR-39 of M0002. Cones of the same track are marked with the same number.

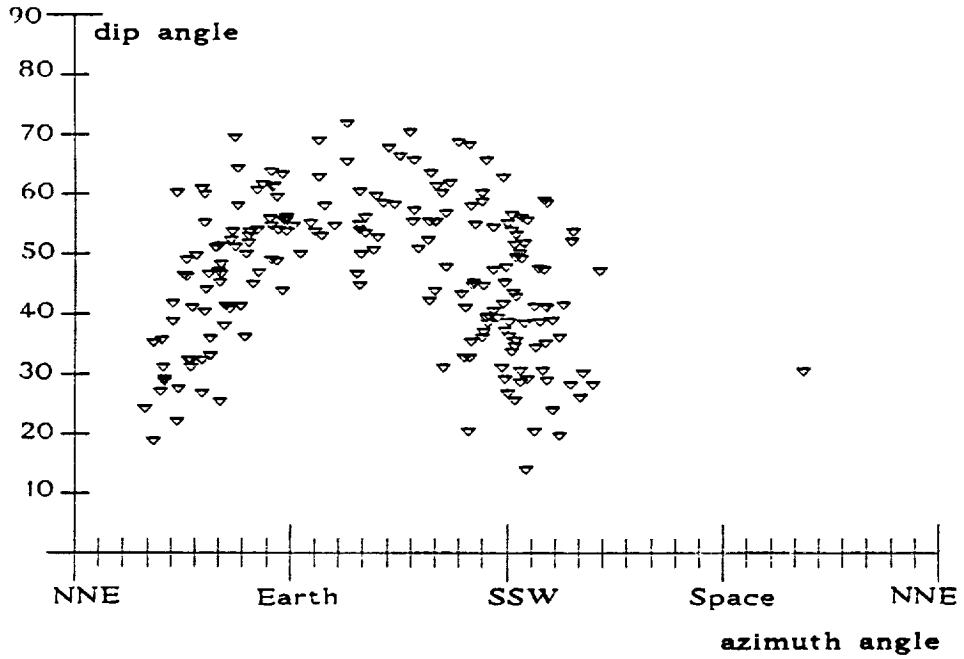

Fig. 2 Arrival directions of 205 particles with $Z \geq 6$ penetrating the topmost Kodak CN foil of A0015 on tray C2.

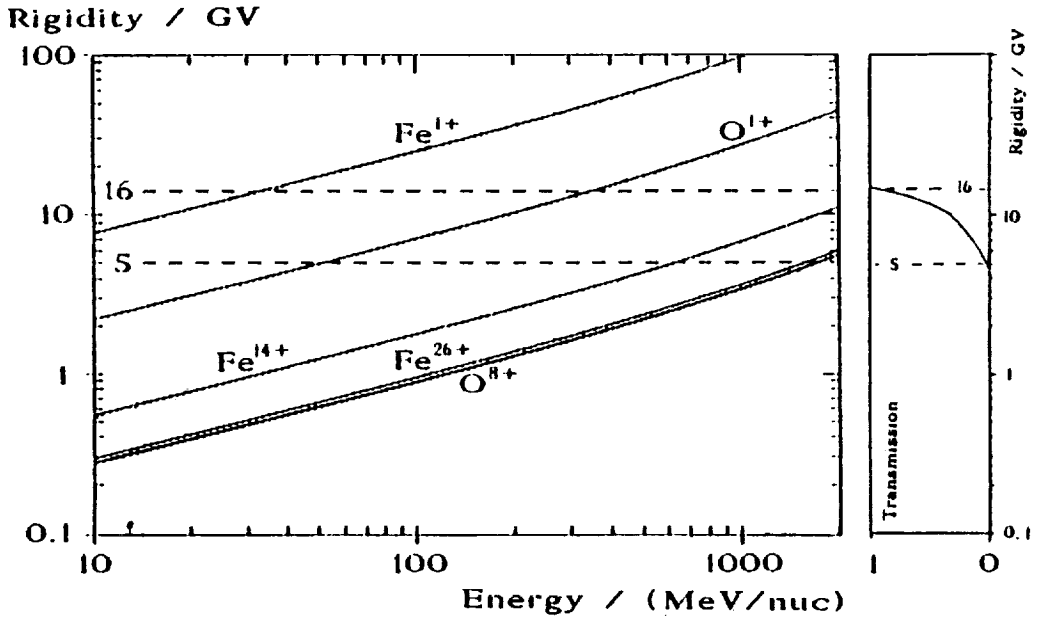

Fig. 3 Rigidity versus kinetic energy for different ions at different charge states. The rough transmission function of LDEF separates the ridigity scale: particles with a rigidity < 5 GV cannot reach LDEF, particles with a rigidity > 16 GV can reach LDEF on the whole orbit.

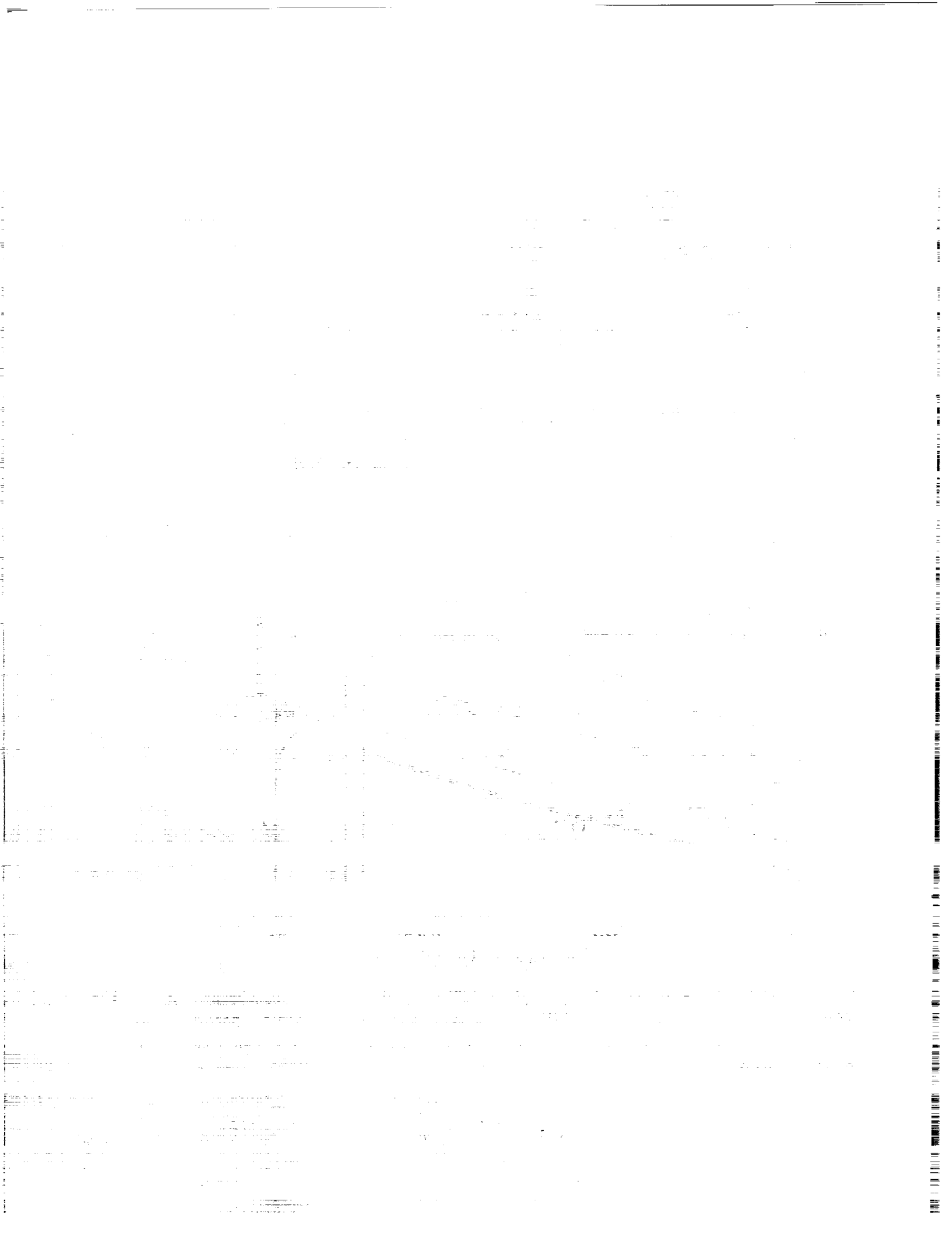

PROGRESS REPORT ON THE HEAVY IONS IN SPACE (HIIS) EXPERIMENT

James H. Adams, Jr., Lorraine P. Beahm, Paul R. Boberg,[1*] and Allan J. Tylka
E. O. Hulburt Center for Space Research
Code 7654, Naval Research Laboratory
Washington, DC 20375-5352
Phone: 202/767-2747, Fax: 202/767-6473

SUMMARY

One of the objectives of the Heavy Ions In Space (HIIS) experiment is to investigate heavy ions which appear at LDEF below the geomagnetic cutoff for fully-ionized galactic cosmic rays. Possible sources of such "below-cutoff" particles are partially-ionized solar energetic particles, the anomalous component of cosmic rays, and magnetospherically-trapped particles. In recent years, there have also been reports of below-cutoff ions which do not appear to be from any known source[1-5]. Although most of these observations are based on only a handful of ions, they have led to speculation about "partially-ionized galactic cosmic rays" and "near-by cosmic ray sources"[4-6]. The collecting power of HIIS is orders of magnitude larger than that of the instruments which reported these results, so HIIS should be able to confirm these observations and perhaps discover the source of these particles. We report here preliminary results on below-cutoff heavy-ions. We compare our observations to possible known sources of such ions.

A second objective of the HIIS experiment is to measure the elemental composition of ultraheavy galactic cosmic rays, beginning in the tin-barium region of the periodic table. We also briefly report on the status of this analysis.

THE HIIS DETECTOR SYSTEM

The HIIS detectors were contained in two trays (H3 and H12) on the space-facing end of LDEF. Each tray contained four modules. Fig. 1 shows one of the HIIS trays and a cut-away of one of the modules. Each module comprised two separate stacks of plastic track detectors, a main stack which was sealed in one atmosphere of dry air and a top stack which was in vacuum. The main stack was constructed primarily of 10-mil thick sheets of CR-39[7], which were cast by Pershore Mouldings Ltd. (Pershore, UK) according to a special process for producing highly-uniform, detector-quality material which we developed[8]. The CR-39 sheets were cast from resin containing 1% dioctylphthalate[9]. The main stack also contained a few 5- and 10-mil thick sheets of Lexan[10]. The Lexan we used was manufactured especially for us without UV stabilizer, so as to make it possible to enhance the latent tracks with ultraviolet light[11]. The top stack consisted of 25 5-mil Lexan sheets. The total vertical thickness of the detector module was ~12 g/cm^2. The total number of detector sheets is 2782, each of which has an area of 1064 cm^2. Total collecting power of the eight detector modules is $A\Omega = 2.0$ m^2-sr. HIIS is one of the largest cosmic ray detectors ever flown in space, second only to the Ultra Heavy Cosmic Ray Experiment (UHCRE)[12], which also flew on LDEF.

Seven of our eight modules were constructed as described above. The eighth module was of a special design so as to extend the detector's range to lower energies. In this module both stacks were sealed in an atmosphere of dry air and the honeycomb lid shown Fig. 1 was replaced with four thin Kapton[13] windows.

[1*] NRC Postdoctoral Research Associate

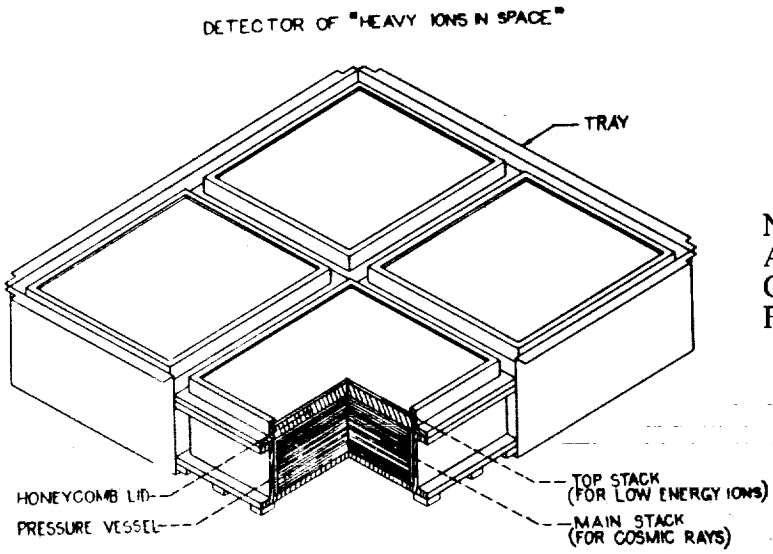

TABLE 1 Stopping Ion Energies (MeV/n)

	Top Stack	Main Stack
Ne	18 - 57	72 - 334
Ar	23 - 89	87 - 767
Ca	26 - 100	106 - 887
Fe	27 - 111	117 -1022

Figure 1: One of the two LDEF trays containing the HIIS experiment. Each tray contained four modules, one of which is shown in a cut-away here. Table 1 at the right shows the energy range for various stopping ions in the top and main detector stacks.

METHOD OF DETECTION

Plastic track detectors record charged particles by the trails of radiation damage they leave as they pass through the detector sheets. These tracks, which are revealed by chemically etching the detectors, are a permanent record of the particle's path and its rate of ionization in the plastic. The response of a plastic track detector is characterized by V_T/V_B, where V_T is the rate at which plastic is etched away along the damage trail and V_B is the rate at which bulk undamaged plastic is dissolved by the etchant. Because of radiation damage to the polymer, $V_T/V_B > 1$. The competition between V_T and V_B leads to the formation of a conically shaped etch pit whenever

$$(V_T/V_B)\cos(\theta) > 1 \qquad (1)$$

where θ is the angle between the trajectory of the charged particle and the normal to the detector sheet[14]. V_T/V_B is empirically found to be an increasing function of the restricted energy loss[15] (REL), which provides a numerical measure of the radiation damage generally dependent upon atomic number Z, mass number A, and the particle velocity β. Etch pits are measured under a high precision microscope. From the displacement of etch pits on the bottom and top surfaces of a detector sheet, the incidence angle θ can be measured. V_T/V_B can be determined by measuring the dimensions of the etch pit[16,17].

Stopping ions are identified by following them to where they came to rest in the detector and by measuring V_T/V_B in each detector surface along the particle's trajectory. When these V_T/V_B values are plotted versus the distance to the end of the track (the so-called "residual range"), they fall upon characteristic curves determined by Z and (weakly) by A. Once the particle's identity is known, its total range in the detector specifies its incident energy.

For relativistic particles, REL (and hence V_T/V_B) is nearly constant as the particle traverses the detector. V_T/V_B can be precisely determined by averaging measurements from many detector surfaces. V_T/V_B depends primarily upon the atomic number Z and only very weakly upon the particle velocity β, so the average V_T/V_B value identifies Z even without a measurement of β.

POST-FLIGHT ASSESSMENT OF THE DETECTOR PERFORMANCE

In the Proceedings of the First LDEF Post-Retrieval Symposium, we published a detailed report on the post-flight condition of the detectors[18]. In this section we briefly summarize those results. The reader is referred to those Proceedings for more detailed information.

Temperature Effects. The single most important factor affecting the performance of track detectors is temperature. In particular, good elemental resolution requires that the temperature of the detector stack be maintained within narrow limits. In HIIS this was accomplished by a carefully-designed passive thermal control system. A detailed post-flight thermal analysis indicated that this system would hold the temperature of the main detector stacks in the range of -7.5 $\pm$ 2.0 °C, a somewhat better performance than predicted in pre-flight analysis.

At some point in the mission, part of the HIIS thermal control system failed: the thermal blankets protecting the HIIS modules partially detached and rolled up, exposing parts of the top detector stacks to solar UV. The pattern of UV and atomic oxygen damage on the surfaces of the blankets suggests that the failure occurred in the last few months of the mission, during which LDEF was at lower altitudes and vulnerable to atomic oxygen damage. The degree of blanket failure varied from module to module. Post-flight examination of the blankets revealed that the failures were due to shrinkage of the top face sheets, perhaps because of the loss of some reactive or volatile component, causing them to tear loose from the modules. Post-flight thermal analysis indicates that without the blankets, the main stacks were colder (average temperature -13.0 °C) and underwent a larger range of temperature (rms width 2.3 °C).

Even with the partial failure of the thermal blankets, it appears that temperature variation had negligible effect on HIIS elemental resolution, at least in the main detector stacks. Although the post-flight examination of the blankets suggests that they failed near the end of the mission, we do not know this for certain. We therefore took a conservative approach in simulating temperature effects on the detectors: we assumed the "worst case" scenario, in which the blankets failed half-way through the mission, thereby producing the widest possible range of temperature variation. We folded this thermal history with results from accelerator studies of temperature effects for particles with comparable V_T/V_B values. Even in this worst case, we find that temperature effects are small: for stopping Fe tracks, the charge peak is broadened by less than 0.05 charge unit. The width of the relativistic Z=60 charge peak increases by less than 0.1 charge unit. For more heavily-ionizing particles, temperature smearing is more severe. In all cases, temperature effects appear to have a minor effect on the elemental resolution.

Post-Flight Condition of the Detectors. The HIIS main detector stacks were originally sealed in 1 atm of dry air. The special module with the Kapton windows leaked because the windows were punctured by micrometeoroids after the thermal blanket rolled up. We analyzed the air in the remaining modules and compared it with air from the bottle used to fill the modules before flight. This air contained 10% helium as a tracer. The same helium concentration was found in the post-flight modules, proving that they did not leak. The analysis of the gas in the modules did, however, reveal a change in composition. The concentration of O_2 varied from module to module, with values in the range of 12-20% of the pre-flight concentration. Most of the O_2 had been replaced by CO_2, but some was no longer in gaseous form. Since the detector sheets almost completely filled the module volume, residual oxidation and polymerization of the CR-39 after the modules were sealed can easily account for the missing oxygen. CR-39 is known to oxidize in room air. Also, oxygen is consumed during the polymerization process. The HIIS CR-39 was manufactured over a six month period, and some sheets were freshly polymerized when the modules were sealed. This could account for the variation among modules in the residual O_2 concentration. If residual polymerization is the explanation of the missing O_2, the oxygen concentrations probably leveled out to near their final value prior to launch.

After analyzing the gas in the detector modules, the main detector stacks were disassembled. The detector sheets in the main stacks were not damaged, discolored, or stuck together. To date we have etched 50 sheets from the main stacks in two detector modules: module C, in which the residual O_2 concentration was lowest; and module E, in which the residual O_2 concentration was highest. (Oxygen plays a role in fixing the radiation damage in CR-39[19].) These two modules also showed different degrees

of thermal blanket failure. In Module C, the thermal blanket was nearly intact, with only a tear in the few topmost layers. Module E had one of the most severely damaged blankets. By choosing these two modules, we believe that our initial examination brackets the range of sensitivities in the HIIS detectors.

In all of the etched sheets, we found both relativistic and stopping cosmic ray tracks. These tracks were easily found by either manual or automated scanning. None of the sheets was overexposed, and surface features did not interfere with measurements of the cosmic ray tracks. On the basis of our measurement and analysis of these tracks, we conclude that the main detector stacks, at least in the seven modules which did not leak, contain valuable cosmic ray data.

With regard to the top detector stacks, six of the seven were partially exposed to the sun. The seventh stack remained protected by a thermal blanket. It appears to be in excellent condition and should be useable for measuring fluxes of low energy particles (see Fig. 1). It is also possible that the protected portions of the other top stacks may be useable as well, since they show no sign of UV exposure.

CALIBRATION OF THE HIIS DETECTORS

We conducted extensive pre-flight Bevalac calibrations of the HIIS detectors. Our present plan, however, is to internally calibrate the detectors, using the cosmic rays themselves. The detector sheets we have etched so far contained tracks, but not in the numbers we expected. Relativistic Fe, for example, appears not to have been recorded[2*] . The density of shallow surface pits (due to trapped protons) was also much less than expected. Such apparent reduction in CR-39's sensitivity has been observed before[20]; it is consistent with the reduced oxygen concentration in the modules[19].[3*]

Because the observed detector response is so different from that in accelerator exposures, we believe that "boot-strapping" from the observed cosmic ray tracks is the most reliable calibration method. This method also ensures that the environmental effects on the HIIS detectors, whatever they may have been, will be reflected in the detector calibration. Also, since the residual oxygen concentration varied from module to module, a separate calibration must be derived for each module.

Because we did not wish to risk losing valuable cosmic ray data to overetching, we began our analysis by etching sheets near the bottoms of Modules C & E, at a vertical depth of ~11 g/cm^2 in the detector. In each module, we found a sample of ~40 long stopping tracks with precisely measured stopping ends. We have used these tracks to calibrate the modules: our thermal modeling indicates that the temperature in the main detector stacks should have been uniform to within 0.3°C, so the calibration should be the same throughout.

To illustrate this internal calibration method, Fig. 2 shows the raw data from stopping tracks in CR-39 near the bottom of Module E. The data organize themselves into densely populated bands, with no tracks above the topmost band. This indicates a sudden drop in the elemental abundance of the ions. According

---

[2*] This absence of relativistic Fe tracks confirms that the HIIS detectors did not go into space with their full sensitivity. On the basis of pre-flight calibrations in 1 atm of air, we expected the HIIS detectors to record 2500/cm^2 relativistic Fe tracks. A detailed manual scan of ~100 cm^2 found no relativistic Fe tracks. We know of no mechanism for the fading of such tracks, since CR-39 detectors on other LDEF experiments and detectors stored on the ground in comparable temperature conditions show no such effect over six years. The absence of recorded relativistic Fe tracks thus indicates that the HIIS detectors could not have been in space at the their normal sensitivity for more than an hour!

[3*] Portions of some detector sheets had been exposed to a stopping Fe beam at the Bevalac before they were sealed in the HIIS modules for flight. After retrieval, we removed these sheets from the modules and exposed them again to the same beam, in 1 atm of air. V_T/V_B measurements in the two sets of tracks are identical to within measurement errors, further confirming that the suppressed detector sensitivity was due to the reduced oxygen concentration in the modules. The comparison between the two sets of tracks also indicates that no significant amount of thermal annealing occurred during the flight.

to the general abundance of elements, there are only two places in the periodic table where such a drop occurs, above Fe and above Pb. Pb ions are far too rare to explain the observed fluxes, so we identified the tracks in the topmost band as Fe. The most-lightly ionizing track in the dataset was identified as S by demanding that its calculated ionization rate at small residual range be consistent with that of the Fe tracks at large residual range. The Fe and S tracks were used to fit the detector response function shown in Fig. 3. (The calibration of Module C was similar. See Ref. 21.)

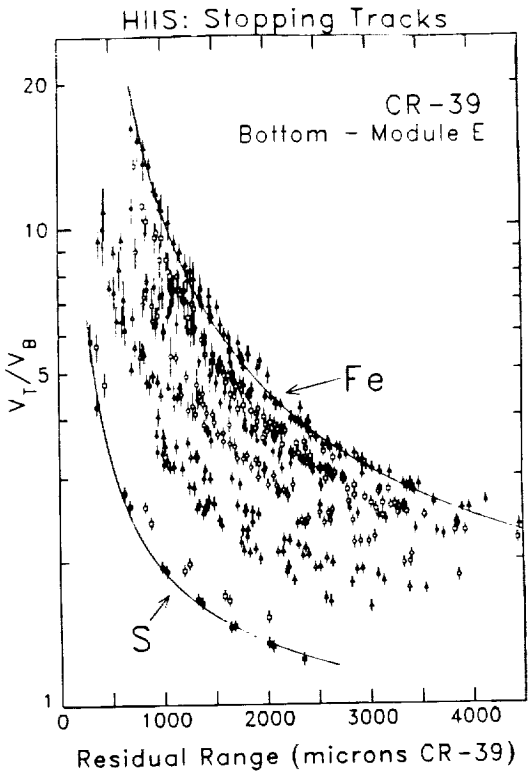

Figure 2: Raw data on stopping tracks found in 10 detector sheets near the bottom of the main stack in Module E. The figure shows data from ~40 cosmic ray tracks, each of which is measured in ~11 detector surfaces on average. The ordinates are the track detector response V_T/V_B and the abscissae are the distance from the stopping end of the track.

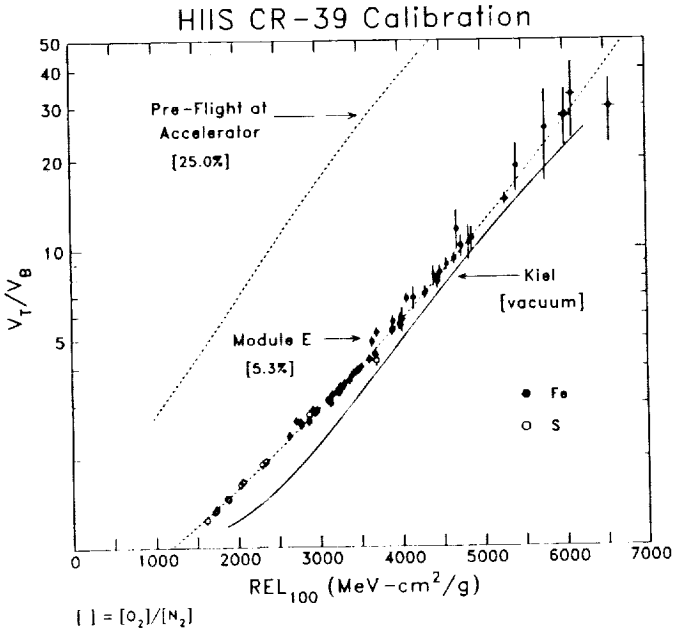

Figure 3: Derived detector response function, as discussed in text. For comparison, also shown are the pre-flight accelerator calibration in air and the Kiel calibration for CR-39 in vacuum[31]. The number in brackets is the measured O_2/N_2 ratio in the detector module's gas volume.

STATUS OF THE STOPPING HEAVY ION ANALYSIS

To date we have used automated scanning to locate 329 stopping tracks in the sheets etched so far, with 70% of the tracks coming from 30 sheets near the top of Module E, under 1.6 g/cm^2 of the detector. Each stopping track was then followed and measured through at least 19 detector surfaces or as many as allowed by the etching condition in equation (1) and/or the restricted number of etched sheets. For each track, the set of V_T/V_B vs. residual range measurements was fitted to the response function of Fig. 3, using a Marquardt minimization of χ^2, allowing two free parameters: the atomic number "Z" (which was allowed to take on non-integer values) and "d", the ion's penetration into the stopping sheet (which was typically measured to within an uncertainty of ~ 10 microns)[4*] . Fig. 4 shows a sample of tracks from the

[4*] The mass number A was assigned from a piecewise continuous function of Z, which interpolated between the average A value at each integer Z.

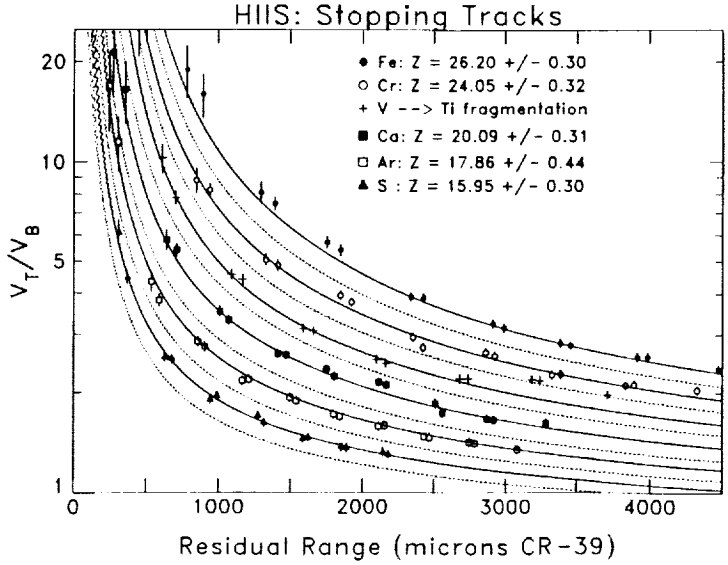

Figure 4: A sample of 6 stopping tracks, each represented with a different symbol. For clarity, only even Z-tracks are shown. The fitted atomic numbers with errors are also shown. Calibration curves, derived from the response function in Fig. 3 are shown for elements 15-26 (solid line: even-Z; dashed line: odd-Z). Note the fragmentation V to Ti.

main stack in Module E, along with the fitted Z values and the formal error calculated by the minimized-χ^2 analysis. In Fig. 5, we show the charge histogram for the 246 successfully-fitted stopping tracks[5*]. To maximize statistics, the figure includes all of the collected stopping tracks, including those which passed through large amounts of shielding by entering through the side or bottom of the detector.

To indicate the quality of the track fits, Fig. 6 shows histograms of the reduced χ^2 and of the errors in the fitted Z value, (as calculated by the minimized-χ^2 analysis) for the successfully fitted tracks. Our track fits give acceptable values of reduced χ^2, and the typical fitted error on Z is ~0.3 charge unit.

Fig. 5 appears to show elemental resolution, with clear peaks centered at integer Z values. We have fitted the charge distribution to a sum of gaussians, leaving the amplitudes, standard deviations, and means as free parameters. This fit, which gives reduced $\chi^2 = 0.6$ for 15 degrees of freedom, is shown in Table 2. Excluding the weak "peaks" at $Z > 26$, $Z < 18$, $Z = 19$, and $Z = 21$, all of the gaussians are centered near integer Z; they have an average $\sigma = 0.30$ charge units. This is good charge resolution for a large space-based plastic-track-detector experiment, comparable to the best results previously achieved[24]. As one would expect, this resolution is consistent with the errors on the individual track fits (Fig. 6b). As shown in Table 2, this resolution is also consistent with Monte Carlo simulations of the detector, which took into account all known factors, including measurement errors, observable track length, the observed non-uniformity in the plastic bulk etch rate, and smearing due to multiple isotopes.

The charge histogram has, however, one surprising feature: the strongest accumulation is at Mn, not Fe. Such a composition is inconsistent with all known sources of cosmic rays, in which the ratio Mn/Fe ~ 0.1 or smaller. This makes it very difficult to believe that the composition shown in Fig. 5 is correct.

[5*] Forty tracks (12% of the total) had too few precise V_T/V_B measurements (because of the restricted number of etched sheets) to be reliably fit; 18 tracks (5%) were identifed as fragmenting in the measured sheets; 25 tracks (8%) failed to give a good χ^2 for unidentifed reasons.

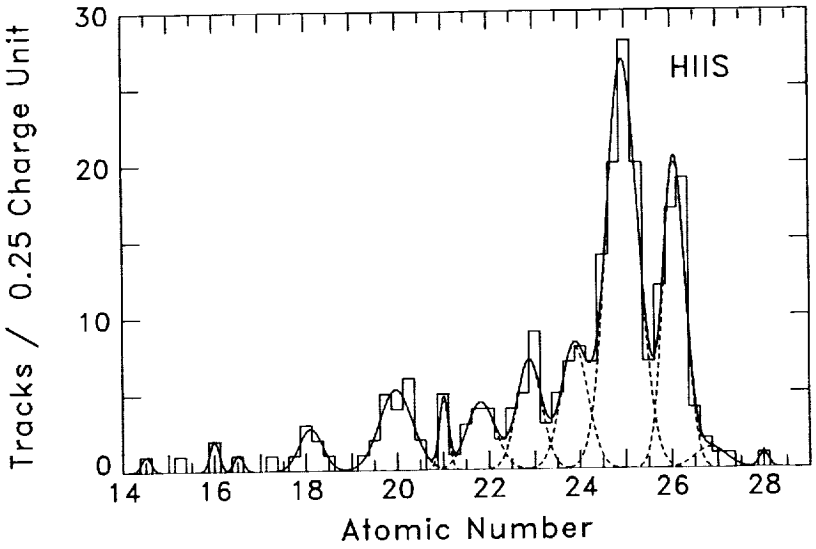

Figure 5: Histogram of fitted atomic numbers of the stopping ions. The histogram was fitted to a sum of gaussians, with results as given in Table 2 below.

TABLE 2 Fit to Sum of Gaussian: Fit Parameters & Their Errors

	No. Tracks	Mean	Sigma	MC Sigma*
S	2.0 ± 1.4	16.00 ± 0.12	0.10 ± 0.11	--
Ar	7.1 ± 3.6	18.10 ± 0.11	0.26 ± 0.12	0.27 ± 0.01
Ca	19.1 ± 5.4	19.97 ± 0.10	0.36 ± 0.07	0.29 ± 0.01
Sc	4.6 ± 2.4	21.02 ± 0.08	0.10 ± 0.05	0.20 ± 0.01
Ti	13.9 ± 5.1	21.83 ± 0.15	0.31 ± 0.15	0.30 ± 0.01
V	19.3 ± 6.5	22.88 ± 0.11	0.27 ± 0.13	0.28 ± 0.01
Cr	23.9 ± 6.7	23.87 ± 0.15	0.30 ± 0.15	0.31 ± 0.01
Mn	91.8 ± 13.9	24.95 ± 0.06	0.34 ± 0.07	0.35 ± 0.02
Fe	48.7 ± 9.2	26.07 ± 0.06	0.24 ± 0.04	0.29 ± 0.02
Co	4.6 ± 3.5	26.85 ± 0.52	0.34 ± 0.36	--
Ni	1.0 ± 1.1	28.00 ± 0.17	0.11 ± 0.18	--

*Fitted widths of a Monte Carlo simulation of this element in the HIIS detectors.

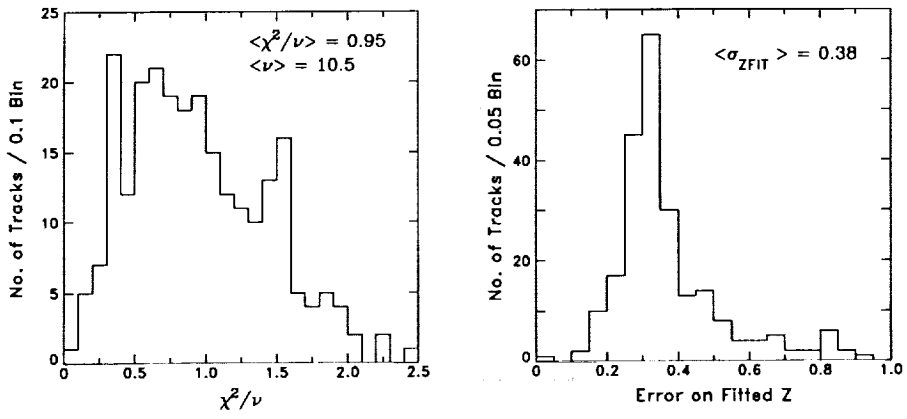

Figure 6: (a) Histogram of the reduced χ^2 values for the tracks in Fig. 5. The average value of reduced χ^2 is 0.95, for an average of 10.5 degrees of freedom. (b) Histogram of the errors on the fitted Z values. The distribution peaks at 0.3, and the average error on the fitted Z is 0.38.

We have made strenuous efforts to understand the "Mn" peak as an error or artifact but have not yet succeeded in doing so. First of all, one cannot simply shift the charge histogram by one unit, since this produces an equally unsatisfactory (Co+Ni)/Fe ratio of ~0.5. Second, the "Mn" peak is obviously not a simple fragmentation effect, since at these energies (> 100 MeV/n), incident Fe would yield fragments uniformly distributed across the sub-Fe elements. Third, the tracks in the "Mn" and "Fe" peaks cannot be separated by selection cuts on quantities like incidence angle, track length, penetration depth into the stopping sheet, χ^2 of the fit, location in the sheets, etc. Finally, the peak structure in Fig. 5 is highly unlikely to be statistical fluctuation: when we force the histogram at $Z > 24$ to fit a single gaussian, we get $\sigma = 0.8$, but with $\chi^2/NDF = 3.2$.

We have also verified that the charge histogram is not an artifact of our analysis software. In particular, our Monte Carlo program yields "simulated data" identical in format to that produced by our microscope data-acquisition programs. We used the Monte Carlo to simulate severely smeared data from a detector with no intrinsic resolution. When we passed these data through an "end-to-end" test of our analysis programs, they produced a flat charge distribution with no statistically significant peaks. The multiple peaks in Fig. 5 are thus a real feature of the data.

At this point, the only detector effects which we have not yet ruled out are (1) a sudden shift in the detector calibration; or (2) a continuous drift in the calibration, with particles collected episodically. In either case, it is further required that the calibration shift correspond almost exactly to $\Delta Z = 1$ unit. Such a calibration shift seems unlikely, but further analysis will enable us to confirm or exclude this possibility. In particular, 85% of the data in Fig. 5 comes from a single module. We have seven other modules, each with a different calibration. Although environmental effects may have conspired to produce a calibration shift of $\Delta Z = 1$ in one module, it is highly unlikely that the shift could be the same in all the modules. When we collect enough tracks from the same depth in a second module, it should be immediately clear whether or not the compositional anomaly shown here is real. Until then, we emphasize that the above results should be regarded as preliminary.

If we take the charge identifications in Fig. 5 at face value, the incident composition of stopping particles apparently varies with energy. When we select the highest energy tracks, with incident energy at the surface of LDEF > 800 MeV/n and which have passed through an average of 33 g/cm^2 of aluminum plus plastic, we observe a (Sc-Mn)/Fe ratio of 2.2 ± 0.6. This agrees with the value of 2.0 we calculate by propagating an incident galactic cosmic ray composition and spectrum through a mass model of the satellite[22] to the observation point. On the other hand, near the top of the stack, under only 2.6 g/cm^2 and at incident energies 140-280 MeV/n, we observe (Sc-Mn)/Fe = 3.2 ± 0.8, grossly inconsistent with both galactic and solar energetic particle (SEP) composition.

At low energies, our composition appears to be consistent with previous reports on below-cutoff heavy-ions observed in the magnetosphere. At 140-280 MeV/n, we observe (Sc-Cr)/Fe = 1.3 ± 0.4. Previously-reported values are 1.2 ± 0.3 (at 25-125 MeV/n; Ref. 3) and 1.5 ± 0.7 (at 50-250 MeV/n; Ref. 4). It should be noted, however, that this apparent good agreement may be accidental because (1) the HIIS data may contain Fe from SEP events, whereas the results from Refs. 3 and 4 are not contaminated by SEPs; and (2) it is not clear from their published data that the other experiments have sufficient resolution to separate Mn and Fe. If Fig. 5 were correct, how they handled Mn would greatly affect their value for this ratio.[6*]

[6*] If we assume that all of our "Mn" tracks are really Fe, we get a low-energy sub-Fe/Fe ratio of ~0.5. This is consistent with normal galactic cosmic ray composition. But at such low energies, fully-ionized galactic cosmic rays cannot reach the LDEF orbit. As discussed below, partially-ionized solar-energetic particles can penetrate to the LDEF orbit. But in that case, we would expect a sub-Fe/Fe ratio of only a few percent. Thus, even if the "Mn" is spurious, the origin of these low-energy Fe group ions remains unclear.

STOPPING HEAVY ION FLUXES

Charge State of Solar Energetic Particles. Fig. 7 shows our results to date on Fe. In this plot, the fluxes are corrected back to the surface of the satellite, taking into account fragmentation losses. (Feed-down from heavier elements is negligible since the abundance of elements heavier than Fe is only ~5% of Fe.) The GCR curve in Fig. 7 is an absolute prediction, averaged over the solar-cycle variation during the HIIS mission[23] and convoluted with the geomagnetic transmission function. The transmission function was calculated using techniques described in Ref. 24 and averaged over the observed arrival directions, which were primarily from the west, where the cutoff is lowest. The transmission function also took into account cutoff suppression caused by geomagnetic storms. To do this, we used the model of Flueckiger, Shea, and Smart (Ref. 25, hereafter FSS) to calculate suppressed cutoffs for nine different levels of geomagnetic activity, corresponding to K_p=0-8$^+$. These nine transmission functions were then combined in a weighted average, with relative weights determined from a survey of the frequency of various K_p conditions during the mission.

At the highest energies, our observed Fe flux is consistent with galactic cosmic rays. Galactic cosmic rays do not, however, account for the observed flux below ~800 MeV/n. We have also argued[26] that the flux at 600 MeV/n is also too large to be due to albedo. These particles may, however, come from the very large SEP events which occurred during the LDEF mission. At ~1 MeV/n, SEP Fe is known to be only partially-ionized[27], with a mean charge of 13.9 $\pm$ 0.5. If this charge state distribution is independent of the energy, SEPs might explain at least part of the observed flux.

To estimate the SEP contribution to the HIIS observations, we obtained from the University of Chicago instrument on IMP-8 a survey[28] of solar flare events during the HIIS mission. Preliminary results from this survey show that only 3 flares (Sept 29, Oct 16, and Oct 24 1989) produced significant Fe flux at

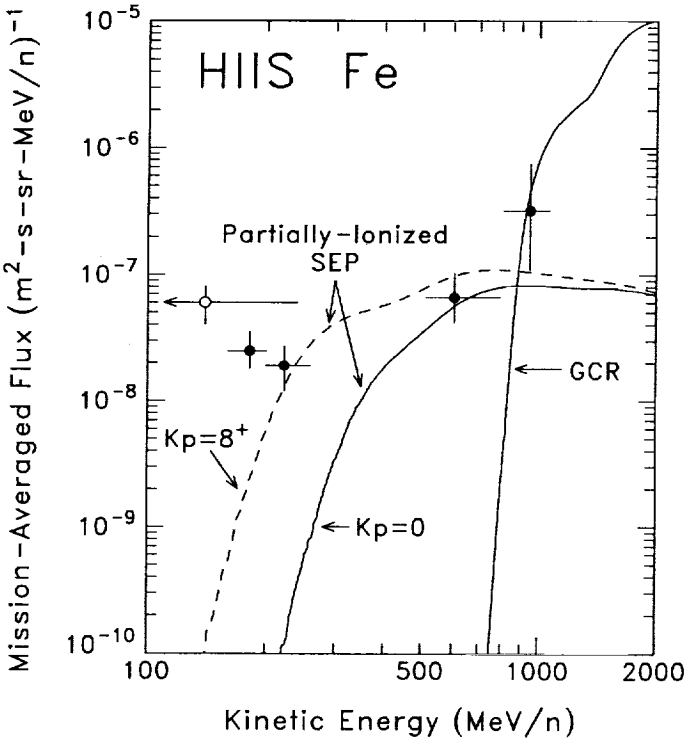

Figure 7: HIIS Fe flux measurements inside the magnetosphere, compared to galactic cosmic rays (GCR) and to partially-ionized SEPs, transmitted through a quiet magnetosphere (K_p=0, solid line) and a stormy magnetosphere (K_p=8$^+$, dashed line). The open circle at 40-240 MeV/n is a measurement from the Kiel experiment[31] on LDEF of Z $\geq$ 20 ions, of which only 30-50% are estimated to be Fe.

200-400 MeV/n. For these three flares, the Chicago instrument provided both fluences and spectral indices. We used these indices to extrapolate to both lower and higher energies. We then transmitted the SEP flux to HIIS, assuming the Fe ions to have the same charge state distribution at all energies as observed at 1 MeV/n. To estimate the effect of geomagnetic storms, we made the calculations twice, once for a quiet magnetosphere (K_p=0) and once for a highly-disturbed magnetosphere (K_p=8^+), using the FSS cutoff suppression model. The results of these calculations are also shown in Fig. 7. At low energies, there is still more flux than this calculation accounts for.[7*] At ~600 MeV/n, however, the HIIS flux agrees well with the extrapolation from the IMP-8 measurements. In fact, assuming all of the observed Fe at 600 MeV/n are solar energetic particles implies an average charge state $\langle Q \rangle = 13.8 \pm 0.9$ (stat) $\pm$ 1.5 (syst), where the statistical error considers only that of the presently available HIIS data and the systematic error is an estimate of the uncertainty in geomagnetic transmission. This preliminary result is in good agreement with the measured mean charge state at 1 MeV/n.

Note that Fig. 7 grossly overstates the range of uncertainty in the SEP flux caused by geomagnetic activity. In particular, our preliminary survey of geomagnetic activity during the HIIS mission shows that a magnetic storm as large as K_p=8^+ never occurred simultaneously with the arrival of solar energetic Fe ions. With a careful phasing of the observed exomagnetospheric SEP fluxes, geomagnetic activity, and the LDEF orbit, the geomagnetic uncertainty in the SEP charge state determination can be greatly reduced.

We will continue our study of solar energetic ions in the HIIS detectors, in order to measure the charge state of solar energetic Fe and possibly other elements, such as Ca. The measurements in Fig. 7, which fall just below and just above the energy range of IMP-8 measurements, come from sheets at the top and bottom of a module. In between there are 240 unetched sheets per module, which we can use to increase statistics and to trace out the Fe spectrum at the same energies as the IMP-8 measurements. Data on composition and arrival directions will also provide unique signatures of solar energetic particles (namely, sub Fe/Fe ~0.01 after correcting for fragmentation in the detector and arrival overwhelmingly from the directions of lowest cutoff). We will reduce uncertainties in the geomagnetic transmission by carefully phasing the SEP flux, geomagnetic activity, and the LDEF orbit. To test the reliability of our cutoff calculations, we will do ray tracing calculations from points along the LDEF orbit, using the program of Flueckiger et al.[29] and the Tsyganenko model[30] of the magnetosphere.

Low Energy Ions of Unknown Origin. Fig. 7 shows a larger Fe flux below 200 MeV/n than even partially-ionized SEPs may be able to account for. (Such a conclusion, however, requires more thorough study of geomagnetic transmission at low rigidities.) As shown in Fig. 7, our observed flux is in good agreement with preliminary results from another LDEF experiment[31]. We also appear to have a strong compositional anomaly at these energies, similar to previous reports[2-5]. At present the origin of these low energy particles is not understood. In future work, we will use the HIIS data to extend observations of these ions, in order to clarify their origin. With the top detector stacks, we can follow the Fe flux down to ~30 MeV/n. This spectral information, combined with our data on composition and arrival directions, may be used to test models for the origin of these particles, such as albedo, quasi-trapping, and a new exomagnetospheric source.

Anomalous Component. We plan to use the HIIS data to extend observations of the anomalous component (AC) to ~300 MeV/n. These particles are known to be singly-ionized[32], which greatly increases their transmission through Earth's magnetic field to LDEF's orbit. At energies below ~100 MeV/n neither galactic cosmic rays nor partially-ionized SEPs can penetrate to the LDEF orbit. At ~100-300 MeV/n, galactic cosmic rays are still geomagnetically excluded, and SEPs should be only a small and calculable background[8*]. Fig. 8 shows a simulation of HIIS measurements of anomalous component Ne

---

[7*] If the "Mn" tracks in Fig. 5 are taken as Fe, the low energy fluxes increase by a factor of ~3, making the apparent excess even larger.

[8*] Arrival direction distributions may be useful in separating SEPs and AC particles at these energies: the singly-charged AC ions have high rigidities which give them unimpeded access from all directions. SEPs at these energies, on the other hand, can only reach HIIS from westerly arrival directions, where the cutoff is lowest.

and Ar. In this figure, the flux expectations are derived from a power-law extension of the AC oxygen flux[33] at ~1 AU, averaged over the solar cycle variation[34] during the LDEF mission, and scaled and shifted in intensity and energy according to the factors given in Ref. 35. The open symbols show the statistical precision we can achieve *using only 10% of the detector area*, except for Ar above 85 MeV/n, where the simulated precision would require all of the available area. If the flux falls more steeply than these extrapolations suggest, we will place upper limits on the high energy AC spectrum. In either case, our results will give new information on the capabilities of the AC accelerator, which is believed to be at the solar wind termination shock.

The solid points in Fig. 8 show the 90% CL upper limits we have obtained so far. The Ar upper limit is actually based on 5 observed tracks. We treated these in an upper limit, pending an estimate of possible background from SEPs and their fragments at E > 150 MeV/n. The Ne flux limit at ~75 MeV/n comes from a null result in scanning 1.2% of the available area, using only a portion of a single detector sheet.

By using Lexan UV enhancement, we should also be able to observe anomalous oxygen at energies of 30-50 MeV/n in the top detector stacks, with statistical precision comparable to that of the Ne simulation in Fig. 8. We will also search for evidence of the anomalous component in the spectra of other elements.

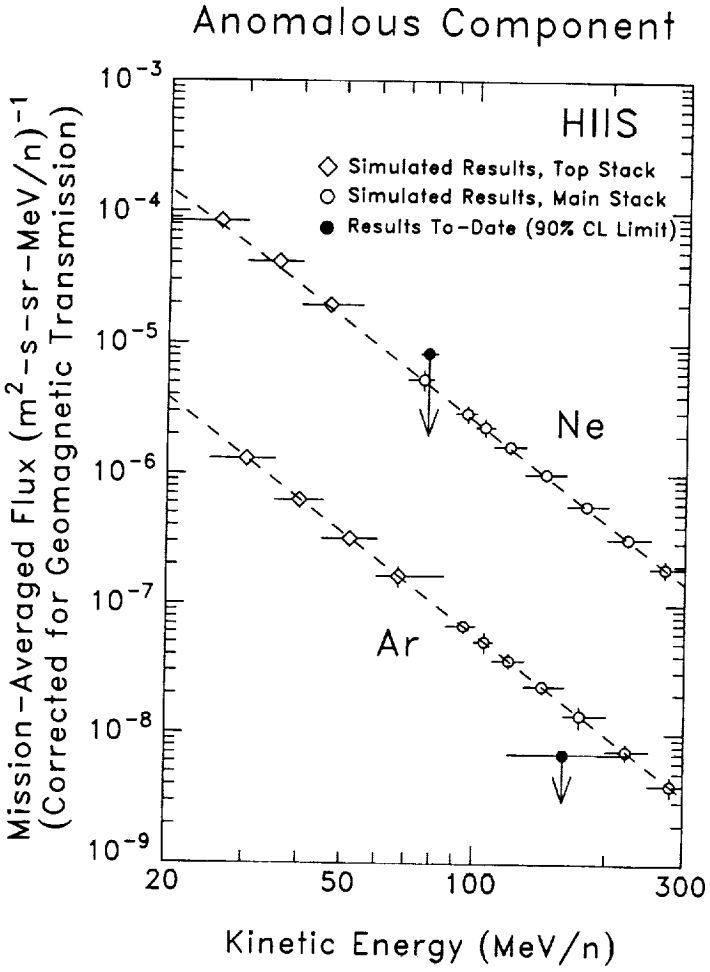

Figure 8: Simulation of HIIS measurements of anomalous component Ne and Ar, assuming they continue as a power law from low energy observations. (Where not visible, the error bars are smaller than the symbols.) Also shown are HIIS upper limits achieved so far. See text for details.

STATUS OF THE ULTRAHEAVY GALACTIC COSMIC RAY ANALYSIS

In Ref. 18, we outlined our method of analyzing ultraheavy galactic cosmic ray tracks. To date we have collected 127 relativistic ultraheavy cosmic rays with $Z > 45$ by scanning a portion of sheets at the top of Module E. Extrapolating from this result, we expect a total of 1120 ± 100 tracks at $Z > 45$ in the seven modules which did not leak. (For comparison, the HEAO dataset[36] contained ~370 nuclei in this charge range.) Based on the time it took to collect and measure the tracks in Module E, we estimate that 3 microscopist-years will be required to obtain the entire ultraheavy dataset.

CONCLUSIONS

The HIIS data appear to show stopping heavy-ions from a several sources, including galactic cosmic rays and solar energetic particles. Below ~200 MeV/n, there also appears to be an additional source, whose nature is not yet understood. At low energies we also appear to have a strong compositional anomaly, with a large sub-Fe/Fe ratio, apparently consistent with earlier reports[2-5] and preliminary results from another LDEF experiment[31].

In future work, we will extend our observations to a second HIIS module, to confirm or refute our compositional anomaly. We will also collect data from the ~250 unetched sheets in the middle of the stack, so as to search for SEPs in the 200-400 MeV/n energy range covered by the IMP-8/Chicago measurements. We will also make more detailed studies of geomagnetic transmission at low rigidities, using the ray-tracing program of Ref. 29, to fully understand the SEP contribution to our data. Once we have understood the SEP contribution, we should be able to separate out the unknown low-energy component. Using detector sheets nearer to the top of the module, we can follow the Fe-group flux down to ~30 MeV/n. This spectral information, combined with our data on composition and arrival directions, may be used to test models for the origin of these particles, such as albedo, quasi-trapping, or a new exomagnetospheric source.

ACKNOWLEDGEMENTS

We greatly thank Bill Dietrich for providing us with preliminary IMP-8 data on SEP events during the HIIS mission. We thank Bonnie Colborn for her generous assistance in running the LDEF mass model program. We also thank Rudolf Beaujean for discussions of his observations of stopping heavy ions on LDEF. This work has been supported by the Office of Naval Research and NASA.

REFERENCES

1. Krause, J.: Magnetische-verbotene Teilchen mittlerer Energie bei der Spacelab 1 Mission, Ph.D. thesis, Institute fuer Kernphysik, Univ. Kiel, FRG, 1986.
2. Biswas, S. et al.: Observation of Low-Energy (30-100 MeV Nucleon^{-1}) Partially Ionized Heavy Ions in Galactic Cosmic Rays. Astrophys. J. Letters, vol. 359, 1990, pp. L5-L9.
3. Biswas, S. et al.: Ratio of Sub-Iron (Sc-Cr) To Iron Ions in Low Energy Galactic Cosmic Rays Inside & Outside of Earth's Magnetosphere. Proc. 22nd ICRC (Dublin), vol. 2, 1991, pp. 308-311.
4. Gargarin, Yu.F. et al.: Sulfur-Nickel Nuclei at Small Energies in Cosmic Rays, Proc. 21st ICRC (Adelaide), vol. 3, 1990, pp. 11-14.
5. Grigorov, N.L. et al.: Heavy Ions in Cosmic Rays. Sov. J. Nucl. Phys. (Yadernaya Fizica), vol. 53, 1991, pp. 827-834.
6. Mitra, B. et al.: Implications of the Observations of Partially Ionised States in Low Energy Galactic Cosmic Rays. Proc. 22nd ICRC (Dublin), vol. 2, 1991 pp. 312-315.
7. CR-39 is poly diethylene glycol bis-alyl carbonate and was invented at Pittsburgh Plate Glass's Columbia Resin Laboratory in Barberton, OH.
8. Adams, J.H.Jr.: A Curing Cycle for Detector-Quality CR-39. Nucl. Tracks: Meth., Inst. and Appl., Suppl. 3, 1982, pp. 145-148.

9. Tarle, G.: Improvement of the Etching Properties of CR-39 Plastic Track Detectors. Proc. 17th ICRC (Paris), vol. 8, 1981, pp. 74-77.
10. Lexan is the trade name for bis-phenol A polycarbonate, as sold by General Electric, Pittsfield MA. It is also sold under the tradenames of Tuffak and Rodyne-P.
11. Stiller, B.; Adams, J.H.Jr.; and Beahm, L.P.: Ultraviolet Enhancement of Tracks in Lexan with Black Fluorescent Lamps. Nucl. Tracks, vol. 12, 1986, pp. 137-40.
12. O'Sullivan, D. et al.: The Ultra Heavy Cosmic Ray Experiment. Proc. First LDEF Post-Retrieval Symposium, NASA CP-3134, Part 1, 1991, pp. 367-375.
13. Kapton is a polyamide plastic manufactured by Du Pont Inc., Wilmington, DE.
14. Fleischer, R.L.; Price, P.B.; and Walker, R.M.: *Nuclear Tracks in Solids: Principles and Applications.* (Berkeley: University of California Press), 1975, pp. 57-63.
15. Benton, E.V. and Nix, W.D.: The Restricted Energy Loss Criterion for Registration of Charged Particles in Plastics. Nucl. Inst. Meth., vol. 67, 1969, pp. 343-7.
16. Henke, R.P. and Benton, E.V.: On Geometry of Tracks in Dielectric Nuclear Track Detectors. Nucl. Inst. Meth., vol. 97, 1971, pp. 483-9; Somogyi, G. and Szalay, S.A.:Track-Diameter Kinetics in Dielectric Track Detectors. Nucl. Inst. Meth., vol. 109, 1973, pp. 211-32.
17. Adams, J.H.Jr.: Automated Track Measurements in CR-39. Nucl. Tracks, vol. 4, 1980, pp. 67-76.
18. Adams, J.H.Jr.; Beahm, L.P.; and Tylka, A.J.: Preliminary Results from the Heavy Ions in Space Experiment. Proc. First LDEF Post-Retrieval Symposium, NASA CP-3134, Part 1, 1991, pp. 377-391.
19. Drach, J. et al.: Effect of Oxygen on Response of Plastic and Glass Track Detectors. Nucl. Inst. Meth., vol. B28, 1987, pp. 364-8.
20. Yadav, J.S. and Singh, R.K.: Change of CR-39(DOP) Track Detector Response as a Result of Space Exposure. Nucl. Tracks Radiat. Meas., vol. 17, 1990, pp. 579-82.
21. Adams, J.H. Jr.; Beahm, L.P.; and Tylka, A.J.: The Heavy Ions in Space Experiment: Preliminary Calibration and Analysis. Proc. 22nd ICRC (Dublin), vol. 2, 1991 pp. 523-526.
22. Colborn, B.L. and Armstrong, T.W.: Geometry and Mass Model of Ionizing Radiation Experiments on the LDEF Satellite. SAIC Report No. SAIC-TN-9202, 1992.
23. Nymmik, R.A. et al: A Model of Galactic Cosmic Ray Fluxes. Nucl. Tracks. & Radiat. Meas., vol. 20, 1992, pp. 427-429.
24. Adams, J.H. Jr.; Beahm, L.P.; and Tylka, A.J.: The Charge State of the Anomalous Component: Results from the Trapped Ions in Space Experiment. Astrophys. J., vol. 377, 1991, pp. 292-305.
25. Flueckiger, E.O.; Smart, D.F., and Shea, M.A.: A Procedure for Estimating the Changes in the Cosmic Ray Cutoff Rigidities and Asymptotic Directions at Low and Middle Latitudes During Periods of Enhanced Geomagnetic Activity. J. Geophys. Res., vol. 91, 1986, pp. 7925-7930.
26. Adams, J.H. Jr.; Beahm, L.P.; and Tylka, A.J.: Observations from LDEF of Heavy Ions Below the Geomagnetic Cutoff. Proc. 22nd ICRC (Dublin), vol. 1, 1991 pp. 619-622.
27. Luhn, A. et al.: Ionic Charge States of N, Ne, Mg, Si, and S in Solar Energetic Particle Events. Adv. in Space Res., vol. 4, 1984, pp. 161-164.
28. Dietrich, W.F. 1992, private communication.
29. Flueckiger, E.O. et al.: A New Concept for the Simulation and Visualization of Cosmic Ray Particle Transport in the Earth's Magnetosphere. Proc. 22nd ICRC (Dublin), vol. 3, 1991, pp. 648-651.
30. Tsyganenko, N.A.: A Magnetospheric Magnetic Field Model with a Warped Tail Current Sheet. Planet. Space Sci., vol. 37, 1989, pp. 5-20.
31. Beaujean, R. et al.: in Second LDEF Post-Retrieval Symposium, NASA CP-3194, 1993. private communication.
32. Adams, J.H.Jr. et al.: The Charge State of the Anomalous Component of Cosmic Rays. Astrophys. J. Lett., vol. 375, 1991, pp. L45-L48.
33. Cummings, A.C. and Stone, E.C.: Energy Spectra of Anomalous Cosmic-Ray Oxygen During 1977-1987. Proc. 20th ICRC (Moscow), vol. 3, 1987, pp. 421-424.
34. Mewaldt, R.A.: Temporal Variations of Anomalous Cosmic Rays and Further Evidence for Anomalous Cosmic Ray Hydrogen. Proc. 21st ICRC (Adelaide), vol. 6, 1990, pp. 160-163.
35. Cummings, A.C. and Stone, E.C.: Elemental Composition of the Anomalous Cosmic-Ray Component. Proc. 20th ICRC (Moscow), vol. 3, 1987, pp. 413-416.
36. Binns, W.R. et al.: Abundances of Ultraheavy Elements in the Cosmic Radiation: Results from HEAO 3. Astrophys. J. vol. 346, 1989, pp. 997-1009.

PROGRESS REPORT ON THE ULTRA HEAVY COSMIC RAY EXPERIMENT (A0178)

A. Thompson, D. O'Sullivan, J.Bosch and R. Keegan
Dublin Institute for Advanced Studies (DIAS), Ireland
Phone: +353-1-774321, Fax: +353-1-682003

K.-P. Wenzel and F. Jansen
Space Science Dept of ESA, ESTEC, Noordwijk, The Netherlands
Phone:+31-1719-83573, Fax: +31-1719-84698

C. Domingo
Universitat Autònoma de Barcelona, Spain
Phone:+34-3-581-1530, Fax: +34-3-581-2155

ABSTRACT

The Ultra Heavy Cosmic Ray Experiment (UHCRE) is based on a modular array of 192 side-viewing solid state nuclear track detector stacks. These stacks were mounted in sets of four in 48 pressure vessels employing sixteen peripheral LDEF trays. The extended duration of the LDEF mission has resulted in a greatly enhanced scientific yield from the UHCRE. The geometry factor for high energy cosmic ray nuclei, allowing for Earth shadowing, was 30 m^2-sr, giving a total exposure factor of 170 m^2-sr-y at an orbital inclination of 28.4 degrees. Scanning results indicate that about 3000 cosmic ray nuclei in the charge region with Z>65 have been collected. This sample is more than ten times the current world data in the field (taken to be the data set from the HEAO-3 mission plus that from the Ariel-6 mission) and is sufficient to provide the world's first statistically significant sample of actinide (Z>88) cosmic rays.

Results to date are presented including details of a sample of ultra-heavy cosmic ray nuclei, analysis of pre-flight and post-flight calibration events and details of track response in the context of detector temperature history. The integrated effect of all temperature and age related latent track variations cause a maximum charge shift of $\pm 0.8e$ for uranium and $\pm$ 0.6e for the platinum-lead group. The precision of charge assignment as a function of energy is derived and evidence for remarkably good charge resolution achieved in the UHCRE is considered. Astrophysical implications of the UHCRE charge spectrum are discussed.

INTRODUCTION

Prior to LDEF there were only two spacecraft which carried experiments dedicated to the investigation of ultra-heavy nuclei. HEAO-3 (Binns et al., 1989) and Ariel 6 (Fowler et al., 1987) were launched in 1979 and employed electronic detectors of geometric factors 5 m^2-sr and 2 m^2-sr respectively. The combined sample from both missions with $Z \geq 65$ comprises approximately 300 events, and the entire sample of actinides ($Z \geq 88$) is only 3.

The experiment on LDEF (Thompson et al., 1990) which was dedicated to the study of ultra-heavy (UH) nuclei consists of an extensive array of primarily lexan polycarbonate solid state nuclear track detectors, of geometric factor 30 m^2-sr, which were mounted within cylindrical aluminium pressure vessels in 16 LDEF experiment trays.

DESCRIPTION OF UHCRE

Since the primary objective of the UHCRE experiment was to study ultra-heavy cosmic ray nuclei of $Z > 65$ and the geomagnetic cut-off was $\sim$ 1 GeV/N, the main detector material chosen was lexan polycarbonate.

Each stack consists of a sandwich of many layers of lexan (approx 70 plates) together with several sheets of lead interleaved. The lead sheets act both as electron strippers and velocity degraders and were chosen because of their low cross section for nuclear interactions.

The stacks are 20.5 cm × 26.0 cm in area and are approximately 5 g/cm^2 thick. All 192 stacks were mounted in sets of four within cylindrical Eccofoam moulds which were then inserted into aluminium pressure vessels (48 in total).

All cylinders, except one, were pressurised to 1.0 bar with a dry oxygen-nitrogen-helium mixture in the ratio of 20:70:10. Three pressurised vessels were mounted on each experiment tray which in turn was mounted on the LDEF framework.

PRESENT UHCRE STATUS

Following an initial scan using wide field Nikon zoom scanning microscopes, it was decided to employ the ammonia scanning technique for event location. This technique, which involves long term etching (of up to 21 days) in 6.25N NaOH at 40°C was undertaken on 2 plates situated approximately at $\frac{1}{3}$ and $\frac{2}{3}$ of a stack depth and correlations between the etched cylinders were sought.

Current scanning gives approximately 15 cosmic ray events per stack bringing the expected number of cosmic ray nuclei recorded to approximately 2800 nuclei.

Having located the UH candidates alternate plates from a set of 20 plates at the top of each stack and a similar set from the bottom of each stack were etched for 5 days at 40°C. The remaining plates in each set were kept for further analysis if required.

Etch cone measurements are carried out on Leitz Ortholux microscopes which have 10x and 12.5x eyepieces and 100x oil-immersion objectives. From these cone measurements, both track etch rate (V_t) and bulk etch rate (V_g) are calculated and the reduced etch rate $\left(S = \frac{V_t}{V_g}\right)$ is then determined. Shown in figures 1,2,3 and 4 are plots of S versus Path Length (lexan equivalent) for various recorded UHCRE events. The small change in etch rate in traversing the stack is typical of relativistic ultra heavy cosmic ray nuclei. Fig. 4 shows an UH nucleus (Z $\approx$ 90) which has interacted after passing through almost 9.5g/cm^2 of matter, losing approximately 10 charge units in the process.

To date approximately 65 cosmic ray events have been measured and processed. Charge identification is based upon the determination of the fractional etch rate gradient (Fowler et al., 1976), defined as

$$G = \frac{1}{S}\frac{dS}{dx}$$

where S is the reduced etch rate and x is the path length, and on the effective reduced etch rate (S_{eff}). The relevant data for a given event is reduced to one point which may be plotted on an $S_{eff} - G$ plot as shown in Fig. 5. All cosmic ray events to date are shown in Fig. 5, together with the location of the Z =80, 72, and 62 preliminary calibration curves which are based on the assumed relation

$$S = g(REL)^h$$

where REL is the restricted energy loss rate and g and h are determined from calibration data. The preliminary UHCRE status report (O'Sullivan et al., 1991) was based on calibration using U nuclei. The present work includes calibration with 1150 MeV/N Au nuclei also. Calibration studies will be extended over the next few months.

CONCLUSIONS AND DISCUSSION

A post flight thermal analysis on the UHCRE was published in March 1992 by Lockheed Engineering and Sciences Co. (Sampair and Berrios, 1992). The results of the thermal analysis showed that the tray located at position C6 had the widest temperature cycle of 28.8°C with a maximum of −2.3°C and a minimum of −31.1°C. The tray position E10 had the smallest temperature cycle of 11.9°C with a temperature range of -26.0°C to - 14.2°C. The analysis also showed that the maximum detector stack thermal gradient was 0.15°C per stack. Hence we expect virtually no difference in sensitivity between the top and bottom of a given stack.

Results of the comparison of the pre-flight and post-flight uranium calibration events in the UHCRE stacks (Thompson et al., 1991) indicate that there is no difference between the two, within the limits of experimental error. This work, when taken into consideration with the long term ageing work (Domingo et al., 1990) and the short term ageing (Thompson et al., 1991) indicate that there should be no appreciable loss in charge resolution under LDEF exposure conditions.

Uranium calibration work indicates that the UHCRE detectors have undergone virtually no change in sensitivity or loss of charge resolution over the 5.8 year exposure period. The initial observations (see Fig.(5)) show a dramatic decrease in flux at approximately charge 83 with most of the events falling into the region $70 \leq Z \leq 83$. The distribution of points indicates a concentration of events in the platinum–lead region. It is also apparent that two actinide cosmic ray nuclei have been located at this stage of the analysis.

C-4

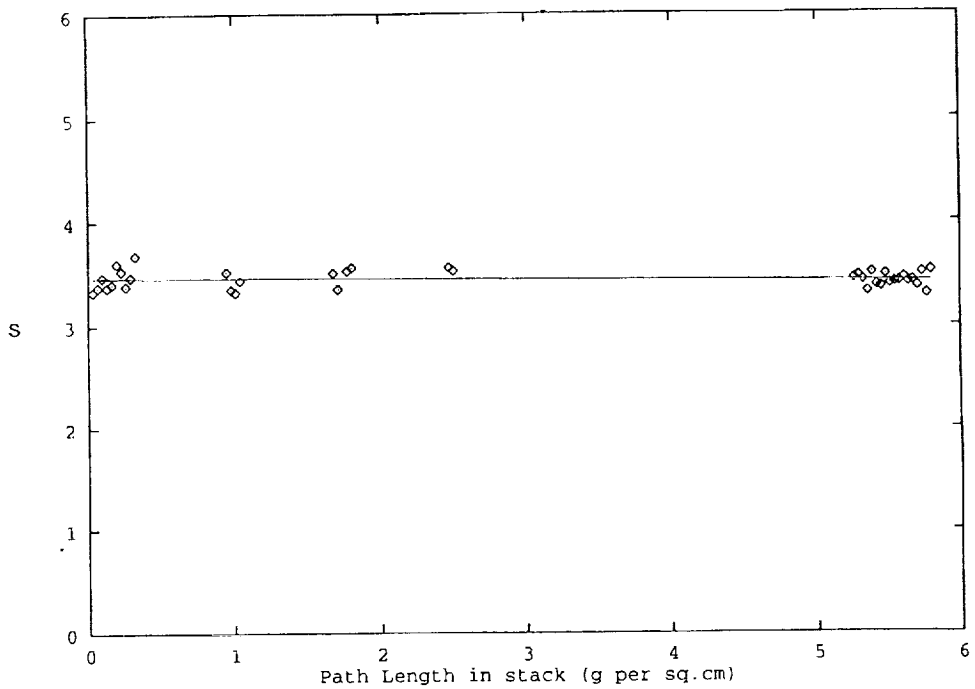

Fig.1 An S versus Path Length plot for Event No. 1 in Stack 86.

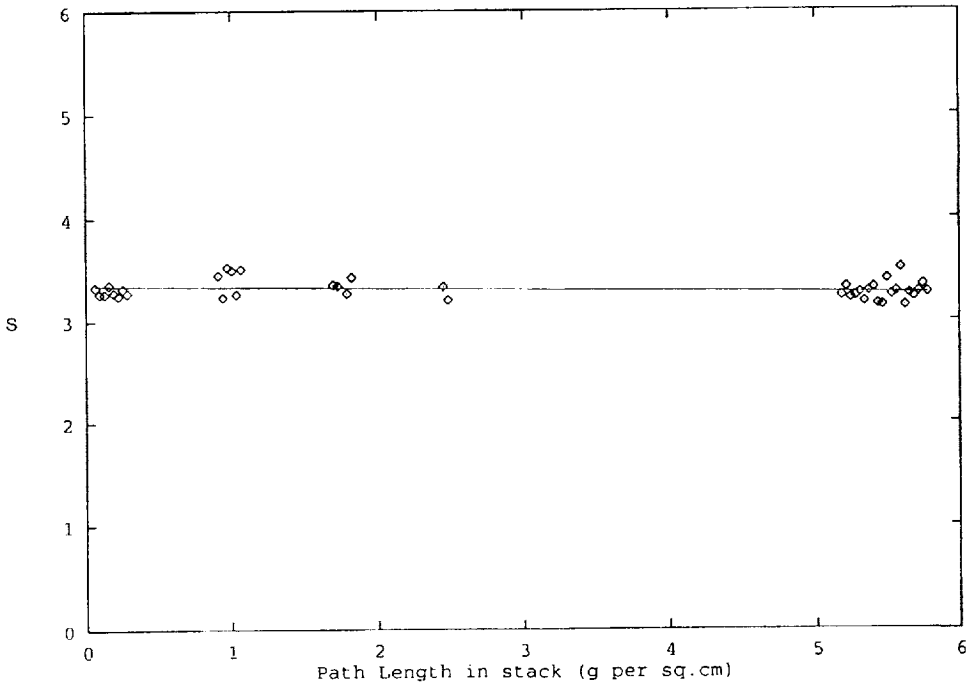

Fig.2 An S versus Path Length plot for Event No. 2 in Stack 40.

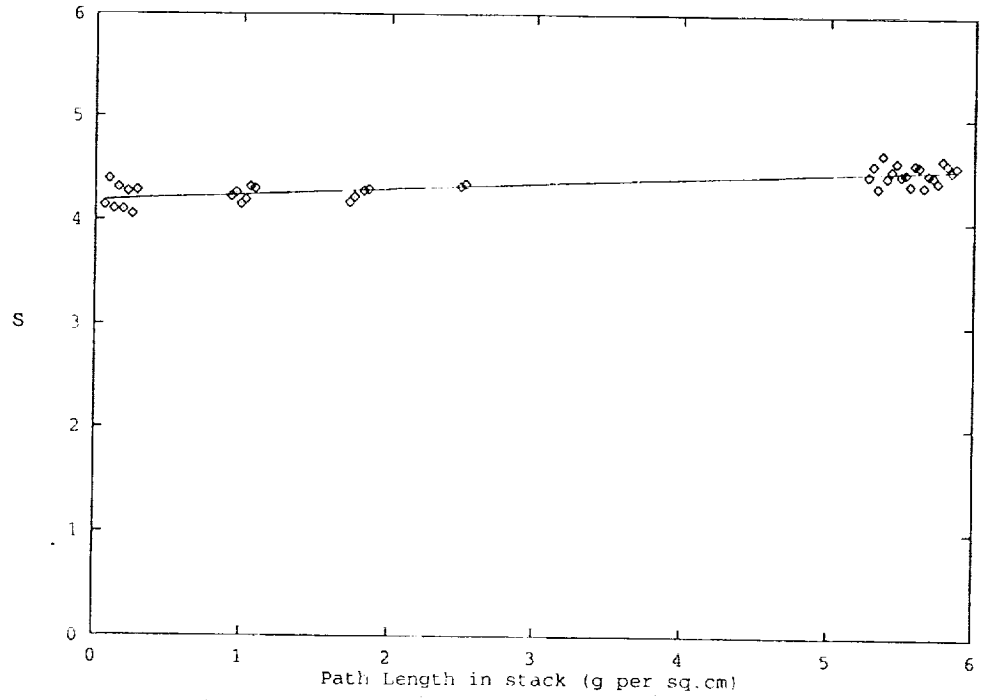

Fig.3 An S versus Path Length plot for Event No. 6 in Stack 40.

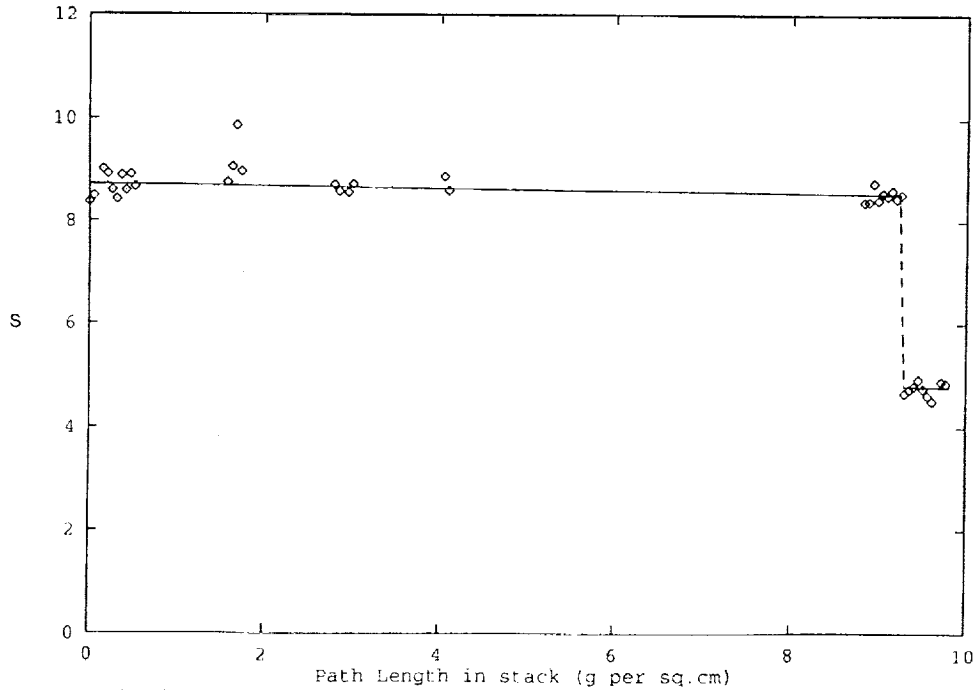

Fig.4 An S versus Path Length plot for Event No. 14 in Stack 123 (Actinide Candidate). Note interaction following path length of $\sim 9.5 \mathrm{g\ cm^{-2}}$ in the stack.

Further measuring and analysis is continuing and it is hoped that a set of data equivalent in size to the present world sample will be available for the next LDEF symposium.

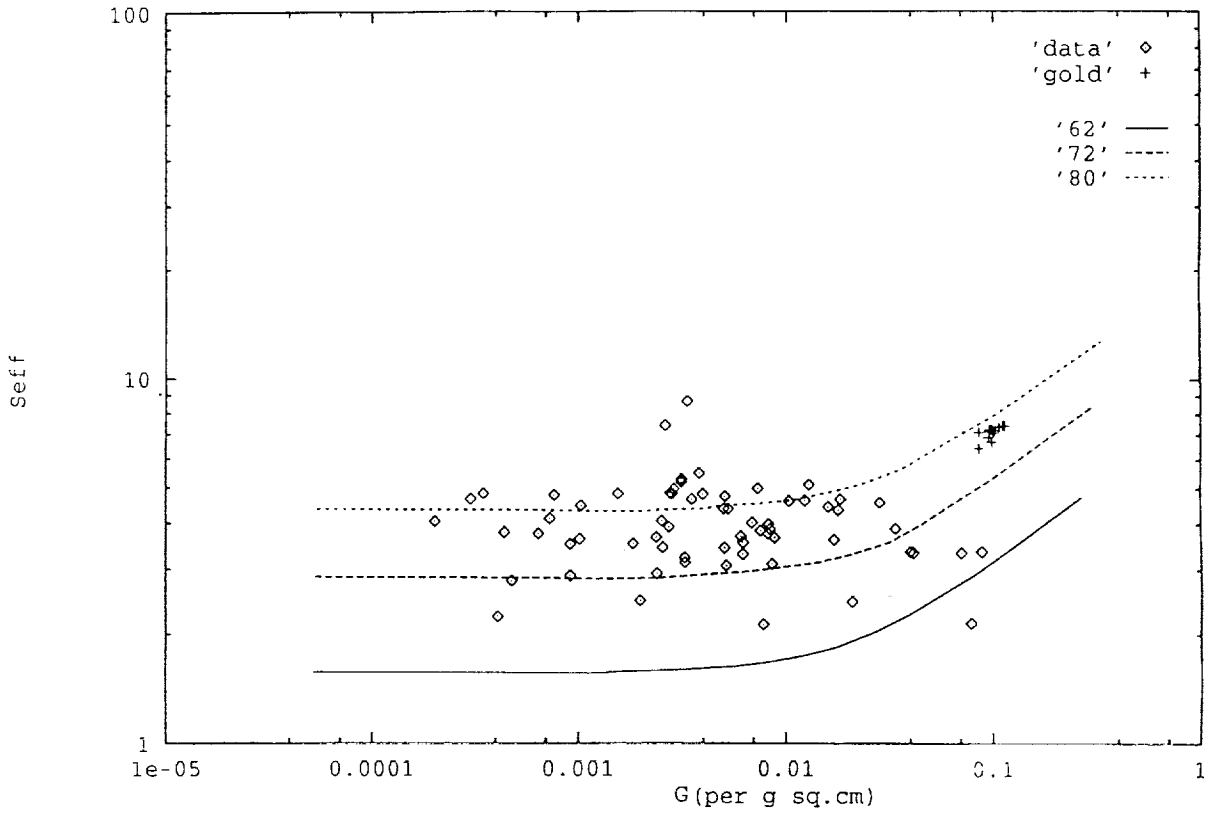

Fig.5 An S_{eff} versus G plot showing all cosmic ray events to date together with some gold calibration events. The preliminary locations of the calibration curves are shown for charges $Z = 80$, 72 and 62.

In view of the excellent quality of the UHCRE data it is hoped that we will be able to distinguish between different cosmic ray source and propagation models when a sufficient sample of nuclei has been analysed. For instance, attempts to describe the abundances of actinides and anti-protons in the cosmic radiation by means of the Leaky Box model have not been satisfactory. Eventually, results from the Dublin–ESTEC experiment will be compared with the predictions of a diffusion model which will be developed to examine the propagation of these particles.

ACKNOWLEDGEMENTS

The authors wish to express their thanks to the LDEF Office Project Staff, in particular J. L. Jones and W. H. Kinard, for their excellent managerial support since LDEF experiment selection. Furthermore they wish to acknowledge the support of many colleagues in ESTEC during hardware development, testing, integration and during de-integration activities. They are indebted to the LBL Bevalac staff, in particular H. Crawford, for continued technical support and assistance with numerous heavy ion exposures for UHCRE calibration and detector development. They wish to express their appreciation to Geraldine Broderick, Eileen Flood, Anne Grace, Susan Ledwidge and Hilary O'Donnell for SSNTD processing, measurement and data reduction. Part of this work was supported by the Spanish CICYT.

REFERENCES

1. Binns W. R., T. L. Garrard, P. S. Gibner, M. H. Israel, M. P. Kertzmann, J. Klarmann, B. J. Newport, E. C. Stone and C. J. Waddington. The Astrophysical Journal, (1989) **346**, 997-1009.

2. Fowler P. H., R. N. F. Walker, M. R. W. Masheder, R. T. Moses, A. Worley and A. M. Gay. The Astrophysical Journal, (1987) **314**, 739-746.

3. Thompson, A., D. O'Sullivan, K.–P. Wenzel, V. Domingo, C. Domingo, J. Daly, A. Smit. Proc. 21st ICRC (1990) 4, 441, Adelaide.

4. Fowler P. H., C. Alexander, V. M. Clapham, D. C. Henshaw, C. O'Ceallaigh, D. O'Sullivan, A. Thompson. High Resolution Study of Nucleonic Cosmic Rays with $Z \geq 34$. Proc. 9th Int. Conf. on SSNTD, Munich, 1976, 1007.

5. O'Sullivan D., A. Thompson, K.-P. Wenzel, C. Domingo, J. Bosch, R. Keegan and A. Smit. LDEF–69 Months in Space, First Post-Retrieval Symposium, (1991), 367-375.

6. Sampair T. R., W. M. Berrios. Post Flight Thermal Analysis, (1992) A0178-UHCRE.

7. Thompson A., D. O'Sullivan, K.-P. Wenzel, J. Bosch, R. Keegan, C. Domingo, J. Daly and A. Smit. Proc. 22nd ICRC Dublin, (1991) **2**, 543-546.

8. Domingo C., A. Thompson, D. O'Sullivan, C. Baixeras, F. Fernandez, A. Vidal-Quadras. Long Term Ageing Effect for Energetic Ultra-Heavy Ion Tracks in Polycarbonate Solid State Nuclear Track Detectors. Nuc. Inst. Meth. B51 (1990), 253.

AUTHOR INDEX

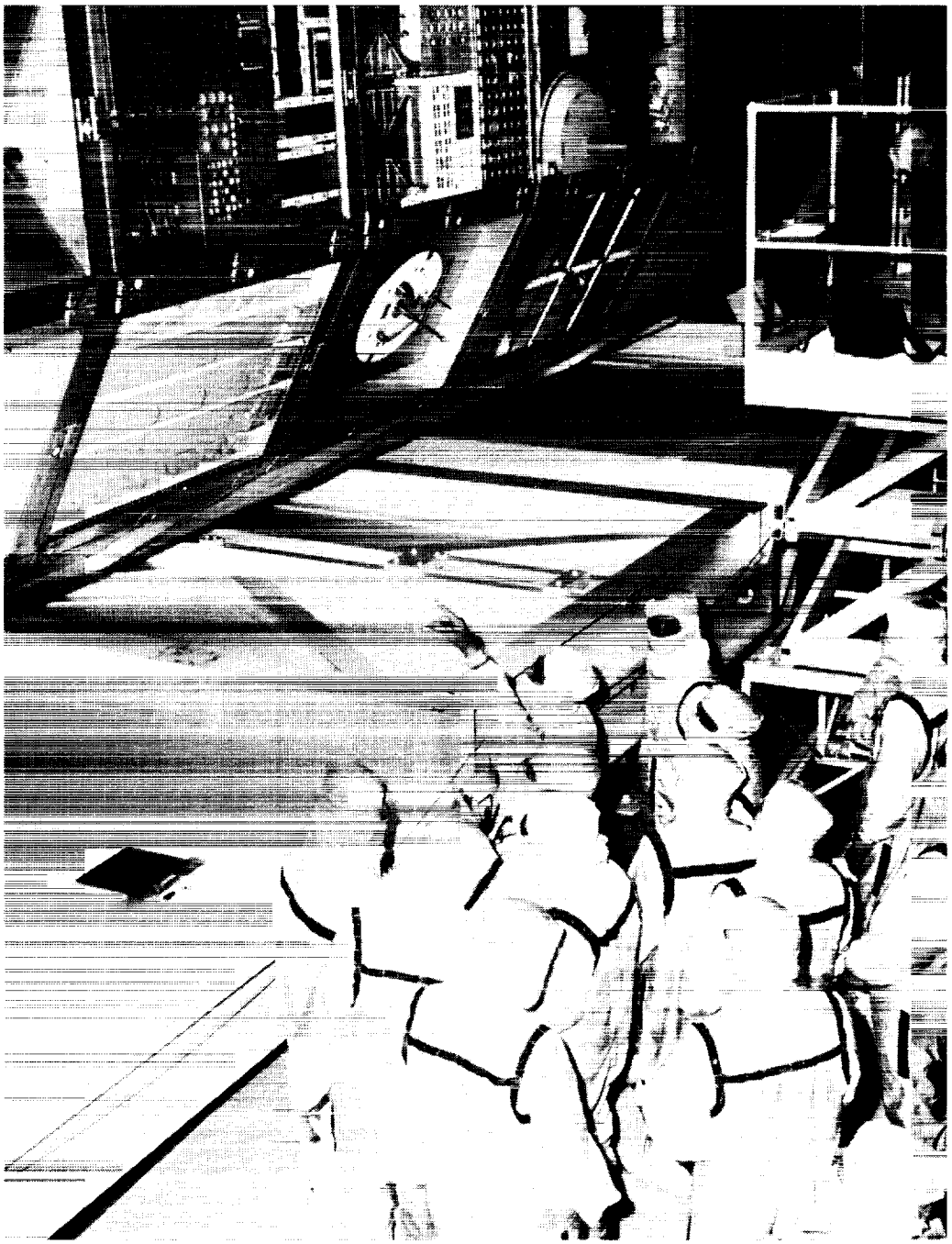

L-90-2127

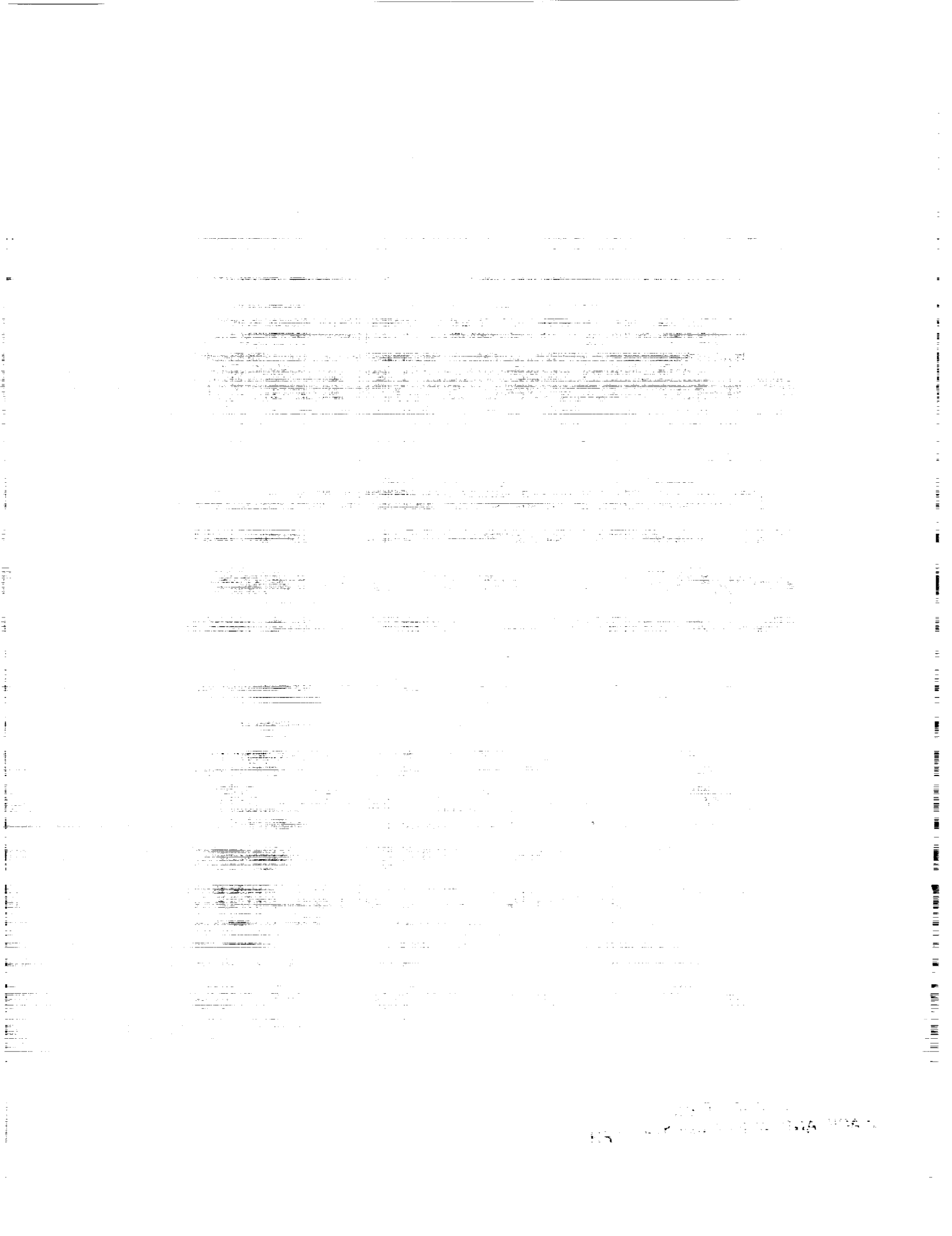

Author Index

Index Guide

Part 1, pages 1–274; Part 2, pages 275–738

Part 3, pages 739–1254; Part 4, pages 1255–1570

REPORT DOCUMENTATION PAGE

Form Approved
OMB No. 0704-0188

1. AGENCY USE ONLY *(Leave blank)*	2. REPORT DATE	3. REPORT TYPE AND DATES COVERED
	April 1993	Conference Publication

4. TITLE AND SUBTITLE
69 Months In Space—Second LDEF Post-Retrieval Symposium

5. FUNDING NUMBERS
506-48-91-11

6. AUTHOR(S)
Arlene S. Levine, Editor

7. PERFORMING ORGANIZATION NAME(S) AND ADDRESS(ES)
NASA Langley Research Center
Hampton, VA 23681-0001

8. PERFORMING ORGANIZATION REPORT NUMBER
L-17196

9. SPONSORING/MONITORING AGENCY NAME(S) AND ADDRESS(ES)
National Aeronautics and Space Administration
Washington, DC 20546-0001

10. SPONSORING/MONITORING AGENCY REPORT NUMBER
NASA CP-3194, Part 1

11. SUPPLEMENTARY NOTES

12a. DISTRIBUTION/AVAILABILITY STATEMENT
Unclassified–Unlimited

Subject Category 99

12b. DISTRIBUTION CODE

13. ABSTRACT *(Maximum 200 words)*
This document is a compilation of papers presented at the Second Long Duration Exposure Facility (LDEF) Post-Retrieval Symposium. The papers represent the data analysis of the 57 experiments flown on the LDEF. The experiments include materials, coatings, thermal systems, power and propulsion, science (cosmic ray, interstellar gas, heavy ions, micrometeoroid, etc.), electronics, optics, and life science.

14. SUBJECT TERMS
Space experiment

15. NUMBER OF PAGES
289

16. PRICE CODE
A13

17. SECURITY CLASSIFICATION OF REPORT	18. SECURITY CLASSIFICATION OF THIS PAGE	19. SECURITY CLASSIFICATION OF ABSTRACT	20. LIMITATION OF ABSTRACT
Unclassified	Unclassified	Unclassified	